# Effect of thermal cycles on rock massif stability

Claudia Juliana Villarraga Diaz

## To cite this version:

Claudia Juliana Villarraga Diaz. Effect of thermal cycles on rock massif stability. Earth Sciences. Universite Toulouse 3 Paul Sabatier (UT3 Paul Sabatier), 2018. English. NNT : . tel-01769973

HAL Id: tel-01769973
https://theses.hal.science/tel-01769973v1

Submitted on 18 Apr 2018

# THÈSE

**En vue de l'obtention du**

## DOCTORAT DE L'UNIVERSITÉ DE TOULOUSE

**Délivré par :**

Université Toulouse 3 Paul Sabatier (UT3 Paul Sabatier)

Cotutelle internationale avec Universitat Politécnica de Catalunya

---

**Présentée et soutenue par :**
**Claudia Juliana VILLARRAGA DIAZ**
**le** mercredi 28 février 2018

**Titre :**

# EFFECT OF THERMAL CYCLES ON ROCK MASSIF STABILITY

---

**École doctorale et discipline ou spécialité :**
ED SDU2E : Sciences de la Terre et des Planètes Solides

**Unité de recherche :**
UMR 5563 - GET - Geosciences Environnement Toulouse

**Directeur/trice(s) de Thèse :**
M. Jose DARROZES
M. Jean VAUNAT
Mme. Muriel GASC-BARBIER

**Jury :**
M. Jean SULEM (Rapporteur)
Mme. Irini DJERAN-MAIGRE (Rapporteur)
Mme. Véronique MERRIEN-SOUKATCHOFF (Rapporteur)
M. Jose MOYA (Examinateur)
M. Guillaume RAMILIEN (Examinateur)

*A mi peje,*

# Acknowledgements

In first place, I would like to express my gratitude to my supervisors for their guidance, ideas, contributions and implication in the development of this thesis. To Jean Vaunat, for his help with the implementations and his academic but also personal support. To Muriel Gasc for giving me the opportunity to develop this project and to Jose Darrozes for his help specially in the geological and mineralogical characterization of the material.

I would like to extend my gratitude to Veronique Merrien-Soukatchoff, Irini Djeran-Maigre and Jean Sulem to have accepted to be the reviewers of this work.

This thesis involves the effort and work of different laboratories. I would like to thank the rock mechanical laboratory staff of the Cerema Toulouse, for their help and availability that allowed me to perform most of the experimental program. To the professors and staff from the laboratory GET in the Université Paul Sabatier and Staff from the Cerema Aix en provence and IFSTTAR for their help with the additional tests for the mineralogical composition analysis and porosimetry evaluation.

Moreover, I would like to thank the administrative personal of the Universitat Politècnica de Cataluña and Université Paul Sabatier for being so helpful to carry out with all the administrative procedures.

This research has been developed thanks to the economic support of the Centre d'études et d'expertise sur les risques, l'environnement, la mobilité et l'aménagement (Cerema) and in the lasts months to the international center for numerical methods in engineering (CIMNE).

Je souhaite aussi remercier tous mes collègues du Cerema Toulouse, notamment la famille REGG ainsi que Gérard, Sébastien, Pierre, Julien et Florence pour avoir été si accueillants et pour m'avoir fait me sentir toujours chez moi, ainsi que pour votre aide constante avec mon français et m'avoir fait connaître tous les délices de la cuisine française. Merci particulièrement à Stéphane, Philippe et Sébastien pour avoir toujours été prêts à m'aider, à Virginie pour son travail dans le laboratoire, à Yahya pour l'aide dans le laboratoire, à Patrick et Vincent pour l'aide avec le carottage des échantillons, à Jean Claude pour tous les « petites services » sans lesquels cette thèse n'aurait pas pu être menée à bien et à Didier pour tous ses conseils et son aide, pour son appui sans lequel cette thèse n'aurait sans doute pas pu exister.

Quisiera agradecer a mis amigos, los que están cerca y los que no, por su apoyo y esfuerzo por hacerme sentir siempre cerca y en casa, a Mauro por siempre estar dispuesto a darme una mano y a Aurore, pour toutes les conversations autour de un café et un désert.

Por último, quisiera agradecer a mi familia por su apoyo incondicional, especialmente a mis padres y hermanas que siempre han sabido estar ahí con la palabra indicada para motivarme a seguir adelante, gracias por todo su cariño y apoyo.

Y por supuesto, a Daniel por toda tu paciencia y amor, por ser un gran apoyo emocional e intelectual. Gracias por todo el esfuerzo, tiempo que has dedicado a este trabajo, tu constante motivación y ayuda. Y a mi peje por ser mi motivación y darme la fuerza que necesitaba en los últimos meses.

# Abstract

The environmental conditions may play a relevant role in the stability of rock slopes. In fact, weathering can contribute to the reduction of strength of the material, while hydro-mechanical loading actions may induce and eventually concentrate internal stresses in the rock massif. This Ph.D. thesis deals with the effect of atmospheric thermal cycles in rocks, from both experimental and numerical point of view.

This research is focused on the real case of La Roque Gageac, a small town located in the south-west of France, which experiences rock fall risk. Installed instrumentation evidenced the main role played by thermal variations in rock falls occurrence.

With the aim of isolating the effect of thermal cycles in the La Roque Gageac limestone, an experimental study is performed. Samples were obtained from blocks felt and intact cores drilled from the cliff face. These samples were submitted to thermal cycles between 10ºC and 50ºC, in order to mimic natural variations.

The damage induced in the samples is evaluated through measurements of strains, elastic wave propagation velocities and uniaxial compressive strength. It is observed that samples experience an accumulation in strains and a reduction in the elastic wave propagation velocity and material strength during the imposition of thermal cycles. The response depends moreover on the mineralogical composition of the rock, which varies from sample to sample, as the cliff presents a large heterogeneity.

Based on the results obtained in the experimental program, principal characteristics of thermal damage have been evaluated, proposing a constitutive model capable to reproduce the macroscopic mechanical response of the rock under the applied thermal cycles.

With this purpose, a constitutive model has been developed. It considers the rock as a composite material made of two components endowed each with its own thermo-mechanical behavior. The model has been further implemented in the Finite element Code_Bright and used to model laboratory tests. Results provide, on the one hand, a validation of the model by the measurements and, on the other hand, insights into a better understanding of the development of internal stress and damage inside the samples during thermal cycles

# Résumé

Les conditions environnementales jouent un rôle important dans la stabilité des massifs rocheux. De fait, les variations climatiques peuvent affecter la résistance du matériau et également augmenter les contraintes internes dans le massif. Cette thèse étudie les effets des cycles thermiques atmosphériques sur les roches, dans une approche expérimentale puis numérique.

Cette recherche est centrée sur le cas de la falaise de La Roque Gageac, un village du sud-ouest de la France, situé au pied d'une falaise qui présente une caverne à mi-hauteur. Cette commune a été affectée par plusieurs éboulements. Les données issues de l'instrumentation du massif montrent que ces instabilités sont liées aux cycles thermiques.

Afin d'isoler l'effet des cycles thermiques dans la roche calcaire de La Roque Gageac, un programme expérimental a été mis en place. Des échantillons ont été prélevés sur deux sites de la falaise (blocs éboulés à l'intérieur de la caverne et carottés dans la face de la falaise). Ces échantillons ont été soumis à des cycles thermiques entre 10ºC et 50ºC afin de simuler les conditions enregistrées sur le site.

L'endommagement de la roche est évalué en laboratoire par le suivi de mesures de déformations, de vitesses de propagation d'ondes élastiques et par l'évolution de la résistance à la compression uniaxial. Une réduction de la vitesse de propagation des ondes élastiques de compression et de cisaillement ainsi que de la résistance à la compression du matériau sont observées. De la même façon, les échantillons enregistrent une accumulation de déformations. De plus, la réponse des échantillons est influencée par la composition minéralogique de la roche. Celle-ci est liée au lieu de prélèvement, le calcaire de la falaise montrant une importante hétérogénéité.

Les résultats du programme expérimental ont permis la détermination des caractéristiques principales du phénomène d'endommagement thermique. Une loi de comportement modélisant l'effet des cycles thermiques sur la roche calcaire de La Roque Gageac d'un point de vue macroscopique a été proposée.

À cette fin, une loi de comportement a été développée. Elle considère la roche comme un matériau composite constitué par de deux composantes, chacune dotée de sa propre loi de comportement thermo-mécanique. Le modèle a été ensuite implémenté dans le code Éléments Finis Code_bright et utilisé pour simuler les essais de laboratoire. Les résultats fournissent, d'une part, une validation du modèle par les mesures expérimentales et, d'autre part, des éléments pour une meilleure compréhension du développement des contraintes internes et de l'endommagement des échantillons pendant les cycles thermiques

# Resumen

Las condiciones ambientales juegan un papel relevante en la estabilidad de taludes de roca, de hecho, las variaciones climáticas pueden afectar tanto la resistencia del material como el nivel de esfuerzos internos a los que el macizo está sometido. Esta tesis doctoral se enfoca en el efecto de los ciclos térmicos atmosféricos en las rocas, desde un punto de vista experimental y numérico.

Esta investigación se centra el caso de La Roque Gageac, un pequeño pueblo localizado en el Sur de Francia, que se ha visto afectado por importantes caídas de rocas, las cuales, de acuerdo con registros de instrumentación parecen estar ligadas a las variaciones de temperatura registradas en el sitio.

Con el objetivo de aislar el efecto de los ciclos térmicos en la caliza de la Roque Gageac un estudio experimental es llevado a cabo, para esto se consideran muestras obtenidas de bloques caídos en eventos anteriores y de núcleos intactos obtenidos de la cara del acantilado. Dichas muestras han sido sometidas a ciclos de temperatura entre 10ºC y 50ºC con el fin de imitar las variaciones naturales.

El daño inducido en las muestras es evaluado a través de medidas de deformación, velocidad de propagación de ondas elásticas y resistencia a la compresión uniaxial. Se observa una acumulación de deformaciones, así como la reducción en la velocidad de propagación de onda y la resistencia del material con la imposición de los ciclos térmicos. Adicionalmente, la respuesta obtenida depende de la composición mineralógica de la roca que varía entre muestras, debido a la heterogeneidad del acantilado.

Con base en los resultados obtenidos en el programa experimental se definen las principales características del fenómeno de daño térmico, con lo cual es posible proponer un modelo numérico capaz de reproducir la respuesta mecánica a nivel macroscópico de la roca cuando es sometida a ciclos térmicos.

Para esto se desarrolló un modelo constitutivo que considera la roca como un material compuesto por dos componentes, dotados con su propio comportamiento termo-mecánico. Dicho modelo fue implementado en el código de elementos finitos Code_Bright y usado para reproducir el comportamiento observado en los ensayos de laboratorio. Los resultados obtenidos validan el modelo considerado y proveen herramientas para una mejor compresión de la generación de esfuerzos internos y daño observado en las muestras durante la aplicación de ciclos térmicos.

# Contents

## 1. Introduction

## 2. La Roque Gageac

## 3. Experimental work

## 4. Numerical modeling

## 5. Conclusions

## Appendices

# List of figures

# List of tables

# 1. Introduction

## 1.1. General aspects.

Rock slopes instabilities can be triggered by different mechanisms, themselves controlled by several factors that determine the occurrence and size of the rockfall. These factors are generally divided into three groups:

1. The predispositions factors. They correspond to the characteristics of the rock slope describing the conditions under which the preparation and triggering factors will act to cause the instability.
2. The preparatory factors. They refer to factors controlling mechanisms of progressive reduction of massif resistance, like, for example, rock weathering.
3. The triggering factors. They are the factors responsible of the occurrence of the rock fall.

Predisposition factors are usually permanent while preparation and triggering factors evolve in time. This distinction is however not always totally clear since the notion of permanent and temporary factors depends on the time scale considered.

The effect of preparation and triggering factors is well-illustrated by the landslide-sequencing model presented by Julian & Anthony (1996) (see Figure 1-1). It schematically represents the time evolution of massif resistance, controlled by the preparation factors, and of the disturbing forces, controlled by the triggering factors. Failure occurs when the disturbing forces reach the resistance level, for example at points 1, 2, 3, 4 or 5.

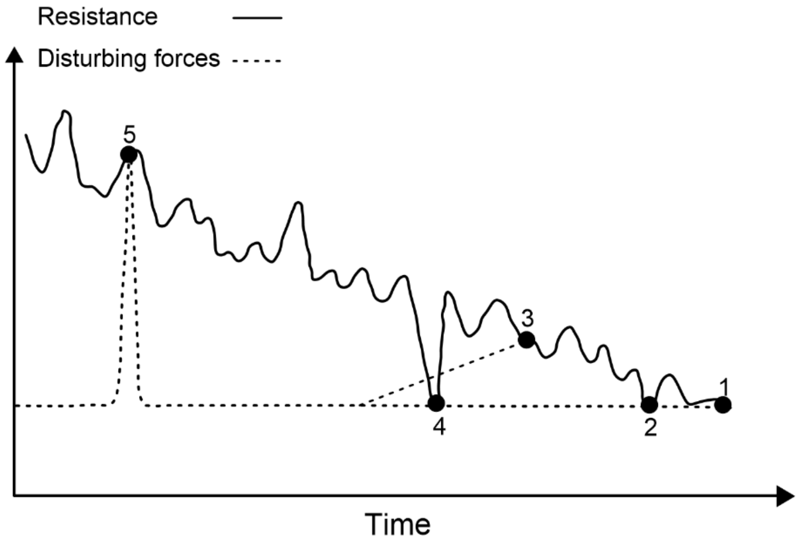

Figure 1-1 Landslide-sequencing model (from Julian & Anthony (1996))

Failure at points 4 or 5 occurs as a result of sudden events that either increase the disturbing forces (for example an earthquake) or makes decrease the resistance (for example a heavy rainfall that increases momentarily the pore pressure inside the slope). Point 3 correspond to the case of a progressive increase of disturbing forces (like for example toe erosion) that overlaps in time with the decrease in strength, leading to failure at an intermediate level of resistance. Failure at points 1 or 2 result from a progressive loss of resistance in absence of changes of the disturbing forces. Point 2 could for example illustrate the case of a rockfall due to the seasonal variations of environmental conditions (pore pressure, temperature, etc.) while point 1 schematizes the case of failure due to long-term reduction in resistance, for example related to geochemical rock weathering. Conditions at points 1 to 3 are related to rockfalls that typically lack of recognizable triggering factors (Julian and Anthony, 1996; Gunzburger, Merrien-Soukatchoff and Guglielmi, 2005).

Rock slopes instabilities linked to the progressive degradation of the material under climatic thermal cycles are quite well-represented by the sequence ending at point 2 in Figure 1-1. In fact, solar radiation and atmospheric temperature variations induce cyclic changes in rock massif temperatures susceptible to induce internal stresses and rock damage. Such process is generally imperceptible for one cycle, but its accumulation over a large number of cycles leads to massif instability without any identifiable triggering factor (Viles, 2013). Abnormal temperature changes may sometimes speed up the time of failure by increasing the thermal gradient in the slope and thus the rock damage.

Most of the studies on rockfalls triggered by climatic thermal variations focus on cases in cold and humid areas where freeze-thaw effects are the driving mechanism of instability. In this case, failure mechanism is related to the generation or propagation of fissures under stresses generated by water freezing in material pores or fractures. Rock moisture and the duration of the period of low temperatures are the most important factors as they control the depth where freezing-thawing acts, and thus the size of the failed blocks (Matsuoka and Sakai, 1999; Matsuoka, 2001; Hall, 2004a, 2004b; Gunzburger, Merrien-Soukatchoff and Guglielmi, 2005; Mufundirwa, Fujii and Kodama, 2010; Hall and Thorn, 2014; Bakun-Mazor and Hatzor, 2015).

There exist less studies on rockfalls under thermal variations in the positive range of temperature and far from extreme values. Vlcko et al. (2009) cited for example the case of a rock cliff instability in Slovakia that jeopardized the ruins of an important medieval castle. Monitoring of cliff stability conditions evidenced that temperature variations can be responsible for failure.

The mechanism generally considered is the production of thermal stresses as a result of the differential thermal expansion inside the rock. If high enough, the build-up of thermal stress can be accompanied by irreversible strain inside the massif, whose accumulation during temperature cycles may lead to failure (Siegesmund et al., 2000; Collins and Stock, 2016).

One of the source for irreversible strains is the propagation of existing fissures inside the material. An example is given by Bakun-Mazor & Hatzor (2015) and Bakun-Mazor et al. (2013), that instrumented a group of fissures in the Masada rock slope (dolomite). They showed the seasonal atmospheric variations could induce permanent plastic displacements.

Rock damage induced by temperature variations remains generally localized into a shallow part of the massif. As a matter of fact, on the basis of studies performed on different granitic rocks, Iñigo & Vicente-Tavera (2002) indicated that the highest temperature variations, and thus the highest mechanical disturbances, occurs in the first 10 cm of the massif. Another example is given by Collins & Stock (2016), who carried out a survey of the evolution of an exfoliation sheet in a granite slope at the Yosemite national park in California. The authors found that sheet deformations follow the temperature cycles whatever is the light intensity and relative humidity, which evidences an essentially temperature driven mechanism. In this case, they estimated that thermal stresses induced by atmospheric temperature variations prevail at depths up to 1m.

Notwithstanding, other studies have shown that thermal stresses may also be responsible of large volume rockfalls, due to the propagation of micro- and macro-fissures that reduces the strength of the whole rock mass (Hall, 1999; Hall and Thorn, 2014).

As an example, Gunzburger et al. (2005) and Merrien-Soukatchoff et al. (2007) presented the case of an large rockfall (almost 2000 $m^3$) that occurred in the southern Alpes (France) in 2000. In absence of an evident triggering factor, the study focused on the hypothesis that the fall was caused by the repetition of small local disturbing events due to fracture weathering and degradation. With this purpose, an instrumentation system was installed in the site, focusing on the measurement of displacements and survey of meteorological conditions. Interpretation of the measurements by a simple numerical model indicated that a likely potential triggering factor corresponded to the atmospheric thermal cycles. It is observed that these cycles generate plastic strains at internal fissures of rock mass, with favors slope instability.

Other examples were provided by Vargas et al. (2004) and Do Amaral Vargas et al. (2013), who studied several rock slopes failures in the region of Rio de Janeiro (Brazil). Most of those instabilities occurred during the winter (dry season), that is during the period of maximal daily temperature variations and in absence of important rains. After analysis of rockfall characteristics, they proposed an experimental study aiming at following the thermal evolution of a block provided with a fissure. The experimental results are interpreted by means of a Finite Element analysis, which showed that thermal stresses induced by the atmospheric temperature variations are able to propagate existing non-persistent fractures and thus to cause rockfalls.

All these cases indicate that thermal actions resulting from the interaction with the atmosphere are able to cause rock instability. Rock bulk damage, on one side, and the progressive accumulation of displacements along pre-existing discontinuities, on the other side, are the mechanisms mostly invoked as driving the rock to failure under the variations of temperature prevailing inside the massif. A comprehensive evaluation of massif stability requires thus the realistic assessment of slope temperature distribution due to atmospheric actions and the right evaluation of all types of rock degradation mechanisms under the determined thermal cycles.

It must be finally mentioned that, as pointed out by Aldred et al. (2016) and Eppes et al. (2010), the geophysical existence of thermal damage is not limited to dry climates but can also produce either in arid or more humid regions. In the last case, it can be reasonably expected that other factors like air relative humidity will play a role in the process of rock degradation, as for example identified by Oldecop and Alonso (2004).

## 1.2. Aims of the research and thesis layout.

The work carried out in this thesis is inscribed in the above mentioned research line about effects of thermal cycles on the stability of rock slopes. It will more particularly focus on the issue of rock bulk damage under thermal cycles. As it will be further explained in the thesis, the damage suffered by the rock mass as the result of the differential thermal expansion of the minerals composing it is in fact forwarded as being one important aspect of rock degradation.

The rationale behind the thesis comes from the current study of an instable rock slope located at the site of La Roque Gageac, France, and reported by Virely and Guittard (2010a, 2010b); Virely, Ansaldi and Baro (2010) and Gasc-Babier et al. (2015). The slope, composed by a calcareous stone, has experienced different types of rockfalls, from surface flaking to medium and large block falls, without any identifiable triggering factors other than atmospheric actions. Site instrumentation has confirmed the strong link existing between slope homogeneous deformations, discontinuities apertures and rock temperature variations. Interpretation of the first-year measurements indicates that the homogeneous deformations can be well-reproduced by an Finite Element model provided with a thermo-elastic law, while the capture of discontinuities apertures require to further provide the model with joint elements with a thermo-mechanical law (Ruiz, 2013). In addition, measurements obtained during the following years evidenced a progressive accumulation of deformations and displacements with thermal cycles, whose rate in the mass and across the discontinuities differ strongly. In relation to that, Gasc-Barbier et al. (2014) carried out laboratory tests on samples obtained from fallen blocks in order to evaluate the deformations and the changes in elastic moduli suffered by the bulk rock during the application of thermal cycles. The necessity to account for all these aspects set up a challenging context for a comprehensive modelling of the slope.

As a first step towards the integration of rock degradation aspects into slope response modelling, the present work will focus on the experimental and numerical evaluation of the damage induced by thermal cycles on rock bulk mass. For this, the experimental program initiated by Gasc-Barbier et al. (2014) is revised and extended to a variety of samples extracted from different locations of the cliff and for longer periods of thermal cycles. Physical, mineralogical, thermal and initial mechanical properties have been determined for the different samples while deformations, elastic wave velocity and uniaxial compressive strength have been determined during and after the application of temperature cycles. Digital image correlation technique has also been used for the sake of gaining insights into fissure generation and propagation.

Experimental results have been then used to feed a constitutive model purposively developed to reproduce bulk rock damage under thermal cycles. With the long-term objective to carry out numerical simulations of the real case, the constitutive law has been developed within a continuum framework, which allows for its efficient implementation in Finite Element code. It is based on an original and relatively simple strategy to combine the behavior of two components in the macroscopic response of the rock. This model allows reproducing the development of internal stresses as the result of the thermal expansion of the two components, which may cause in turn rock damage. The constitutive law has been implemented in the thermo-hydro-mechanical Finite element code Code_bright and the response of the samples has been modelled as boundary value problems. Numerical computations provide degradation of elastic moduli under thermal cycles, which can be favorably compared with the experimental results. At the present stage of research, there exists therefore a numerical tool provided with a constitutive law for bulk rock damage that can be used to solve boundary values problems at the field scale. It must be enhanced with regularization techniques in order to further model the generation, propagation and degradation of discontinuities under thermal load.

This thesis is divided into an introduction (present chapter), three main chapters, a conclusion (Chapter 5), a list of references and three appendices.

Chapter 2 presents the context of the real case of La Roque Gageac (LaRG). It describes the geology, climatological characteristics, most important rockfalls events as well as current instrumentation set-up and measurements results.

Chapter 3 deals with the experimental program carried out in order to evaluate the effect of thermal cycles on the limestone rock. A complete characterization of the rock is first presented, followed by the detailed description of the experimental program. The results obtained are further presented and analyzed. They show that thermal cycles are susceptible to induce damage in the material.

In chapter 4, the numerical model is presented. After stating the scope of the model, the equations of the constitutive law are detailed. Then, its implementation within a Finite Element scheme is presented and verified by comparison with an algebraic solution obtained using an explicit scheme. Afterwards, the performance of the model is analyzed by carrying out sensitivity analysis on several parameters. Finally, the numerical model is used to simulate the experimental tests as boundary value problems and conclusions drawn.

Chapter 5 gives a summary of the principal results obtained, provides concluding remarks and proposals for future works.

At the end of the manuscript, a section with three appendices is presented. Appendix A presents the results of Mercury Intrusion Porosimetry tests performed on samples after different numbers of thermal cycles. Appendix B provides the results of digital image correlation analysis for two cubical samples (sample C1 and C3). Appendix C presents the discrete equations and the numerical procedure to integrate the constitutive law within the Finite element scheme.

# 2. La Roque Gageac

## 2.1. Introduction.

The objective of this research is to evaluate the effect of thermal cycles on rock slopes. This analysis is based on the real case of the rock slope instabilities observed in La Roque Gageac, a small town located in France, placed at the toe of a limestone rock cliff.

The town has been suffering several rockfalls events that could not be related to any evident triggering factors, like rain seasons or earthquakes. Thus, other possible phenomena or causes are evaluated, and natural thermal cycles seem to be the factor most related to cliff deformations and possibly failure in the site.

The last important event occurred in 2010 leads a precarious stability condition in the cliff, augmenting the risk for the population and visitors of the town. Therefore, in order to evaluate the risk level and proposed a stability solution, The *Centre d´Etudes Techniques de l´Equipement du Sud-Ouest* realized a study, including an instrumentation system that has been following the cliff stability condition since July 2010 to nowadays.

In this chapter, a complete description of La Roque Gageac case is presented, involving general aspects, as well as, the characteristics of the principal events reported, the stability conditions after the last important rockfall event, the instrumentation system installed and preliminary analysis realized.

This information is extracted from the technical report presented by the *Centre d´Etudes Techniques de l´Equipement du Sud-Ouest in 2010* (Virely and Guittard, 2010a, 2010b; Virely, Ansaldi and Baro, 2010), the master thesis of Ruiz (2013) and technical visits realized to the site.

## 2.2. Site location.

La Roque Gageac is a small town located in the south-west of France. It is placed in the north-west of the Aquitaine basin in the department of La Dordogne (Figure 2-1). Although this village has a small population, more or less 450 people, the tourism is the principal economic activity, with more than 2 million visitors each year in the region.

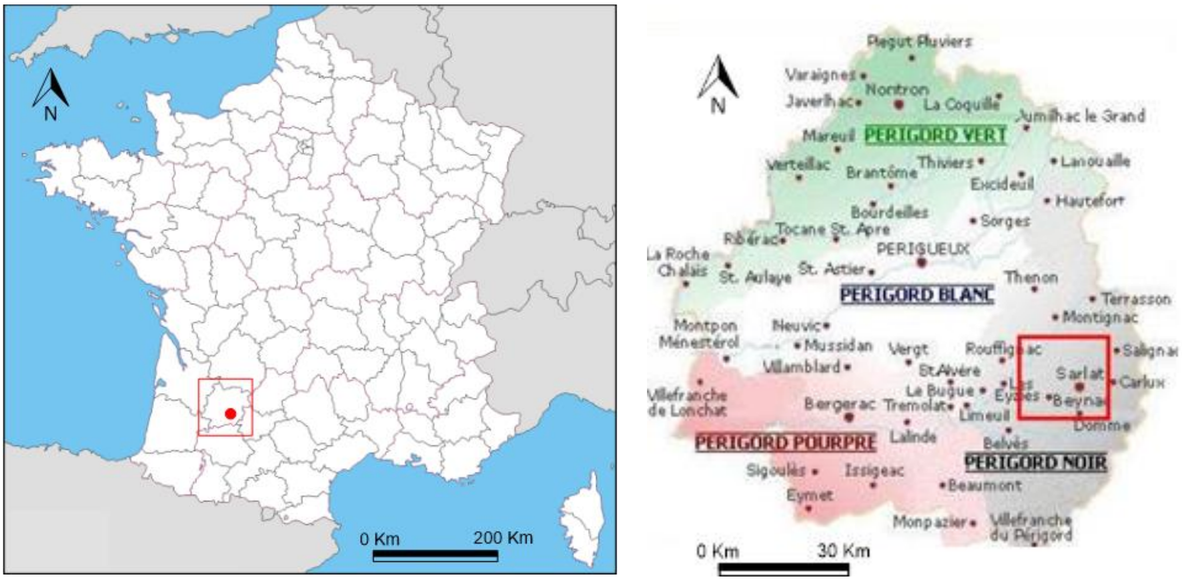

a) b)

Figure 2-1 Location of la Roque Gageac a) Position of La Dordogne department inside of France b) Situation of La Roque Gageac in the department

This town is located at the right bank of the Dordogne River, in a regional area denominated The Périgord noir (Figure 2-1b), at the toe of a limestone rock-cliff of more or less 100 meters high. In this cliff, there is an ancient troglodyte fort located at 50 m high (see Figure 2-2). Which was used as a refuge during the Hundred Years' War, which makes it one of the tourist attraction for the region.

Figure 2-2 situation of La Roque Gageac in relation to the Dordogne river and the cliff

### 2.3. Geology.

The Périgord Noir landscape developed along the Dordogne river curse is mainly characterized by deep valleys. Nevertheless, the geomorphology of this region depends on the geological material that the river cross.

This fluvial system goes through different types of formations like, massive limestone of the middle and late Jurassic where the landscape is tight (deep valleys) with small meanders. And zones of argillite rocks and marbles, where the river shows large and important meanders with gentle slopes.

When the river reaches the upper cretaceous sandy limestone, where our zone of interest is located, (Figure 2-3) the morphology presents a succession of large rectilinear zones and tight sections with meanders. These morphological differences are related to the geological heterogeneity in the Aquitaine basin. Which is composed by soft limestones with a high sand content, where the river shows a rectilinear course, and, by strong sandy limestones favorable to meanders formation.

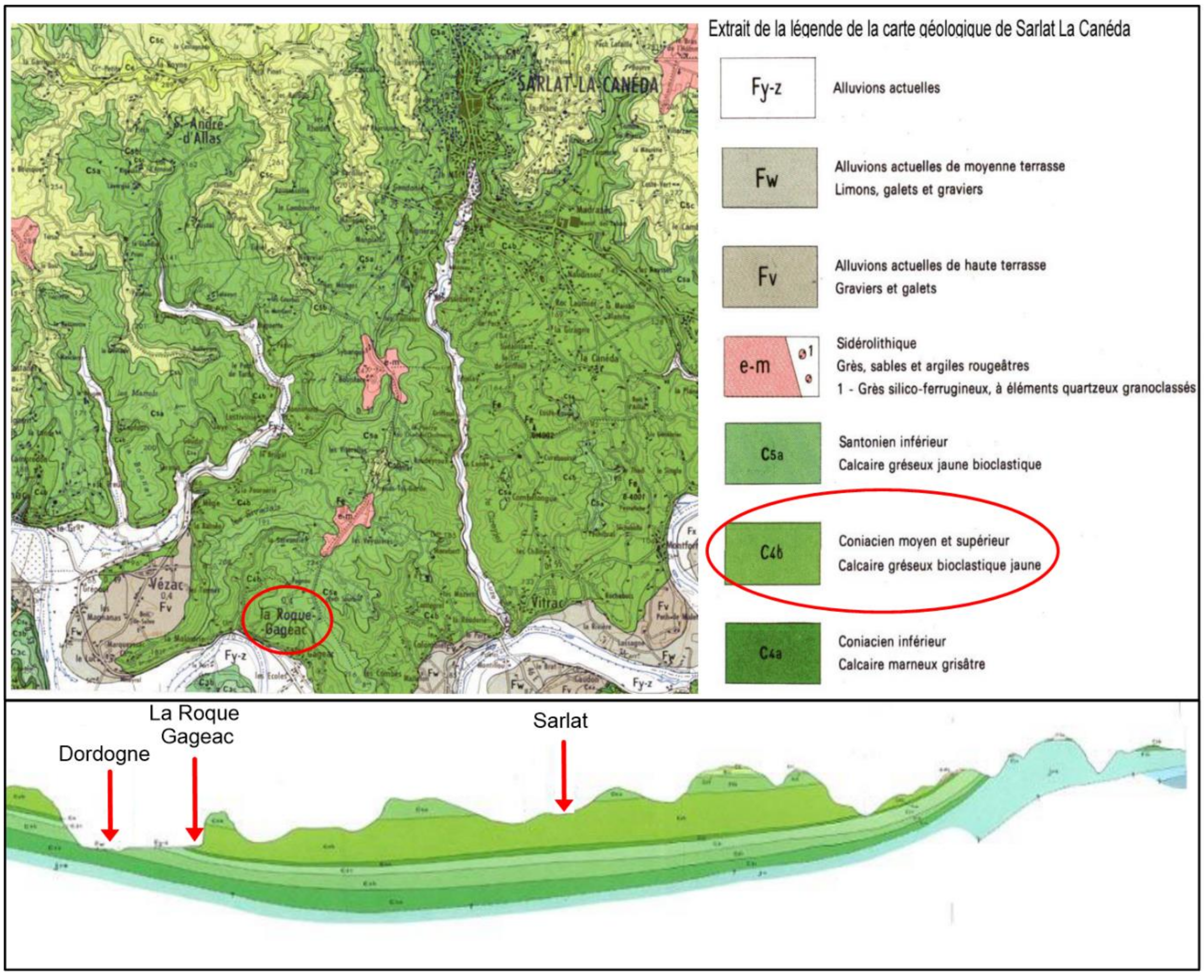

Figure 2-3 Geological situation of La Roque Gageac (from Virely and Guittard, (2010a) extracted from the geological map from Sarlat La-Canéda – (BRGM, 1987))

The Aquitaine basin is composed by Coniancian limestones. This geological formation can be divided into two types of materials, those belonging to the lower Coniancian, that are marine impermeable limestones, and those belonging to the middle and upper Coniancian, a layer of sandy limestones, porous, weak and prone to karstification phenomena. La Roque Gageac is placed over the limestone of the lower Coniancian, however, the cliff is composed of an upper Coniancian rock.

In fact, where La Roque Gageac is located, the Dordogne River has eroded the sandy limestone of the upper and middle Coniancian, to reach the lower Coniancian layer. This geological process has generated the cliff and induced a modification in the stress balance of the massif, producing a phenomenon of decompression in the cliff.

The geological formations of the middle and upper Coniancian show a succession of marine and lacustrine deposits. These deposits are characterized by oblique lithologies with different inclinations delimited in some cases by erosion superficies and showing different types and size of material. Figure 2-4 shows a contact between different types of deposits, where the green line delimits an oblique layer and the red line an erosional surface.

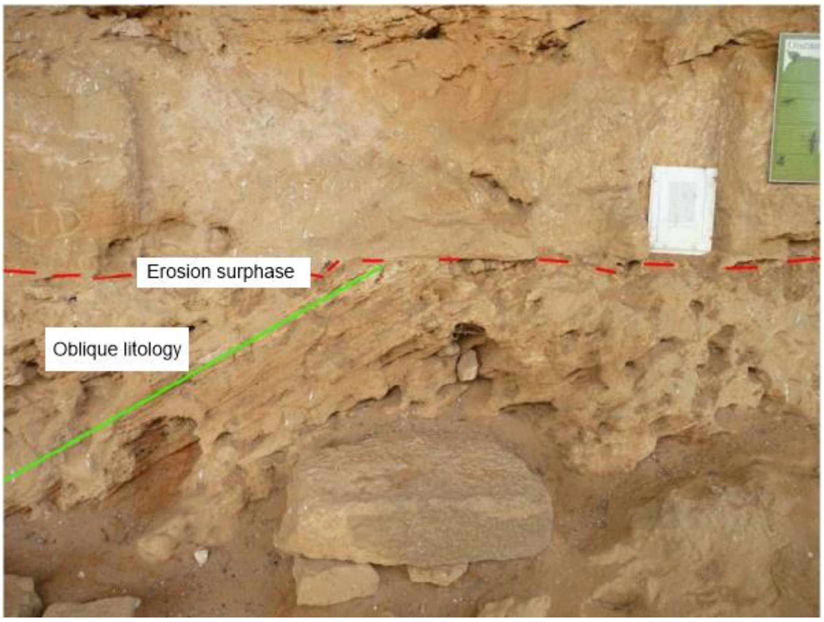

Figure 2-4 Example of a hydraulic deposit with different shapes and surfaces

This geological history is responsible for the strong material heterogeneity and the poor mechanical properties of this rock. Additionally, this material is prone to karstification processes.

Due to the heterogeneity of this formation, the cliff is composed of a succession of permeable and impermeable layers. Therefore, the karstification networks cannot be completely developed in the vertical sense. In fact, the troglodyte fort observed in the cliff of La Roque Gageac belongs to an inactive paleo-karstification network that was not completely developed.

Because the calcareous nature of the rock from the cliff under analysis the chemical effect of the water might play an important role in the behavior of this material. Nevertheless, the dissolution rates registered in the region are inferior to 1 mm per year (Trauth et al., 1985; PLatel, 1987, 1996, 1999; Astruc, 1988; Virely and Guittard, 2010a).

## *2.4. Climate.*

The climate of the department of La Dordogne is temperate with an important oceanic influence. During the winter, the proximity to the *Massif Central* influence the weather*,* and in the summer, it suffers the presence of warm air masses coming from the Mediterranean Sea.

At a regional scale, the annual rain is around 860 mm, with a historical maximum of 100 mm in one day, registered in May 1971. The maximal temperatures range varies from 27ºC to 32ºC and the minimal between -10ºC and -15ºC.

These large temperature variations may be the responsible of the flaking observed in the face of the cliff, especially if we consider that the cliff is oriented to the south and the high albedo value that this rock presents (Virely and Guittard, 2010a; Gasc-Babier, Virely and Guittard, 2015).

## 2.5. Historical rockfall events.

Since the beginning of the 20th Century, four important events have been registered in this town, the latest occurred in the winter of 2010 when a part of the roof of the troglodyte cavern collapsed (Virely and Guittard, 2010a, 2010b; Gasc-Babier, Virely and Guittard, 2015). Since there is no external load over the cliff (no buildings or any type of constructions) and no hydrological changes, all these rockfalls have been attributed to the geological conditions of the rock and the possible effects of climate over this material.

Figure 2-5 shows the location of three of the four principal events registered in the zone of interest:

1920: A block of several thousand of $m^3$ fell in the town from the east side of the cliff, without casualties. (Figure 2-6a)
1957: At the west of the village a large block fell and kill 3 people (Figure 2-6b)
1994: Several small blocks were detached from the cliff
2010: Collapse of the roof of the cavern (Figure 2-7)

Figure 2-5 Location of principal events observed in the town (Virely and Guittard, 2010a)

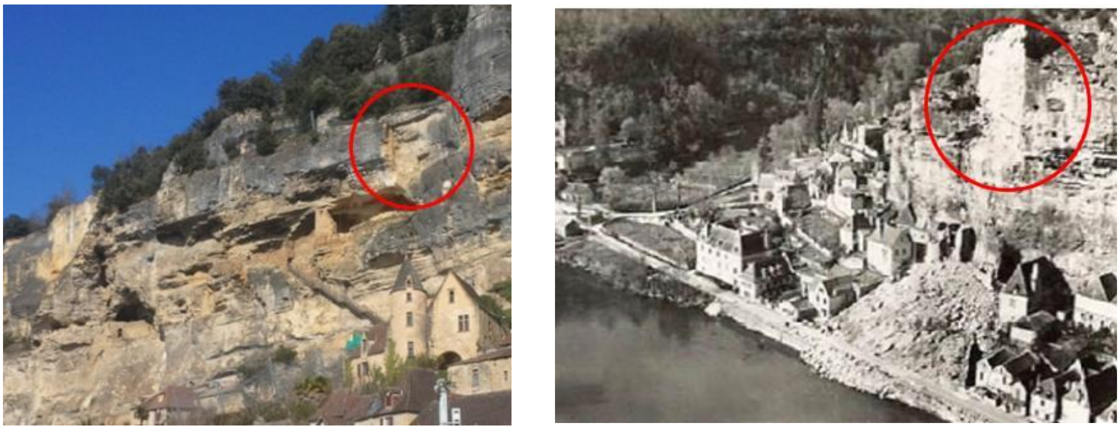

a) b)

Figure 2-6 Source of rockfalls registered in 1920 (a) and in 1957 (b)

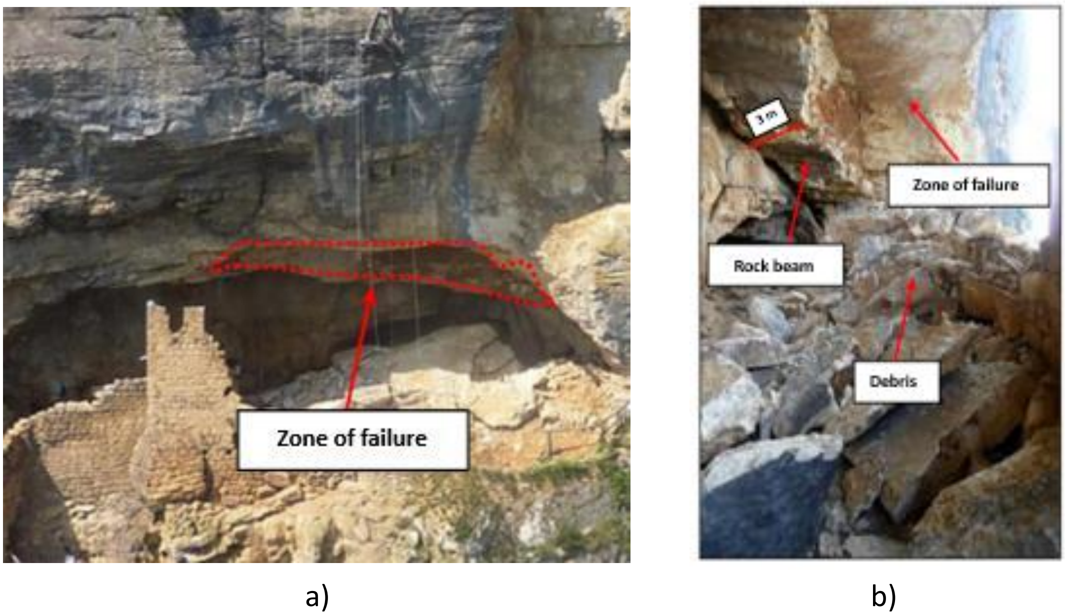

Figure 2-7 Details of the collapse occurred in 2010 (from Ruiz, 2013) a) zone of failure b) view inside the cavern

## 2.6. Current risk.

After 2010's event, it can be considered that three levels of risk remain in La Roque Gageac's cliff, with different associated volume:

- Fall of small blocks detached from the cliff, this level of risk also includes the material felt from the roof of the cavern and remaining in it, after the latest important event.
- The residual rock beam inside the cavern that presents a poor stability condition.
- The general stability above the cavern.

After the event of 2010, a high volume of small blocks remained inside the fort generating an extra risk for the population of the town. The situation just after the collapse can be observed in Figure 2-8a. In addition, the cliff presents a high frequency of small blocks fall (less than 0.01 m$^3$), more than 40 events per year. This phenomenon can be associated with the flaking, observed in the face of this rock massif and shown in Figure 2-9.

This response can be associated with a physicochemical degradation of the rock related to the climate actions. The *Centre d'Études Techniques de l'Équipement du Sud-Ouest* attributes this type of flaking especially to the thermal stress induced by the natural thermal cycles.

In order to reduce the first level of risk, the blocks were removed from the cavern, and a wire mesh was installed in order to avoid all the small and medium size (0.01 – 2 m$^3$) blocks detached reach the village, see Figure 2-8b.

a) b)

Figure 2-8 First level of risk a) Remaining blocks inside the cavern b) Wire mesh installed

Figure 2-9 Flacking observed in the face of the cliff

The second level of risk is associated with the failure of the rock beam that remains inside the cavern after 2010's event. This beam is almost completely detached from all its faces. It is fully detached in the back, so, it is only supported on two contact points (Figure 2-10) that shows important fissures, closed in the east side but open in the west base. Therefore, it behaves more like a cantilevered beam. Nevertheless, some additional resistance may be attributed to friction at the west support and to rock-bridges in the open fracture at the back of the beam.

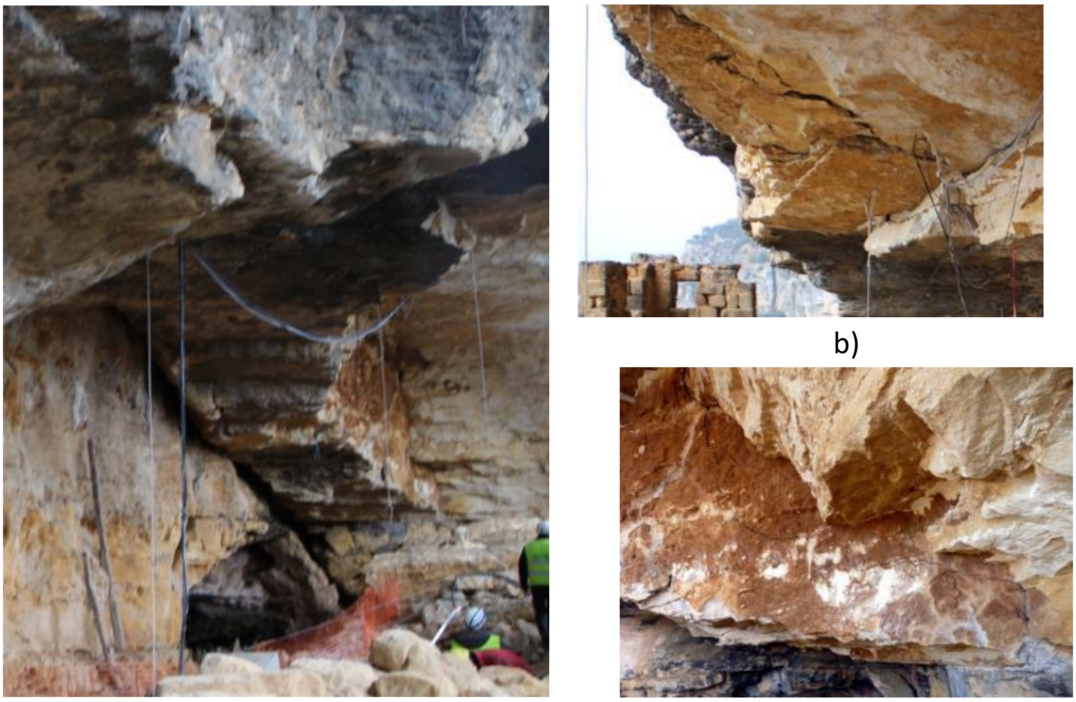

b)

a) b)

Figure 2-10 Stability condition of the beam a) General situation b) West support c) East support

Finally, the third level of risk considers a much higher volume of material. It considers the stability of the cliff above the cavern, which is controlled by the two principal discontinuities and the stratification planes (Figure 2-11). These joints (family 1 and 2 in Figure 2-11) were developed with the decompression generated by the valley formation geological process. As can be observed in Figure 2-11 a large block is delimited by the discontinuities mentioned. Moreover, the stability of this block may be affected if the beam inside the fort fails.

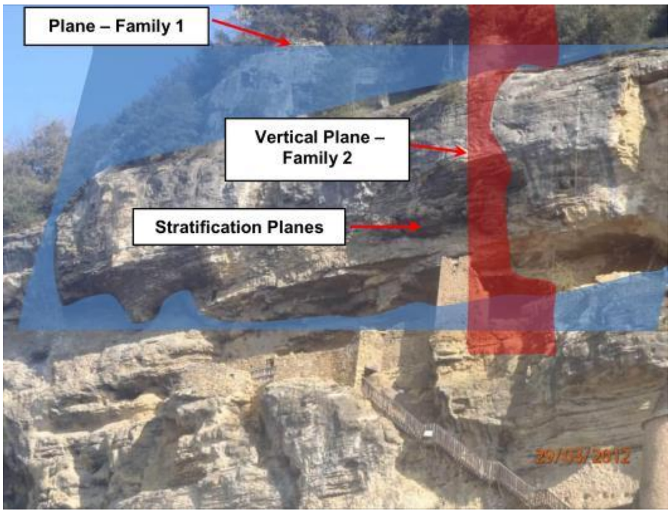

Figure 2-11 Principal discontinuities families observed ( Ruiz, 2013)

All the fractures that defined this block are open, and they emerge on the top of the massif. This suggests the existence of rock-bridges inside the fracture that controls de stability, as was assumed when we consider the stability of the beam. If this large block is supported by rock-bridges the climate cycle induced degradation, may play an important role for the generation of important rockfalls event. Besides that, the presence of ancient karstification networks increase the instability conditions on the cliff (Virely and Guittard, 2010b; Virely, Ansaldi and Baro, 2010).

To reduce the second level of instability risk and probably the third level too, several portico structures were constructed inside the troglodyte fort (Figure 2-12), with the aim of providing more stability to the roof of the cavern and for instance to the above part of the cliff, by stabilizing the unstable beam.

Figure 2-12 Supporting structures inside the cavern

## 2.7. Instrumentation system.

With the aim to follow the stability conditions of the cliff after the event registered in January 2010, an instrumentation system was installed inside and around the troglodyte cavern. This instrumentation system recorded two principal features: weather conditions and deformations (Ruiz, 2013; Gasc-Babier, Virely and Guittard, 2015).

The closest meteorological station to the site is the Sarlat-La Canéda it is located at 10 km north-west from La Roque Gageac. Figure 2-13 presents the temperatures and rains observed in this station for one-year period (June 2010 to July 2011).

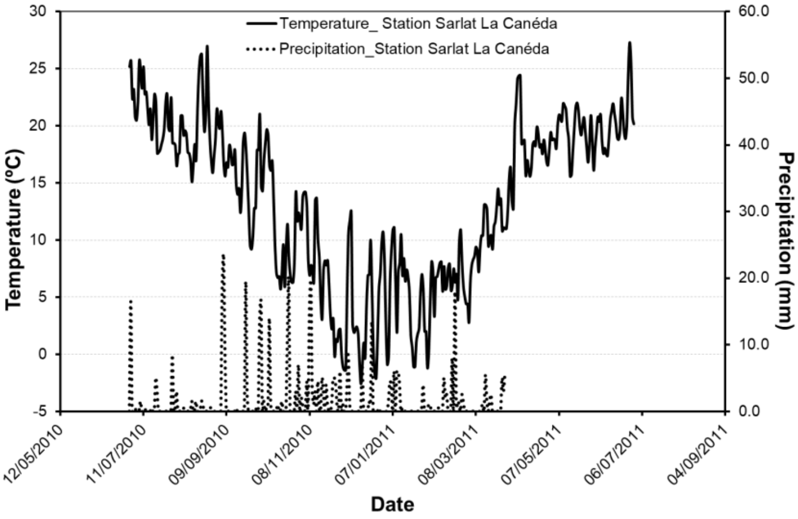

Figure 2-13 Meteorological station data

The data recorded by the meteorological station indicate that the major rain period occurs during the autumn, when any rockfall event has been registered. This condition coupled with the absence of karstification in the face of the cliff or the aerial surface around the cavern, suggests that water is not the principal degradation factor in this area.

Accordingly, even if the rain effects cannot be completely excluded, the weather variable recorded with the instrumentation was the temperature. The temperature registered in the cliff correspond properly with the regional temperatures recorded by the meteorological station.

Deformation in the cliff was followed with two extensometers type RockTest/Télémac distofor@. These borehole extensometers were located over the cavern (D1 and D2 in Figure 2-14) and were prepared with three displacements measuring points at 2, 4 and 6 m from the cliff face and two temperature-measuring points at 2 and 6m.

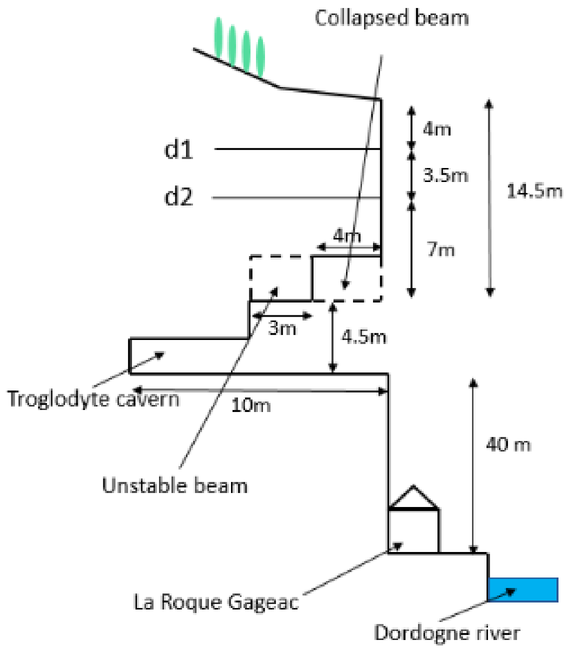

Figure 2-14 Cross-section scheme of the cliff with the localization of the extensometers (D1 and D2)

Additionally, five jointmeters were installed in cracks inside the fort (see Figure 2-15). These jointmeters consist of LVDT strain gauges that measure the displacement between their two extremes with an accuracy of 1/100. The extensometer registered the evolution of the rock mass and the jointmeters survey the evolution of the relative displacement of the fissures that delimit the unstable beam:

- Relative opening of the joints located at both supports west and east (jointmeters 1 and 2)
- Vertical aperture of the horizontal discontinuity between the roof of the cavern and the beam (Jointmeter 3)
- Horizontal aperture of the vertical crack in the roof of the cavern, close to the west support (Jointmeter 4)
- Horizontal aperture of the vertical crack in the roof of the cavern, close to the beam (Jointmeter 5)

It is important to mention that jointmeter J-1 was initially installed in horizontal position to measure the aperture of the vertical crack situated at the east support, but in December 2010 this device was re-localized in a horizontal segment of the same crack, which is its current position.

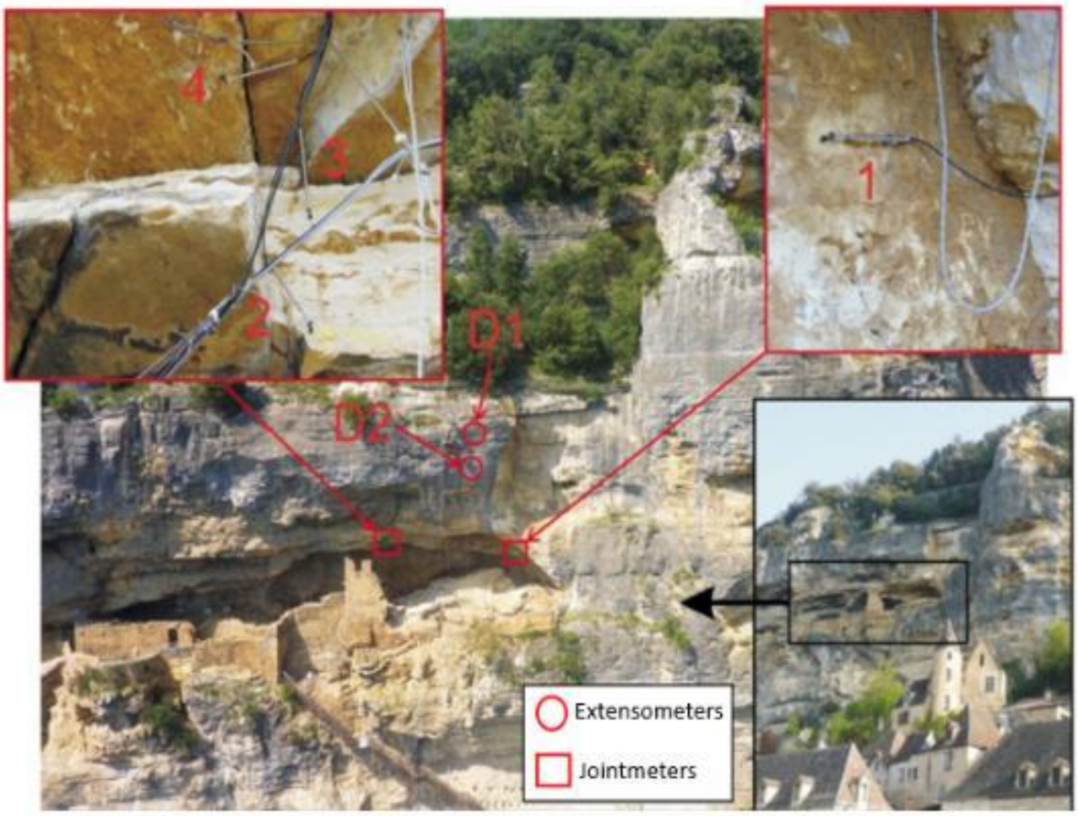

Figure 2-15 Localization of the instrumentation devices ( from Gasc-Babier, Virely and Guittard, 2015)

## 2.8. Instrumentation results.

The instrumentation system presented in section 2.7, has been recording the cliff displacements and external temperature for more than 6 years including several months after the construction of the stability structure inside the cavern, presented in Figure 2-12

The extensometers located in the upper part of the cliff, (Figure 2-14) measure the displacement and temperature at two different points: 2, and 6 meters from the face of the cliff. Figure 2-16 shows the evolution of temperature inside the cliff for extensometer D1, compared to the exterior temperature. The response observed shows a considerable phase delay, related to the distance between the points of measurement and the cliff's face. In fact, between measurements at 2 and 6 meters depth, the delay observed is about 40 days.

Besides this delay, the temperature evolution shows an important attenuation in maximal and minimum values as the measure is deeper. In addition, the hourly and daily thermal effects decrease. In consequence, the response observed at 6m is only related to seasonal changes.

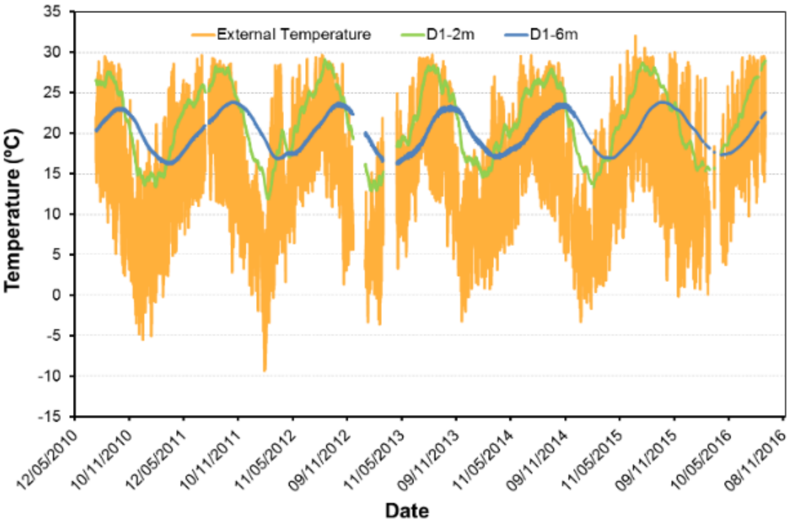

Figure 2-16 Temperature evolution at 2 and 6 meters from the Cliff face

An extensometer measures a relative displacement between the points of interest (2, 4 and 6 m depth from the cliff face) and the end of the device, which is considered fixe. The negative displacements values observed represent a reduction in this distance, associated with the contraction of the rock mass, due to the temperature decrease. Hence, the positive values denote an expansion of the cliff and negatives the compression.

Figure 2-17 presents the displacements response recorded with the two extensometers for 6 years. In both devices, the response observed can be directly related to the external temperature. Reinforcing the hypothesis of natural thermal conditions as the main cause of deformations in the cliff.

It is important to mention that as the instrumentation system was installed during the summer (July 2010) measurements are taken in relation to the cliff situation at this precise moment, this is why the amplitude for negative displacements (compression) are higher than the amplitude for positive displacements (expansion).

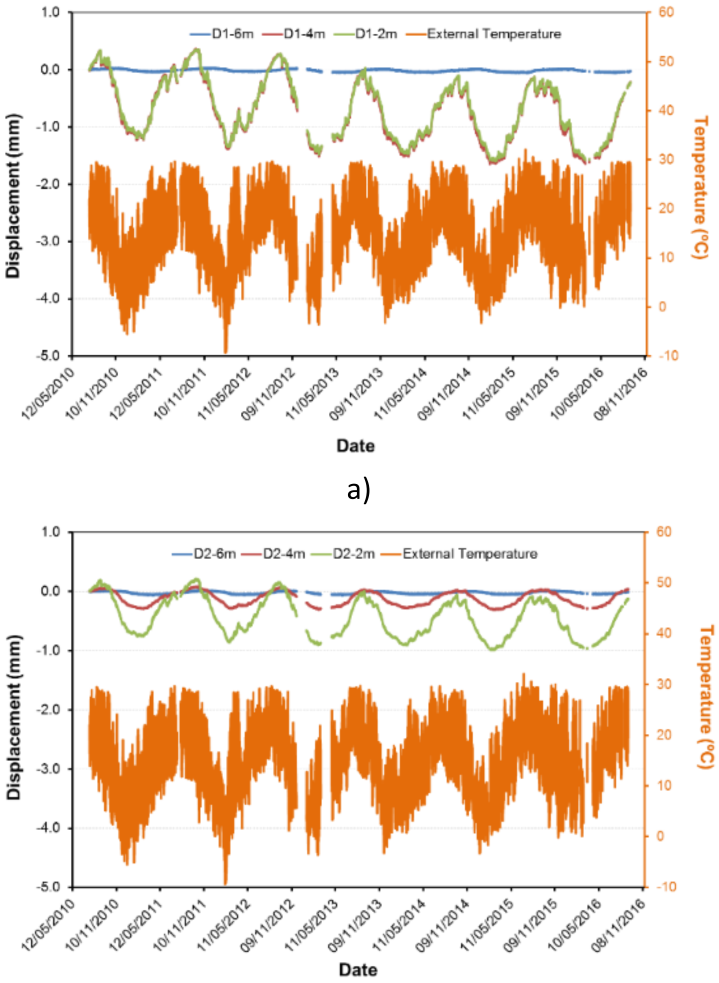

a)

b)

Figure 2-17 Extensometers measures: a) D1 b) D2

In general, displacements recorded with the extensometer D1 are higher than those observed with extensometer D2. It is interesting to point out that measures at 2 and 4 meters in extensometer D1 have the same behavior, while extensometer D2 shows smaller displacement amplitude at 4 meters than at 2 m, as it is expected when considering the thermal flux and deformations inside the cliff.

The difference in the behavior observed in both devices D1 and D2 may be explained by the presence of a discontinuity, that go through the extensometer D1 in a point between 4 and 6 meters, as illustrated in Figure 2-18. Generating that displacements at 2 and 4 meters in device D1 present a block behavior, while displacements register with the extensometer D2 show a regular thermal induced response.

Moreover, from Figure 2-17a it can be observed that the response recorded with the device D1 presents an accumulation of displacements at 2 and 4 m, around 0.5 mm after 6 years. While the displacements recorded at 6 meters do not show any accumulation, they are almost imperceptibles.

For the case of extensometer D2 (Figure 2-17b), displacements measured at 2 meters present a higher strain accumulation than displacements recorded at 4 and 6 m. Measurements at 2m shows an accumulation around 0.6 mm after 6 years that is less than the half of what is experienced with the device D1.

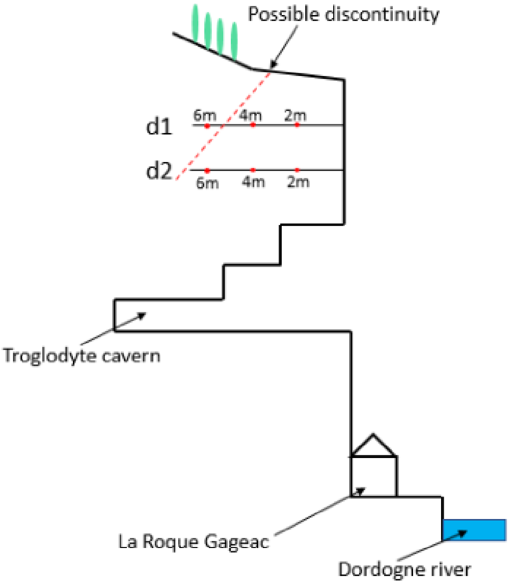

Figure 2-18 Possible discontinuity across the extensometers.

For instance, Figure 2-19, Figure 2-20 and Figure 2-21 presents the relationship between external temperature and displacements measured with the extensometer D2 at 6, 4 and 2m respectively, for the periods between August 2011 and August 2012 (orange curve) and between August 2013 to August 2014 (red curve). It can be observed that displacements come back close to their initial values after the annual climatic cycle. Moreover, at 4 and 6 m, there is no accumulation of horizontal displacement across the years (Figure 2-19 and Figure 2-20). However, at 2 m that is in the zone of higher temperatures and temperature gradients variations, a displacements accumulation is observed after 2 years.

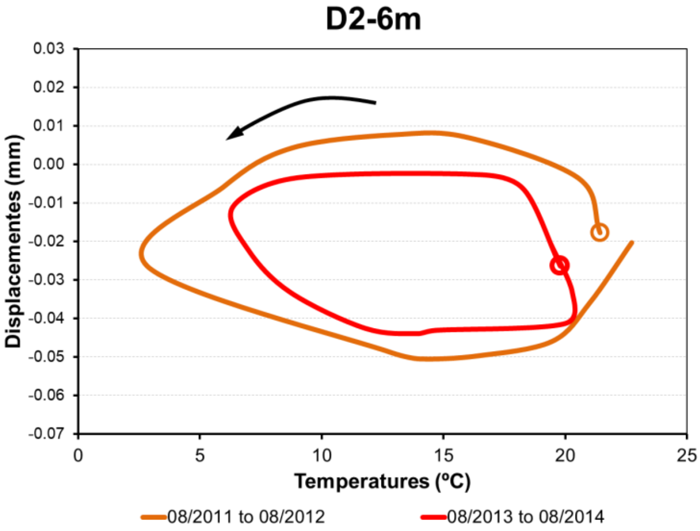

Figure 2-19 Displacements vs temperature extensometer D2-6m.

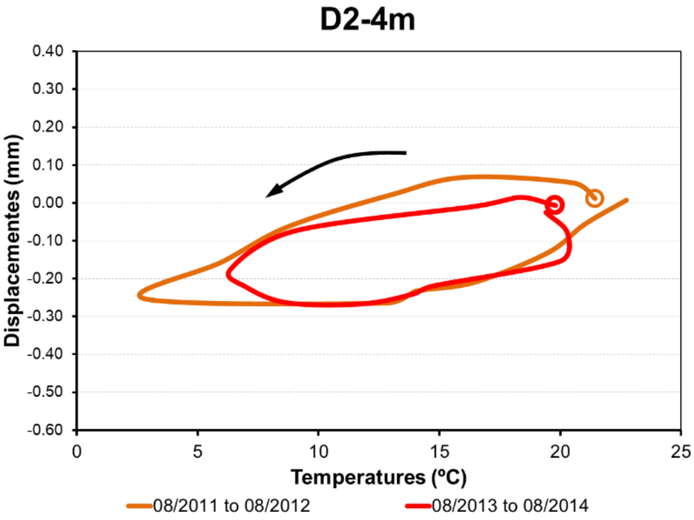

Figure 2-20 Displacements vs temperature extensometer D2-4m.

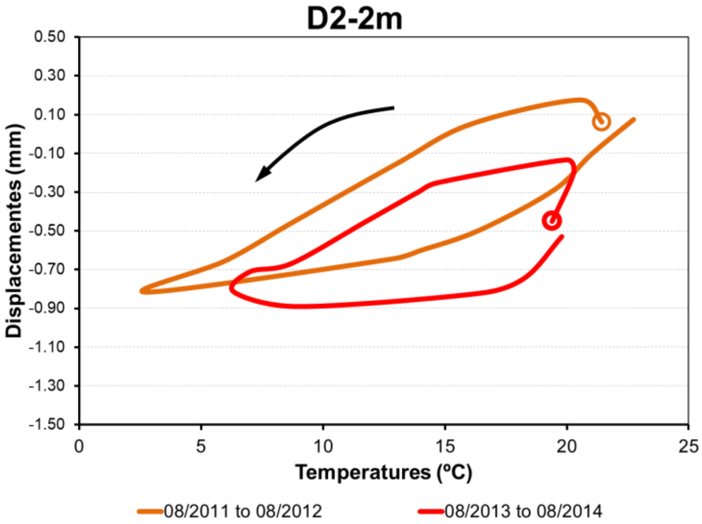

Figure 2-21 Displacements vs temperature extensometer D2-2m.

The time evolution of the displacements recorded by all the jointmeters is presented in Figure 2-22 in comparison with the temperature evolution. Jointmeters measure the relative normal displacement across the joint with a negative value in case of opening. From a general point of view, measurements show a direct relationship between the displacement and the temperature. Moreover, they indicate joint opening during the cold season and closure during the hot season, which is consistent with the mechanism drawn in Figure 2-23. During a decrease of temperature, there is a contraction of the blocks on both sides of the joint and thus an opening of the joint. When the temperature increases, the opposite mechanism takes place.

More specifically, the jointmeters located on the roof (J-3, J-4 and J-5) present reversible relative displacements of large amplitude (2.5 mm). As can be observed in Figure 2-24, which relates displacements to temperatures for device J-5 for two one-year periods, from August 2011 and August 2012 (orange curve) and between August 2013 to August 2014 (red curve).

For each year, displacements come back to their initial value. Moreover, after two years, the time-displacement curve did not experience any shift.

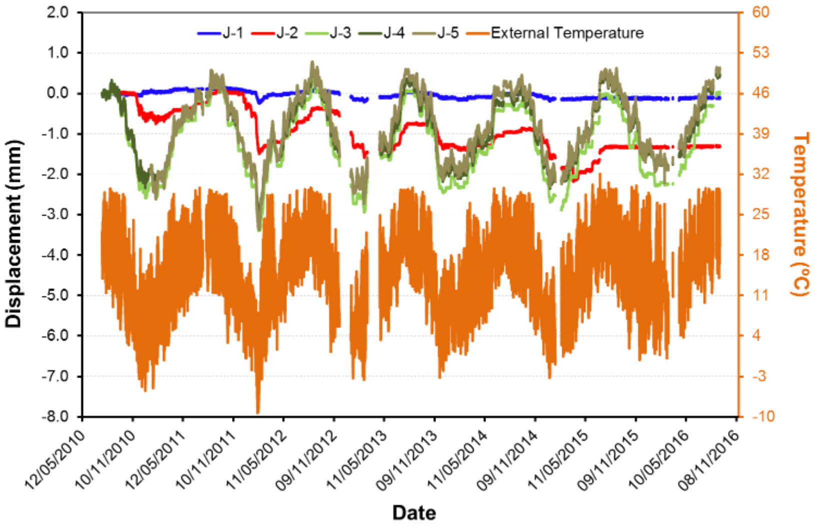

Figure 2-22 Jointmeters displacement and temperature inside the cavern

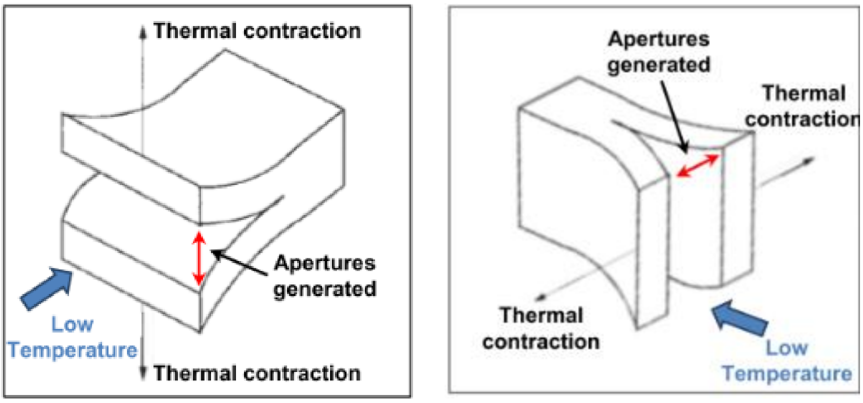

a) b)

Figure 2-23 Joint behavior under low temperatures a) Horizontal crack b) Vertical crack (Ruiz 2013)

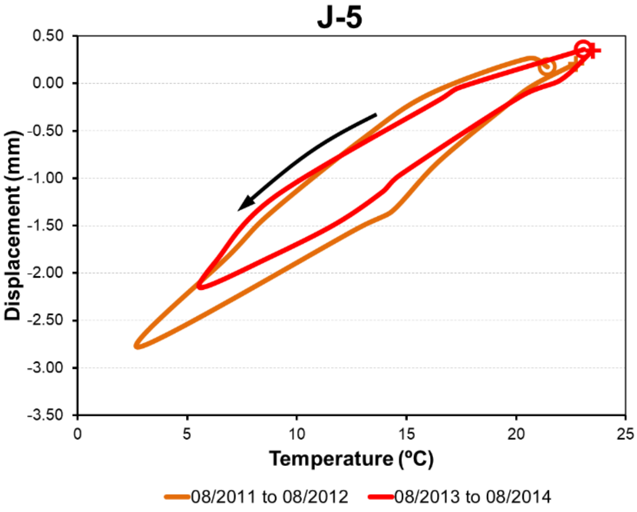

Figure 2-24 Displacements vs temperature J-5

Conversely, devices J-1 and J-2, which follow the apertures of joints located at the supports of the beam, present lower displacements amplitudes than jointmeters J3,J4 and J5 but exhibit a clear accumulation with the cycles of temperature. This can be remarked from Figure 2-25 which presents the time evolution of jointmeters J-1 and J-2 for the whole instrumentation period. It is worth noting that displacements measured on the beam became stable after July 2015, time at which the supporting frames for the beam showed in Figure 2-12 have been constructed. The jointmeters located at the roof of the cavern, do not appear to experience any change in their response. This seems to indicate that most of the displacement registered by the latter devices is related to massif deformation under thermal cycles.

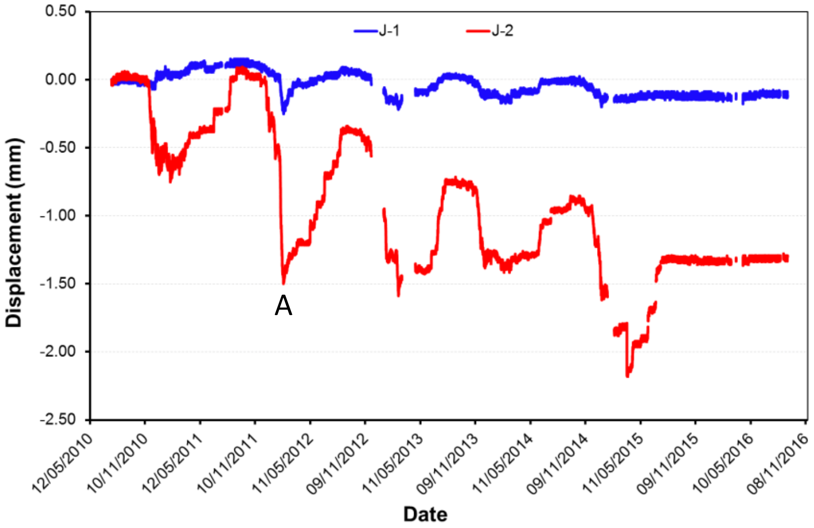

Figure 2-25 displacement obtained with Jointmeters J-1 and J-2

Another remarkable fact is the sudden and large increase in relative displacement observed at jointmeter J2 (and, in a lesser way, at J1) during February 2012 (point A in Figure 2-25). This is due to particularly low temperatures registered during this month. This displacement did not recover afterwards, which may indicate that there is a temperature threshold below which irreversible joint opening takes place. An explanation could be that, due to abnormal beam retraction, the horizontal stress, and thus the friction, diminishes along the joints delimitating the beam, leading the more marginal stability.

Figure 2-26 presents finally the curves temperature-displacements for J-2 device for the period between August 2011 to August 2014. The annual accumulation of displacement can be clearly observed as well as the strong displacement increasing during the abnormal cold period in winter 2012.

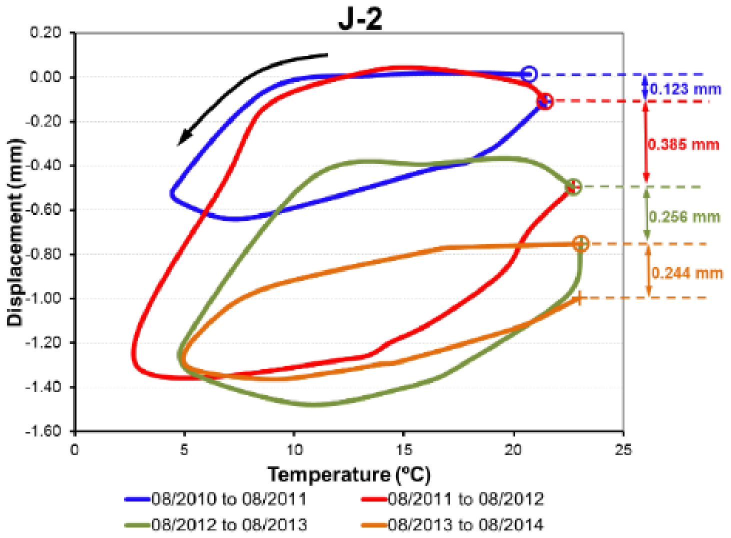

Figure 2-26 Displacements vs temperature J-2

## 2.9. Preliminary numerical modelling.

Ruiz (2013) presented a series of numerical modeling developed in order to evaluate the interaction mechanisms between the atmosphere and the cliff of La Roque Gageac during the period from August 2011 to August 2012. For this purpose, an elastic thermo-mechanical coupled finite element model has been considered.

This numerical model were performed using the Finite Element Method code Code_Bright (Olivella et al., 1994) developed to model Thermo-Hydro-Mechanical coupled problems in geological media.

The atmosphere-rock interactions were evaluated with a special boundary condition, accounting for atmospheric actions. As the problem under evaluation was only thermo-mechanical, the boundary condition applied on the rock face consisted in radiation and air temperature provided by the meteorological station.

As a first approximation, a 2D plane strain model is considered, which geometry and mesh are shown in Figure 2-27. Results obtained showed a remarkable agreement between temperatures measured in the extensometers and computed by the model considering solar radiation and air temperature variation as boundary condition (dot curve in Figure 2-28). Conversely, if only air temperature variations are considered, the temperatures computed by the model are systematically 5ºC lower that the measurements of extensometer D1 (dashed curve in Figure 2-28). Similar results have been found at the location of D2 extensometer. This highlights the importance of the solar radiation in the thermal equilibrium established between the massif and the atmosphere.

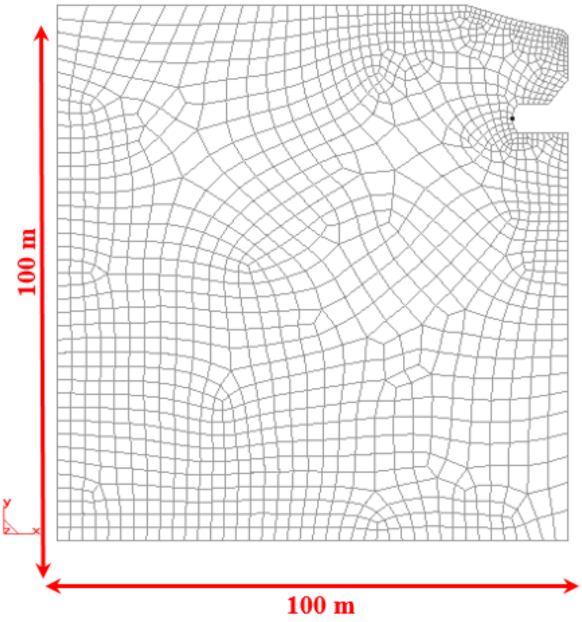

Figure 2-27 Mesh for the 2D cliff model

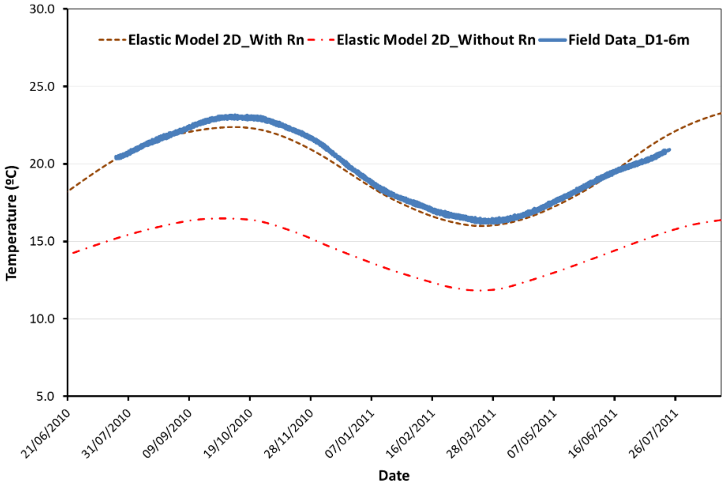

a)

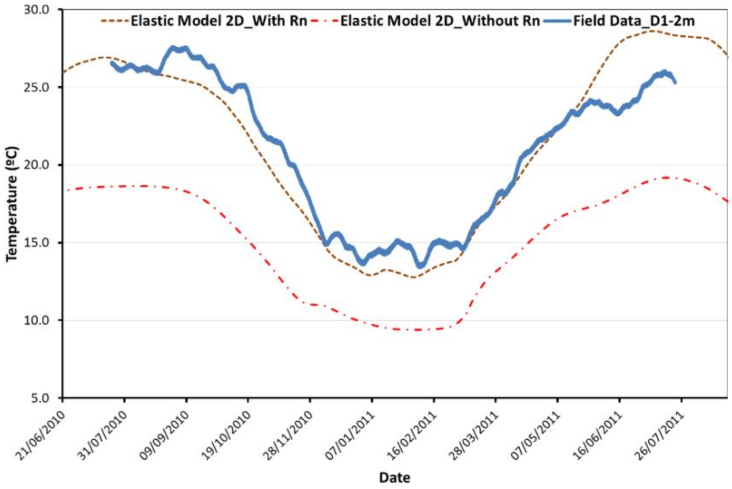

b)

Figure 2-28 Temperature evolution at extensometer D1 considering net radiation and without net radiation a) measurements at D1-6m b) measurements at D1-2m.

The analysis of displacements has been performed in two steps. In a first step, the massif deformations registered by the extensometers were evaluated in order to verify if they are only due to temperatures effects. For the sake of considering eventual arching effects on top of the cavern, a 3D model was built using a thermo-elastic law for the material. The corresponding mesh is shown in Figure 2-29.

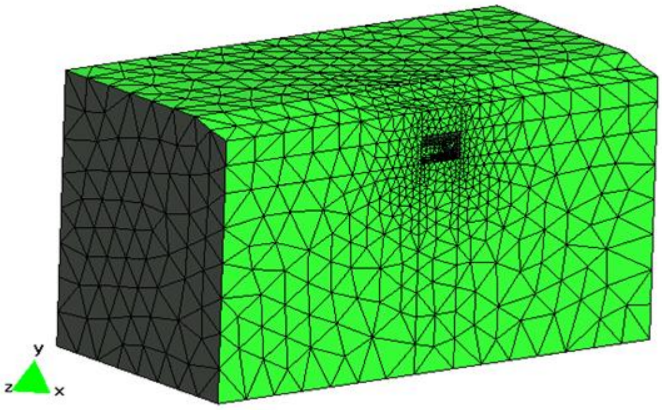

Figure 2-29 Mesh of the 3D elastic model

Figure 2-30 presents the temperatures and displacements computed using the 2D and 3D numerical models at points corresponding to a depth of 2m along the D2 extensometer. It can be observed that measured displacement are well-captured, which supports the hypothesis that they essentially result from the effect of rock temperature variations under climatic actions for the one-year period considered. This modelling further indicates that the response registered at D2 extensometer can be adequately reproduced by considering the rock cliff as a continuum and allowed to back-analyzed the field thermal conductivity (2 W.m.K-1) and thermal expansion (6. $10^{-6}$ º$C^{-1}$). Comparison between the 2D and 3D models also indicate that 3D effects are not relevant at extensometer locations.

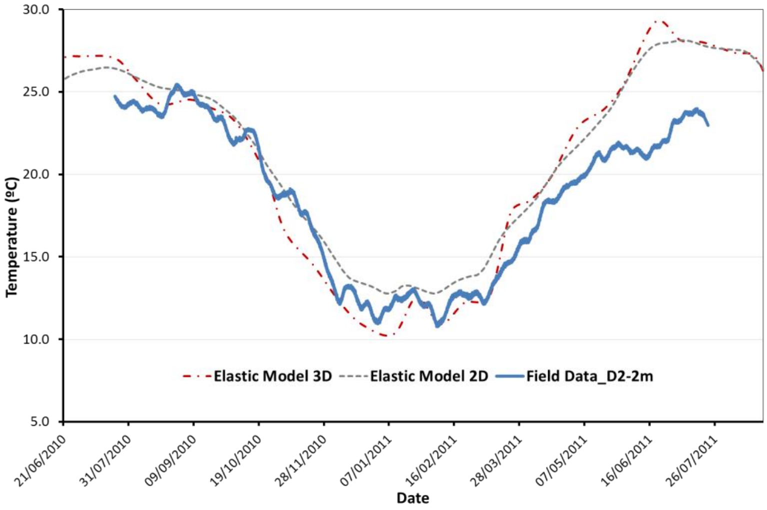

a)

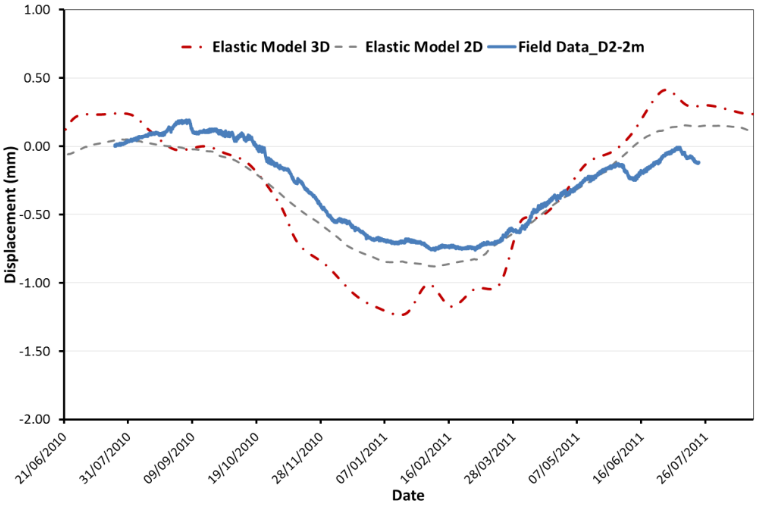

b)

Figure 2-30 Response obtained with the 2D and 3D elastic model for extensometer D2-2m a) temperature b) displacements.

In a second step, displacements registered by the jointmeters have been analyzed using a local two-dimensional model for the residual beam including joints elements to represent the most relevant discontinuities. The geometry and mesh considered are presented in Figure 2-31, where J1, J2 and J3 indicate the location of the three joint-elements considered in the model. Numerical joints are zero-thickness elements provided with a thermo-mechanical law.

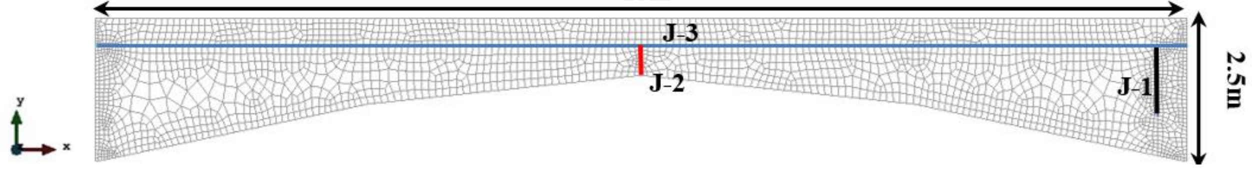

Figure 2-31 Geometry of the finite element model of roof of the cavern

Figure 2-32, Figure 2-33 and Figure 2-34 presents a comparison between the displacements obtained with the numerical model and the measurements at joints J1, J2 and J3, respectively. Agreement is good for jointmeters J2 and J3 and for the first months of measurements at J1. It is important to remember that after December 2010, the position of J1 has been changed thus it is no more possible to compare the measurements with the response of the model. Form a general point of view results indicate the necessity to model rock discontinuities with specific numerical tools in order to reproduce adequately the response of the beam inside the cavern.

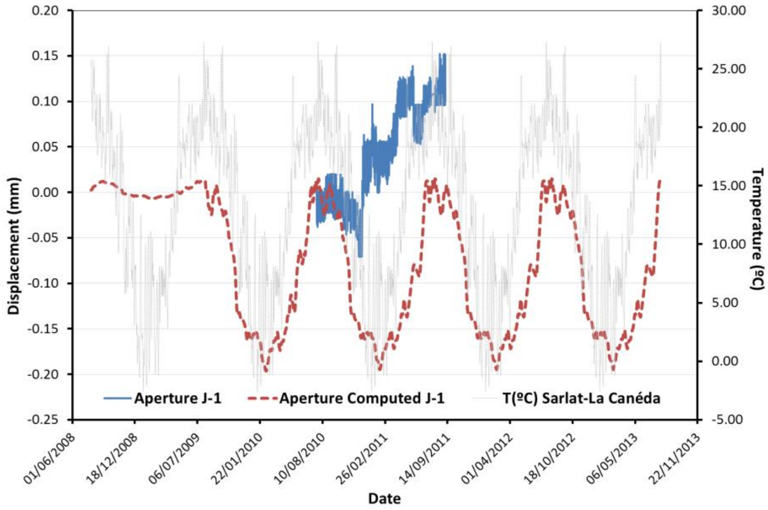

Figure 2-32 Aperture computed at the joint J1

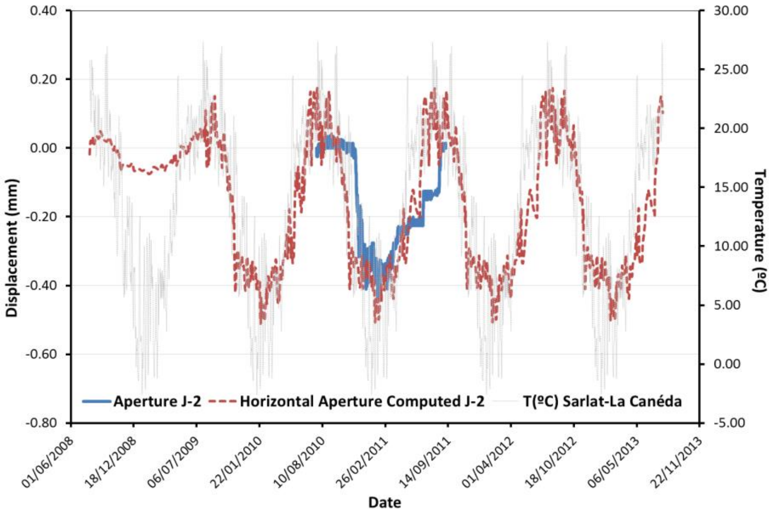

Figure 2-33 Aperture computed at the joint J2

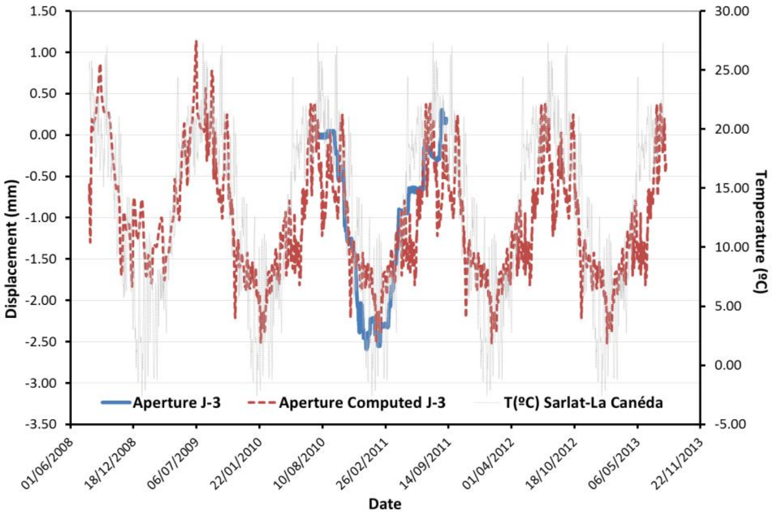

Figure 2-34 Aperture computed at the joint J3

## 2.10. Concluding remarks on the field case.

The cliff from La Roque Gageac has been submitted to recurrent rockfalls, in the last century four important events were registered, that cannot be attributed to any evident triggering factor. The last event was registered in 2010, leading a poor stability condition in the cliff, especially the zone where the troglodyte cavern is placed.

For this reason, an instrumentation system was installed in the site and has been following the cliff response for the last years, suggesting that atmospheric thermal cycles have a strong relationship with the deformations of the cliff.

Other specific observations are mentioned below:

- Because the orientation of the cliff (south) it can be considered that sun radiation have an important role in the response of the cliff, in fact, all the flacking observed at the face of it is considered to be related to daily thermal variations suffer at the cliff.

- Measurements of temperature registered inside the rock mass shows a phase delay, related to the distance to the cliff face, moreover, as the measurement is deeper the values of maximal and minimal temperature are attenuated, and the daily effect are lost. In fact, the temperature evolution observed at 6m is only related to seasonal changes.

- The extensometers placed above the troglodyte cavern shows an important strains accumulation with the increment of seasonal thermal cycles. Furthermore, measurements on extensometer D1 suggest the presence of a discontinuity.

- Jointmeter measurements indicate that the fractures tend to open during cold seasons and close during hot seasons. Explaining the irreversible joint opening event registered in 2010 occurred during the winter.

- The jointmeters located at the fissures around the residual beam shows an important relationship between crack openings and closings and temperatures. Moreover, an abnormal cold period registered in the winter 2012 generated an irreversible opening of these fissures.

- A portico structure was built within the troglodyte cavern with the purpose of giving more stability to the residual beam and possibly to the upper part of the cliff. Based on the instrumentation data registered, it can be observed that once this structure was installed the fissures around the beam present almost any additional evolution after the installation of the portico. However the response of the extensometers placed above the cavern are not affected by this structure.

- Preliminary numerical modelling results indicate that thermal variations are the main responsible of displacements registered in the cliff.

- The response observed in the extensometers (particularly D2) can related to the thermal deformation of the rock matrix and can be reproduce considering the rock mass as a continuum, while to reproduce adequately the response of the jointmeters a special element must be included in order to consider the separation of the rock blocks that define the joint.

# 3. Experimental Work

## 3.1. Introduction.

The behavior of a rock massif is the result of the combined response of the rock matrix and the discontinuities that divide the rock mass, delimiting rock blocks. The instrumentation system installed in La Roque Gageac's cliff and presented in chapter shows an important relationship between of deformations and thermal atmospheric cycles at the discontinuities and rock mass.

The cliff position (oriented to the south) and the important thermal range experienced on the site, suggest that the rock matrix is also affected by those atmospheric thermal cycles. As is observed with the measurements of extensometer D2. Moreover, preliminary numerical models suggest that thermal cycles are the principal cause of strains variations in the rock cliff.

Therefore, an experimental program was developed to evaluate the possible damage induced in the rock matrix due to climatic thermal conditions. In order to evaluate the effect of thermal degradation, different rock properties are considered to examine its evolution through thermal cycles with an atmospheric range.

Rocks weathering due to thermal stress can appear under two different phenomena: the thermal fatigue; that is related to temperature variations that lead to repeated stress, below the rock strength, but its cycling effect induces permanent damage in the material. In the other hand, the thermal shock is related to a single event of a sudden change of temperature that generates an excess of stress that rock is incapable of absorbing other than through instantaneous failure.

The thermal degradation of rocks is mostly influenced by the different thermal properties of the minerals that compose the rock. Differences in thermal expansion, thermal conductivity and principal axis direction, controls the mineral to mineral thermal stresses induced by the thermal variations. Hence, additional stresses can be induced leading to failures across the minerals boundaries, and lines of weakness, generating some intergranular disintegration and propagation of existent fissures (Hall, 1999; Siegesmund et al., 2000; Walsh and Lomov, 2013; Hall and Thorn, 2014).

Under laboratory conditions, the thermal deterioration of rocks has been mostly studied for high temperatures (more than 100ºC) like those experienced during fires (Brotóns et al., 2013) or in nuclear waste disposal (Chen et al., 2014). Nevertheless, some studies are focused on weather induced phenomena like freeze-thaw (Malaga-Starzec et al., 2006), thermal shock (Yavuz, 2011) or cold – heat cycles (Goudie and Viles, 2000).

The elastic wave propagation velocity is a common parameter used to evaluate damage in rocks. Since, this parameter is extremely sensitive to the presence of defects in the sample, (like the internal fissures) due to the considerable difference between the air and the solid materials wave propagation velocity (Martínez-martínez, Benavente and García-del-cura, 2011; Brotóns et al., 2013; Inserra, Biwa and Chen, 2013).

There is a relation between the elastic wave propagation velocity and the dynamic Young modulus and Poisson ratio, allowing the comparison with the results obtained with mechanical tests (Kendrick et al., 2013). Moreover, this parameter is obtained with a nondestructive test, hence, is possible to evaluate its evolution in the same sample through the whole laboratory study.

This parameter has been widely used to evaluate the effect of thermal stresses over different lithologies, like: marbles (Luque et al. 2011; Yavuz et al. 2006; Malaga-Starzec et al. 2006; Yavuz et al. 2010), limestones (Yavuz et al., 2006; Martínez, 2008; Yavuz, Demirdag and Caran, 2010)( or Andesites (Yavuz, 2011). Even if these studies do not consider similar thermal ranges, in all of them a decay in the elastic wave propagation velocities with the imposition of thermal cycles is observed, suggesting an internal micro-fissuration of the samples, even if there is no evidence of external fissures (Yavuz et al., 2006).

Another interesting physical property to consider is the effective porosity. In fact, the initial effective porosity of the material may influence the thermal weathering of the rocks, because if the material presents a high porosity, the expansion of the minerals may be absorbed by the porosity, reducing the internal stresses induced (Sousa et al., 2005). Additionally, an augmentation in the values of effective porosity and variations in the pore size distribution can also be related to the fissuration of the rock due to thermal weathering. For example, Koch & Siegesmund (2004) observed an augmentation in the pore size radius and porosity percentage of marbles after imposing 40 cycles between 20ºC to 80ºC. In the same way, Luque et al. (2011) and Franzoni et al. (2013) obtained a variation in the pore size distribution of marbles and granites respectively after inducing thermal degradation.

As mentioned before, the thermal weathering is a process that begins in the mineral to mineral boundaries. To evaluate the phenomena at a mineral scale, environmental scanning electron microscopy (ESEM) and scanning electron microscopy (SEM) images are generally used. For instance, Luque et al. (2011) present the evolution of a specific fissure over a marble while it is heated between 20ºC to 90ºC, showing the widening of the fissures while the temperature increase. In the same way, Goudie & Viles (2000) use SEM observations to show that mineral boundary wide increase as the samples are subjected to a higher number of thermal cycles.

At macroscopical scale the mechanical properties of the rocks may also be affected by the thermal weathering. This phenomenon has been evaluated using different mechanical tests types such as: Brazilian test (Mahmutoglu, 1998), Schmidt hardness (Yavuz et al., 2006; Yavuz, 2011) or uniaxial compression test (Mahmutoglu, 1998; Franzoni et al., 2013; Chen et al., 2014). The laboratory study developed by Mahmutoglu (1998) over samples of marble and limestones, heated between 20ºC to 600ºC shows that uniaxial compression and tensile strength reduce when samples are exposed to thermal cycles. In fact, marble samples show a reduction of 50% of their Uniaxial compressive strength and 80% of their tensile strength after 16 cycles. This response was also observed when smaller thermal ranges were considered, Chen et al., 2014 presented the results obtained for granite samples subjected to thermal cycles between -20ºC and 65ºC, obtaining a reduction of 30% in the Uniaxial compressive strength value after 40 thermal cycles.

In the same way, Yavuz et al. (2006) obtain the response of a marble and a limestone subjected to thermal cycles between -20ºC and 20ºC. This experimental program evaluates the mechanical response of the material but also some physical properties such as porosity and

P- wave propagation velocity (Vp). Showing that when this material experiences 20 cycles the strength and Vp value of the rock decrease and the porosity increases.

In order to evaluate the thermal weathering over the limestone of La Roque Gageac (LaRG), two groups of samples were considered: the first group correspond to samples obtained from remaining blocks from inside the troglodyte cavern after the 2010's event, and mainly conformed by calcite. The second group is composed by samples directly drilled from the face of the cliff nearby the troglodyte cavern; these samples are composed by quartz and calcite.

Both groups of samples were subjected to thermal cycles with a thermal range of 40ºC (10ºC to 50ºC). The effect of these thermal cycles over this limestone was evaluated through different physical and mechanical properties, such as deformations, elastic wave propagation velocities, fissuration and propagation of fissures, and Uniaxial compressive strength. In this chapter, a description of the complete experimental program and its results are presented.

## 3.2. La Roque Gageac's limestone general characterization.

After the event of 2010 some physical and mechanical tests were performed, to have a complete characterization of La Roque Gageac (LaRG) limestone. These tests were realized on samples obtained from 2 blocks dropped from the roof of the troglodyte cavern during the 2010's event. It is important to mention that samples obtained from the block defined as A were obtained in the perpendicular direction to the stratification planes, however, block B does not show any evidence of the stratification planes direction.

The results obtained are presented in the report of the DO-SMS project report realized by Centre d'Études Techniques de l'Equipement du Sud-Ouest (now Cerema) (Virely and Guittard, 2010a).

### 3.2.1. Physical properties.

The density and elastic wave propagation velocity of the rock were obtained from 13 different samples. The mean density obtained is 2382 kg/m3 with a standard deviation of 45 kg/m3. The mean P-wave propagation velocity (Vp) is 4651 m/s, and the shear-wave propagation velocity, obtained from measures realized in two perpendicular directions, has a mean value of 2671 m/s. Table 3-1 gives the results obtained for the 13 samples.

Table 3-1 Density and elastic wave propagation velocity

| Sample | Block | Density (kg/m$^3$) | Vp (m/s) | Vs1 (m/s) | Vs2 (m/s) |
|---|---|---|---|---|---|
| 998 | A | 2434 | 5420 | 3014 | 3016 |
| 999 | A | 2399 | 5046 | 2814 | 2870 |
| 1000 | A | 2444 | 5029 | 2875 | 2856 |
| 1013 | A | 2317 | 4757 | 2736 | 2840 |
| 1014 | A | 2437 | 3269 | 2675 | 2602 |
| 1015 | A | 2340 | 4684 | 2731 | 2811 |
| 1016 | A | 2400 | 4786 | 2537 | 2612 |
| 1017 | A | 2290 | 4681 | 2561 | 2477 |
| 1018 | A | 2423 | 5241 | 2675 | 2720 |
| 1019 | A | 2367 | 4884 | 2572 | 2663 |
| 1020 | B | 2373 | 4431 | 2427 | 2462 |
| 1021 | B | 2366 | 4078 | 2376 | 2411 |
| 1022 | B | 2377 | 4153 | 2571 | 2563 |
| Mean |  | 2382 | 4651 | 2659 | 2683 |
| St deviation |  | 45 | 545 | 171 | 178 |

To complete the physical characterization of La Roque Gageac limestone, the porosity and the saturated water content were obtained. These results are summarized in Table 3-2.

Table 3-2 Porosity for La Roque Gageac Limestone

| Sample | $\rho_d$ (kg/m$^3$) | $\rho_s$ (kg/m$^3$) | $n_c$ Connected porosity | $n_t$ Total porosity | $W_{sat}$ (%) |
|---|---|---|---|---|---|
| Block1 | 2356 | 2868 | 0.111 | 0.179 | 4.7 |
| Block2 | 2329 | 2835 | 0.113 | 0.179 | 4.8 |

### 3.2.2. Mechanical properties.

The mechanical properties of LaRG limestone were determined by 3 types of tests: Uniaxial compressive strength, Brazilian tensile strength and triaxial test. Table 3-3 summarizes the results obtained.

Uniaxial compressive strength was obtained from 10 different samples: 7 from block A and 3 from block B, the mean value obtained is 47.39 MPa with a standard deviation of 9.63. This last value is quite high, this characteristic may be related to the heterogeneity of the material, associated to its geological composition.

Table 3-3 Mechanical properties LaRG limestone

| Sample | Block | $\sigma_c$ (MPa) | $\sigma_{tb}$ (MPa) | $\sigma_c$ (MPa) | | E (GPa) | $\mu$ |
|---|---|---|---|---|---|---|---|
| | | | | $\sigma_1$ | $\sigma_3$ | | |
| 998 | A | | | 80.2 | 5.0 | 42.58 | 0.15 |
| 999 | A | | | 81.68 | 10.0 | 46.97 | 0.12 |
| 1000 | A | | | 65.00 | 2.5 | 38.35 | 0.15 |
| 1008 | A | | 6.18 | | | | |
| 1009 | A | | 5.49 | | | | |
| 1010 | A | | 5.10 | | | | |
| 1011 | A | | 4.16 | | | | |
| 1012 | A | | 5.44 | | | | |
| 1013 | A | 47.44 | | | | | |
| 1014 | A | 47.28 | | | | | |
| 1015 | A | 53.73 | | | | | |
| 1016 | A | 59.71 | | | | | |
| 1017 | A | 35.44 | | | | | |
| 1018 | A | 31.30 | | | | | |
| 1019 | A | 63.29 | | | | | |
| 1020 | B | 51.68 | | | | | |
| 1021 | B | 43.20 | | | | | |
| 1022 | B | 40.65 | | | | | |
| 1343 | C | | 5.63 | | | | |
| 1344 | C | | 4.91 | | | | |
| 1345 | C | | 5.86 | | | | |
| 1346 | C | | 5.50 | | | | |
| 1347 | C | | 5.58 | | | | |
| 1348 | C | | 5.51 | | | | |
| Mean | C | 47.37 | 5.39 | | | 42.63 | 0.14 |
| St deviation | | 9.63 | 0.50 | | | 3.52 | 0.01 |

From Table 3-3 can be appreciated that samples 1017 and 1018 present the lowest UCS values obtained from the 10 samples. This can be related to the fact that those two samples presented a vertical discontinuity, as shown in Figure 3-1. In fact, the mean UCS value for this two samples, is 33.30 MPa. Whereas, the mean value obtained for all the samples is 47.39 MPa. If these two samples are not considered, the mean UCS value increase to 50.87 MPa and the standard deviation becomes 7.32. Nevertheless, such a standard deviation value is still associated to a heterogeneous rock.

Figure 3-1 Discontinuity in sample 1018

Besides the mechanical tests performed within the framework of the DO-SMS project, some additional Brazilian tensile strength tests were performed on samples obtained from a third block (Block C) fell during the 2010's event and removed in February 2015. Including these last tests, the mean value of tensile strength is 5.39 MPa with a standard deviation of 0.50. The small standard deviation value obtained can be related to the probabilistic density associated with this type of test and the volume of the specimen associated, as illustrated in Figure 3-2.

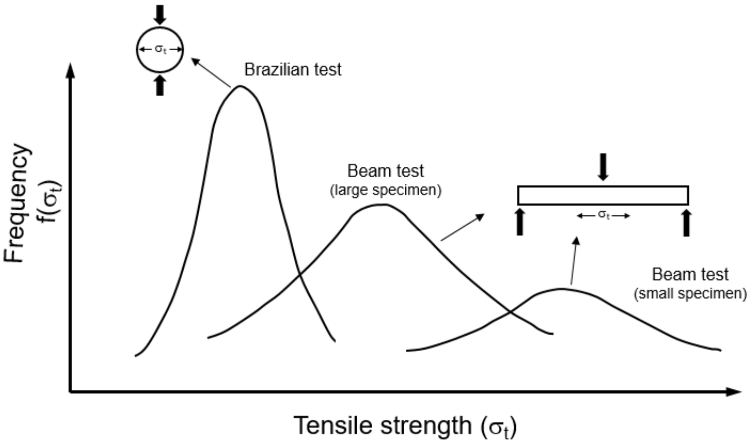

Figure 3-2 Tensile strength variation as function of type of test and specimen volume from (Hudson & Harrison 1997)

Finally, triaxial test were performed over 3 samples under 2.5, 5 and 10 MPa confining pressure. The results obtained are presented on Figure 3-3 and Table 3-3. The response observed with these triaxial tests includes the transition between a fragile behavior to a ductile one, associated to the level of confining pressure (Hudson & Harrison 1997) . In fact, in Figure 3-3 it can be observed that samples under lower confining pressure show a fragile behavior, while sample under 10 MPa of confining pressure has a ductile response.

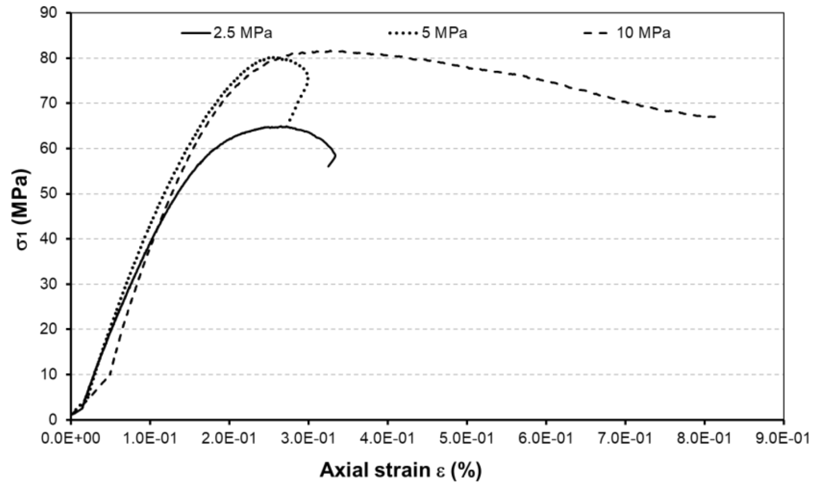

Figure 3-3 Triaxial test results

Based on the mechanical properties obtained and the in-situ observation, the *Laboratoire Régional des Ponts et Chaussées de Toulouse* performed a RMR evaluation. Table 3-4 summarize the parameters determined.

Table 3-4 RMR evaluation

| Property | Value | Note |
|---|---|---|
| Strength | $\sigma_c$=47.4 MPa | 4 |
| RQD | 75 – 90% | 17 |
| Discontinuities separation | 200 – 600 mm | 10 |
| Discontinuities roughness | Roughness surface | 25 |
| water | dry | 15 |
| **RMR** | | **71** |

Hoek & Brown (1997) proposed a modification of the original Hoek & Brown (1980) failure criterium defined for intact rocks, to include the real conditions of the massif, like joins and discontinuities. This modification considers the geological strength index (GSI) as a parameter to reduce the strength of the material based on the geological condition of the massif. The modified Hoek-Brown failure criterion is defined by Eq. 3-1:

$$\sigma'_1 = \sigma'_3 + \sigma_{ci}\left(m_b \frac{\sigma'_3}{\sigma_{ci}} + s\right)^a \qquad \text{Eq. 3-1}$$

Where, $\sigma_{ci}$ is the Uniaxial compressive strength of the rock and $m_b$ s and a are parameters that depend upon characteristics of the rock mass, based on the GSI parameter. For LaRG limestone the GSI determined is 76 associated to the blocky structure of the massif. Under this consideration the parameters consider for modified Hoek-Brown failure criterion are: $m_b$ = 4.24, s = 0.0695 and a= 0.501.

### 3.2.3. Thermal properties.

#### Thermal expansion.

The thermal expansion of the material was determined with the procedure proposed by the French standard NF-EN 14581 method B (AFNOR, 2005). For this, strain gages were glued in vertical (vert) and horizontal (hor) direction on two prismatic and two cylindrical samples.

This standard considers than samples should be placed in an oven at 20ºC for two hours, then the temperature increases until 80ºC with a rate of 0.5ºc/min and remain constant at 80ºC for two more hours. Strains should be measured at each change of temperature. Finally, thermal expansion is defined as:

$$\alpha_{\mathrm{i}} = \frac{\varepsilon_{\mathrm{i}}}{\Delta \mathrm{T}} \qquad \text{Eq. 3-2}$$

Where, $\alpha_i$ is the thermal expansion in direction i, $\varepsilon_i$ represents the strains induced by the temperature variation, measured for direction i and ΔT is the thermal variation (60ºC). Table *3-5* presents the values of thermal expansion obtained with the four samples considered. Note that for prismatic samples two different pairs of gauges were used to measure horizontal deformation.

Table 3-5 Thermal expansion results

| Prismatic samples | P1 hor 1 | P1 vert | P1 hor 2 | P2 hor 1 | P2 vert | P2 hor 2 |
|---|---|---|---|---|---|---|
| $\alpha(10^{-6}$ º$C^{-1})$ | 3.1 | 14.2 | 7.0 | 6.2 | 4.8 | 1.6 |

| Cylindrical samples | C1 vert | C1 hor | C2 vert | C2 hor |
|---|---|---|---|---|
| $\alpha(10^{-6}$ º$C^{-1})$ | 6.1 | 9.7 | 7.6 | 10.6 |

It is important to mention that Ruiz (2013) determined a valued of thermal expansion for the rock massif equal to 6x$10^{-6}$ º$C^{-1}$. This value was obtained with a numerical back-analysis from the extensometer measurements as presented in section 2.9.

## 3.3. Samples description.

To evaluate the damage of LaRG limestone due to thermal cycles, two geometries of samples are considered: cylindrical and prismatic. The use of each geometry depends on the type of test to be performed on the sample.

Furthermore, for this experimental program, two groups of samples are considered. The first set corresponds to samples drilled from 2 blocks (see Figure 3-4) fell during the 2010 event and removed in December 2014 (block 1) and February 2015 (block2).

Figure 3-4 Samples obtained from blocks- February 2015

The second set consist of samples directly drilled from the cliff face, nearby the troglodyte cavern, as illustrated in Figure 3-5a. For this second group of samples, two types of specimens are extracted, half of the samples were drilled in vertical sense (Figure 3-5b) and the other half in horizontal sense (Figure 3-5c). It is important to mention that around the troglodyte cavern the cliff shows an almost horizontal stratification (see Figure 3-5a), therefore horizontally drilled samples are parallel to the stratification planes while vertical samples are perpendicular to it.

Each sample obtained in vertical direction was obtained from one borehole, with cores of maximum 20 cm long, as illustrated in Figure 3-6. Therefore, all vertical samples belong to the first 20 cm of the cliff.

Longer cores were obtained from the horizontal boreholes, almost 40 cm long. Thus, several horizontal samples were obtained from the same rock core. For this reason, even if these samples still be part of the most superficial zone of the cliff, some of them belong to a deeper zone.

In total 35 samples are evaluated, 30 cylindrical and 4 prismatic. Table 3-6 presents the characteristics of the cylindrical samples and Table 3-7 of the prismatic ones. It is important to mention, that prismatic sample from group 2 (C4) is a sample with natural fissures, removed during a technical visited realized in April 2016.

Porosity of the samples is obtained based on the density of the samples and the specific weight obtained in laboratory: 2.72 g/cm$^3$ for samples from blocks and 2.76 g/cm$^3$ for samples directly drilled from the face of the cliff.

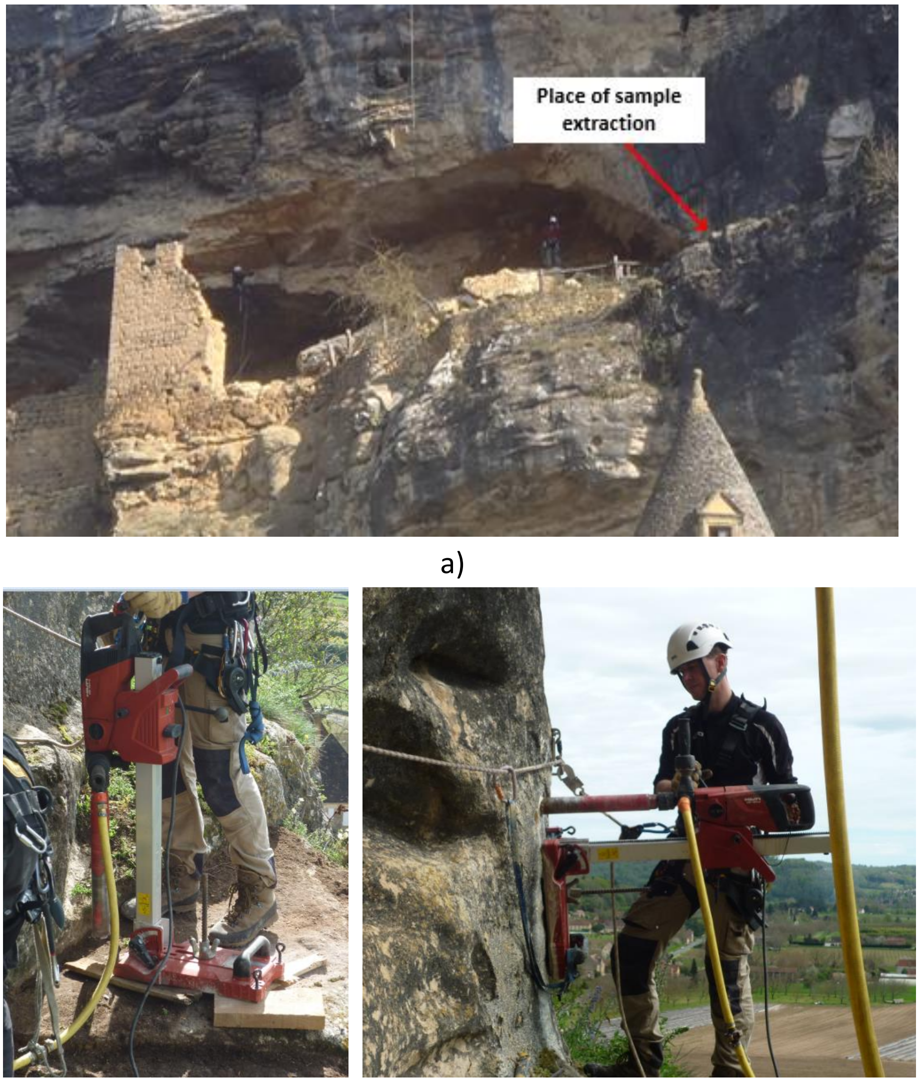

a)

b) b)

Figure 3-5 Sample extraction from the face of the Cliff- April 2016: a) location b) Samples obtained in vertical sense c) samples obtained in horizontal sense

a) b)

Figure 3-6 Extraction of vertical samples: a) Boreholes b) Core from perforation 5 (sample CV5)

Table 3-6 Geometry and characteristics cylindrical samples (CV: samples drilled in vertical sense from the face of the cliff, CH: Samples drilled in horizontal sense from the face of the cliff)

| Sample | Group | Diameter (mm) | Height (mm) | Weight (gr) | VP (m/s) | Porosity (%) |
|---|---|---|---|---|---|---|
| B1 | Group 1- Block 1 | 51.03 | 101.07 | 473.00 | 4347 | 15.86 |
| B2 | Group 1- Block 1 | 50.79 | 100.96 | 500.00 | 4637 | 10.13 |
| B3 | Group 1- Block 1 | 50.85 | 101.13 | 493.00 | 4480 | 11.75 |
| B4 | Group 1- Block 1 | 50.93 | 100.99 |  | 4252 |  |
| B5 | Group 1- Block 1 | 51.02 | 100.96 | 474.52 | 4342 | 15.47 |
| B6 | Group 1- Block 1 | 50.40 | 100.86 | 458.29 | 4282 | 16.29 |
| B7 | Group 1- Block 1 | 50.61 | 101.31 | 457.44 | 4177 | 17.49 |
| B8 | Group 1- Block 1 | 51.03 | 100.92 | 475.08 | 4407 | 15.38 |
| B9 | Group 1- Block 1 | 50.05 | 101.02 | 457.96 | 4404 | 15.29 |
| B10 | Group 1- Block 2 | 49.71 | 112.04 | 511.48 | 4321 | 13.52 |
| B11 | Group 1- Block 2 | 50.03 | 112.07 | 511.02 | 4373 | 14.73 |
| B12 | Group 1- Block 2 | 50.21 | 112.16 | 514.57 | 4402 | 14.80 |
| B13 | Group 1- Block 2 | 49.84 | 112.03 | 512.04 | 4485 | 13.88 |
| B14 | Group 1- Block 2 | 49.43 | 112.07 | 501.35 | 4486 | 14.29 |
| B15 | Group 1- Block 2 | 49.22 | 112.07 | 498.09 | 4389 | 14.13 |
| B16 | Group 1- Block 2 | 49.31 | 112.06 | 504.65 | 4441 | 13.29 |
| B17 | Group 1- Block 2 | 49.83 | 112.02 | 511.27 | 4381 | 13.95 |
| B18 | Group 1- Block 2 | 49.64 | 112.07 | 510.63 | 4483 | 13.45 |
| B19 | Group 1- Block 2 | 49.26 | 111.98 | 495.98 | 4380 | 14.56 |
| B20 | Group 1 – Block1 | 50.66 | 96.60 | 472.72 |  |  |
| CV1 | Group 2 | 50.77 | 111.31 | 505.71 | 3165 | 18.40 |
| CV2 | Group 2 | 50.73 | 111.17 | 490.70 | 2831 | 20.87 |
| CV3 | Group 2 | 50.73 | 111.23 | 503.15 | 2517 | 18.91 |
| CV4 | Group 2 | 50.68 | 111.01 | 498.78 | 2831 | 20.76 |
| CV5 | Group 2 | 50.75 | 111.33 | 497.87 | 2727 | 19.91 |
| CH1 | Group 2 | 50.89 | 111.14 | 509.87 | 3027 | 18.29 |
| CH2 | Group 2 | 50.85 | 111.02 | 5106.6 | 3039 | 17.93 |
| CH3 | Group 2 | 50.90 | 111.08 | 514.87 | 3348 | 17.46 |
| CH4 | Group 2 | 50.88 | 111.09 | 498.57 | 2880 | 20.03 |
| CH5 | Group 2 | 50.82 | 111.11 | 493.33 | 2829 | 20.70 |

Table 3-7 Geometry and characteristics prismatic samples

| Sample | Group | Width (mm) | Length (mm) | Height (mm) | Weight (gr) |
|---|---|---|---|---|---|
| C1 | Group 1 | 81.50 | 61.02 | 83.56 | 983.04 |
| C2 | Group 1 | 81.44 | 61.72 | 81.11 | 920.08 |
| C3 | Group 1 | 82.09 | 61.62 | 80.87 | 973.69 |
| C4 | Group 2 | 82.80* | 72.90* | 74.80* | 953.46 |

*Approximated measurements because the irregular shape of the sample (Natural sample)

### *3.3.1. Mineralogy.*

The mineralogical composition of each group of samples was determined, to evaluate if there are any mineralogical differences between them. For this, three types of tests were performed: spectrometry, X-Ray diffraction and thin sections analysis. X-ray test was only realized over samples belonging to the second group, See Table 3-8.

The samples used for the mineralogical analysis came from cylindrical samples prepared for this experimental program but rejected because they didn't follow the geometry conditions for the mechanical tests (parallelism between faces and/or dimensions). In total 5 samples were used.

Table 3-8 Mineralogical analysis samples

| Sample | Group | Thin sections | Spectrometry | Rx |
|---|---|---|---|---|
| M1 | Group 1 – block 1 | X | X | |
| M2 | Group 1 – block 2 | X | X | |
| M3 | Group 2 | X | X | |
| M4 | Group 2 | | | X |
| M5 | Group 2 | | | X |

#### Infrared spectrometry.

Infrared spectrometry (IRA) analysis were performed over three samples: M1, M2 and M3. This technique is based on the evaluation of the behavior of electromagnetic waves that are reflected or absorbed by a solid body. The percentage of absorption and reflectance are controlled by physical and chemical characteristics of the body.

The spectrum obtained for each sample can be compared to typical spectra of different minerals in order to determine the principal minerals that compose the rock. This technique does not give a mineral content percentage but allows to identify the principal composing mineral if it is predominant.

Figure 3-7 presents the spectrometry results obtained for the three analyzed samples, compared with the typical characteristics bands observed for calcite (Huang and Kerr, 1960; Vazquez-Moreno and BLanco-Varela, 1981; Gunasekaran, Anbalagan and Pandi, 2006). Note that spectra obtained for sample M1 and M2 follows precisely the calcite bands. However, spectra of sample M3 does not match either with typical calcite or quartz bands. Therefore, it can be concluded that samples from the face of the cliff (sample M3) are not composed by just one principal mineral and samples M1 and M2 are mainly composed by calcite.

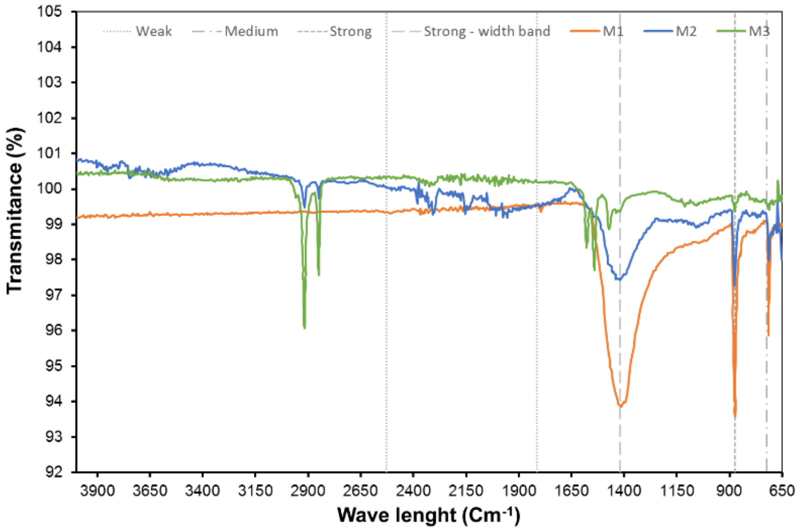

Figure 3-7 Infrared spectra for simple M1, M2 and M3, compared with typical calcite bands

## X-Ray diffraction.

As from spectrometry test was not possible to determine the mineralogical composition of samples from the face of the cliff, X-Ray diffraction (XDR) analysis were performed on samples M4 and M5 belonging to group 2. It is important to mention that sample M4 was obtained from a sample drilled in the vertical direction and sample M5 in the horizontal direction both close to the face of the cliff.

The XDR technique allows to obtain the mineralogical composition of the sample by collecting the X-ray reflected by the powder sample. These diffraction peaks are converted to d-spacing allowing to identify the minerals components because each mineral has a set of d-spacing characteristic.

XDR results for samples M4 and M5 are shown in Figure 3-8 and Figure 3-9 respectively. It can be observed that both samples are composed almost in a 50-50 relation by quartz and calcite. More precisely sample M4 is composed in a 55% by quartz and 42% by calcite and sample M5 in a 47% quartz and 48% calcite.

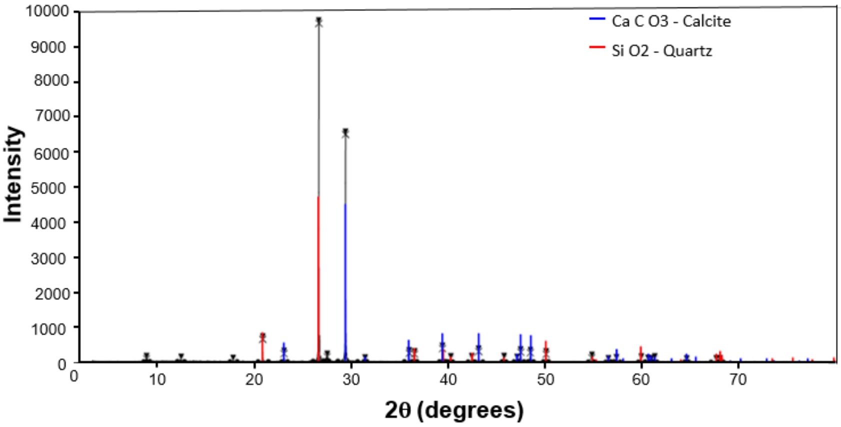

Figure 3-8 Rx- diffraction results for sample M4

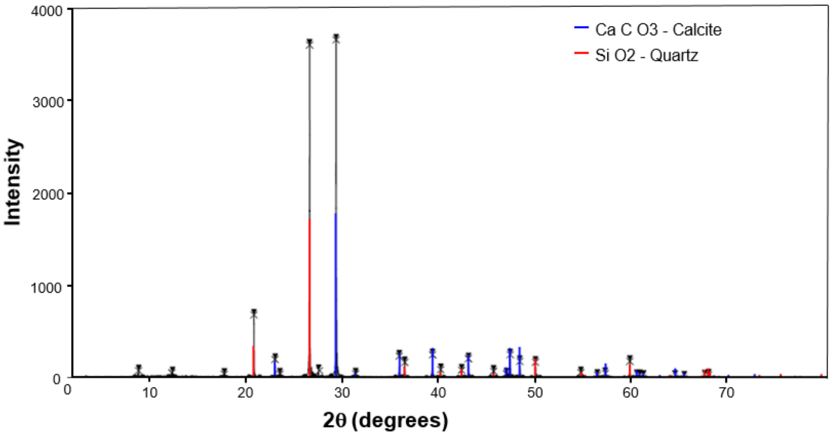

Figure 3-9 Rx- diffraction results for Sample M5

### Thin sections.

In order to complement the information obtained from the IRA and XDR tests and to evaluate mineralogical characteristics of the two groups of samples, thin sections were created from samples of each group. Those thin sections were scanned under natural and polarized light, the mineralogical analysis is performed over these images.

The analysis of the thin section images allows to obtain a mineral composition percentage, but also, the shape and size distribution of minerals composing the rock. For this, an image-based analysis is performed using the software SPO (Launeau et al. 1990; Launeau & Robin 1996). This program works with processed images, in which each color represents a mineral. Therefore, it allows to determine the area percentage composed by each mineral. Additionally, based on the intercepts method (Launeau and Cruden, 1998) and the shape preferred orientation (SPO), the mean shape of the minerals and their shape ratio distribution can be determined.

As the minerals have an irregular shape, the SPO analysis transforms this shapes in ellipsoids. In this way is possible to determine the mean shape of the minerals and the shape ratio distribution, considered as the relation length – width of the ellipsoids. The principal results obtained with the SPO analysis are: the percentage area cover by each mineral and the shape ratio distribution. From these characteristics is possible to determine the predominant minerals and the relative size of the minerals that compose the rock.

Two thin sections were created from both samples belonging to group 1 (sample M1 and M2) and only one from group 2 (M3). Figure 3-10 presents the thin sections images obtained under natural light.

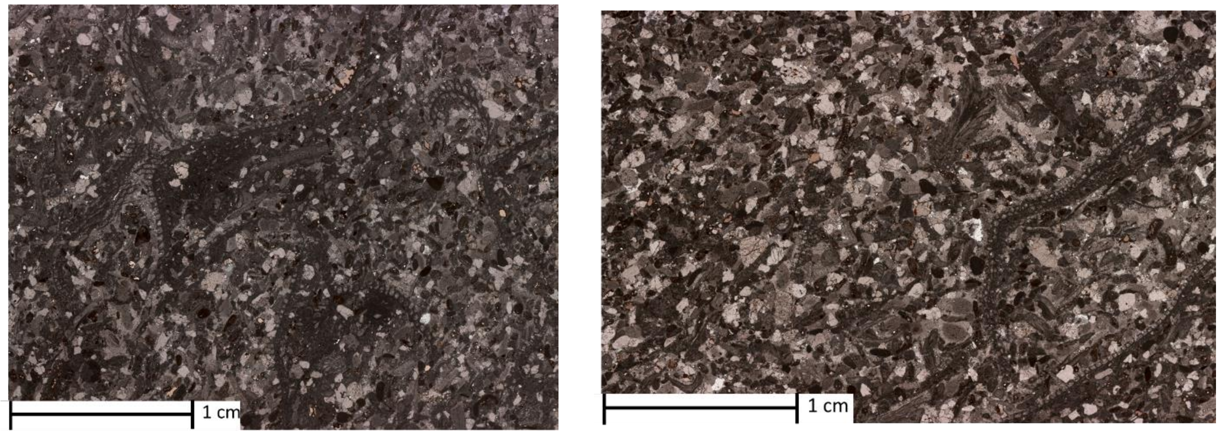

Sample M1-A Sample M1-B

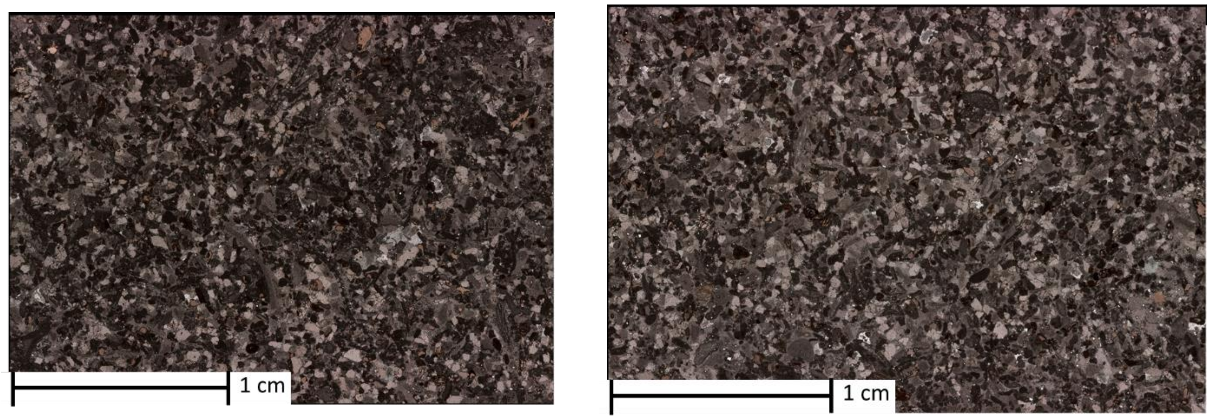

Sample M2-A Sample M2-B

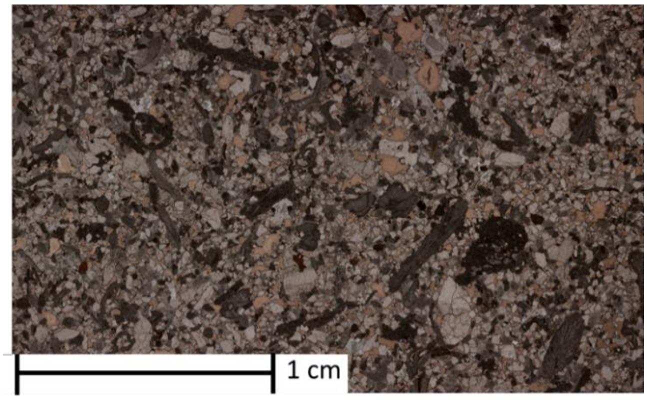

Sample M3

Figure 3-10 Thin sections images under natural light

From thin sections of samples M1 and M2, it is observed that these two samples are mainly composed by calcite, just like was obtained from the spectrometry test. Calcite is present in two types of crystallinity: micrite, darker and without crystalline shape and sparite, that is the lighter part with coarse crystalline shape. In fact, almost any other type of mineral is observed, just a little portion of quartz (colorless minerals with low positive relief in natural light).

For instance, Figure 3-11 presents the typical appearance of the calcite and quartz observed in sample M2. Some fossils are identified in samples M1 and M2. these fossils are mainly composed by calcite in micrite crystallinity.

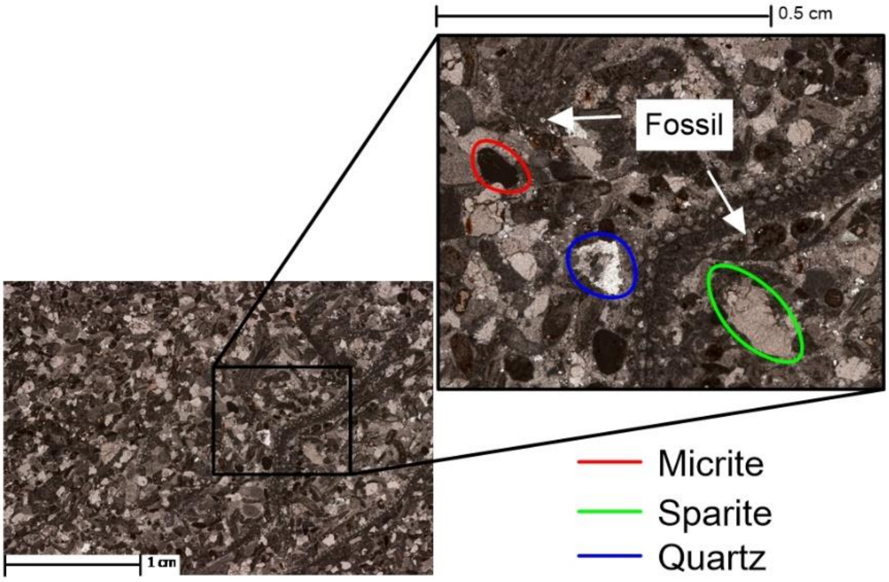

Figure 3-11 Mineral identification sample M1-B

In the same way, sample M3 also shows minerals of calcite, in both types of textures, sparite and micrite. However, an important percentage of voids are observed in the thin section, as illustrated in Figure 3-12 (light grey/light pink zones). These voids can represent either the sample porosity of the presence or minerals that were lost during the preparation of the samples. This last cause is the one assumed to be the explanation for the voids observed in sample M3 because the porosity of LaRG limestone is not that high. In fact, for this sample, the porosity measured is only 9%.

Considering the DXR results it was observed that the sample M3 presents an important quartz content. For this reason, it is assumed that the voids observed in the thin sections represent the quartz content. Unfortunately, from this sample is not possible to evaluate the quartz crystals shape ratio, as it is not possible to know if each void was composed by just one crystal or several crystals.

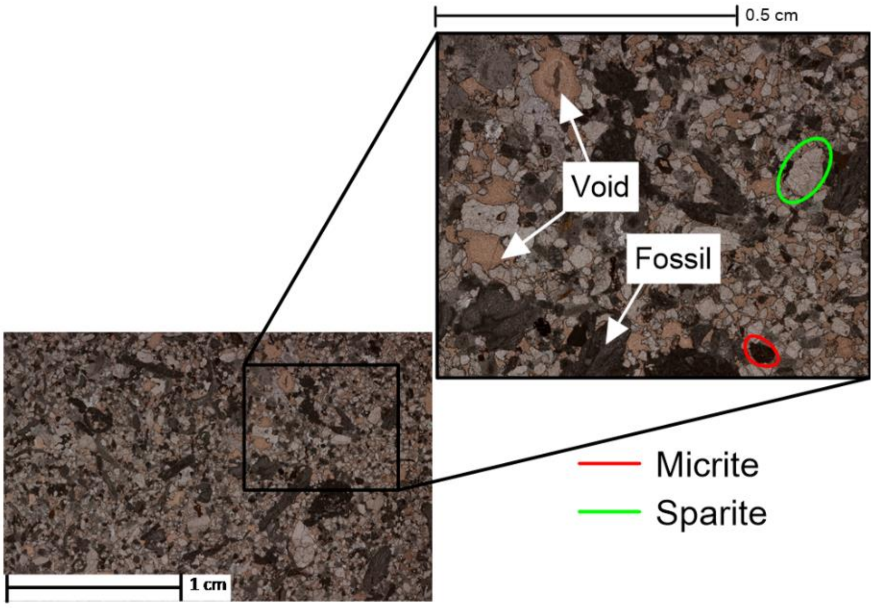

Figure 3-12 Holes observed in thin section of sample M3

Taking into account the considerations presented before, the modal composition of the samples is presented in Figure 3-13. It can be observed that calcite is the predominant mineral for the three samples. Nevertheless, for samples obtained from inside the cavern (M1 and M2) calcite is mainly observed in sparite texture and for the sample obtained from the face of the cavern (M3) in micrite. In the other hand, sample M3 presents a considerable quartz content in comparison with samples M1 and M2.

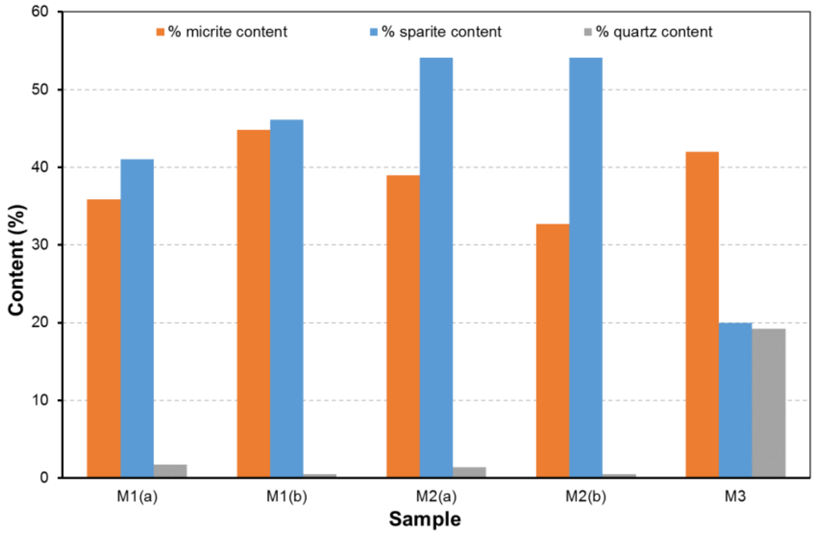

Figure 3-13 Modal composition computed from image analyses of the thin sections.

From the shape ratio distribution, it is possible to determine the predominant shape ratio for a specific mineral. Figure 3-14 presents the shape ratio distribution for the calcite in micrite shape, it can be observed that samples obtained from inside the cavern have a predominant shape ratio of 1.4, while this value for the sample drilled in the face is 1.6, which means that micrite crystals for sample M3 are longer than for samples M1 and M2.

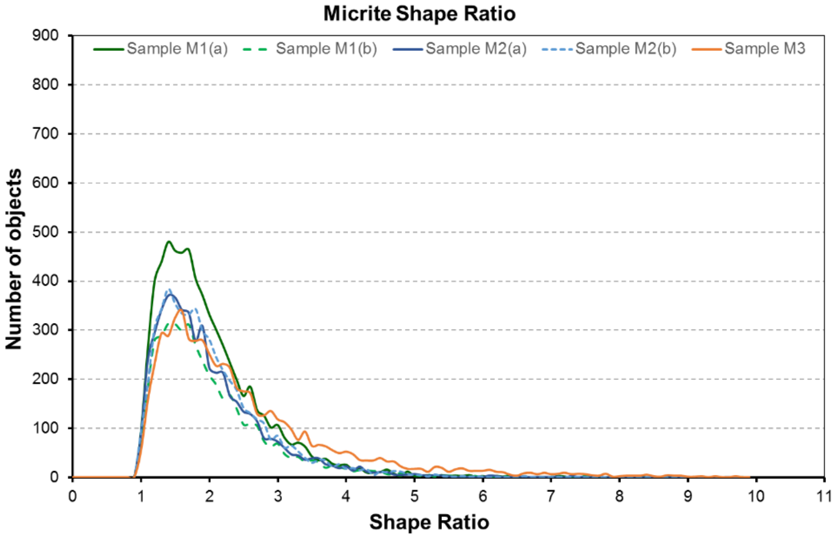

Figure 3-14 Shape ratio distribution for calcite type micrite

It is interesting to point out that the large number of objects observed in sample M1(b) may be related to the fact that this sample also experienced the highest percentage of micrite content. In the same way, the number of micrite objects observed for sample M3 is similar to the values observed for samples M1(a) and M2, nevertheless, its micrite percentage is higher. Suggesting that the micrite crystals observed in the face of the cliff are bigger than those of samples drilled from blocks within the cavern.

In the other hand, the shape ratio distribution for sparite is presented in Figure 3-15, where can be observed that for all samples evaluated the predominant shape ratio is 1.5. In other words, most of sparite crystals are 50% longer than width. Note that the number of objects observed for sample M2 are the lowest of all the samples analyzed. If we consider that this sample also present the major sparite content (Figure 3-13), can be concluded that the sparite crystals observed in this sample are bigger than in the other samples.

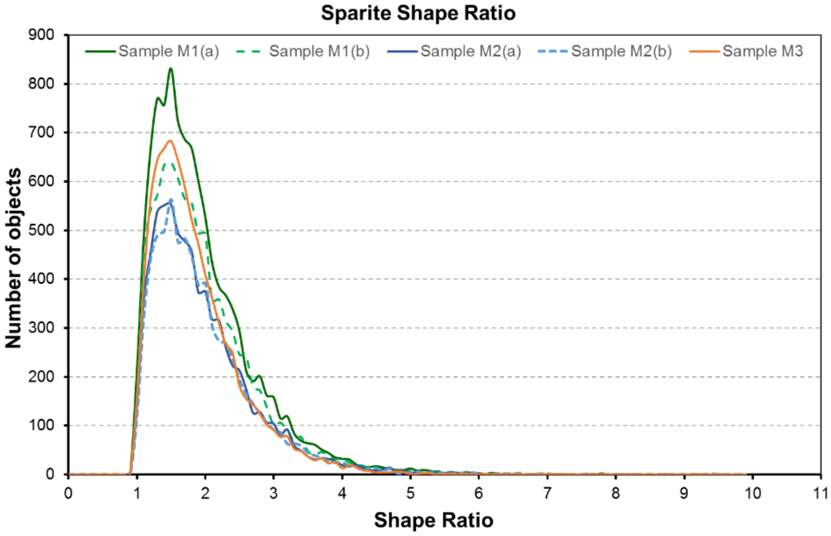

Figure 3-15 Shape ratio distribution for calcite type sparite

Sample M3 is the sample with the lowest sparite content, only 20%, nevertheless, its number of objects is quite important, more than sample M2 and almost the same that sample M1(b), suggesting that its crystals are smaller than those observed in samples obtained from within the cavern.

Finally, Figure 3-16 presents the shape distribution for quartz, it is important to remember that because of the thin sections characteristics from sample M3 is not possible to obtain the quartz shape ratio distribution for this sample. It can be observed that the predominant shape ratio in samples M1 and M2 varies from 1.3 to 1.5. Some differences are observed between thin sections a and b of samples M1 and M2, nevertheless, as the number of objects (Figure 3-16) and quartz content (Figure 3-13) is very low, it can be considered that these differences are negligible.

Besides the mineralogical composition, another important condition that can be analyzed from the thin sections is the minerals fissures density. This characteristic may be important for our analysis, because the presence of pre-existing fractures may indicate a more fragile behavior, hence, a large damage level after the thermal weathering. Not to mention that the existing crack density level may control the mineralogical thermal response of the rock (Hall and Thorn, 2014).

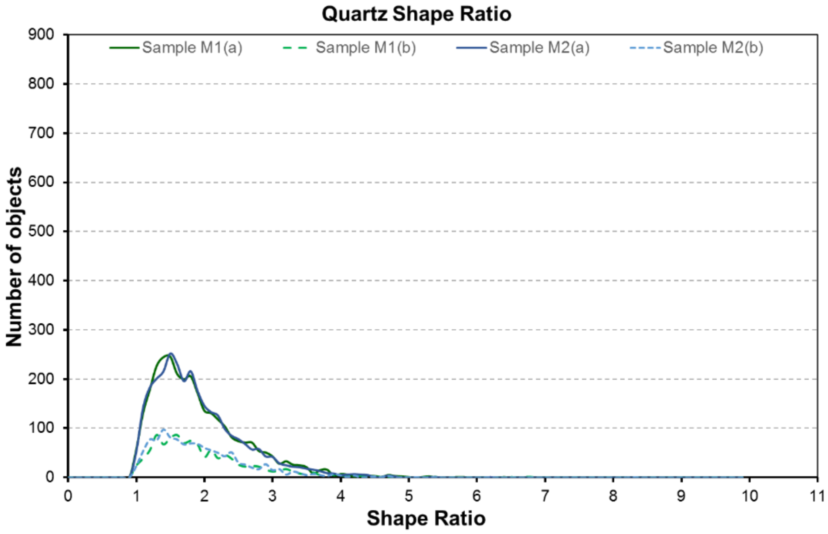

Figure 3-16 Shape ratio distribution for quartz

To evaluate this fissuration density an equal grid should be draw in each thin section image. Then, the number of cracks is count in each cell. Finally, the density of pre-existing cracks is calculated, considering the area of each cell. Figure 3-17 presents the cracks density observed for the thin sections evaluated, where any particular difference is observed between them, except by the fact that sample M1 shows a slightly inferior quantity of fissures by mm2.

From visuals observations can be determined that sample M1 also shows a major quantity of fossils. This condition may explain why the cracks density observed is slight inferior, as the fossils do not have fissuration.

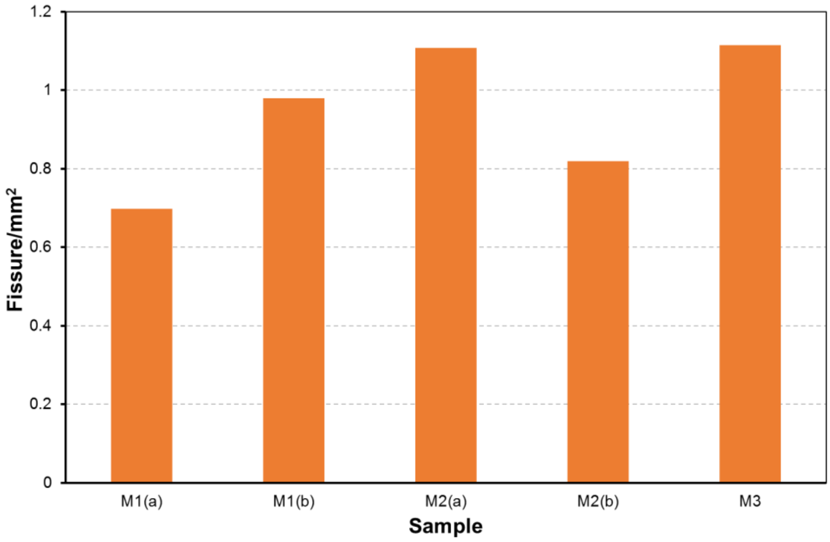

Figure 3-17 crystals fissure density

## Mineralogical analysis remarks.

The three types of mineralogical analysis performed shows similar results. Spectrometry and DRX results corroborate what is observed with the most visual technique, thin sections images. Samples obtained from blocks inside the cavern (group 1) are principally constituted by calcite, and samples from the cliff face (group 2) are composed by calcite and quartz in a relationship that can reach the 50- 50. This mineralogical characteristic may lead to a different mechanical response. More precisely samples from group 2 can develop more thermal degradation associated with the strong thermal interaction between the calcite and quartz minerals, as mentioned by Hall & Thorn (2014).

On Table 3-6 it can be observed that samples from group 1 present a mean elastic wave propagation value of 4400 m/s, a similar value to the one obtained by *the Laboratoire Régional des Ponts et Chaussées de Toulouse* (chapter 3.1.1) over samples obtained from blocks from inside the troglodyte caver. Nevertheless, the mean P-wave propagation velocity obtained for samples from group 2 is 2900 m/s. This variation in P-wave velocity can be associated with the mineralogical composition of the rock, but also, to the fact that samples from group 2 were obtained near the face of the cliff and thus may present a higher initial deterioration, thus lower stiffness.

## 3.4. Experimental layout.

In order to evaluate the thermal weathering of LaRG limestone, an experimental program is developed. This program is based on the laboratory study performed by Gasc-Barbier et al. (2014), in which four samples of limestone were submitted to 700 thermal cycles and measurements of deformation and elastic wave propagation velocity were performed to evaluate the effects of thermal fatigue in the samples.

The experimental program consists in submitting the samples described in Table 3-7 and Table 3-6 to thermal cycles. As the aim of this analysis is to evaluate the weathering of the rock matrix, the thermal rang employed is close to the one experienced in atmospheric conditions.

The effect of thermal cycles was evaluated through the measures of deformation (Def), elastic wave propagation velocity (Vp-Vs) Uniaxial compressive strength (UCS) and the evaluation of generation and propagation of fissures by digital image correlation technique (DIC). The number of cycles applied for each sample depends on the type of measurement that would be performed. Table 3-9 summarizes the experimental layout of each sample.

Table 3-9 Number of cycles imposed and test performed for each sample

| Sample | Cycles applied | Def | Vp-Vs | UCS | DIC |
|---|---|---|---|---|---|
| B1 | 948 | X | | | |
| B2 | 948 | X | X | | |
| B3 | 948 | X | X | | |
| B4 | Measure of temperature inside the sample | | | | |
| B5 | 828 | | X | X | |
| B6 | 828 | | X | X | |
| B7 | 828 | | X | X | |
| B8 | 624 | | | X | |
| B9 | 624 | | | X | |
| B10 | 624 | | | X | |
| B11 | 420 | | | X | |
| B12 | 420 | | | X | |
| B13 | 420 | | | X | |
| B14 | 210 | | | X | |
| B15 | 210 | | | X | |
| B16 | 210 | | | X | |
| B17 | 0 | | | X | |
| B18 | 0 | | | X | |
| B19 | 0 | | | X | |
| B20 | 396 | | | | X |
| CV1 | 910 | X | X | | |
| CV2 | 1222 | | X | | |
| CV3 | 1222 | | X | | |

| Sample | Cycles applied | Def | Vp-Vs | UCS | DIC |
|---|---|---|---|---|---|
| CV4 | 910 | X | X | | |
| CV5 | 1222 | | X | | |
| CH1 | 1222 | | X | | |
| CH2 | 910 | X | X | | |
| CH3 | 1222 | | X | | |
| CH4 | 1222 | | X | | |
| CH5 | 910 | X | X | | |
| C1 | 948 | | | | X |
| C2 | 948 | | | | X |
| C3 | 948 | | | | X |
| C4 | 1080 | | | | X |

### 3.4.1. Heating - cooling treatment.

The thermal cycles were imposed with the climatic chamber presented in Figure 3-18. With this climatic chamber, thermal cycles can be program for the whole experimental program, it allows temperatures between -45ºC to 180ºC. Additionally, it is equipped with a humidor that allows to impose wet thermal cycles. However, the relative humidity cannot be controlled. Our experimental program is developed under dry conditions.

Figure 3-18 Climatic chamber employed

The typical thermal cycle imposed lasts 3.5 hours and consists in: 45 minutes at 10ºC, then one hour to go from 10ºC to 50ºC, later, 45 minutes at 50ºC and finally, 1 hour to go from 50ºC to 10ºC, as illustrated in Figure 3-19. The external measurements (Vp-Vs and DIC) are performed each day during an interval of tree hours with a constant temperature of 10ºC.

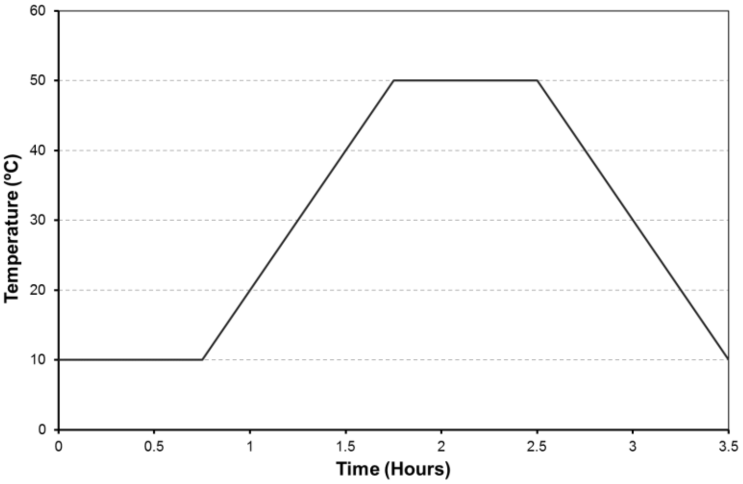

Figure 3-19 Thermal cycle imposed

During the experimental process, it was notice that the temperature felt by the samples at the surface was not exactly the one imposed, because of the thermal regularization system of the climatic chamber. To assure the temperature imposed on the samples, the variations of temperature were measured with a thermal probe as shown in Figure 3-20. The probe was fixed to the face of sample B4, to measure the real imposed temperature, then the probe was placed in a small borehole performed in the center of sample B4, to measure the temperature in the specimen.

a) b)

Figure 3-20 Thermal probe on sample B4: a) Sample face b) within the sample

The measured temperatures are shown in Figure 3-21. The temperature on the face and within the samples varies with a rate of 0.35ºC/min, much less than the rate of 1ºC/min, defined by Hall & Thorn (2014) as the threshold for destructive internal effects for thermal shock. In the same way, the maximal temperature difference between the face and the center of the sample is 2ºC.

Therefore, all the possible damage that may be induced in the samples because the heating/cooling cycles will be related to a process of thermal fatigue. This means, that in this experimental program it is only considered the rock deterioration related to typical thermal variations, and not to exceptional changes of temperature, like the one registered in February of 2012 that generated a significant irreversible deformation, observed in the joint-meters installed in the cavern. (see chapter 2.8).

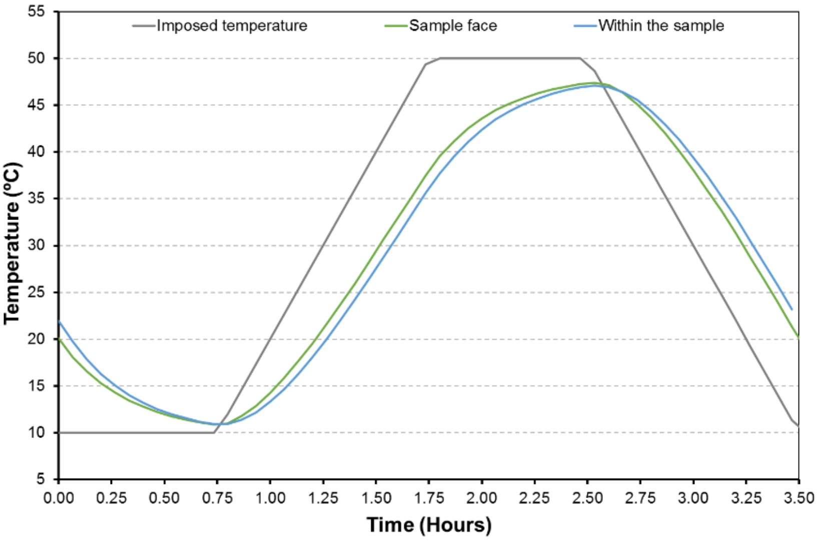

Figure 3-21 Temperature variation experienced by the samples

Thermal conductivity could not have been measured in the laboratory, as no layout was available. Nevertheless, as this parameter may present some valuable information, especially to the modeling phase of this work, a back-analysis was performed to estimate it, based on the temperature measurements on sample B4. This back-analysis was performed with the finite element method software CODE_BRIGHT (Olivella et al., 1996).

The value of thermal conductivity obtained was: 1 W.m.K-1 considering a specific heat of 800 J.Kg-1.K-1, because the sample is dry. Figure 3-22 presents the good agreement obtained from the modeling with these values of thermal conductivity and specific heat. Likewise, Ruiz (2013) obtained from back-analysis from the instrumentation data, a value of thermal conductivity for the rock cliff, a value of 2 W.m.K-1 with a specific heat of 1200 J.Kg-1.K-1.

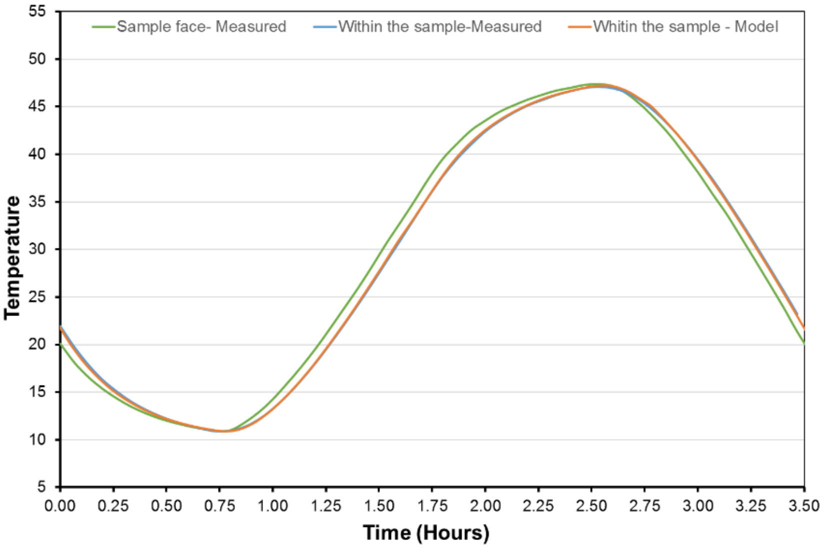

Figure 3-22 Thermal conductivity back analysis result

### 3.4.2. Deformations.

Deformation measurements are performed with strain gauges. Two pairs of strain gauges, with a nominal resistance of 120 Ω, were glued on each sample: a pair in vertical position, to measure the axial deformation, and a pair in horizontal position, to measure the radial deformation, as illustrated in Figure 3-23. As the strain gauges are submitted to thermal variations, they are installed in half-bridge circuit with a thermal compensation.

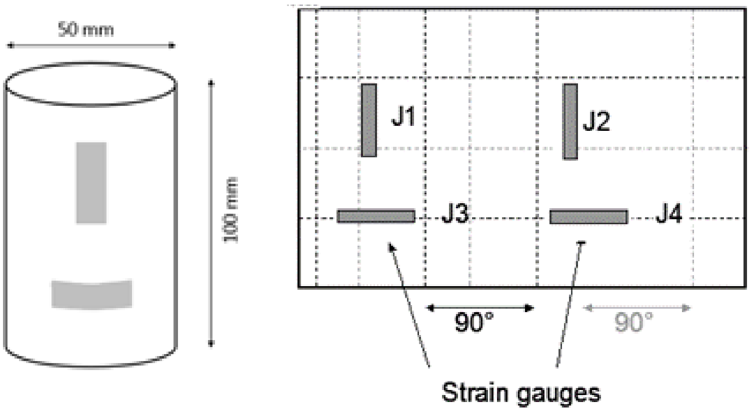

Figure 3-23 Scheme strain gauges installation

Measurements are performed with an amplifier type MJCplus, connected to a personal computer equipped with a data acquisition software. The measurements of voltage variation (mV) are registered each five minutes, during the whole experimental program. Based on the gauge characteristics (gage factor and nominal resistance) and voltage measurements deformation variations are calculated. As an example, Figure 3-24 presents the strain gauges glued on samples B1 and sample CH5.

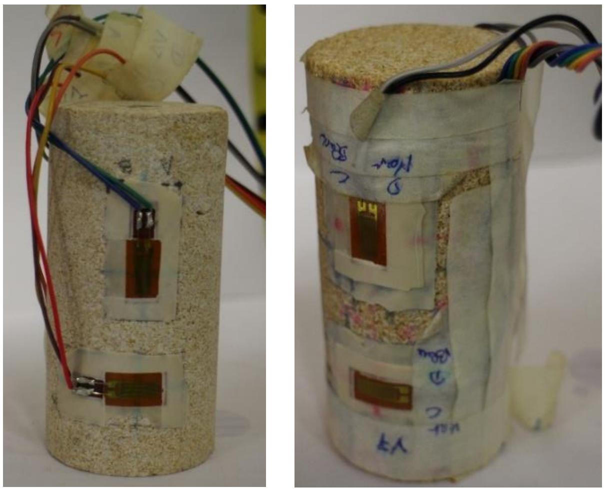

a) b)

Figure 3-24 Strain gauges position a) Sample B1 (Group 1) b) Sample CH5 (Group 2)

### 3.4.3. Elastic wave propagation velocity.

The elastic wave propagation velocity is performed at least once a week. It is also a preliminary measure that it is performed for all cylindrical samples to have an initial characterization and comparison parameter (see Table 3-6).

The measure is performed by the ultrasonic pulse technique described by the French Standard NF P 94-411 (AFNOR, 2002), that requires the equipment presented in Figure 3-25. For this, an electric pulse generator that produces waves higher than 250 volts for a maximum rise duration of 0.2 ms is used to induce compression waves (P-waves) and shear waves (S-waves) in two perpendicular directions (S1 and S2).

This generator is connected to the transmitter and receptor transducers with a resonance frequency from 25 kHz to 1 MHz. The sample is fixed between the transmitter and receptor transducers in a frame provided with a uniaxial pump, to assure good contact between the sample and the transducers, without applying a mechanical load to the sample. A force transducer is used to control that the applied load is 2 kN. To have a proper wave transmission between the sample and the transducers, very thin sheets of lead are fixed with honey on the transducers face. Finally, the signals are registered by an oscilloscope with a time resolution of 10 ns connected to a personal computer equipped with a signal registration software.

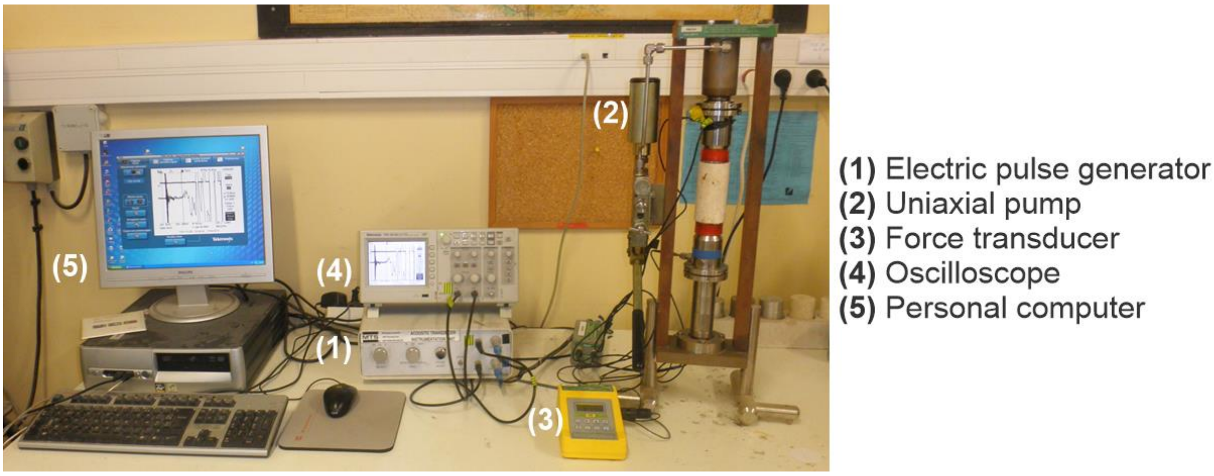

Figure 3-25 Elastic wave propagation velocities measurement equipment.

From the signal, registered by the equipment presented before, is possible to obtain the time of arrival of the wave, as illustrated in Figure 3-26.Then the elastic wave velocity is calculated as:

$$\mathrm{V_i} = \frac{\mathrm{L_i}}{\mathrm{t_i}} \qquad \text{Eq. 3-3}$$

Where, Vi is the elastic wave propagation velocity for samples i, Li is the sample large and ti the wave arrival time.

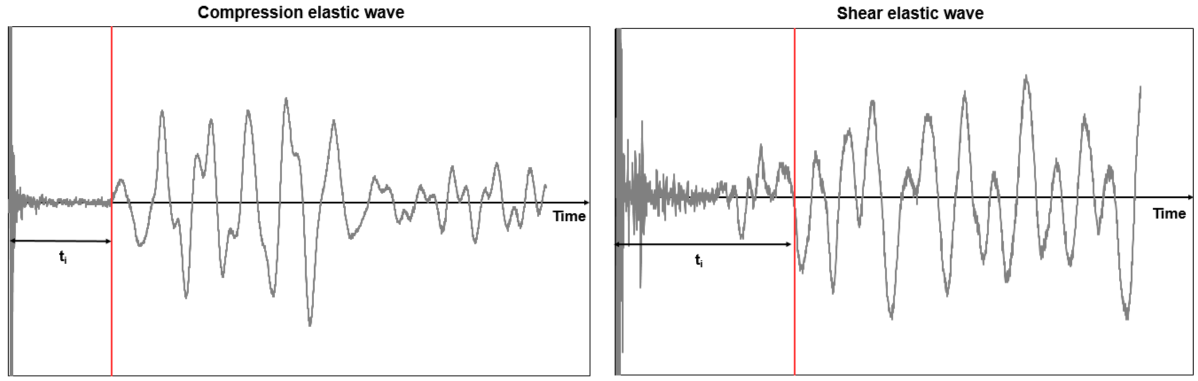

a) b)

Figure 3-26 Typical arrivals elastic wave time a) P-waves b) S-waves

From the measures of compression (Vp) and shear (Vs) elastic wave propagation velocity it is possible to determine the dynamic Young modulus ($E_d$) and dynamic Poisson ratio ($\upsilon_d$) following the next equations, where ρ is the bulk density:

$$E_d = \rho \frac{V_s^2(3V_p^2 - 4V_s^2)}{(V_p^2 - V_s^2)} \qquad \text{Eq. 3-4}$$

$$\upsilon_d = \frac{(V_p^2 - 2V_s^2)}{2(V_p^2 - V_s^2)} \qquad \text{Eq. 3-5}$$

### 3.4.4. Uniaxial compressive strength.

Uniaxial compressive strength test is performed only on samples from group 1, following the ASTM D7012-10 standard (ASTM, 2010). An MTS system (Figure 3-27) is used, with a stiffness of 109 N/mm, able to perform compression and shearing tests. To evaluate the static Young modulus loading/unloading cycles were realized at 50% and 80% of the Uniaxial compressive strength previously estimated (47.3 MPa) and presented in chapter 3.1.2 using a loading/unloading rate of 0.15 MPa/s.

Fifteen cylindrical samples are considered to evaluate the effect of thermal cycles in the rock strength. They are divided into groups of tree samples submitted to a different number of cycles (0, 210, 420, 624 and 828) as detailed in Table 3-9.

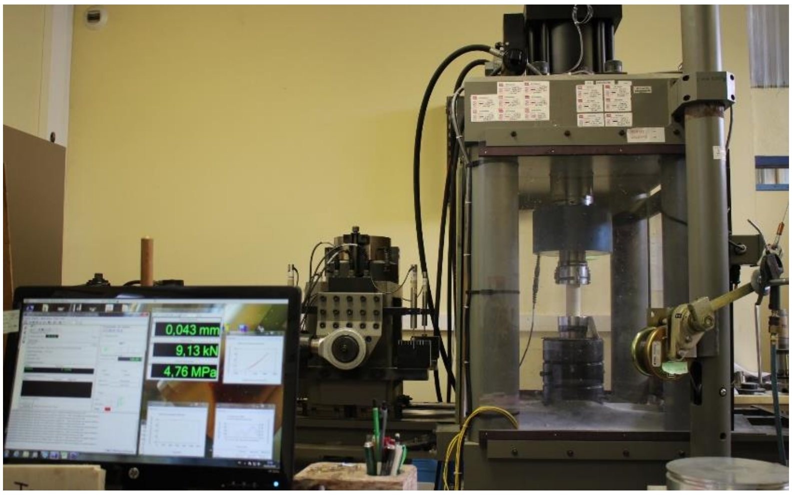

Figure 3-27 MTS rock test system 816

### 3.4.5. Digital image correlation.

During the laboratory study presented by Gasc-Barbier et al. (2014) also performed on LaRG samples, some fissures were observed in the samples, as shown in Figure 3-28. In order to evaluate if the thermal cycles are capable to induce that kind of fissures, a specific test is considered, to determine the apparition of fissures and the propagation of existing ones.

Figure 3-28 Fissures observed in a former experimental study, Gasc-Barbier et al. (2014)

For this, the samples (see Table 3-9) are photographed each day. These photos are analyzed with the Digital image correlation software Ncorr (Blaber, Adair and Antoniou, 2015), an open source code that works in a Matlab environment.

The digital image correlation (DIC) technique has been widely used to evaluate the behavior of rocks under compressive loads (Dautriat et al., 2011; Yang et al., 2011). It allows to determine the apparition of punctual defects, but also, the general strains field of the sample even when they are low. DIC analysis is mostly used to evaluate the apparition and evolution of fissures. For instance, it is commonly used to analyze the responses observed with the Brazilian disk test, from photos taken with a regular digital camera: more than 50μm/pixel (Hild and Roux, 2006; Lagneau, 2014). But also from macro-scale photographs as in the study presented by Casperson et al. (2014) in which DIC analysis on macro photographs (2μm/pixel) were used to observe the closure of a crack under high temperatures (600ºC).

The principal goal of this technique is to obtain displacements and strains fields for a material undergoing deformation, through images processing, as the images are taken while the material deforms.

In brief, the DIC method consists in obtaining one to one correspondence between points in the image of reference and in the current condition. For this, the images are divided in small sections called subsets and deformation of each subset is obtained by the transformation used to match the position of the subset in the current image (Hild and Roux, 2006; Bornert et al., 2009; Blaber, Adair and Antoniou, 2015), as follows:

$$\tilde{x}_{\mathrm{cur\,i}} = x_{\mathrm{refi}} + u_{\mathrm{rc}} + \frac{\partial u}{\partial x_{\mathrm{rc}}}(x_{\mathrm{ref\,i}} - x_{\mathrm{refc}}) + \frac{\partial u}{\partial y_{\mathrm{rc}}}(y_{\mathrm{refi}} - y_{\mathrm{refc}}) \qquad \text{Eq. 3-6}$$

$$\tilde{y}_{\mathrm{cur\,i}} = y_{\mathrm{refi}} + v_{\mathrm{rc}} + \frac{\partial v}{\partial x_{\mathrm{rc}}}(x_{\mathrm{refi}} - x_{\mathrm{refc}}) + \frac{\partial v}{\partial y_{\mathrm{rc}}}(y_{\mathrm{refi}} - y_{\mathrm{refc}}) \qquad \text{Eq. 3-7}$$

$$P = \left\{ u \; v \; \frac{\partial u}{\partial x} \; \frac{\partial u}{\partial y} \; \frac{\partial v}{\partial x} \; \frac{\partial v}{\partial y} \right\} \qquad \text{Eq. 3-8}$$

Where $x_{\mathrm{refi}}$ and $y_{\mathrm{refi}}$ are x and y coordinates of an initial reference subset point, $x_{\mathrm{refc}}$ and $y_{\mathrm{refc}}$ are the X and Y coordinates for the center of the initial reference subset point $\tilde{x}_{\mathrm{curi}}$ and $\tilde{y}_{\mathrm{curi}}$ are the x and Y coordinates of a final current subset point, and, P is the deformation vector.

Then, the deformation of each point in the subset will be defined by the optimal vector P. That is to say, a deformation vector that gives the best match between xref i and xcur i and yref i and ycur i.

To realize properly this analysis, the photos should be taken with the samples exactly in the same position. For this purpose, a specific device to fix the samples was created (Figure 3-29). It allows to put the sample in the same position each time, having the camera immobile during the whole experimental program. To reduce the light noise, photos are taken in a dark room, employing just a fixed lamp as light source.

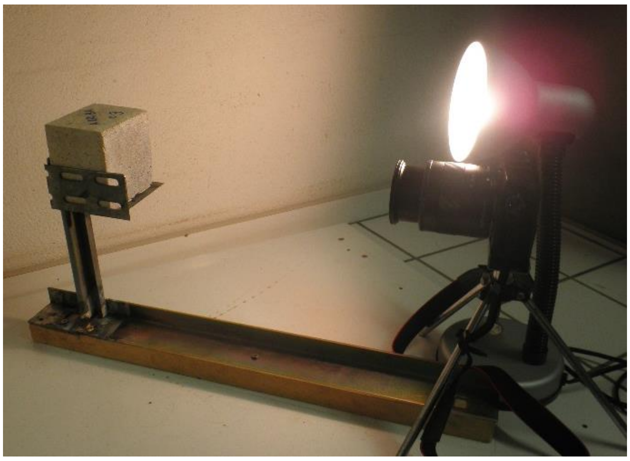

Figure 3-29 Fixing device

## 3.5. Mechanical response.

To evaluate the damage induced in LaRG limestone due to atmospheric thermal cycles, the mechanical response of samples of this rock was evaluated through the temperature variations. The response obtained for deformations, elastic wave propagation velocity and Uniaxial compressive strength is presented below.

### 3.5.1. Deformations.

Three samples obtained from blocks fell inside the cavern (group 1 – samples B1, B2 and B3) and four samples drilled from the face of the cliff (group 2), two horizontally drilled: samples CV1 and CV4 and two vertically drilled: samples CH2 and CH5 were considered for deformation measurements (see Table 3-9).

As mentioned before, these measures are performed with strain gauges, allowing to have the response even when the thermal cycles are imposed. Is important to consider that positive values of deformation represent expansion and negative values contraction.

#### General tendency.

*Axial strains.*

Axial deformations evolutions are presented in Figure 3-30 for samples from group 1 and in Figure 3-31 for group 2 samples.

In first place, it can be observed that all the samples do not evolve in the same way. Some of them accumulate positive deformations (expansion) due to thermal cycles while some of them contract. For instance, samples B1, B3 and CV4 are similar: an augmentation of deformation is observed through the imposition of thermal cycles. Whereas, samples B2, CV1, CH2 and CH5 presents a global decay response, even if sample B2 shows a positive tendency until cycle 250.

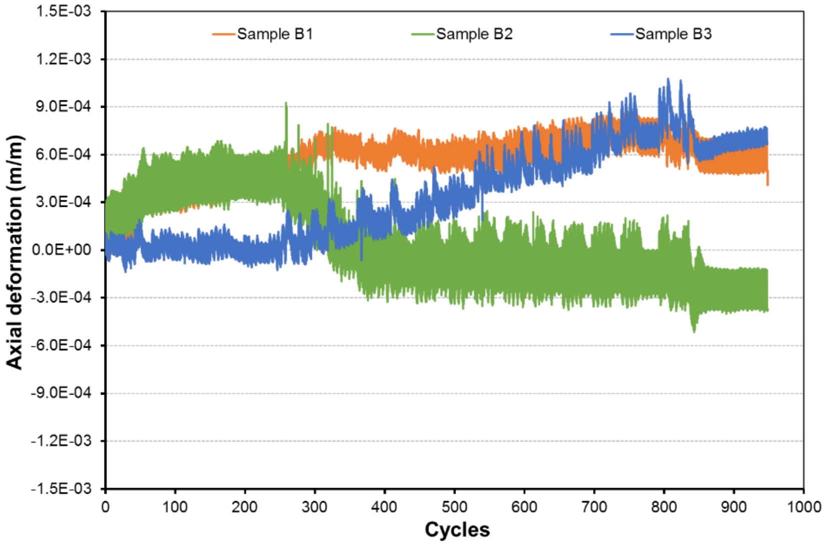

Figure 3-30 Vertical deformations for samples B1, B2 and B3

After 948 cycles, sample B1 accumulates a vertical deformation of 6.8e-4 m/m, sample B3 behaves in the same way with an accumulated deformation of 8.5e-4 m/m. While, the accumulated vertical strains for sample B2 is only 3.6e-4 m/m but in the negative direction.

In the other hand, Samples CV1, CV4, CH2 and CH5 that were submitted to 910 thermal cycles. Presents an accumulated deformation of -3e-4 m/m for sample CV1, 3.6e-4 m/m for sample CV4, sample CH2 shows -27e-4 m/m and sample CH5: -8e-4 m/m.

All samples considered shows an erratic response in the first cycles, until cycle 70 in group 1 and until cycle 50 in group 2. This is evidenced mostly on samples B1 and B2, where a big accumulation of deformations is observed and in samples CV1, CH5 and CH2 where an important drop of vertical strains is observed.

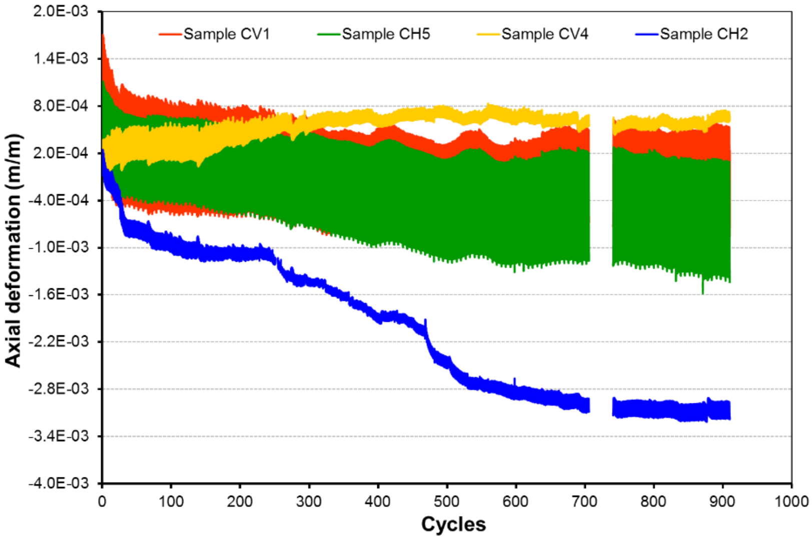

Figure 3-31 Vertical deformation samples CV1, CV4, CH2 and CH5

By eliminating the data obtained for this firsts cycles (70 for group 1 and 50 for group 2) Table 3-10 presents the final accumulated deformations. It can be observed that samples drilled in horizontal direction (samples CH2 and CH5) show a higher amount of accumulated axial deformations than samples obtained in vertical direction (samples CV1 and CV4).

Table 3-10 Accumulated axial strains

| Samples obtained from blocks (group 1) | | Samples obtained from the cliff face (group 2) | |
|---|---|---|---|
| Sample | Axial accumulated strain (mm/mm) | Sample | Axial accumulated strain (mm/mm) |
| B1 | 2.7e-4 | CV1 | -2.6e-4 |
| B2 | - 8.1e-4 | CV4 | 2.5e-4 |
| B3 | 9.0e-4 | CH2 | -26.0e-4 |
| | | CH5 | -8.6e-4 |

Another remarkable observation is that, between 250 and 400 cycles an important value of irreversible deformations is observed, especially in samples B1, B2 and CH2. Moreover, after this interval the strains remain constant. Nonetheless, this can’t be observed on sample B3 and CV4 response, in this case the deformation keeps a constant positive tendency since cycle 200 until the end.

In addition, sample CV4 presents a variation in the axial deformations amplitude, it decreases until 300 cycles where it becomes stable until the end of the experimental program.

### Radial strains.

The evolution of radial deformations through the imposition of thermal cycles is presented in Figure 3-32 and Figure 3-33 for samples from group 1 and group 2 respectively. For this last group, the evolution of sample CH5 was not considered in the analysis because it presents a peculiar response that it will be describe afterwards.

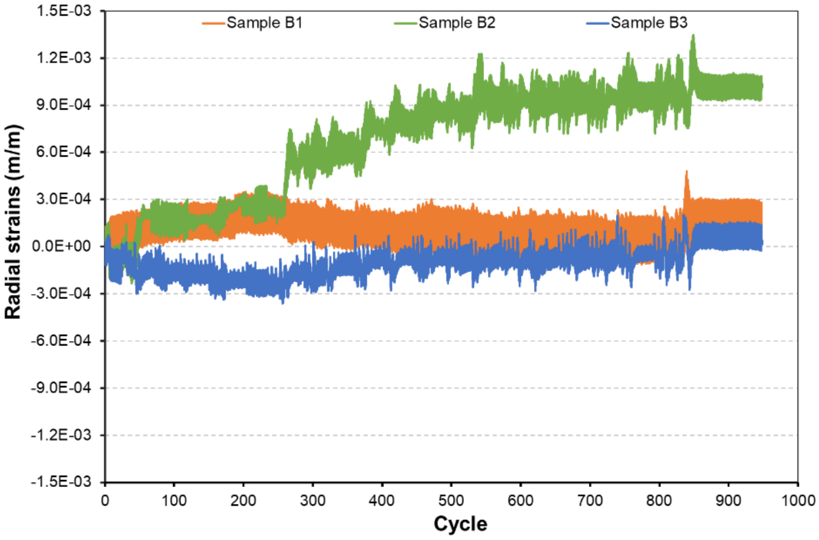

Figure 3-32 Radial deformation for samples B1, B2 and B3

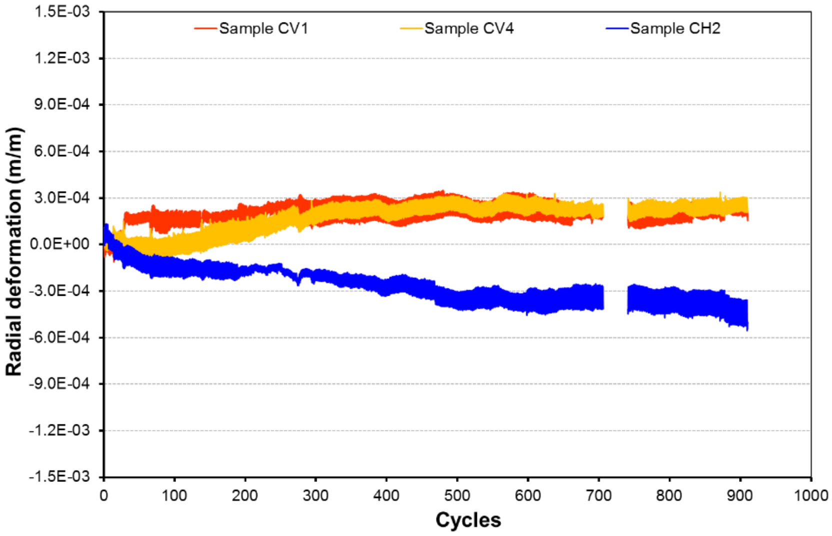

Figure 3-33 Radial deformation evolution samples CV1, CV4 and CH2

From a global point of view, it can be observed that except for sample CH2, (the only sample drilled in horizontal direction) all of them behave in the same way, radial deformations increase. Nevertheless, sample B2 presents a much higher value of final deformation than the other 4 samples (sample B1, B3, CV1 and CV4).

By considering the samples from group 2, where the direction of extraction in relation with the cliff's face is known, it can be remark that samples vertically drilled (sample CV1 and CV4) radial deformation presents a positive tendency with similar final strains accumulation value: 2.7e-4 m/m for sample CV1 and 3.2e-4 m/m for sample CV4. In the other hand, sample CH2 (horizontally drilled sample) radial strains decrease, just as its axial strains, but with a lower accumulated strain, only 4.6e-4 m/m in comparison to the 27e-4 m/m obtained in axial direction.

The radial strains shown an erratic response until cycle 70 for samples obtained from blocks and until cycle 50 for the ones that were obtained from the cliff face, similar to the response observed for vertical strains. In this case, it is mostly evidenced in samples B2 and CV1 by a considerable increment and in sample B3, by a strain decrease.

As mention earlier, the experimental programs for samples from blocks and drilled from the face of the cliff were not performed at the same time. Which means that the strain gages glued on samples of group 1 and samples of group 2 were not connected to the acquisition system at the same moment. In fact, it is only possible to connect 4 pairs of strain gages in the equipment used. Therefore, the erratic response observed with both groups of samples for the first cycles cannot be related to electrical punctual variations, but may be related to a stabilization time of the gauges.

After excluding the response observed in the first cycles the obtained accumulated radial strains are presented in Table 3-11, where, it can be observed that sample B1 and CV1 presents a radial accumulated strain very small in relation with the other values obtained, it can be assumed that this samples do not accumulate strains in this direction.

Table 3-11 Accumulated radial strains

| Samples obtained from blocks (group 1) | | Samples obtained from the cliff face (group 2) | |
|---|---|---|---|
| Sample | Axial accumulated strain (mm/mm) | Sample | Axial accumulated strain (mm/mm) |
| B1 | -0.9e-4 | CV1 | 0.26e-4 |
| B2 | 9.0e-4 | CV4 | 2.5e-4 |
| B3 | 2.7e-4 | CH2 | -3.3e-4 |

Moreover, sample CH2 presenters a variation in the strains amplitude between 200 to 300 cycles (see Figure 3-33), after the 300th cycle, the response stabilizes and returns to its original amplitude value.

As mention before, sample CH5 was not considered for the analysis because its evolution shows a peculiar response, see Figure 3-34. The strains amplitude observed this sample is very high in comparison with the other radial deformation measurements observed and its daily response is very different from the behavior observed for the other radial measurements; it is more similar to a vertical direction behavior.

In addition, its strains amplitude increases radically in cycle 270, and then decreases, stabilizing only after the cycle 400, with a higher value than the one observed before cycle 270. These variations in amplitude are also observed in other samples response (see daily response), but in these other samples, the strains amplitude remains stable after cycle 300. These characteristics may be related to electrical issues, or to gauges installation differences. Despite different manipulations, it was not possible to purpose a reliable reason.

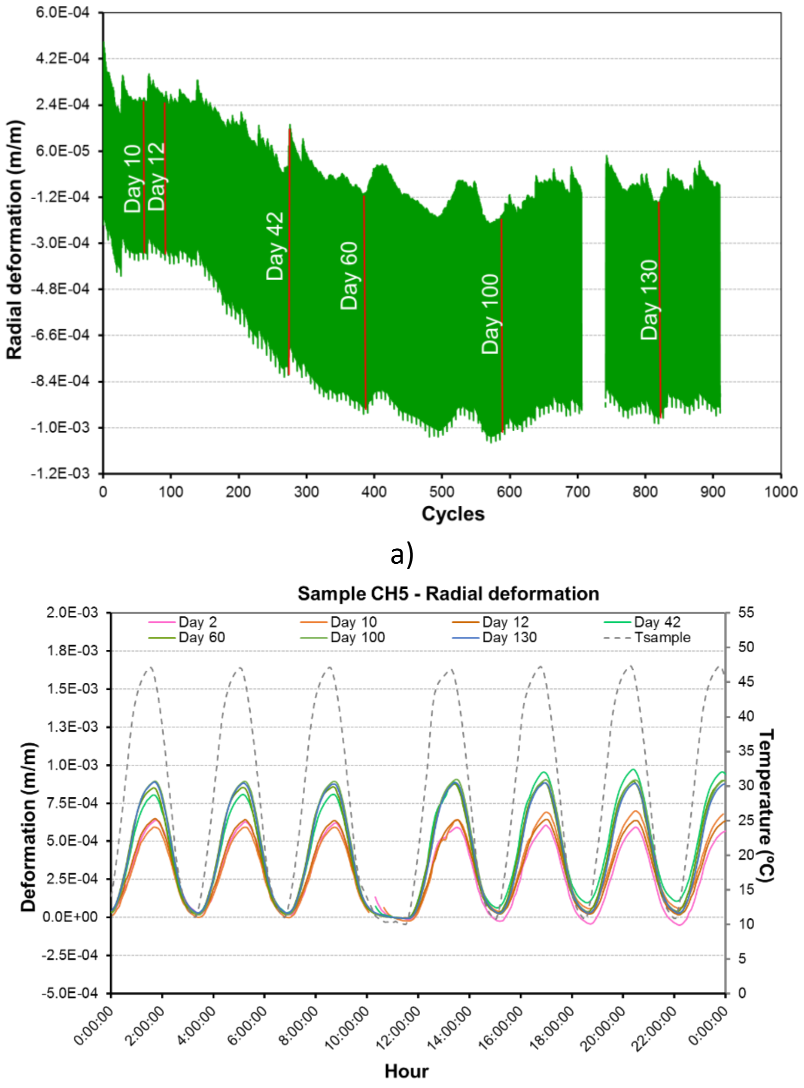

a)

b)

Figure 3-34 Radial deformation evolution for sample CH5: a) General tendency b) Daily response

Altogether, Samples drilled in vertical direction presents general positive strains tendencies in both directions. Conversely, samples obtained in horizontal direction presents a negative tendency. Note that even if results of radial strains for sample CH5 were rejected, their tendency is negative. Regarding the accumulated strains, samples CV1 and CV4 (vertical) shows similar values for axial and radial directions, otherwise, sample CH2 (horizontal) presents a major strains accumulation in axial direction.

By considering the response observed in axial and radial deformation for all the samples evaluated it can be observed that in general terms, the highest strain accumulation is observed in vertical direction. Except for sample B2 and CV4 where the absolute values of the cumulated deformations were very similar in both directions: 8.0e-4 mm/mm and 9.0e-4 mm/mm for vertical strains and radial strains respectively for sample B2, and 2.5e-4 mm/mm in both directions for sample CV4.

However, from results observed in axial and radial strains (Figure 3-30, Figure 3-31, Figure 3-32 and Figure 3-33) it is not possible to determine a specific behavior regarding the direction of the sample to the cliff's face, that may indicate the global direction for the samples from group 1 regarding to the face of the cliff. The strains evolution in time do not follow any identifiable response.

### Daily response.

In order to, evaluate the response of the gauges during the heating-cooling process, as it is not possible to observe it from the general tendency because of the scale, the daily strains response is evaluated for some punctual days.

Here it is important to point out that the heating treatment used for samples from group 2 is slightly different from the one performed over samples of group 1: the interval time used to perform measures pass from 3 hours to 2 hours, this allows to perform 6.5 instead of 6 cycles per day.

For this reason, the experimental program for samples obtained from blocks (group 1) with a total of 948 thermal cycles, lasts 158 days. While samples drilled from the cliff face (group 2) were subjected to 900 cycles in 138 days. An important consequence of this variation is that, for example, thermal cycle number 100 belongs to testing day 16 for group 1, and to testing day 15 for group 2.

Deformations measured during 5 different days (0, 2, 10, 100 and last day) are compared, in the first place to evaluate if the heating/cooling cycles may induce a variation in the deformation response and in the second place to compare the direction of strains during the heating/cooling cycles.

Results blocks samples are presented in Figure 3-35, Figure 3-36 and Figure 3-37 for samples B1, B2 and B3 respectively. It is important to mention that the temperature evolution presented correspond to the temperature measured at the face of the specimen (chapter 3.3.1).

In the same way, the responses registered for samples drilled from the cliff's face are presented in Figure 3-38 and Figure 3-39 for samples vertically drilled (samples CV1 and CV4) and in Figure 3-40 Figure 3-41 for samples horizontally drilled (samples CH2 and CH5). These evolutions are also compared with the temperature measured at the face of the sample.

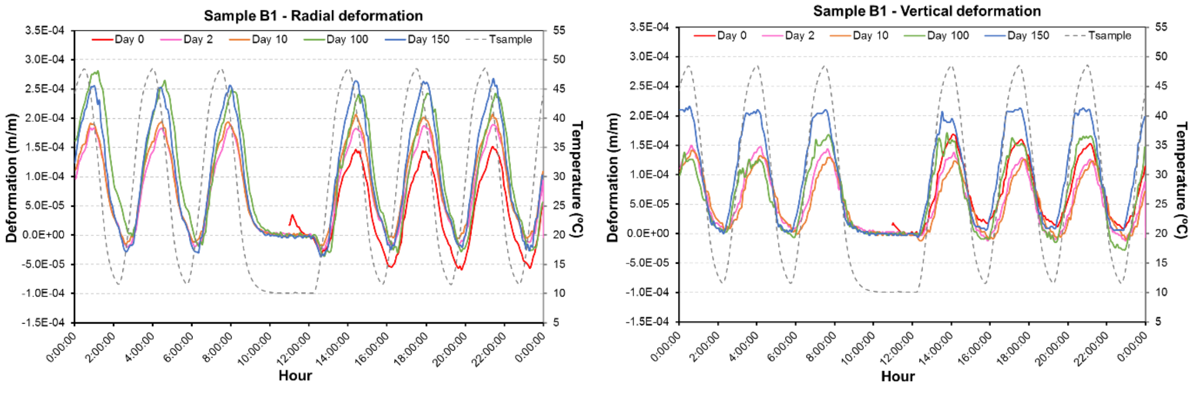

a) a)

Figure 3-35 Daily deformations response for sample B1: a) vertical deformation b) Radial deformation.

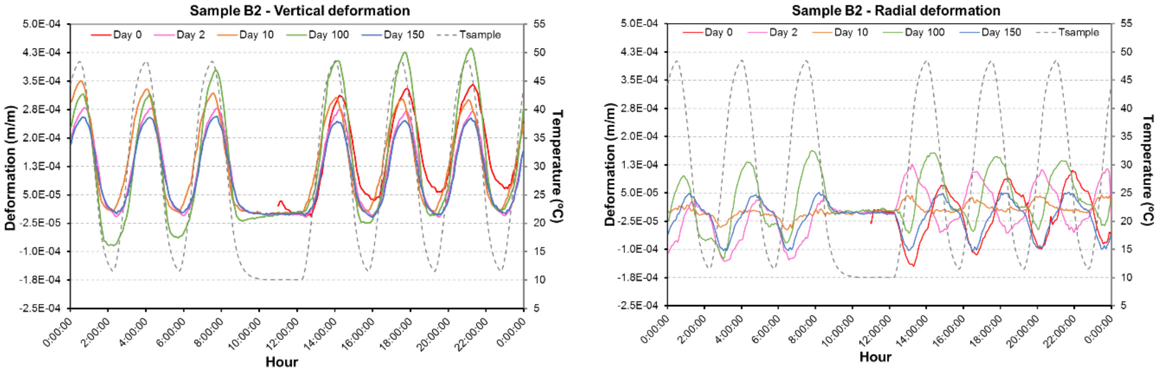

a) b)

Figure 3-36 Daily deformations response for sample B2: a) vertical deformation b) Radial deformation

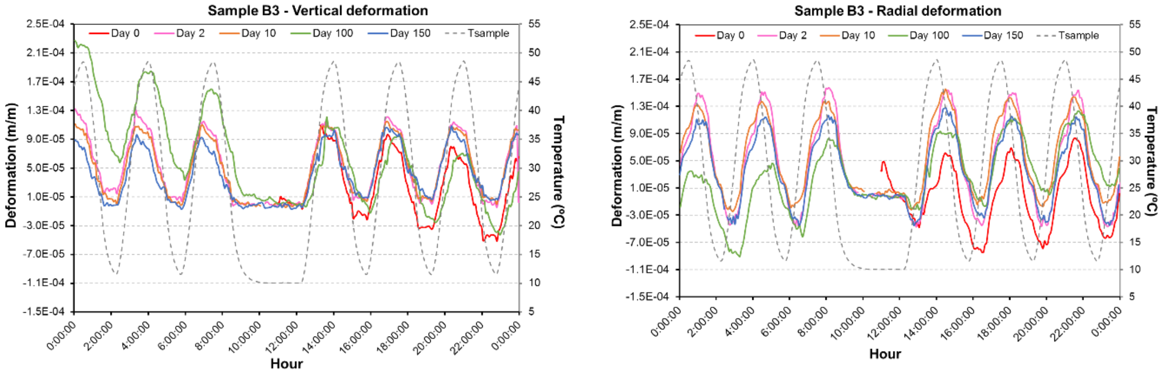

a) b)

Figure 3-37 Daily deformations response for sample B3: a) vertical deformation b) Radial deformation

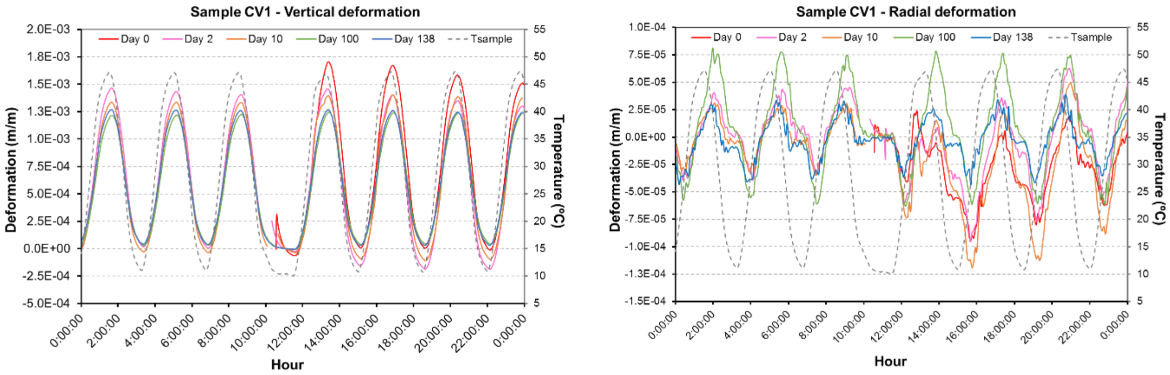

a) b)

Figure 3-38 Daily deformations response for sample CV1: a) vertical deformation b) Radial deformation.

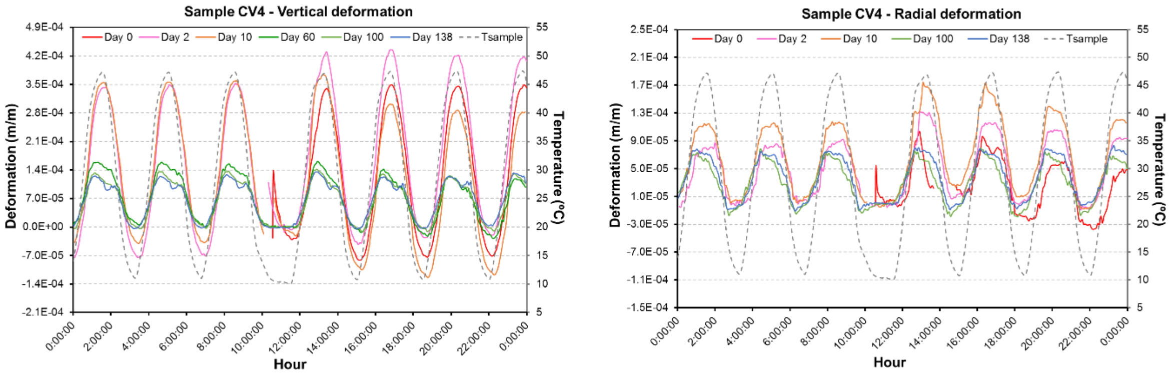

a) b)

Figure 3-39 Daily deformations response for sample CV4: a) vertical deformation b) Radial deformation.

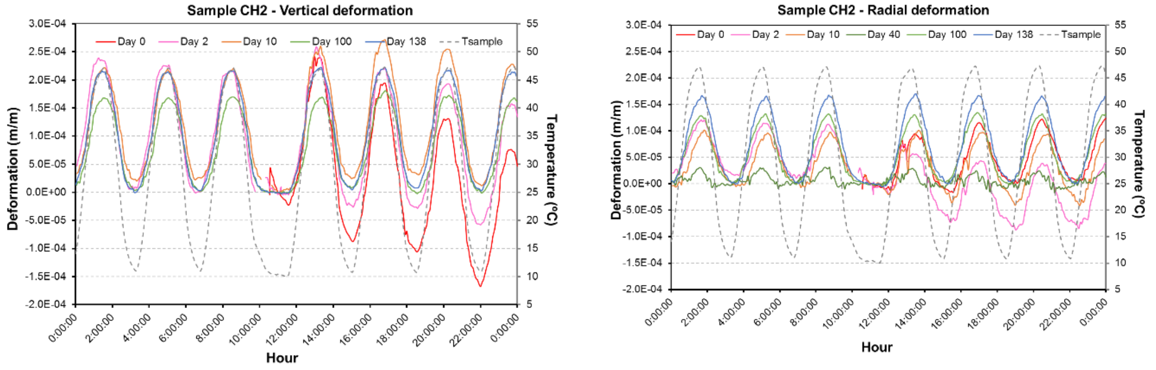

a) b)

Figure 3-40 Daily deformations response for sample CH2: a) vertical deformation b) Radial deformation

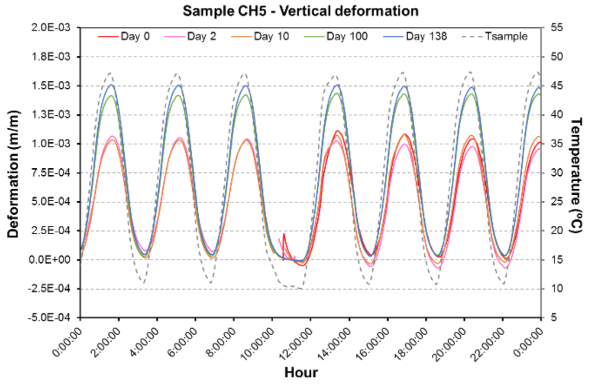

Figure 3-41 Daily deformations response for sample CH5 - vertical deformation

From these figures, it can be observed that strains augments during heating (sample expand) and decrease during cooling, just as expected. In fact, all the vertical responses show an evolution that follows closely the temperature variations. Nevertheless, in some radial evolution, a slight delay is observed.

It is interesting to note that even if the general tendency of strains is negative (like radial deformation for sample CH2 and axial strains for sample B2), the daily response continues to be expansion for heating and contraction for cooling.

Samples obtained from blocks show an interesting behavior, note that for radial deformation evolution (Figure 3-35b, Figure 3-36b, and Figure 3-37b) a slight strains decrease is registered in all the samples, when the temperature starts to increase after the 3 hours interval at 10ºC, that is used to perform the measures. In fact, this drop is registered between 12:00 to 13:00 and the begging of the heating ramp is registered in the face at 12:00.

It is also important is to mention, that deformations recorded for radial deformation in sample B2 (Figure 3-36b) present a peculiar behavior for days 2 and 10. In first place, the slightly drop registered in all the samples after the 3 hours interval is not observed. Moreover, it seems that the sample expands during cooling and contract during heating. This phenomenon is only observed for this sample. Nevertheless, remember that for the first 70 cycles (12 days) an erratic response is observed.

From Figure 3-38 it can be noted that sample CV1 shows a delay between radial stains and the temperature variations, additionally, the vertical strains amplitude presents a slight decrease through the chosen days.

In the other hand, from Figure 3-40b it can be observed that radial deformations for sample CH2 follow the temperature variations: there is no delay between thermal changes and deformations, but a slight increase in the strains amplitude is observed through the test duration. As observed from the general tendency for sample CH2 (Figure 3-33) between 200 cycles and 300 cycles the amplitude of strains decrease, in Figure 3-40b, the response obtained at day 40 (cycle 260-266.5) is included, it can be observed that the amplitude obtained for day 40 is 5 times lower than the value obtained for day 100.

In the same way, sample CV4 shows a decrease in vertical strains amplitude, just as it was observed from the general tendency response (Figure 3-31). In fact, vertical strains amplitude observed for sample CV4, for one cycle of day 10, cycle 65 for instance, is 3 times higher than the value observed for cycle 390 (day 60). Nevertheless, the amplitude remains constant for days 0, 2 and 10; and afterward for days 60, 100, 138. Actually, in the general strains evolution (Figure 3-31) it can be observed that this change in amplitude is quite fast: it happens between cycle 200 (day 30) and cycle 300 (day 46).

Generally speaking, samples obtained from blocks shows similar strains amplitudes for radial and axial direction, and any evolution is observed through the thermal cycling. Nevertheless, samples drilled from the cliff's face presents a higher amplitude strains in the vertical direction. Furthermore, sample CV1 and CV4 show a change in the vertical strains amplitude in a short time, between day 30 (cycle 200) and day 46 (cycle 300), this characteristic is also observed in radial strains for sample CH2.

Although, these variations in amplitude between 200 to 300 cycles are observed in several samples response. This phenomenon is reversible only in sample CH2 in the radial response, in other words, the strains amplitude before and after the interval between 200 (day 30) to 300 (day 46) cycles are similar.

### Cyclic response.

With the aim of evaluating the deformation response for one thermal cycle (10ºC-50ºC-10ºC), temperature-deformation graphs are considering, using 5 punctual cycles to be analyzed. The temperature used for this analysis is the one measured at the face of the samples and presented in Figure 3-42. In order to compare the general behavior, only 6 typical cycles are considered: cycle 1, 50, 100, 200, 500 and 900. Results obtained for samples obtained from blocks are presented in Figure 3-43 to Figure 3-45, and for samples drilled from the face of the cliff in Figure 3-38 to Figure 3-41.

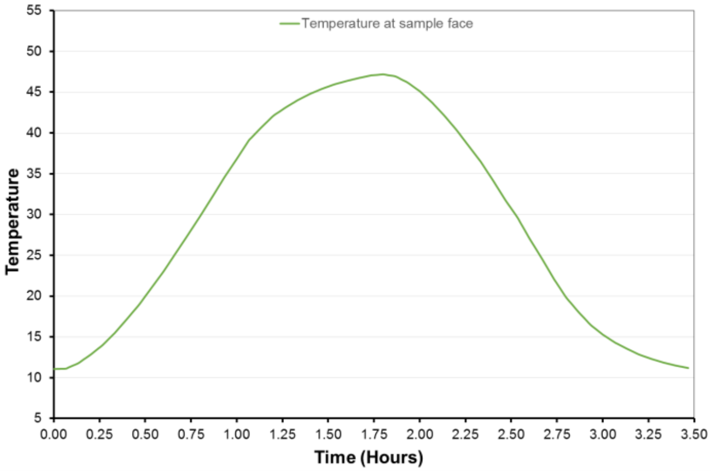

Figure 3-42 Typical thermal cycle considered

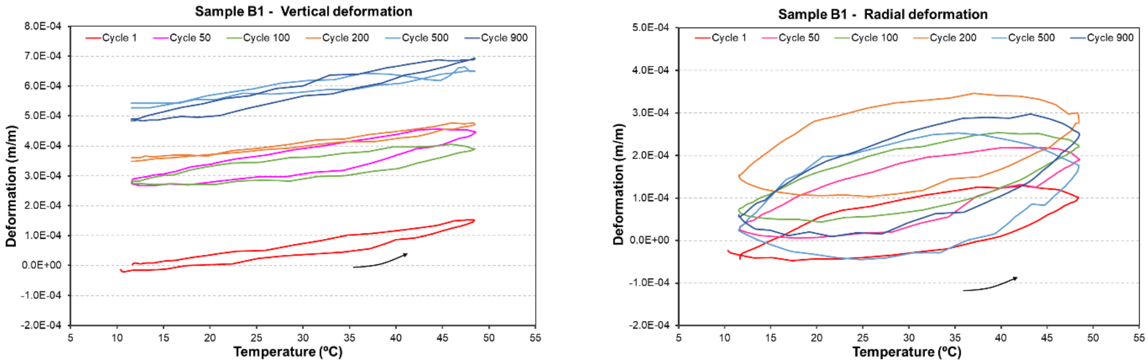

a) b)

Figure 3-43 Temperature – deformation evolution sample B1: a) Vertical deformation b) Radial deformation

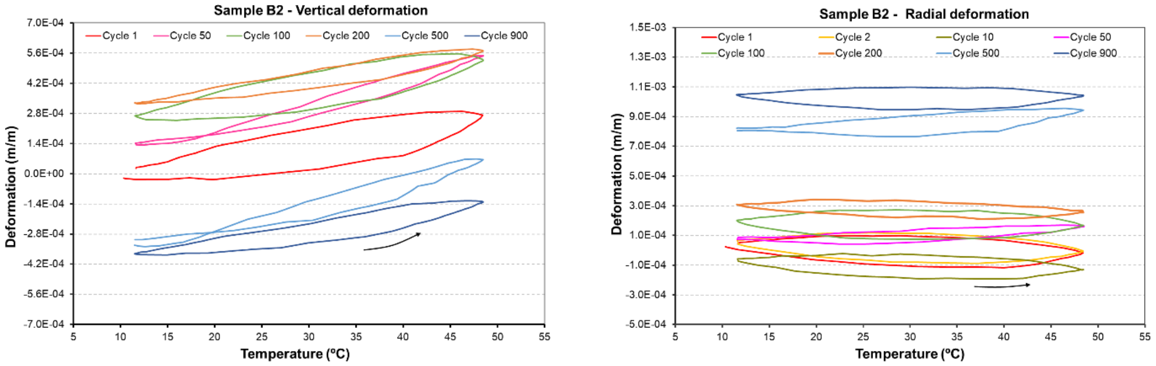

a) b)

Figure 3-44 Temperature – deformation evolution sample B2: a) Vertical deformation b) Radial deformation

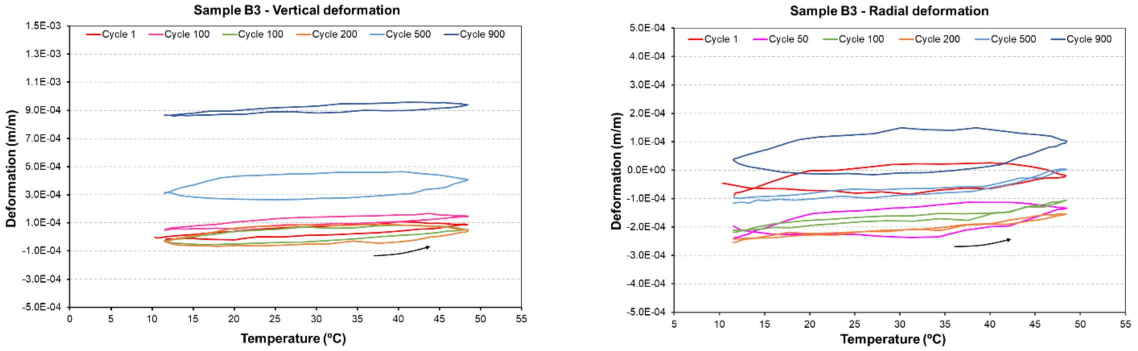

a) b)

Figure 3-45 Temperature – deformation evolution sample B3: a) Vertical deformation b) Radial deformation

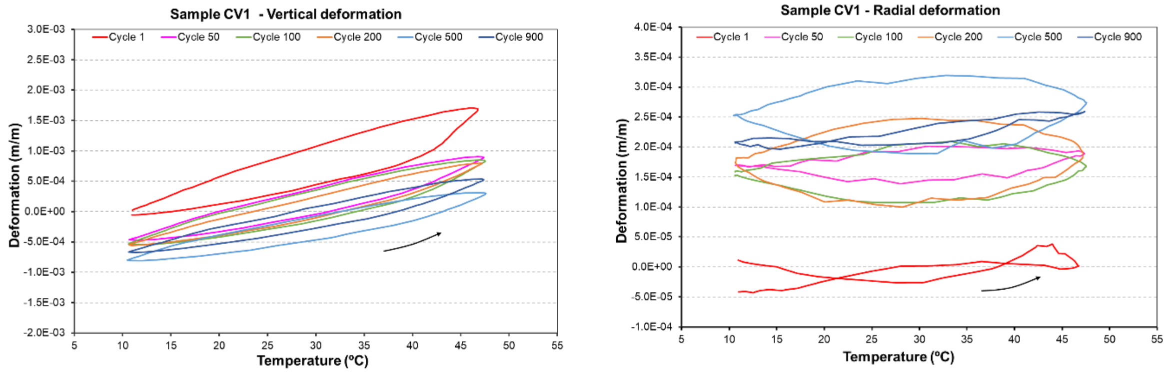

a) b)

Figure 3-46 Temperature – deformation evolution sample CV1: a) Vertical deformation b) Radial deformation

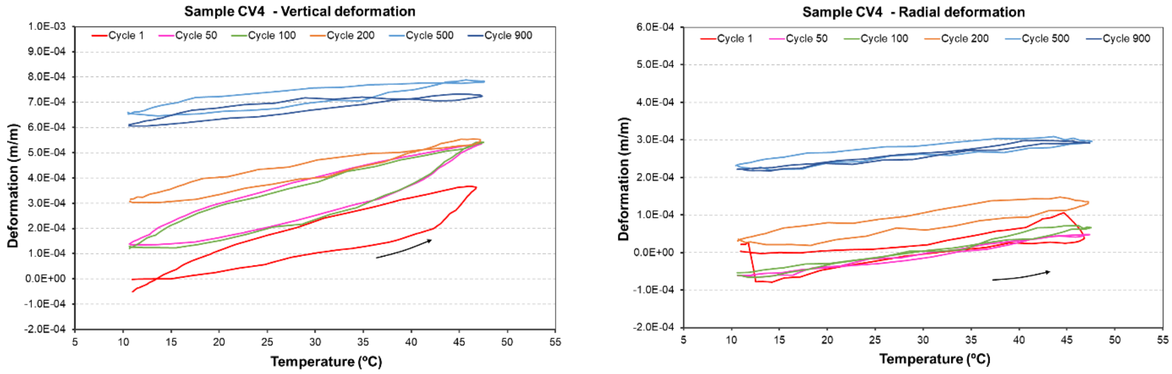

a) b)

Figure 3-47 Temperature – deformation evolution sample CV4: a) Vertical deformation b) Radial deformation

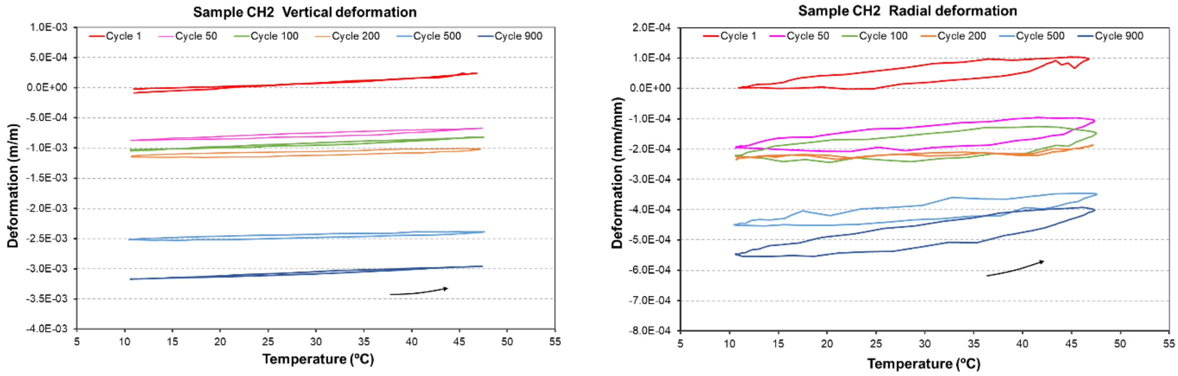

a) b)

Figure 3-48 Temperature – deformation evolution sample CH2: a) Vertical deformation b) Radial deformation

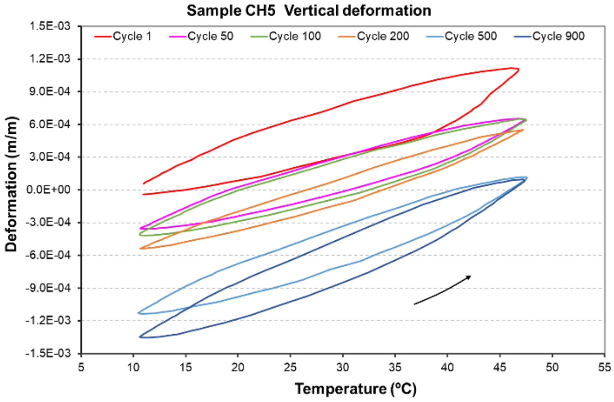

Figure 3-49 Temperature – deformation evolution sample CH5 - Vertical deformation

As expected and observed in the daily response, deformation tends to increase (sample expands) with the augmentation of temperature. However, radial deformation for sample B2 (Figure 3-44b), shows an opposite tendency for the firsts cycles, cycles 2 and 10 are included in Figure 3-44b to illustrate this feature. Note that for these cycles, sample contract during the heating. This confirms what was observed in Figure 3-36 and Figure 3-36b. But still consider, that an irregular response is observed until cycle 70.

In fact, the evolution observed in cycle 500 is as expected: expansion during heating. However, radial strains at cycle 100 and 900 for sample B2, have almost none evolution. Deformation register at maximal and minimal temperatures are almost the same: 2.03e-4 m/m and 2.01e-4 m/m respectively for cycle 100 and 1.03e-4 m/m and 1.04e-4 m/m for cycle 900.

It is interesting to point out, that even if the strains globally decrease the temperature-strains response shows an expansion of the sample during heating. As example, the response of vertical strains for sample CV1 (Figure 3-46a) can be observed. Even if, for each cycle the deformations due to thermal variations are positive, the evolution for cycle 100 is placed under the evolution of cycle 50 and so on. In other words, the initial strain for each cycle decrease with the increase of number of cycles. Similar response is observed for vertical and radial strains for sample CH2 (Figure 3-48), vertical strains for sample CH5 (Figure 3-49a).

Conversely, the opposite response is observed on sample CV1 for its radial deformation and on sample B1, B3 and CV4 for both radial and vertical deformation. That has a general positive strains tendency, and the initial strain for each cycle increase with the number of cycles.

Moreover, sample B2 in vertical direction has a mixed response related to its general strains evolution. From Figure 3-30 it is observed that radial strains tend to increase until cycle 200, but then, they decrease. Thus, the initial strains for each cycle tend to increase from cycle 1 to cycle 200. In other words, cycle 50 is placed above cycle 1 and so on. Nevertheless, the response for cycle 500 is placed under cycle 1 response.

Another remarkable effect that can be observed is that strains do not follow the same path for heating and cooling. It exists like a delay in the strains evolution. In fact, at the same temperature, deformations are higher when the temperature decreases (cooling) than when the temperature increases (heating). Thus thermal-strains evolution has an oval shape instead of a line. Furthermore, the amplitude of this oval is not the same for all the samples and all the directions.

If we consider that the maximal amplitude is located at the mean temperature (29.5ºC), the mean radial and vertical amplitude are presented in Table 3-12. Regarding to these amplitudes is important to realize that samples mostly composed by calcite presents a higher strains amplitude in radial sense. Whereas, all samples (vertically and horizontally drilled) composed by calcite and quartz show a larger amplitude in axial direction.

Table 3-12 Mean deformations amplitude for thermal-strains evolution

| Sample | Vertical (m/m) | Radial (m/m) |
|---|---|---|
| B1 | 2.87e-5 | 17.5e-5 |
| B2 | 14.1e-5 | 17.3e-5 |
| B3 | 6.84e-5 | 10.3e-5 |
| CV1 | 46.9e-5 | 7.14e.5 |
| CV4 | 12.3e-5 | 1.77e-5 |
| CH2 | 28.6e-5 | 2.86e-5 |
| CH5 | 38.4e-5 | |

The thermal expansion coefficient can be defined as the slope of a linear tendency adjusted to the temperature-strains results. Table 3-13 presents the values obtained for these coefficients at the cycles considered for the analysis for samples from group 1 and Table 3-14 for samples from group 2. In general, the values of thermal expansion found are similar to those found by the Laboratoire Régional des Ponts et Chaussées de Toulouse during their characterization of LaRG limestone, between 14.2e-6 ºC-1 and 1.4e-6 ºC-1 (see chapter 3.1.4). Nevertheless, the value obtained for sample B2 in radial direction is negative and smaller than the one found for the LaRG limestone. This condition may be associated to the response observed for this sample in this specific direction.

In the same way coefficients found for sample CV1 and CH5, are quite different from the values obtained during the characterization of LaRG. In fact, thermal expansion coefficient for radial strains in sample CV1 is 2.5 times lower than the minimal value formerly presented (1.4e-6 ºC-1). Moreover, the coefficient obtained for axial direction in samples CV1 and CH5 is 2.5 times higher than the maximal value obtained from the thermal expansion coefficient test.

Nonetheless, it is important to remember that the strains amplitudes observed in vertical direction for samples CV1 and CH5 are exceptionally high, in comparison with what was found for the other samples considered. Additionally, is important to remember that the tests performed by Laboratoire Régional des Ponts et Chaussées de Toulouse were realized on samples obtained from blocks fell inside the cavern, therefore the mineralogical composition of samples used should be similar to group 1 samples.

Moreover, from Table 3-13 and Table 3-14 it can be remarked that the thermal expansion coefficient remains constant, despite the general strains evolution observed through the thermal cycles, like the initial deformation at each cycle.

Table 3-13 Thermal expansion coefficient, from strains measurements – Samples group1

| Cycle | Sample B1 |  | Sample B2 |  | Sample B3 |  |
|---|---|---|---|---|---|---|
|  | Vertical (ºC$^{-1}$) | Radial (ºC$^{-1}$) | Vertical (ºC$^{-1}$) | Radial (ºC$^{-1}$) | Vertical (ºC$^{-1}$) | Radial (ºC$^{-1}$) |
| 1 | 4.0e-6 | 3.0e-6 | 7.0e-6 | -2.0e-6 | 3.0e-6 | 1.0e-6 |
| 2 | 4.0e-6 | 4.0e-6 | 7.0e-6 | -2.0e-6 | 3.0e-6 | 2.0e-6 |
| 10 | 4.0e-6 | 4.0e-6 | 7.0e-6 | -2.0e-6 | 3.0e-6 | 2.0e-6 |
| 100 | 3.0e-6 | 3.0e-6 | 7.0e-6 | -0.9e-6 | 3.0e-6 | 3.0e-6 |
| 500 | 3.0e-6 | 4.0e-6 | 10.0e-6 | 3.0e-6 | 2.0e-6 | 3.0e-6 |
| 900 | 6.0e-6 | 5.0e-6 | 7.0e-6 | 0.2e-6 | 2.0e-6 | 2.0e-6 |
| mean | 4.0e-6 | 3.8e-6 | 11.3e-6 | -0.9e-6 | 2.7e-6 | 2.2e-6 |

Table 3-14 Thermal expansion coefficient, from strains measurements – Samples group2

| Cycle | Sample CV1 |  | Sample CV4 |  | Sample CH2 |  | Sample CH5 |
|---|---|---|---|---|---|---|---|
|  | Vertical (ºC$^{-1}$) | Radial (ºC$^{-1}$) | Vertical (ºC$^{-1}$) | Radial (ºC$^{-1}$) | Vertical (ºC$^{-1}$) | Radial (ºC$^{-1}$) | Vertical (ºC$^{-1}$) |
| 1 | 40e-6 | 1.0e-6 | 10.e-6 | 3.0e-6 | 8.0e-6 | 2.0e-6 | 30e-6 |
| 2 | 40e-6 | 0.6e-6 | 10e-6 | 3.0e-6 | 8.0e-6 | 3.0e-6 | 30e-6 |
| 10 | 40e-6 | 0.4e-6 | 10e-6 | 2.0e-6 | 7.0e-6 | 2.0e-6 | 30e-6 |
| 100 | 40e-6 | 0.2e-6 | 10e-6 | 4.0e-6 | 6.0e-6 | 2.0e-6 | 30e-6 |
| 500 | 30e-6 | 0.2e-6 | 3e-6 | 2.0e-6 | 3.0e-6 | 3.0e-6 | 30e-6 |
| 900 | 30e-6 | 1.0e-6 | 3e-6 | 2.0e-6 | 6.0e-6 | 4.0e-6 | 40e-6 |
| mean | 36.7e-6 | 0.6e-6 | 7.7e-6 | 2.7e-6 | 6.3e-6 | 2.7e-6 | 31.7e-6 |

As mentioned before, samples from group 2 were drilled form the face of the cliff, considering two different directions (parallel and perpendicular to the cliff's face). It can be observed that these samples present higher thermal expansions in axial direction, which means that samples expand the most in perpendicular direction to the face cliff, which can be related to the direction where the cliff suffered a decompression during the valley formation geological process.

It can be remarked that samples B1 and B3 from group 1 present a similar thermal expansion coefficient in both directions and have a higher temperature-strains evolution amplitude for radial deformation (oval amplitude). Conversely, sample B2 has higher thermal expansion coefficient in axial direction and its temperature-strains evolution is similar for vertical and radial direction.

These conditions may be related to a preferential deformation direction in the sample (anisotropy), perhaps related to its direction in relation to the cliff. However, as mention before, because of the nature of these samples, there is no information about its original position in the cliff and from the results obtained is not possible to infer their directions.

From Figure 3-43 to Figure 3-49 it may be assumed that there is no strains accumulation after each thermal cycle, which means that the deformation at the beginning and the end of each cycle are the same. Nevertheless, because the strains evolution observed thought the imposition of thermal cycles this is not the case.

Therefore, even if small a strains accumulation should be observed in each cycle, as was observed by calculating the difference between initial and final strains at each cycle. Figure 3-50 and Figure 3-51 present the accumulated strains through thermal cycles, in vertical and radial direction respectively for samples from group 1, and Figure 3-52, Figure 3-53, for samples obtained from the face of the cliff. It is important to mention that for these figures; a logarithmical scale is considered in the cycles axis only for visual purposes.

Negative values of accumulated strains represent cycles were the final deformation is smaller than the initial one. This condition is observed when the cycle belongs to an interval where the global strains decrease. For instance, sample CH2 that present a negative tendency in the strains evolution for both directions (see Figure 3-31 and Figure 3-33) has negative values of cumulative strains for all the cycles considered, except for radial strains at cycle 2 and 200. However, despite axial deformation at sample B3 have a positive tendency the irreversible deformations after each cycle presents negative values.

No tendency is observed for the evolution of irreversible deformations; nevertheless, for all the samples and directions at 900 cycles, this value is very close to zero. Moreover, the variation of radial irreversible strains through thermal cycles for samples from group 2, tends to decrease with the imposition of thermal cycles.

From the general tendency and the daily and cycle strains response is not possible to determine any feature regarding to the mineralogical composition or the original sample direction to the face cliff, that may indicate for instance the original direction of group 1 samples.

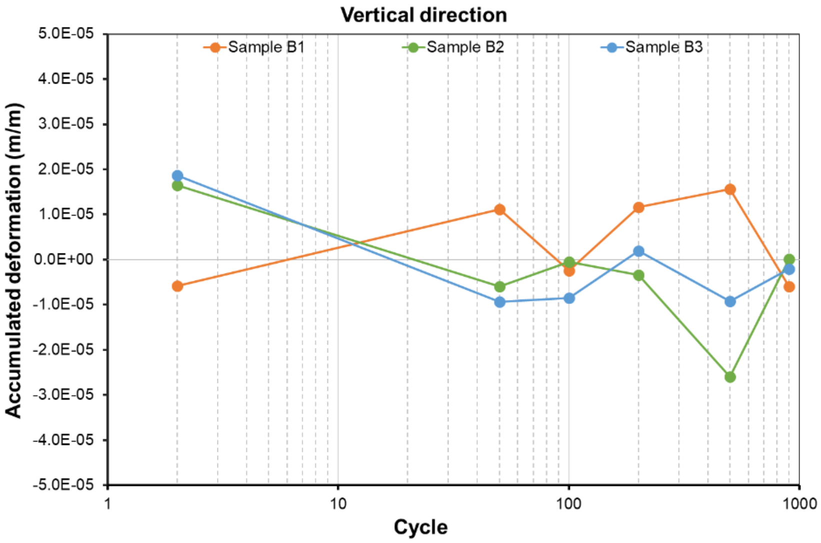

*Figure 3-50 Vertical direction accumulated deformation – samples group 1*

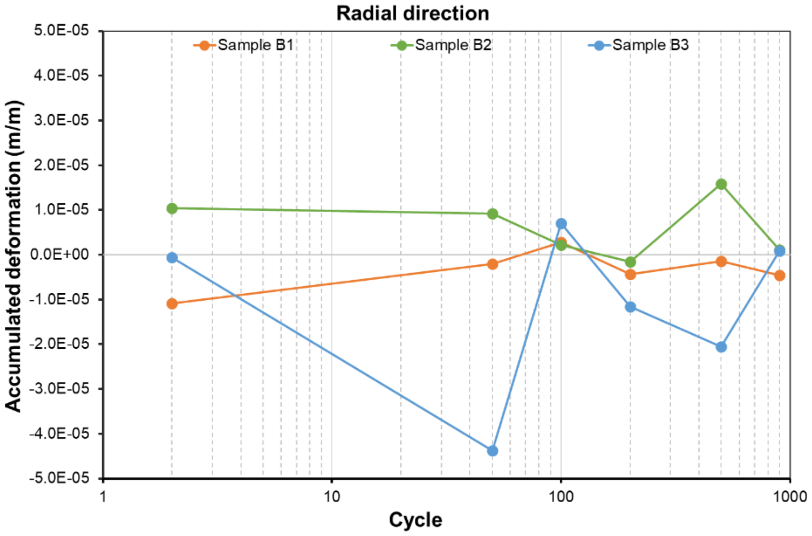

Figure 3-51 Radial direction accumulated deformation – samples group 1

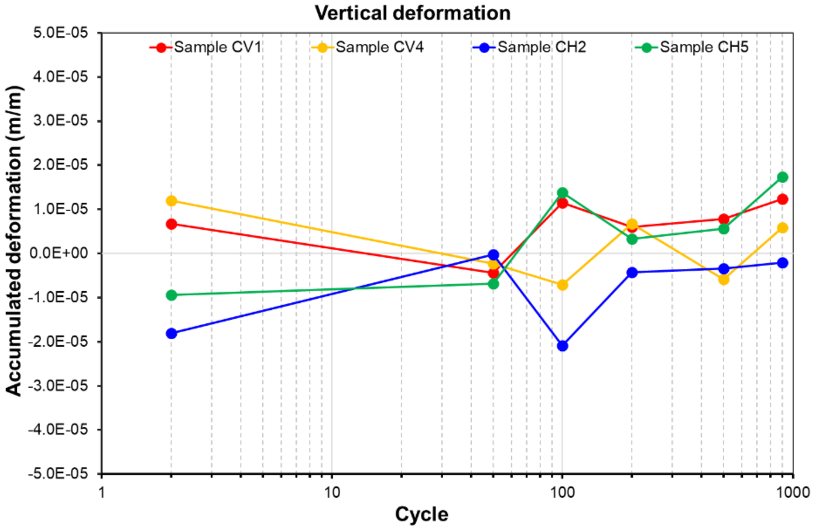

Figure 3-52 Vertical direction accumulated deformation – samples group 2

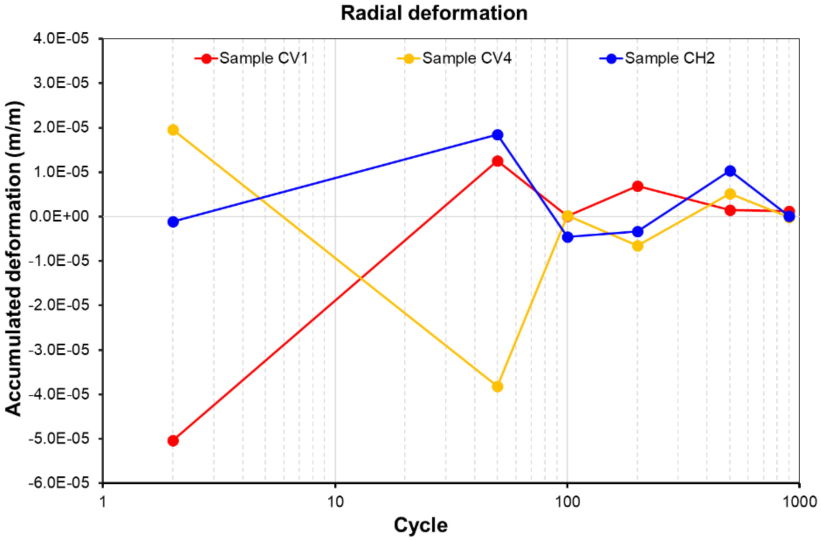

Figure 3-53 Radial direction accumulated deformation – samples group 2

### 3.5.2. Elastic wave propagation velocities.

Elastic wave propagation velocities are measured at least once a week for 15 samples: 5 obtained from blocks, 5 drilled in the face of the cliff in vertical direction and 5 in horizontal direction. The samples used to measure deformations, except sample B1 that is only used for strains measurements, are included. Furthermore, this parameter is measured for all the cylindrical samples at least before and after the heating/cooling treatment, to have an extra characterization of the rock.

For the purpose to evaluate if strain gauges have any effect in the elastic wave propagation velocities, measurements were performed on samples B2, B3, CV1, CV4, CH2 and CH5, with and without the gauges strains glued; results obtained are presented in Table 3-15. It can be observed that similar values were found for both conditions. That means that any elastic wave propagation changes are induced by the strain gauges system.

Table 3-15 Vp measurements without and with strain gauges

| Sample | Vp- without gages (m/s) | Vp- with gages (m/s) |
|---|---|---|
| B2 | 4651 | 4637 |
| B3 | 4470 | 4480 |
| CV1 | 3247 | 3227 |
| CV4 | 2842 | 2810 |
| CH2 | 3037 | 3042 |
| CH5 | 2830 | 2827 |

La Roque Gageac cliff is characterized by its heterogeneity (see chapter 2.3-Geology). This condition is highlight by the mineralogical compositions differences found between samples from inside the cavern and outside of it. Yet, this heterogeneity is also evidenced in samples from the same mineralogical composition. For instance, from Table 3-6 it can be observed that initial Vp value obtained for samples B2 and B3 are higher than the Vp value found for samples B5, B6 and B7.

The difference observed in the initial Vp value may explained, why after 950 thermal cycles almost any evolution of this parameter is observed for samples B1 and B2, while, samples B5, B6 and B7 experience a decay of 4% of the initial Vp value, for 828 cycles, as can be observed in Figure 3-54.

In the other hand, Figure 3-55 presents the evolution of compressive elastic wave velocity (Vp) for samples obtained from the face of the cliff. These samples have a lower initial value of Vp than block samples, as is presented in Table 3-6, they shows a decrease in the Vp value through the thermal cycles; after 910 cycles, this value decreases about 8% of its initial value. Samples oriented vertically present a mean decrease for the Vp value around 10%, while horizontal samples show a mean decay of 7%. That means that samples drilled vertically present more damage associated to thermal fatigue.

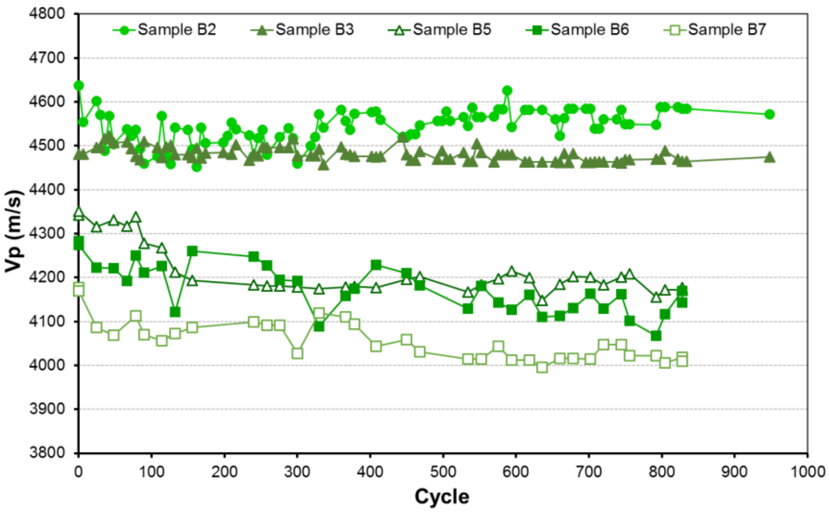

Figure 3-54 Compressive elastic wave velocity evolution samples group 1

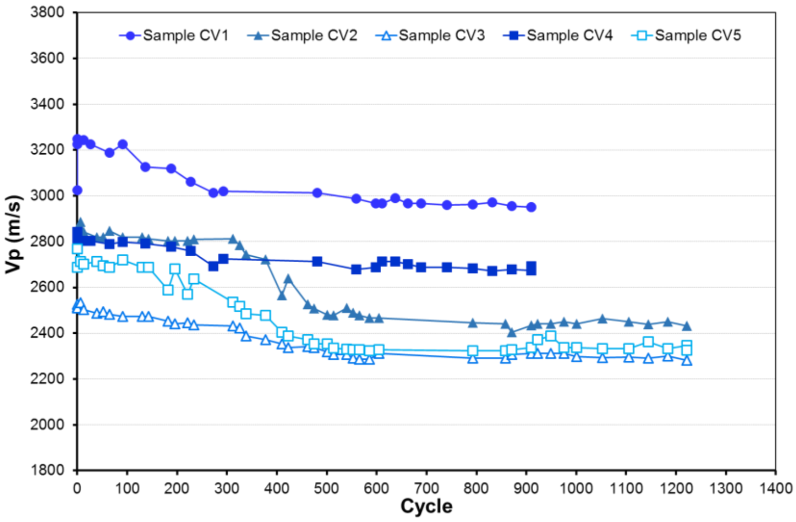

a)

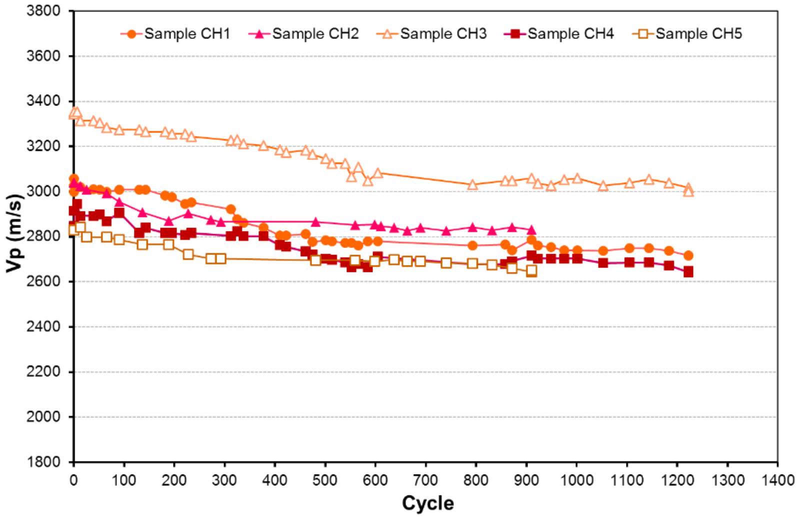

b)

Figure 3-55 Compression elastic wave propagation velocity evolution- samples group 2: a) samples drilled in vertical direction b) samples drilled in horizontal direction

From Figure 3-54 and Figure 3-55, it can be observed that the reduction observed in the compression wave velocities through thermal cycles is not constant for the whole experiment time. In fact, it can be observed that the Vp values of seem tend to a stable value, at the end of the experimental program, after cycle 600. Moreover, it can be observed that the highest Vp evolution is registered in the firsts cycles, samples CV2, CV3 and CV5 evolves the most between the cycle 200 and 300 while samples B5, B6 and B7 presents a steeped evolution for the first 100 cycles.

It is important to remember that, as mentioned in chapter 3.2 (samples description), samples obtained in horizontal sense may belong to the same rock core. This is the case of samples CH1, CH2 and CH3 and samples CH4 and CH5. Figure 3-56 illustrates the position of each sample and its relative position to the face of the cliff.

Therefore, from Figure 3-55B, it can be observed that sample CH3 present the highest initial value of Vp, this can be explained by the fact that this sample present an inferior initial alteration level, because its original distance to the face of the cliff is larger and therefore climatic variations have less impact. Even if the remaining core placed after sample CH5 was not considered for this experimental program, its value of Vp was measured obtaining a value of 3200 m/s, much higher than the initial value obtained for samples CH4 and CH5, that are, in fact, very similar.

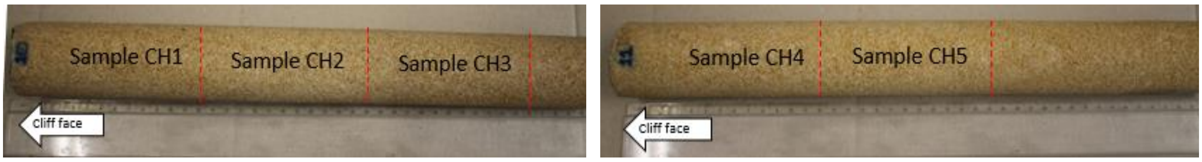

a) b)

Figure 3-56 Rock cores obtained in horizontal direction: a) Core 10 – samples CH1, CH2 and CH3 b) Core 11 – Samples CH4 and CH5

Moreover, sample CH3 shows a higher Vp reduction than the other samples that composed the rock core 10, after 900 cycles the Vp value for sample CH3 decreases a 9 while sample CH2 and CH1 decreases only a 7%. It is also remarkable that, even if samples CH2 and CH5 were originally located deeper than samples CH1 and CH4 respectively, their initial Vp values and evolution through thermal cycles are very similar. This may indicate that the effect of climatic solicitations in the cliff is mainly evidenced in the first 25 cm.

In the same way, it is interesting to observe that despite vertical samples were all obtained in the first 20 cm of the cliff, they show more heterogeneity in the values of initial Vp, with a range of 685 m/s in comparison with the range of 226 m/s observed for horizontal samples, (excluding sample CH3).

Furthermore, horizontally drilled samples show more heterogeneity in the amount of damage induced by the thermal cycles, evidenced by the decrease in the Vp value (between 5% to 14% of the initial measurement), as observed with the horizontal samples. This drop of wave propagation velocity is stronger in samples with higher initial velocity.

Figure 3-57 presents the evolution of shear elastic wave propagation velocity (Vs) for group 1 samples and Figure 3-58 for samples from group 2. The Vs value is calculated as the mean Vs value from the measures realized in two perpendicular directions.

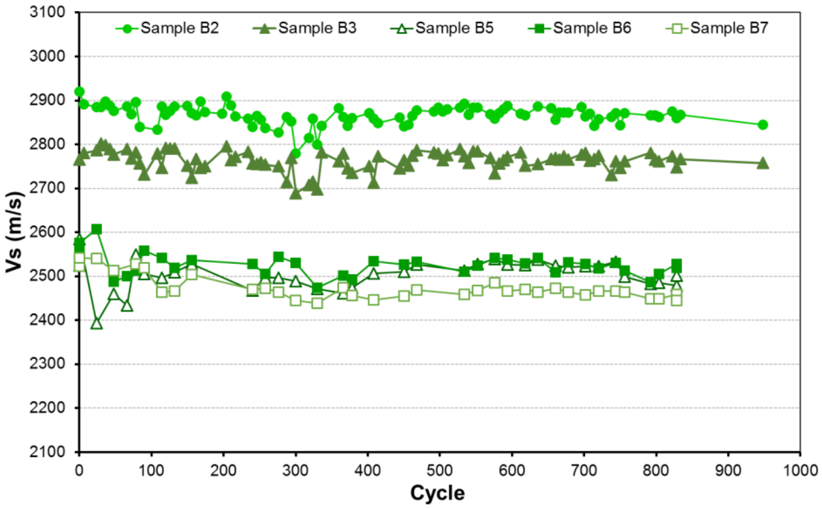

Figure 3-57 Shear elastic wave velocity evolution - samples group 1

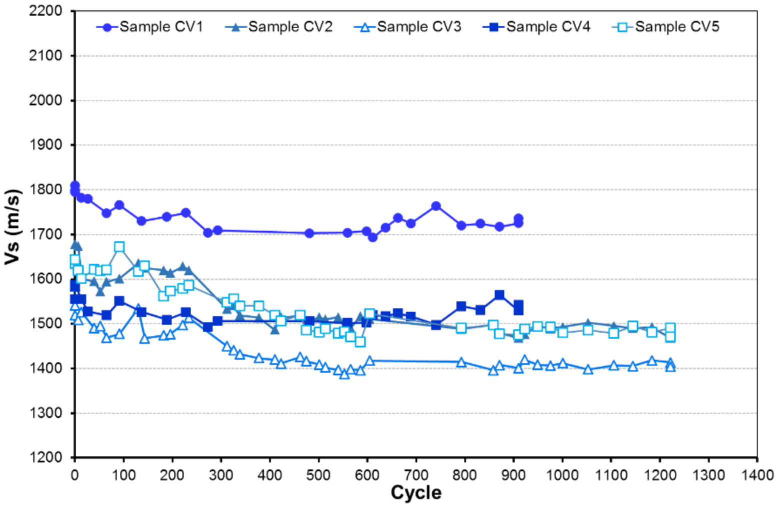

a)

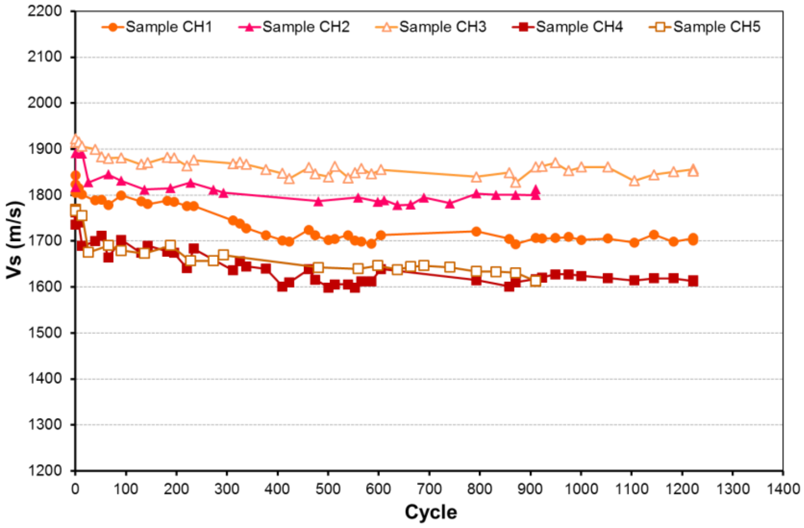

b)

Figure 3-58 Shear elastic wave propagation velocity evolution- samples group 2: a) samples drilled in vertical direction b) samples drilled in horizontal direction

From these figures, it can be remarked that the Vs evolution is similar to the one found for compressive waves, samples from group 1 presents almost any evolution of Vs with the thermal cycles, samples B1 and B2 show a decay of only 1%, and for samples B5, B6 and B7 this parameter reduces a 3% from the initial value.

Moreover, samples from group 2 show an important heterogeneity in the value of initial Vs value in samples vertically drilled, even if all these samples are obtained very close to the cliff face. Samples with a higher decrease in the Vs value are samples CV2, CV4 and CV5 (mean decay of 12% of their initial value). Moreover, sample CV1, the one that has a higher initial value shows the lowest evolution through heating/cooling cycles, only 4% after 900 cycles.

In the other hand, as was observed for the compressive wave evolutions, sample CH3 shows the higher initial value of the horizontally drilled samples. It is also the sample were the Vs value evolves the less, only 4% in comparison with the 7% observed for the other horizontal samples.

From Figure 3-58b, it can be observed that initial Vs values and their evolution for samples CH1, CH2 and CH3, follow a response that can be related to the position of the samples in the cliff. Note that Vs for sample CH3 is higher than for sample CH2 and this last value is higher than the measurement obtained in sample CH1. Nevertheless, for samples CH4 and CH5 this cannot be observed.

The measurements of elastic wave propagation can be used to directly calculate the dynamic Young modulus and Poisson ratio, through the equations 3-4 and 3-5 finally, the dynamic bulk modulus can be calculated by the equation 3-9, where $E_d$ and $\upsilon_d$ are the dynamic Young modulus and Poisson ratio, respectively.

$$\mathrm{K_d} = \frac{\mathrm{E_d}}{3(1 - 2\,\upsilon_\mathrm{d})} \qquad \text{Eq. 3-9}$$

The bulk modulus evolution through the imposition of thermal cycles can be observed in Figure 3-59 for samples obtained from blocks and in Figure 3-60 for samples directly drilled from the face of the cliff.

It can be noted the bulk modulus evolves very similar to the values of VP and Vs. Samples B5, B6 and B7 show a mean decrease of 6% from the initial value, for samples from group 2 a mean decreases of 20% of the initial stiffness value is observed. However, samples B2 and B3 experience a mean stiffness value decrease of only 2% of the initial value. The stiffness variations between the initial values and the measurements after the thermal treatment are detailed in Table 3-16.

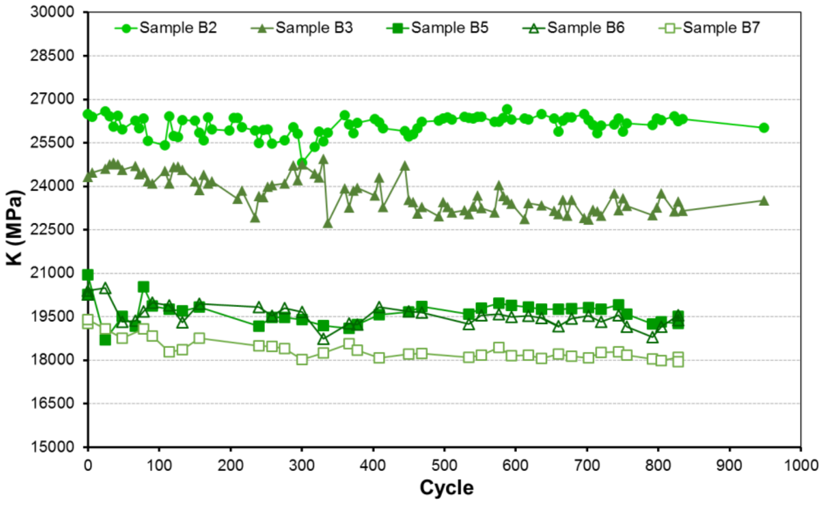

Figure 3-59 Bulk modulus evolution – samples group 1

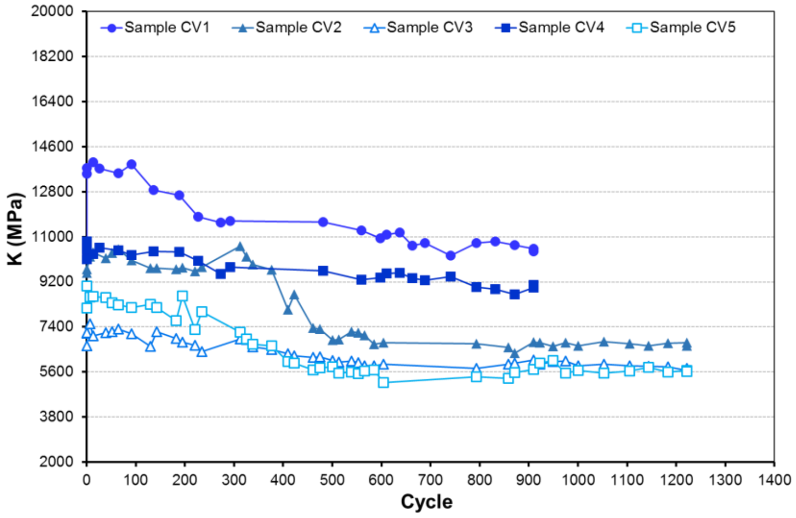

a)

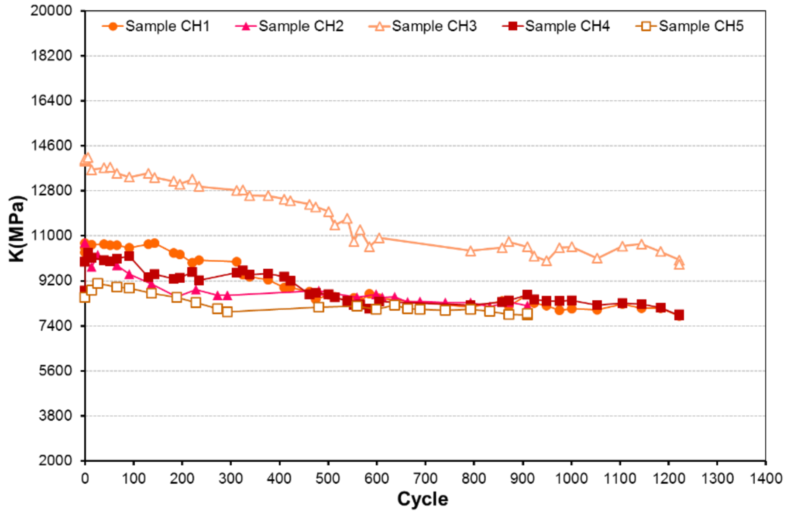

b)

Figure 3-60 Bulk modulus evolution – samples group 2: a) samples drilled in vertical direction b) samples drilled in horizontal direction

Table 3-16 Bulk modulus evolution

| Sample | Initial K (MPa) | Final K (MPa) | Variation (%) |
|---|---|---|---|
| B2 | 26500 | 26024 | 1.7 |
| B3 | 24300 | 23500 | 3.0 |
| B5 | 20600 | 19400 | 6.0 |
| B6 | 20300 | 19460 | 4.5 |
| B7 | 19330 | 18025 | 6.7 |
| CV1 | 13638 | 1068 | 23.2 |
| CV2 | 9630 | 6700 | 30.4 |
| CV3 | 7160 | 5694 | 20.5 |
| CV4 | 10470 | 9020 | 13.8 |
| CV5 | 8590 | 5630 | 34.4 |
| CH1 | 10610 | 7814 | 26.4 |
| CH2 | 10360 | 8145 | 21.3 |
| CH3 | 14030 | 9950 | 29.1 |
| CH4 | 9389 | 7840 | 16.5 |
| CH5 | 8539 | 7870 | 7.80 |

### 3.5.3. Uniaxial compressive strength.

Uniaxial compressive strength tests are performed on 15 samples that have been submitted to a different number of thermal cycles (see Table 3-9). The initial and final elastic compression wave propagation velocities are considered as comparison parameters. Table 3-17 presents the results obtained for each sample considered, related to its initial and final Vp value.

It can be observed, that samples with a higher Vp value (final Vp) present a superior strength (UCS) value, even if the sample has been submitted to a different amount of thermal cycles. For instance, sample B13 has an initial Vp value of 4485 m/s, after 420 cycles of temperature the elastic wave propagation velocity decrease until 4450 m/s. Nevertheless, its UCS value (47.77 MPa) is similar to the value obtained in sample B18 (47.54 MPa), that has a similar initial Vp value, but that has suffered no thermal cycles.

Table 3-17 Uniaxial compressive strength results

| Sample | Cycles imposed | Initial VP (m/s) | final VP (m/s) | UCS (MPa) |
|---|---|---|---|---|
| B5 | 828 | 4342 | 4175 | 41.23 |
| B6 | 828 | 4282 | 4151 | 38.03 |
| B7 | 828 | 4177 | 3981 | 37.56 |
| B8 | 624 | 4407 | 4181 | 39.08 |
| B9 | 624 | 4404 | 4181 | 39.93 |
| B10 | 624 | 4321 | 4130 | 40.01 |
| B11 | 420 | 4373 | 4198 | 41.96 |
| B12 | 420 | 4402 | 4154 | 41.72 |

| Sample | Cycles imposed | Initial VP (m/s) | final VP (m/s) | UCS (MPa) |
|---|---|---|---|---|
| B13 | 420 | 4485 | 4442 | 47.77 |
| B14 | 210 | 4486 | 4407 | 44.67 |
| B15 | 210 | 4389 | 4197 | 44.17 |
| B16 | 210 | 4441 | 4408 | 47.26 |
| B17 | 0 | 4381 | 4391 | 39.14 |
| B18 | 0 | 4483 | 4483 | 47.54 |
| B19 | 0 | 4380 | 4380 | 44.81 |

Figure 3-61, shows the deformation-stress evolution for samples that have known different number of thermal cycles. It is observed that samples submitted to a larger number of cycles, has a lower value of Uniaxial compressive strength, coupled with a lower bent in the strains-strength evolution, related to lower values of Young modulus.

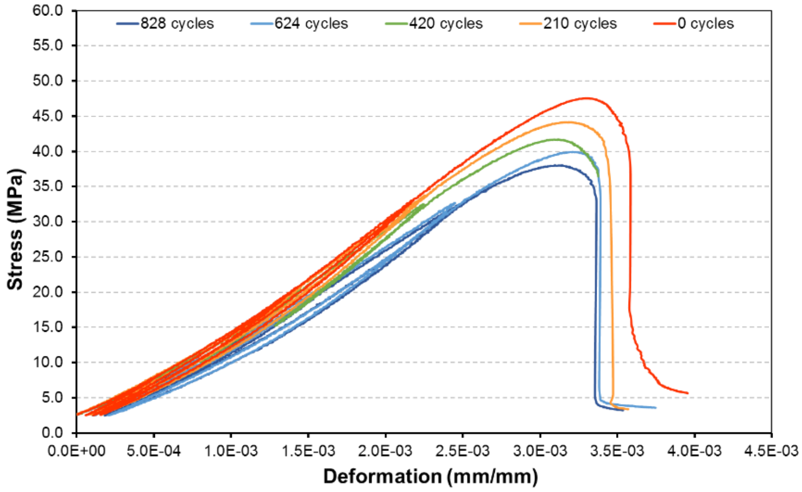

Figure 3-61 Deformation - stress evolution

The variation of UCS through the thermal cycles, as the evolution of elastic wave propagation velocities (Vp final), is shown in Figure 3-62. It can be observed a decrease in the elastic wave propagation velocity, coupled with a decrease in the rock strength.

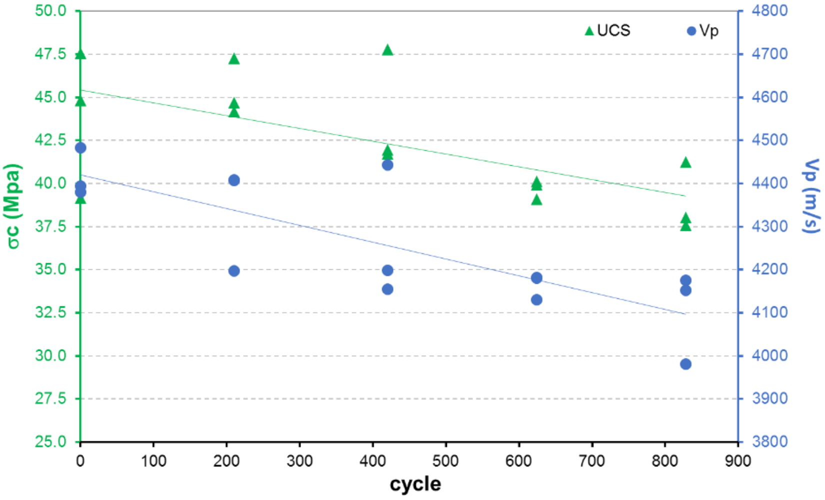

Figure 3-62 UCS and VP evolution

The mean UCS value found for samples submitted to 828 thermal cycles is 15% lower than the mean value obtained for samples without thermal treatment. In fact, the variation of Uniaxial compressive strength with the number of cycles follows the equation 3-10,

$$\sigma_c(\mathrm{MPa}) = 0.0075 * \text{Number of cycles} + 45.044 \qquad \text{Eq. 3-10}$$

From the stress-strain evolution, the Young modulus can be calculated, as the slope of the virgin loading path. The ASTM standard stated that this modulus might be obtained by any of the next methods:

a) The tangent slope at a stress level, which is fixed as a percentage of the maximum strength.
b) The tangent average slope of the strain line portion of the stress-strain curve.
c) The secant slope, from zero stress to some percentage of the maximum strength.

Moreover, as mentioned before for the uniaxial compression test performed, two unloading/ loading cycles were considered at 50% and 80% of the Uniaxial compressive strength estimated in the characterization of LaRG limestone (47.5MPa). The Young modulus can be obtained also as the slope of the unloading paths.

In order to evaluate the effect of thermal cycles in the rock Young modulus, this value was calculated from the virgin stress-strain paths as the average slope of the stress-strain portion ($E_{tan}$) from 1/3 $\sigma$c and 2/3 $\sigma$c, and as the secant modulus ($E_{sec}$) from zero to 70% $\sigma$c. But also, as the slope from the unloading path at 50% ($E_{50}$) and at 80% ($E_{50}$). The obtained young module values are listed in Table 3-18.

Table 3-18 calculated Young modulus

| Sample | $E_{tan}$ (GPa) | $E_{sec}$ (GPa) | $E_{50}$ (GPa) | $E_{80}$ (GPa) |
|---|---|---|---|---|
| B5 | 13.86 | 12.03 | 17.58 | 17.50 |
| B6 | 13.37 | 11.74 | 15.30 | 15.08 |
| B7 | 13.24 | 11.68 | 15.29 | 14.84 |
| B8 | 13.79 | 11.74 | 15.70 | 15.78 |
| B9 | 13.40 | 12.02 | 15.81 | 15.76 |
| B10 | 14.50 | 12.76 | 16.94 | 16.73 |
| B11 | 15.10 | 12.09 | 15.03 | 15.59 |
| B12 | 15.13 | 13.11 | 16.90 | 17.33 |
| B13 | 16.21 | 13.86 | 17.95 | 18.47 |
| B14 | 15.69 | 13.60 | 17.39 | 15.59 |
| B15 | 15.59 | 13.67 | 17.38 | 17.57 |
| B16 | 16.00 | 14.09 | 17.73 | 18.20 |
| B17 | 14.30 | 12.84 | 16.66 | 16.30 |
| B18 | 16.22 | 14.08 | 17.78 | 18.30 |
| B19 | 15.41 | 13.83 | 17.59 | 17.60 |

It can be observed that the Young modulus value obtained as the slope of the linear virgin stress-strain is higher than the one obtained as the secant slope. Moreover, the Young moduli observed with the unloading paths are similar between them and higher than the moduli measured at the virgin loading. Similar results are observed by Al-Shayea (2004), in limestone samples (99% calcite), where it is also stated that the Young modulus value has less variation when it is obtained from unloading paths and it is almost constant regardless of the stress level.

Figure 3-63 presents the evolution of Young modulus through the imposition of thermal cycles. As was observed whit the uniaxial compressive strength, this modulus shows a reduction with the increment of thermal cycles. The reduction observed is very similar for all the methods considered to determine this parameter, in a general, after 900 cycles this value decays in a 10%.

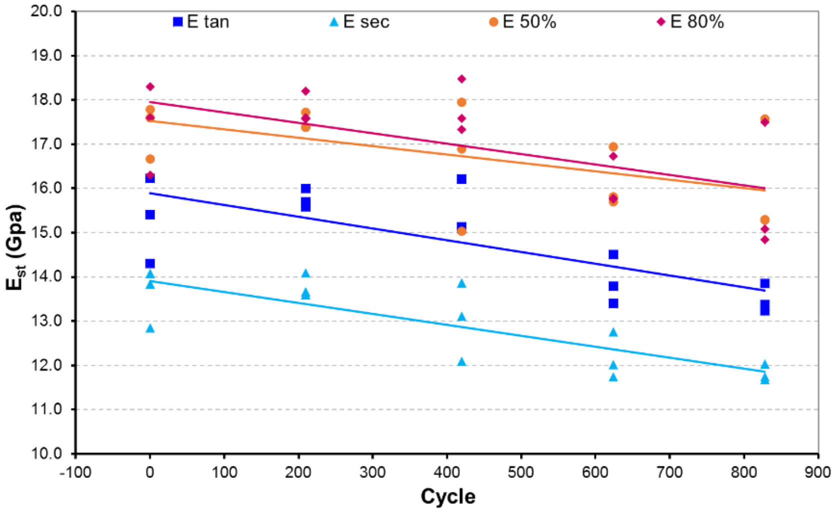

Figure 3-63 Young modulus evolution through thermal cycles

To be able to obtain the static young modulus from elastic wave propagation velocities, a dimensionless parameter K= Ed/Est should be included in the equation 3-4. Therefore, the new equation to calculate the static young modulus from the elastic wave propagation velocities is defined as:

$$E_{st} = \frac{1}{K}\rho\frac{V_s^2(3V_p^2 - 4V_s^2)}{(V_p^2 - V_s^2)} \qquad \text{Eq. 3-11}$$

The ideal K value will be 1, which means that the static young modulus is perfectly calculated from the equation 3-1. However, this is not always the case, in the literature, different values of K are found regarding to the type of material.

For instance, Ciccotti & Mulargia (2004) found for a mudstone-limestone with a calcite content of 50% that the K value varies from 1 to 1.3. In the same way, Martínez-Martínez et al. (2012) found for limestones composed of 90% of calcite that K varies from 0.5 to 1.9. It is important to mention that for Martínez-Martínez et al. (2012) study the static young modulus was obtained as the secant slope to the 70% of the maximal strength. Moreover, in the study performed by Najibi et al. (2015) on a similar limestone, a higher range for K value was found, between 1.4 to 3.8.

The mean K value obtained by considering the three method mentioned to calculate the static Young modulus is presented in Figure 3-64, the parameter K is higher when considering the secant method for the Young modulus calculation. If the static Young modulus is defined as the slope of the unloading path, which is the more consistent method (with less variations) the parameter K varies from 1.9 to 2.5.

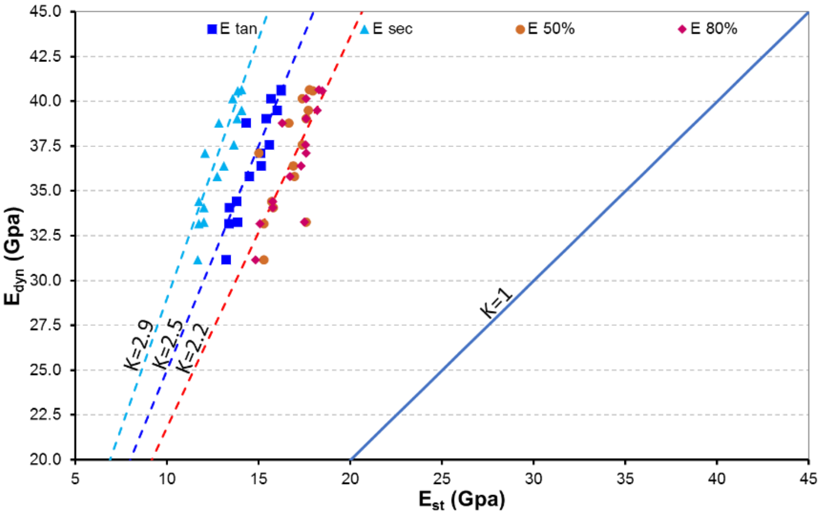

Figure 3-64 Relation between $E_{st}$ and $E_{dyn}$

### 3.5.4. Discussion on the mechanical response.

In addition to the measurements of strains, elastic wave propagation velocity and Uniaxial compressive strength, the effect of thermal cycles over LaRG limestone porosity was evaluated through mercury intrusion porosity test performed on samples that were submitted to a different amount of cycles: 0, 216, 420 and 630. However, any remarkable response can be observed. The obtained results are presented in appendix A.

After more than 1000 thermal cycles between 10ºC to 50ºC, no visible cracks were observed on the samples. Nevertheless the decrease in the Vp suggest a thermal fissuration of the samples, (Martínez-martínez, Benavente and García-del-cura, 2011; Brotóns et al., 2013; Inserra, Biwa and Chen, 2013) related to the propagation or generation of internal micro-fissures and voids, that generally appear in the boundary of the grains (Malaga-Starzec et al., 2006; Yavuz et al., 2006). In fact, P-wave velocity has shown to be very sensitive to quantify and evaluate the thermal damage on rocks (Yavuz et al., 2006; Martínez, 2008; Wanne and Young, 2008; Luque et al., 2011).

In this experimental program, the elastic wave propagation velocities was always measured at least at the beginning and the end of the thermal treatment to have an extra characterization parameter, in addition, the porosity of the samples was also calculated. Table *3-6* presents all the characteristics of the 30 cylindrical samples considered, including the Vp and porosity.

It is interesting to point out that samples obtained from blocks (group 1) present a lower porosity and high elastic wave propagation velocity, a relation that may be expected as the measures of Vp is highly influenced by the porosity of the rock. Conversely, samples obtained from the face of the cliff (group 2) shows a higher porosity coupled with lower values of elastic wave propagation velocities. Nevertheless, samples from group 1 present a linear relation between porosity and Vp, whereas, group 2 samples has a more disperse relationship between Vp and porosity, as illustrated in Figure 3-65.

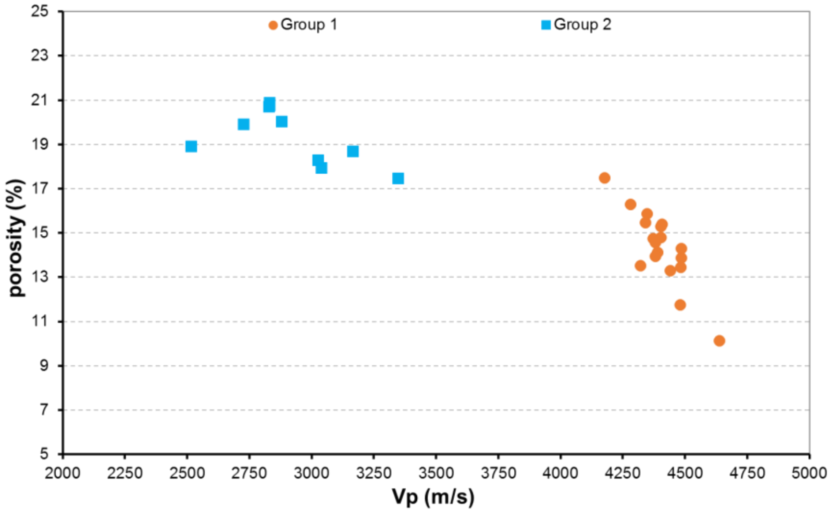

Figure 3-65 Initial Vp and porosity relation

Moreover, from Figure 3-66 it can be observed that samples obtained from blocks with higher porosity develop more damage (evaluated as the reduction of Vp) associated with thermal cycling. In the other hand, the Vp values measured on samples drilled from the face of the cliff decrease more for samples with lower porosity.

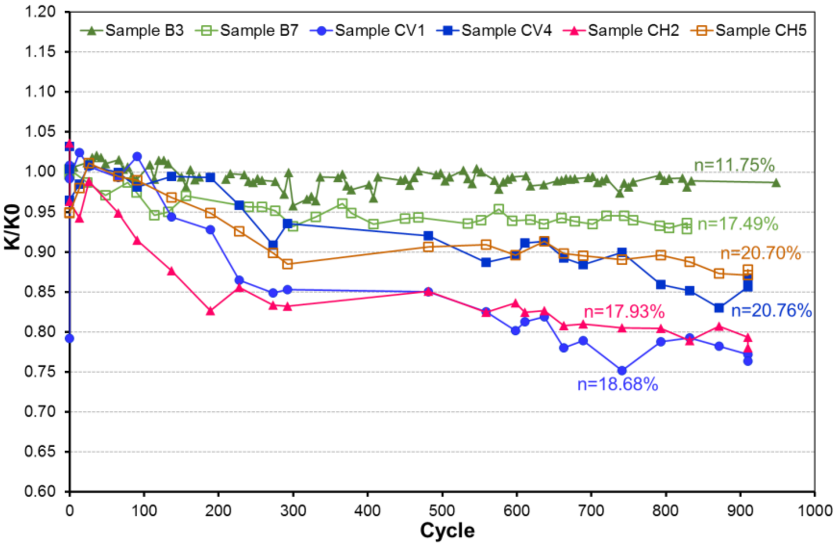

Figure 3-66 Bulk modulus variation (Calculated from Vp-Vs) with initial porosity (n)

It is important to note that horizontally drilled samples, present more porosity the closer they were placed to the face of the cliff, as presented in chapter 3.5.2, the original location in relation to the cliff face has an impact on the evolution of Vp through thermal cycles, samples placed deeper (lower porosity) present more important decrease of their Vp.

Another interesting point is that sample B7 shows a similar initial porosity than sample CV1 and CH2. Nevertheless, the reduction in Vp and Vs, and therefore in bulk modulus, is less important in sample B7 than in samples CV1 and CH2. This condition may be related to the mineralogical composition of the samples, remember that sample B7 is mainly composed by calcite, while samples CV1 and CH2 are composed by calcite and quartz. The thermal response between quartz and calcite minerals may induce some additional stresses on the grains boundaries that can be the responsible for the presented response (Hall and Thorn, 2014; Hartlieb et al., 2016). In fact, other experimental analysis (Malaga-Starzec et al., 2006; Tiskatine et al., 2016) found that the presence of quartz may control the response of the rock under thermal cycling due to its large and variable thermal expansion coefficient, even below 650ºC, where this mineral suffers important changes.

On samples, provided with strain gages for deformation measurements, the evolution of the elastic wave propagation velocities is also evaluated (except for sample B1). The deformation and Vp evolution are compared for one sample of each type: sample B3 obtained from blocks, sample CV4 drilled in the face of the cliff in vertical sense and sample CH2 drilled from the face of the cliff in horizontal sense.

Figure 3-67, presents the strains and Vp evolution of sample B3. It can be observed that vertical and radial strains increase for the whole experimental program, but Vp remains constant, nevertheless, despite this positive tendency vertical strains accumulate almost no deformation after 800 cycles.

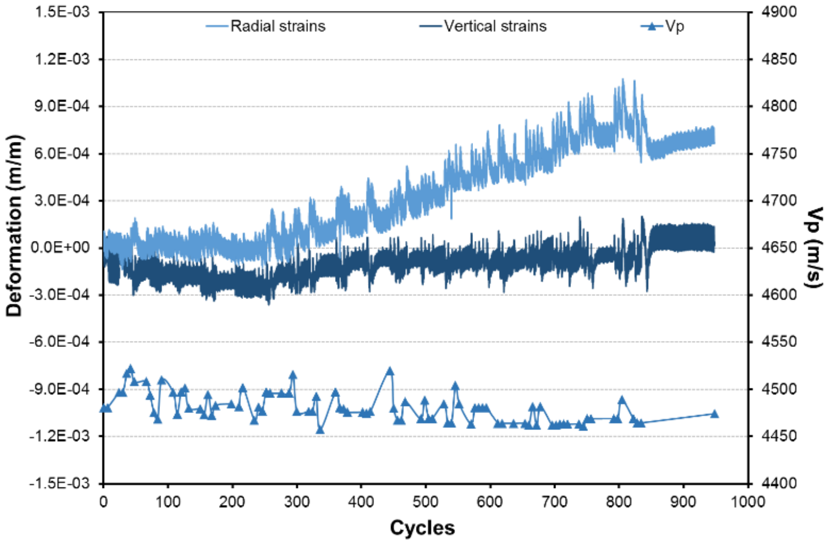

Figure 3-67 deformations and VP evolution - sample B3

Furthermore, between cycles 800 to the end of the test, any Vp measure is performed and the strains evolution has less dispersion. Nonetheless, from Figure 3-30 and Figure 3-32, it can be observed that this variation in the strains evolution tendency is also observed in sample B1 where any measure of Vp is realized.

In the same way, Figure 3-68 shows the strains and Vp evolution for sample CV4. In first place, it can be remarked that vertical and radial strains have similar evolutions. Moreover, an important reduction in Vp for the first 300 cycles is observed, for this period the radial and vertical strains present a high accumulation. Additionally, vertical strains present a variation in the strains amplitude, after cycle 300 it decreases.

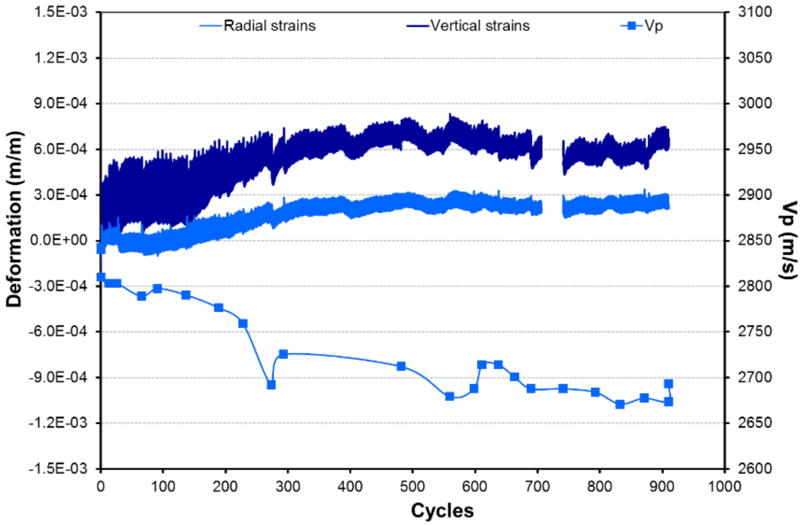

Figure 3-68 deformations and VP evolution - sample CV4

After cycle 300, thermal cycles accumulate less deformations. From Figure 3-52 and Figure 3-53Figure *3-53* it can be observed that irreversible strain tend to zero, especially for radial strains, and, Vp tend to a value of 2690 m/s.

Finally, Figure 3-69 illustrates the strains and Vp evolution for sample CH2, drilled in the cliff in horizontal direction, for this case it can be observed that vertical and radial strains have different responses, even if in both cases their tendency is negative (compression), the final accumulated vertical deformation is 6 times the radial.

The radial strains evolution for sample CH2 is more important between 200 to 600 cycles, where the Vp begins to have a less steep response. After cycle 600 Vp tends to 2830 m/s. In the same way, from cycle 600 to the end of the test, radial and vertical strains remain nearly constant.

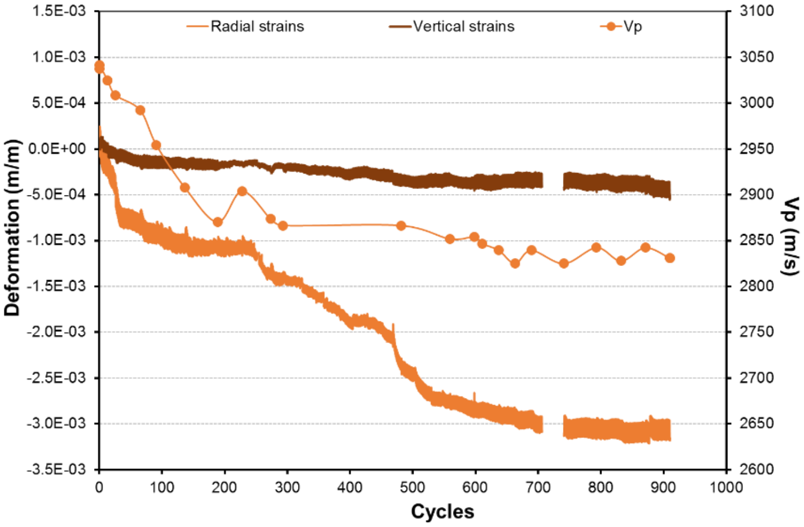

Figure 3-69 deformations and VP evolution - sample CH2

According to Najibi et al. (2015) it is possible to obtain an empirical potential relationship between VP and Uniaxial compressive strength since the porosity and density has a direct effect in UCS. Having this in mind for samples mainly composed by calcite the uniaxial compressive strength can be predicted from the Vp value by the equation Eq. 3-12, where Vp is in Km/s and UCS in MPa. Obtaining a good agreement (R2=0.8308) when eliminating results of sample B17, as illustrated in Figure 3-70.

$$\sigma_c = 1.8905 Vp^{2.1516}$$ Eq. 3-12

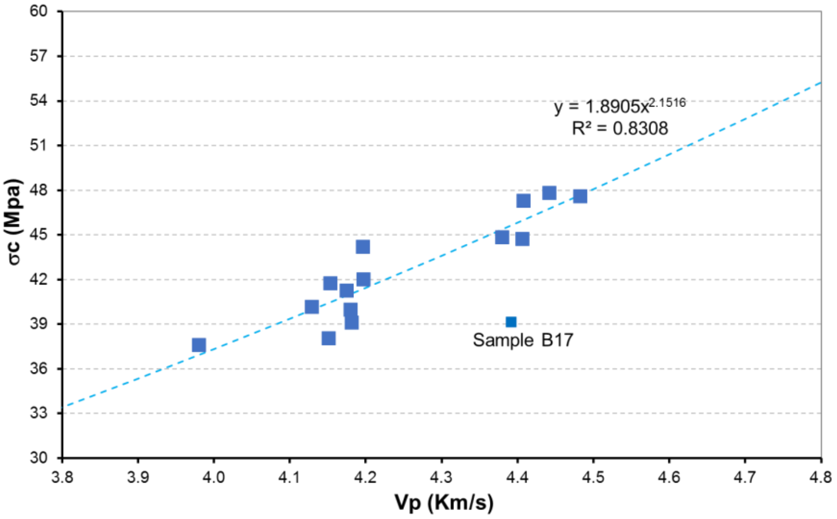

Figure 3-70 VP -UCS relation

## 3.6. Generation and propagation of fissures.

From the mechanical results, it is observed that samples submitted to thermal cycles experience damage that can be identified by a drop in P-wave propagation velocity and reduction in the strength. This damage can be related to the generation or propagation of fissures developed generally in the grains boundaries (Goudie and Viles, 2000; Luque et al., 2011; Hayatdavoudi, Chitila and Boukadi, 2015)

Moreover, during a former experimental program developed on samples from LaRG, some important macro-fissures were observed (Gasc-Babier, Girmaand and Gendre, 2014). Therefore, to evaluate the generation and propagation of fissures (at photo-scale) due to thermal damage, photos were taken on samples (see Table 3-9) submitted to thermal cycles. These photos were analyzed with the digital image correlation technique through the software N-corr (Blaber, Adair and Antoniou, 2015). Results obtained with this analysis are presented in this section.

### 3.6.1. Brazilian test.

The digital image correlation (DIC) technique is widely used to analyzed samples submitted to tensile strength test, like the Brazilian test. Therefore, to evaluate the results obtained with the N-corr software photos were taken to samples 1343 to 1348 (see Table 3-3) during the loading path of Brazilian test.

Moreover, a common practice for DIC analysis is to generate a speckle pattern in the samples with white and black paint to enhance the natural contrast from the rock texture (Hild and Roux, 2006; Tung and Sui, 2010; Nguyen et al., 2011). For this reason, half of the samples considered were painted and the other half was left with the natural contrast, to evaluate if different responses are obtained with and without the pattern. Figure 3-71 compare the look of one sample with the speckle pattern (sample 1345) and one sample without it (sample 1346)

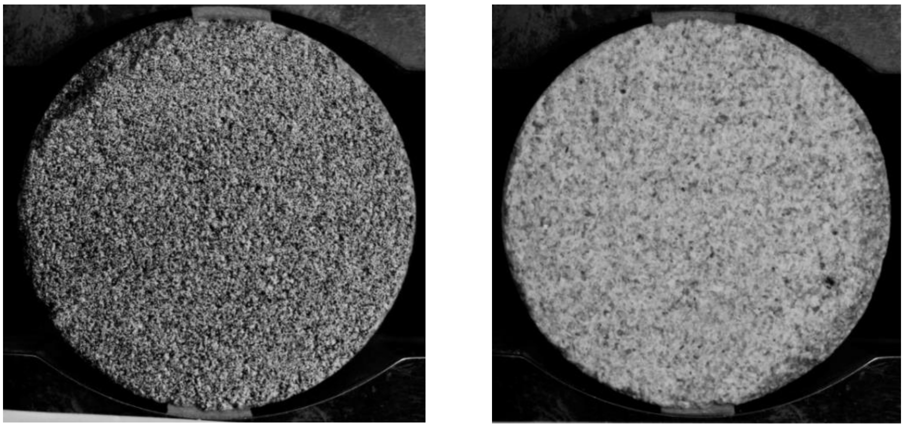

a) b)

Figure 3-71 a) sample 1345, with speckle pattern b) sample 1346 without speckle pattern

All samples considered (1343 to 1348) presents similar results. To illustrate the results obtained with DIC, the analysis obtained for samples 1345 (with the paint treatment) and 1346 (without paint treatment) are presented in Figure 3-72 and Figure 3-73, respectively. It can be observed that comparable results are obtained for both types of samples (with and without the speckle pattern), additionally, similar displacements field results are obtained by Lagneau (2014) with DIC analysis performed on Brazilian test results.

Moreover, the response obtained with this technique agree with the experimental observations: the left side of the sample moves to the left (negative displacements values) while the right side moves to the right (positive displacements value), the division of these two parts of the samples is delimited by the apparition of the crack. In addition, sample 1345 presents more displacements in the upper part of the sample, while, sample 1346 has more displacement in the lower part. In fact, the crack observed in sample 1345 propagates from the top of the sample, while in sample 1346 it propagates from the bottom, this characteristic is also observed in the horizontal strains field.

Even if the strains values obtained from the DIC analysis are quite high, almost 30%, they show a clear evolution of the crack appearance and aperture, even when the fissure can't be visually identified, see photo 3 on Figure 3-72. The strains field results are helpful to identify the appearance of cracks in the sample and to evaluate the aperture and propagation of them, as presented by Morgan (2015).

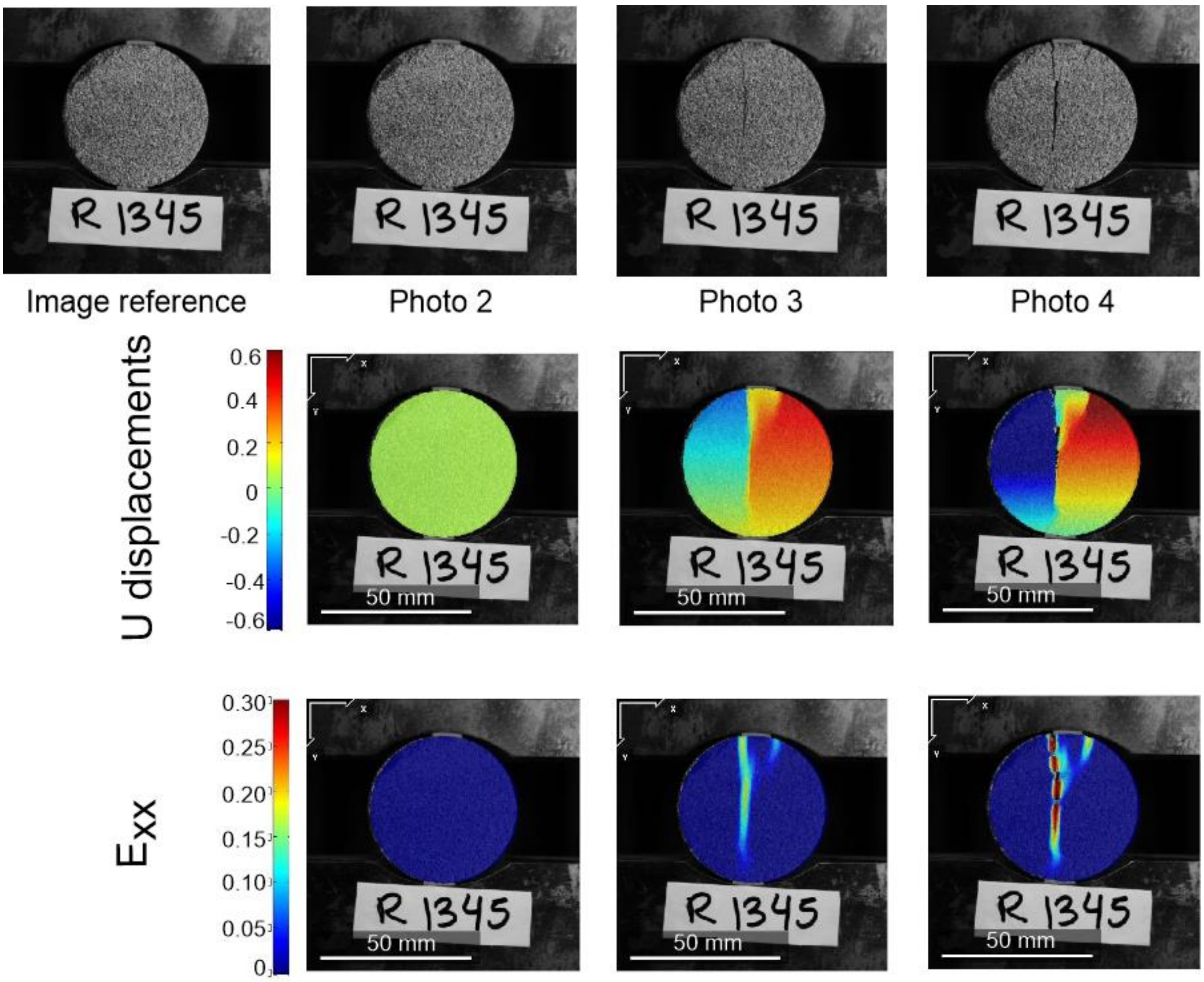

Figure 3-72 Digital image correlation results - sample 1345

The imposition of a speckle pattern in the samples do not necessarily help to have better results in the digital image correlation analysis on samples from LaRG. This can be explained by the fact that this rock is composed by minerals with different colors and sizes (see section 3.3.1), therefore it has already good contrast.

Nevertheless, one face of samples C1, C2 and C3 were painted to have this pattern, because these samples were used to evaluate the generation of fissures associated with thermal cycles that may be thinner than those observed in the Brazilian tests, thus an additional contrast may help in the analysis. In the other hand, samples B20 and C4 were not painted since there were used to evaluate the propagation of fissures and it was observed that the natural contrast of the samples is enough to evaluate the propagation of a crack visually identifiable.

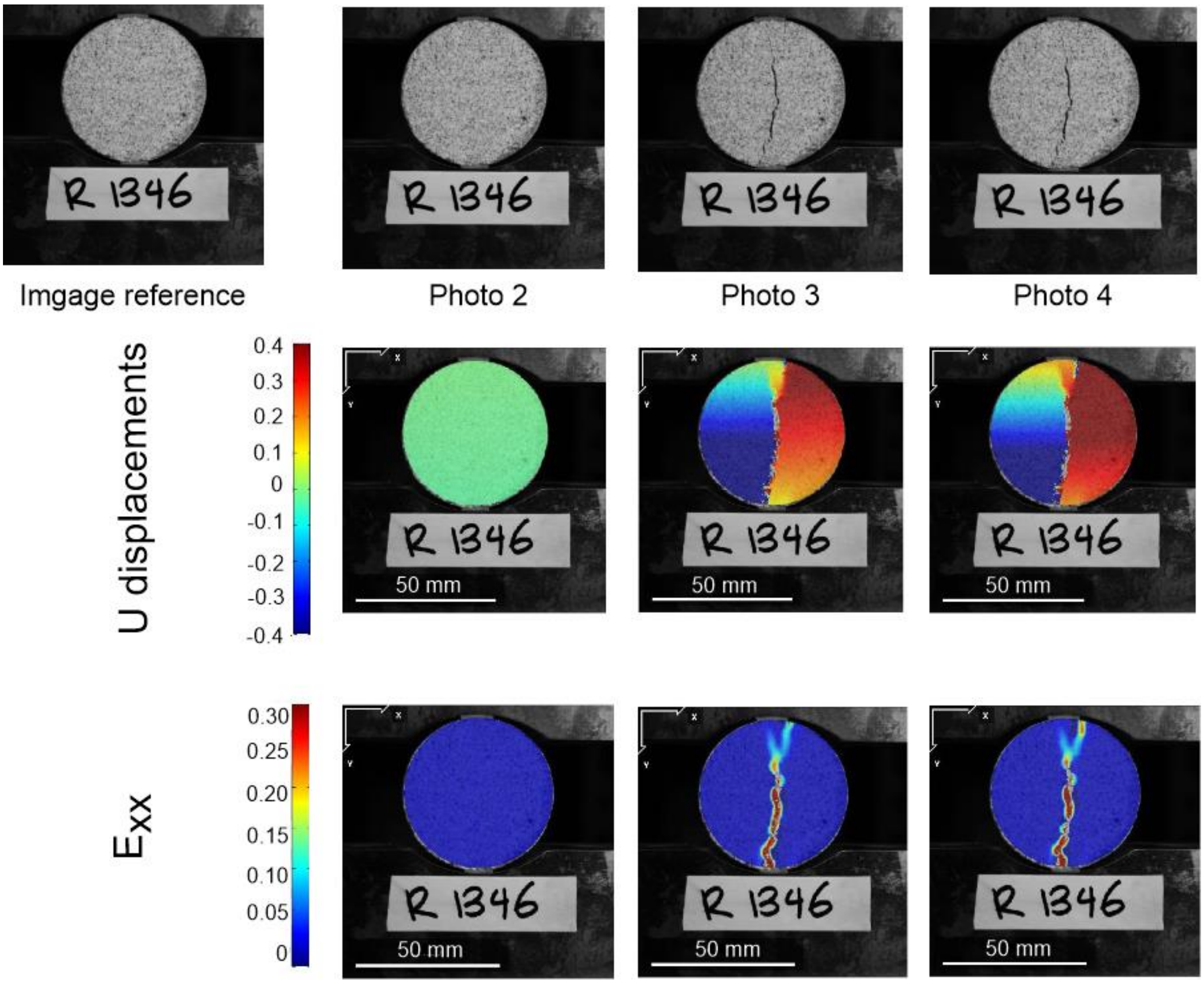

Figure 3-73 Digital image correlation results sample 1346

### 3.6.2. Fissures generation.

To evaluate the appearance of cracks due to thermal cycles, 3 prismatic samples (C1, C2 and C3, see Table 3-7) were photographed at least once a week and evaluated with the DIC technique, as detailed in section 3.4.5. These samples were subjected to 948 cycles of temperature.

Any new fissure was detected on the surface of samples C1, C2 and C3, at least from a visual examination, as was observed on the cylindrical samples (presented before). Nevertheless, DIC analysis was performed to evaluate if any pixel-scale fissures can be observed. Is important to mention that photos considered present a scale of 0.08mm/pixel.

Figure 3-74 and Figure 3-75 present the DIC results obtained for sample C2 for two different faces of the sample, one with a speckle pattern done with black and white paint (Figure 3-74) and the other one under natural conditions (Figure 3-75). Note that no identifiable crack can be observed from these analyses, similar results are observed by Leiss & Weiss (2000) on different types of marbles, subjected to heating until 50ºC.

The strains values observed are very small in comparison with what was observed in Brazilian tests. The small variations observed in the strains fields can be related to slight variations in the illumination imposed to the samples. Those variations may generate that some pixels are darker than others. Nevertheless, it is interesting to observe that sample with the speckle pattern shows less noise associated to changes in light. Note that the strains obtained from the DIC analysis present less dispersion and have a smaller range for the face with the speckle pattern (Figure 3-74) than for the face under natural conditions (Figure 3-75). Similar results are obtained in sample C1 and C3, presented in Appendix B.

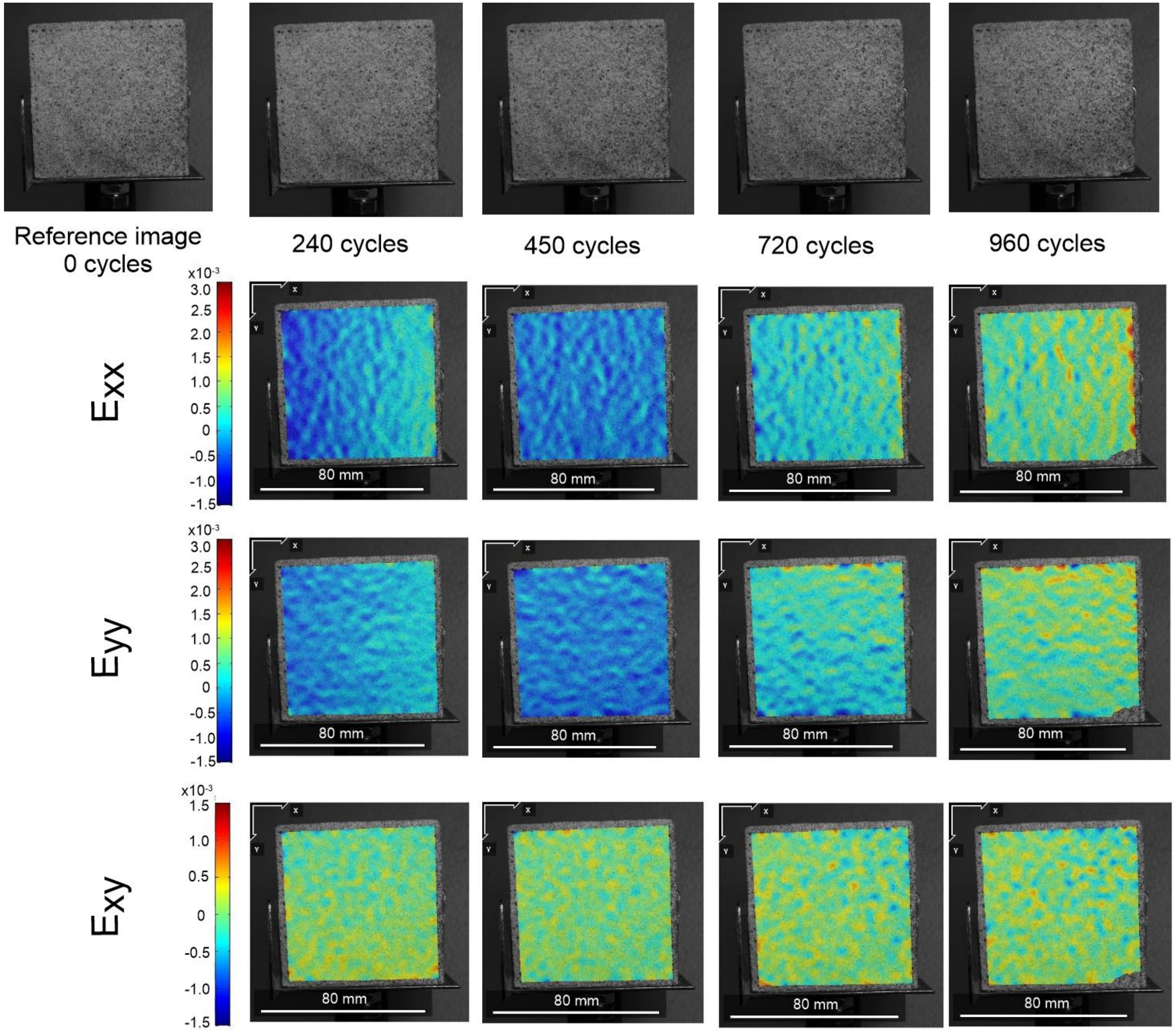

Figure 3-74 DIC analysis for sample C2 – face with speckle pattern

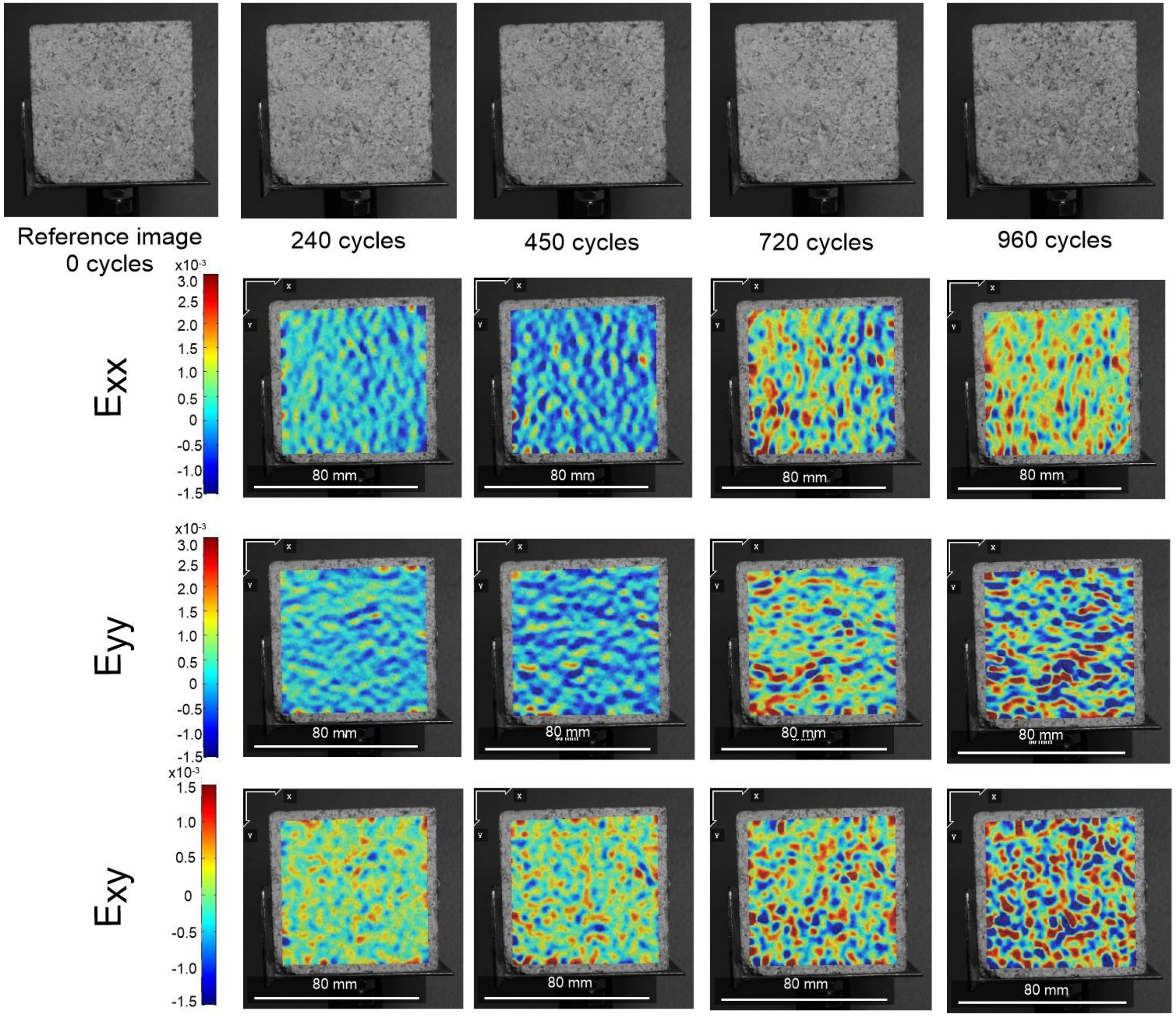

Figure 3-75 DIC analysis for sample C2 – face without speckle pattern

### 3.6.3. Fissures propagation.

Failure of rocks due to thermal damage associated with a process of thermal fatigue generally occurs where a pre-existing weakness is located, such as minerals boundaries, or pre-existing fractures. In fact, when the rock matrix present cracks, the thermal cycles will generate preferable the propagation of these fractures (Hall, 1999; Gómez-Heras, Smith and Fort, 2006; Walsh and Lomov, 2013; Hall and Thorn, 2014).

With the purpose of evaluating the propagation of cracks due to thermal cycling, two types of samples (with an artificial fissure and with a natural one) subjected to thermal treatment are photographed at least once a week. These images are also analyzed with the DIC technique.

#### Artificial fissured sample.

A crack was generated in cylindrical sample B20, thought a hammer impact, the fissure obtained is presented in Figure 3-76. This sample was submitted to a total of 396 cycles between 10ºC to 50ºC. Based only on visual inspection, a clear evolution of the crack can be observed during the test. Figure 3-77 presents the evolution of the crack for three specific moments: 0, 150 and 396 cycles. It can be observed that the thermal cycles induce a propagation of the crack but also a widening of it.

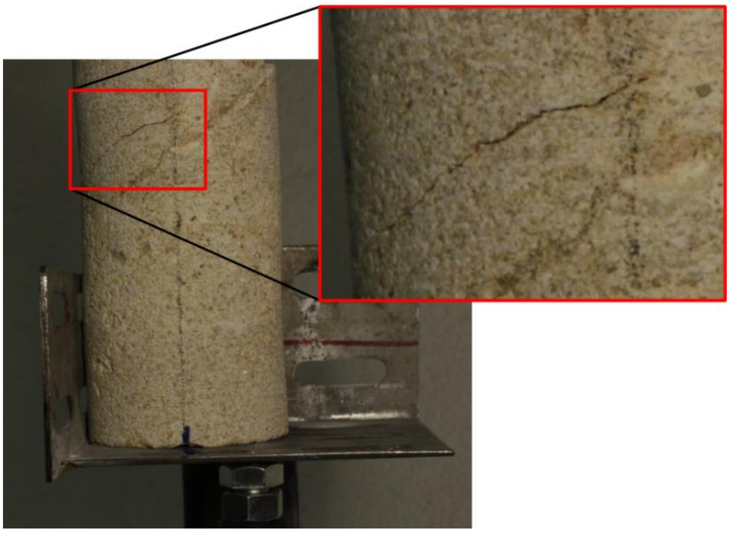

Figure 3-76 Fissure generated on samples B20.

Furthermore, Figure 3-78 presents the results obtained from the DIC analysis performed on samples B20, first it can be observed that the maximal and minimal strains values obtained are higher than those observed in samples C1, C2 and C3, but much lower than the strains obtained for the analysis with the Brazilian test. Moreover, from this analysis it is possible to identify the location and response of the fissure, vertical strains ($E_{yy}$) shows that the crack gets wider with the imposition of cycles of temperature, additionally, horizontal strains ($E_{xx}$) concentrate above and below the tip of the main crack. The results of $E_{yy}$ and $E_{xx}$ suggest that at the tip of the crack the fissure opens. From the combination of the strains, it can be concluded that the main strain presents a direction that is perpendicular to the crack.

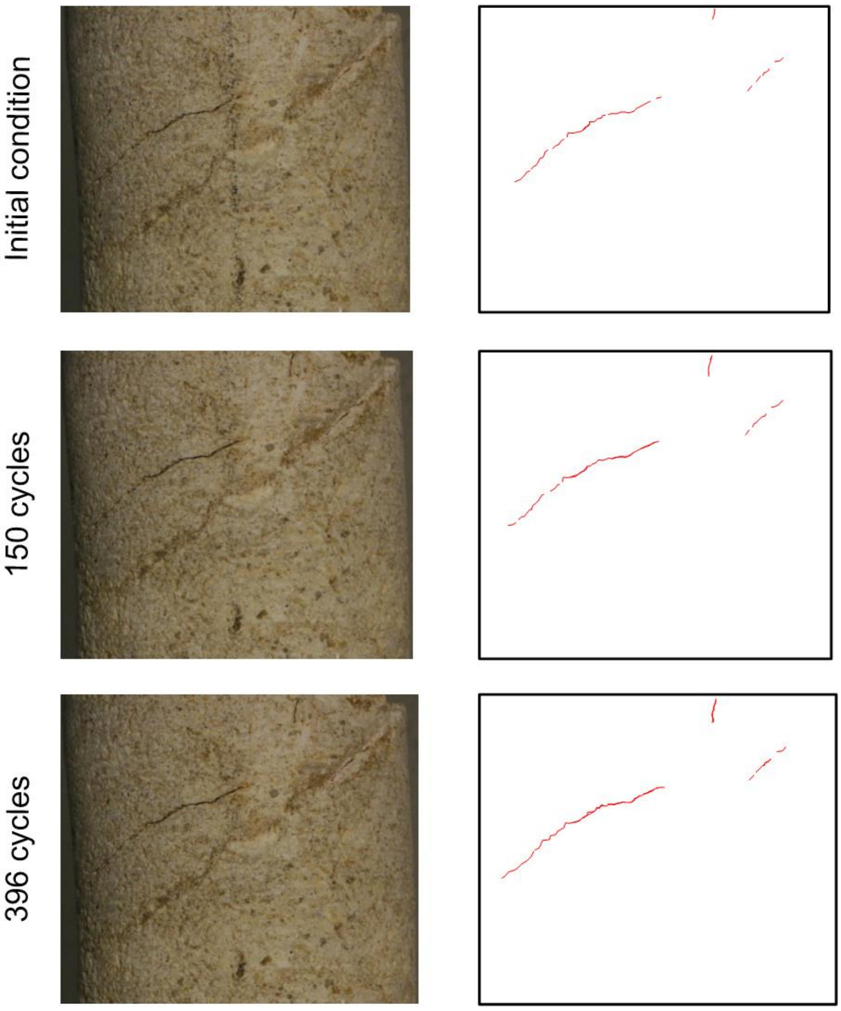

Figure 3-77 Fissure evolution for sample B20

In the same way, shear strains (Exy) also concentrate at the tip of the main crack, showing the shear effect associated with the propagation of the crack. Figure 3-77 shows that between the initial condition and cycle 150 a small fissure located at the top of the sample propagates. In fact, it seems that this fissure could reach the main crack, (Figure 3-76), delimiting a block. These phenomena can also be observed with the DIC analysis (Figure 3-78). Note that from cycle 150 a concentration of strains is observed at this location, delimiting the mentioned block, from vertical and shear field strains from cycle 280 and over.

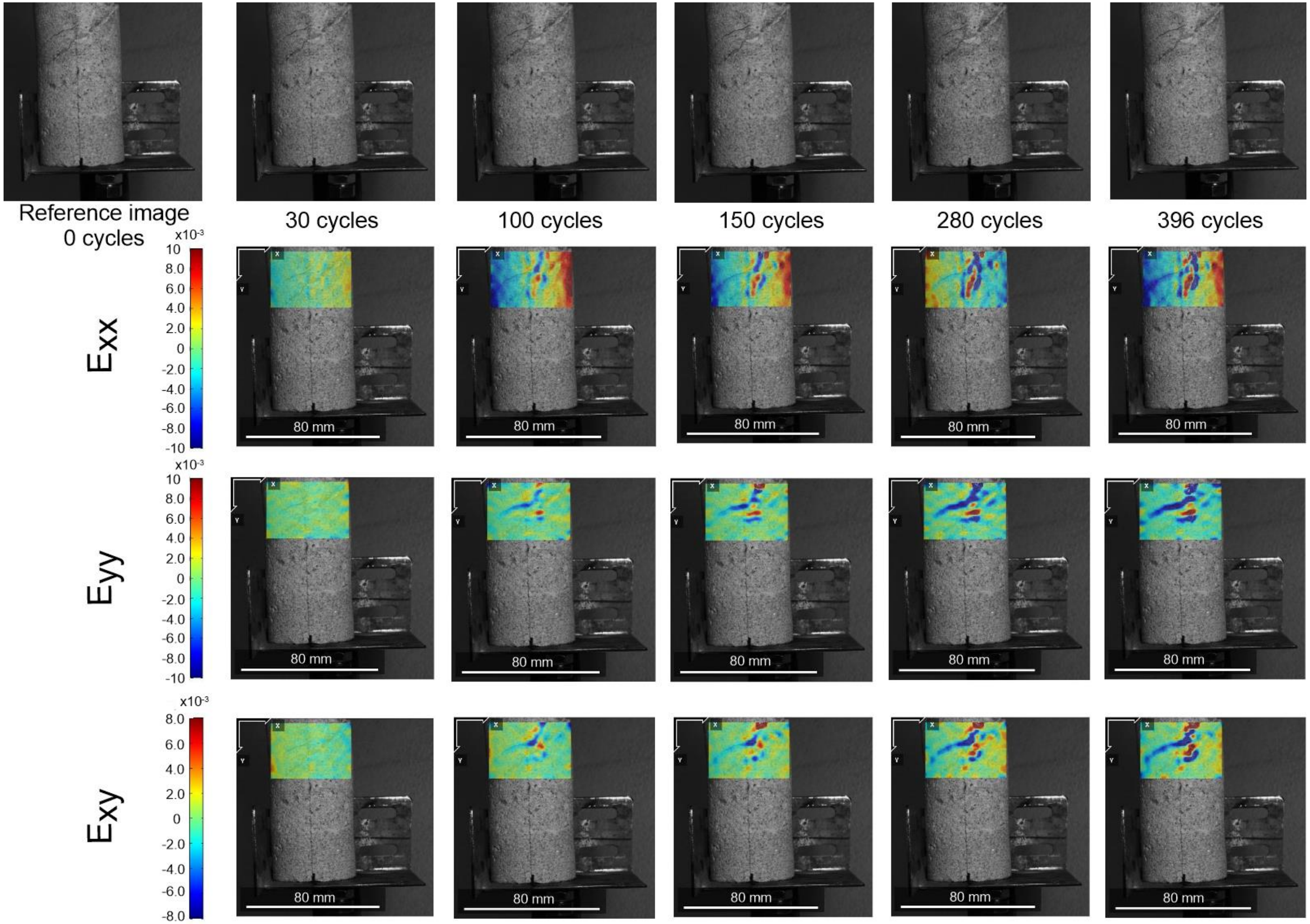

Figure 3-78 DIC analysis for sample B20

### Natural fissured sample.

A small block that has a natural fissure was collected from the troglodyte cavern located in the cliff of La Roque Gageac during a technical visit to the site. This block was prepared to obtained flat surfaces (more favorable for the DIC technique) obtaining a prismatic sample with a crack (samples C4 – characteristics in Table 3-7), see Figure 3-79. This sample was submitted to 1046 thermal cycles, with a rate of 6.5 cycles per day, and photos were taken once a week on two opposite faces of the sample.

Figure 3-79 Sample C4

Unlike the case of sample B20, is not possible to visually identify the propagation of fissures in samples C4, except by the fact that between test day 150 (cycles 972 to 978.5) and 155 (cycles 1004.5 to 1011) a small block was detached from the top of the sample, as is presented in  Figure 3-80.

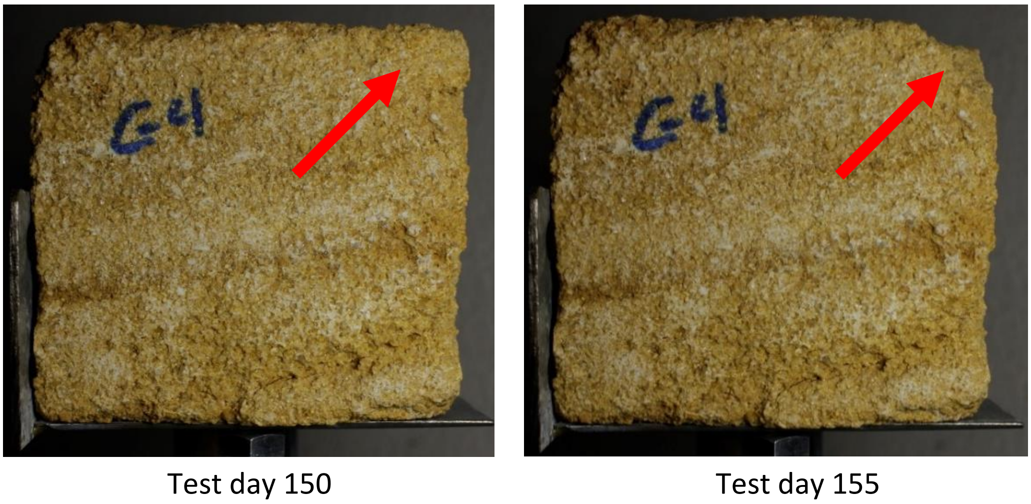

Test day 150 Test day 155

Figure 3-80 sample C4 condition at test day 150 and 155

Even if from visual inspections was not possible to determine the evolution of the cracks observed in sample C4, a DIC analysis was performed over the two faces of the sample. Despite the precautions taken to assure that the sample was placed in the same position, between test day 45 (cycles 290 to 296.5) and 52 (cycles 322 to 328.5), the camera slightly moves, leading that photos taken before and after this days were not comparable. Therefore, the DIC analysis should be performed in two sets: from the begging of the test until test day 45 (Cycle 290) and from test day 52 (cycle 325) until the end. Results obtained from the DIC analysis are presented below.

### *Sample C4 - face 1.*

The evolution of the main crack observed in samples C4 is followed by photos taken of face 1. Results of the DIC analysis are presented in Figure 3-82 for cycles 0 to 290 and Figure 3-83 for cycles 325 to 1047. Note that for cycles 0 to 293 horizontal ($E_{xx}$) strains are concentrated along the fissure. It is interesting to point out that the value of strains is negative, suggesting a closure of the crack associated with the thermal cycles, which is a completely opposite response from what is observed in sample B20 (Figure 3-82). Moreover, shear strains ($E_{xy}$) shows a concentration with positive values along the fissure but mostly in the lower part of the fissure, where the crack is composed by two different paths. From vertical strains ($E_{yy}$) not clear evolution can be observed for the complete fissure, nevertheless, it can be observed that $E_{yy}$ present a higher value at the tip of the crack. This characteristic is also observed in $E_{xx}$ and $E_{xy}$, indicating a propagation of the fissure.

From cycles 325 to 1047, a less evident evolution of the complete crack can be observed. The strains fields obtained here are related to the condition at cycle 325. Nevertheless, it can be observed that all strains fields considered ($E_{xx}$, $E_{yy}$ and $E_{xy}$) show higher strains values where the fissure is composed by two paths, just as observed from cycle 0 to 293.

Furthermore, from this last photo set it can be observed that, from cycle 820, a point of high strains is observed at more or less the middle of the crack length. This strains accumulation is associated to the felt of a grain, as can be observed on Figure 3-81, that focus on this point at cycle 730 and cycle 820. This observation reinforces the idea that thermal damage induces fissures along the grain boundaries.

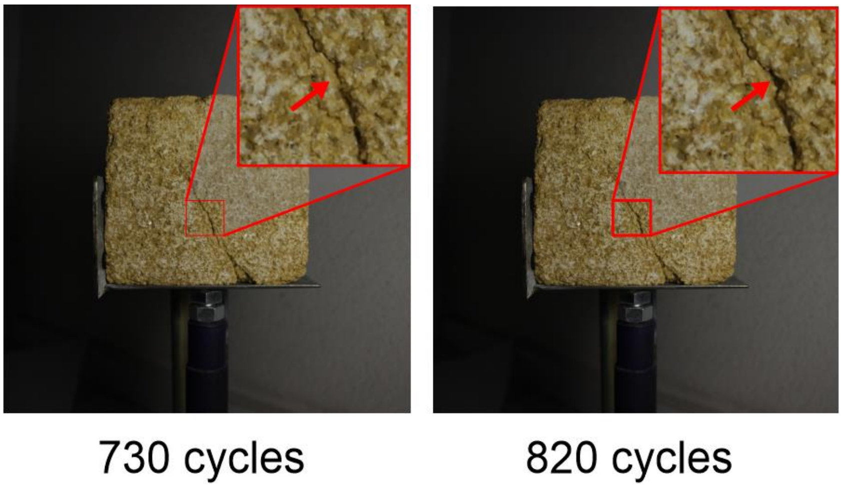

Figure 3-81 Sample C4 condition at 730 and 820 cycles.

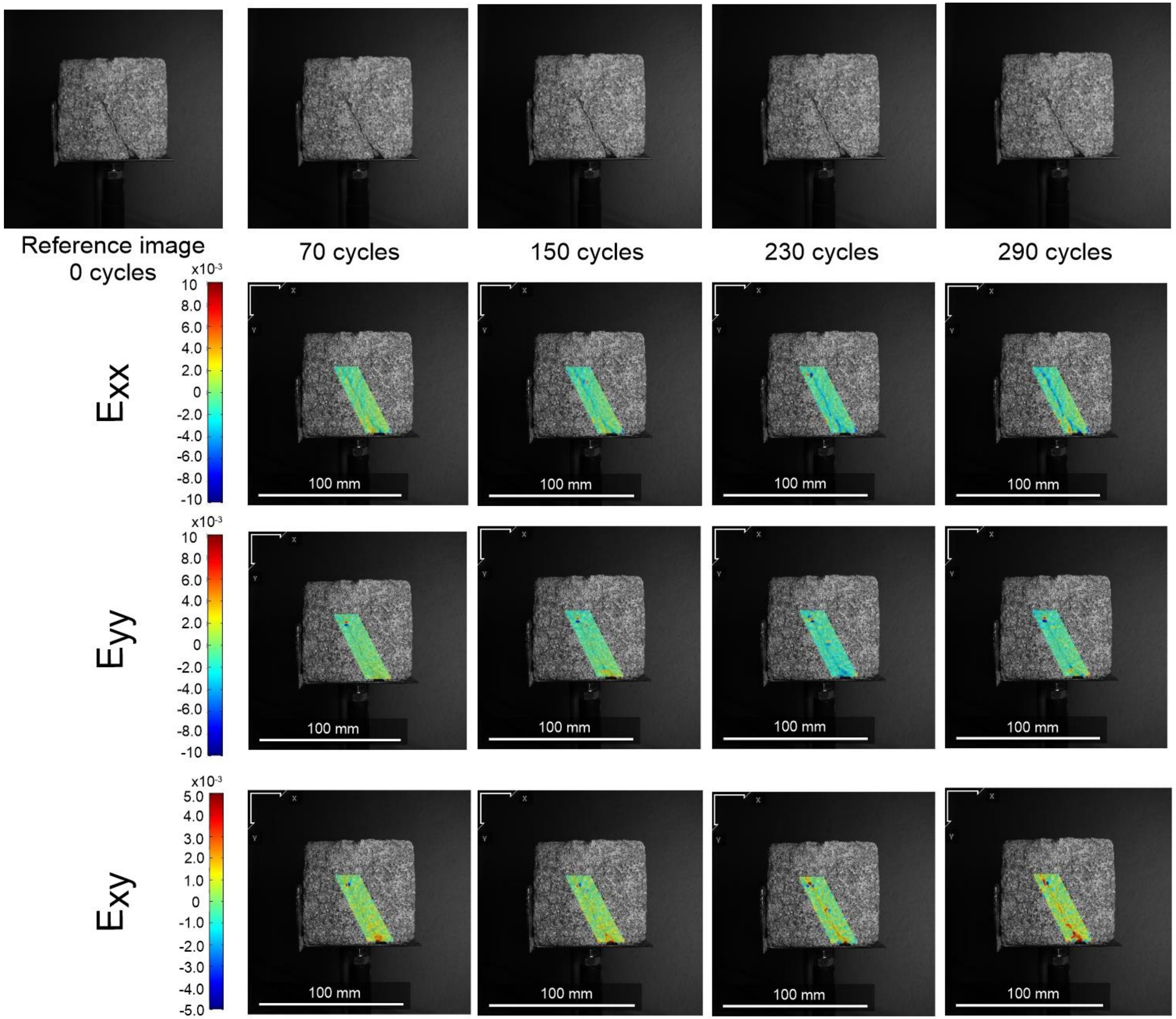

Figure 3-82 DIC analysis for sample C4-face1 from 0 to 293 cycles

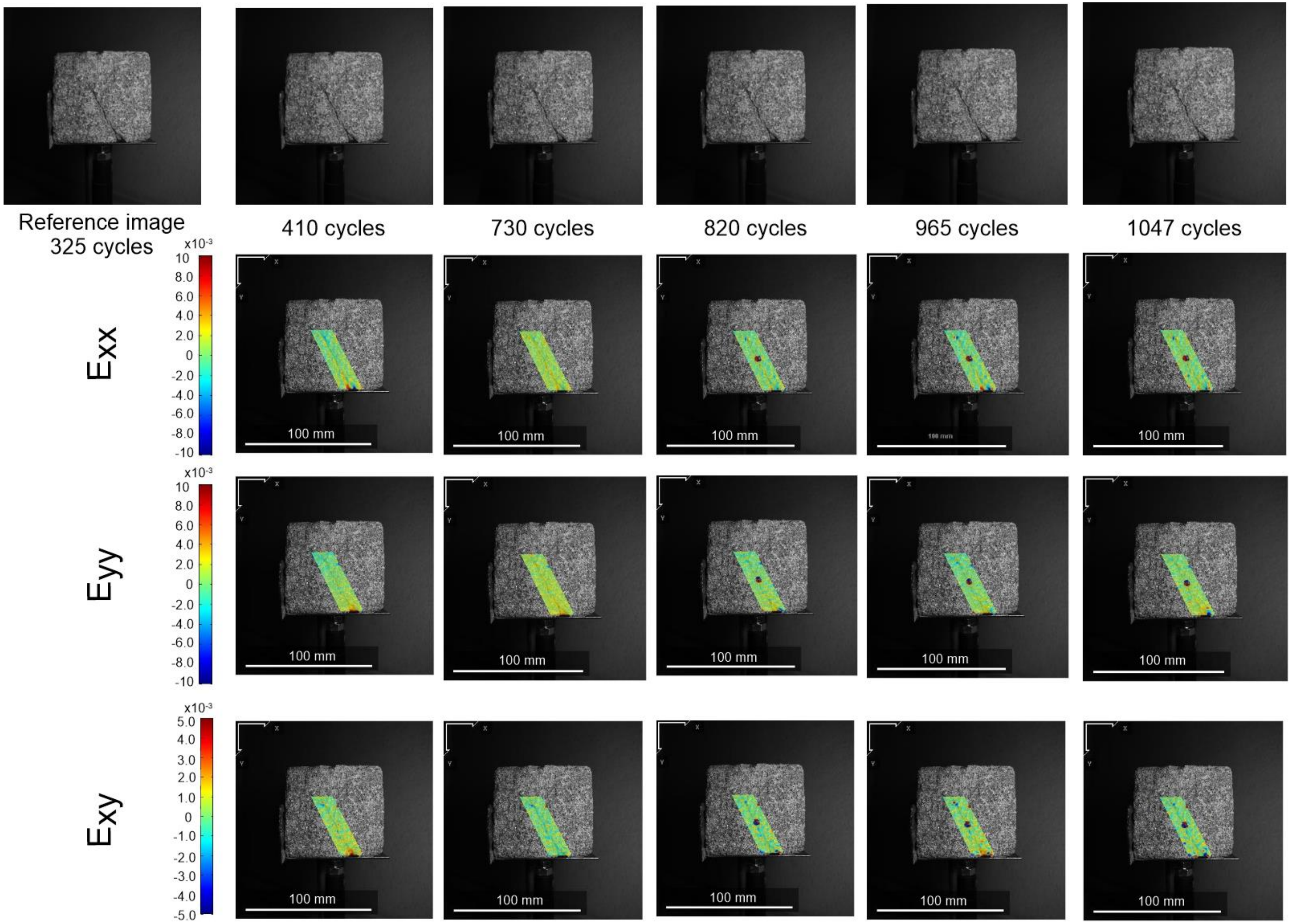

Figure 3-83 DIC analysis for sample C4-face1 from 340 to 1047 cycles

### *Sample C4 - face 2.*

The second face considered in the analysis of sample C4, is the one that presented the detachment of the small block. The DIC analysis was performed in two stages: the first one goes from cycle 0 to cycle 290, and the second one goes from cycle 425 to 975, which is the last moment registered before the complete detachment of the block, the DIC analysis of this last group is related to the sample condition at cycle 325.

Figure 3-84 and Figure 3-85 present the DIC analysis obtained for the two sets of photos, it can be observed that at cycle 975 a high strains concentration that clearly defines the block detached is observed, even before it really fell. Moreover, it is interesting to observe that, even if from visual observations it is not possible to identify a crack in this zone, the results of DIC analysis, see Figure 3-84, show a strains concentration at the block level since cycle 240.

Since Cycle 390 (see Figure 3-85) in addition to the strains that delimit the block a second strains concentration is observed, that may be related to the appearance of a fissure, however, from visual inspections is not possible to identify a crack at this place.

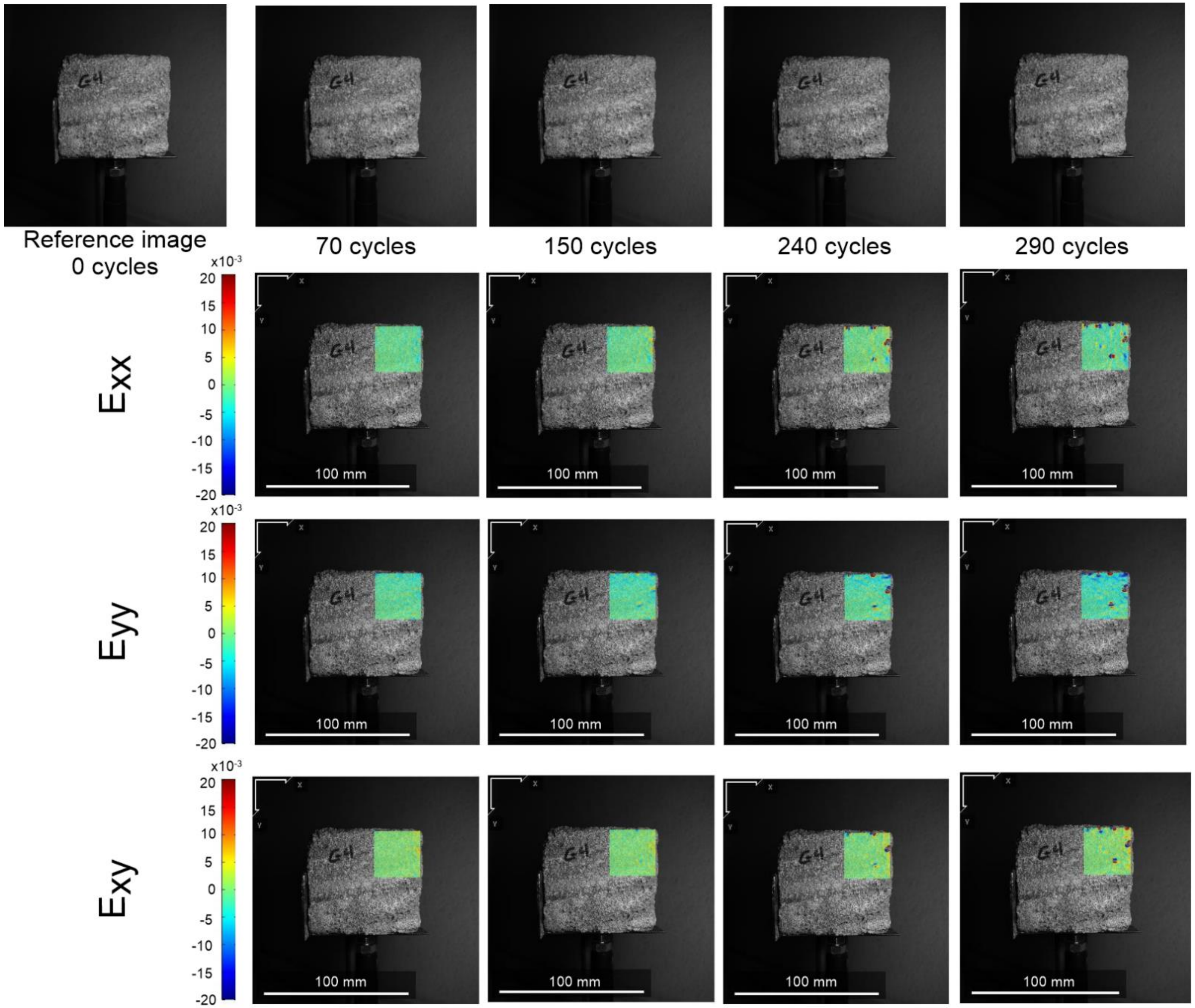

Figure 3-84 DIC analysis for sample C4-face2 from 0 to 290 cycles

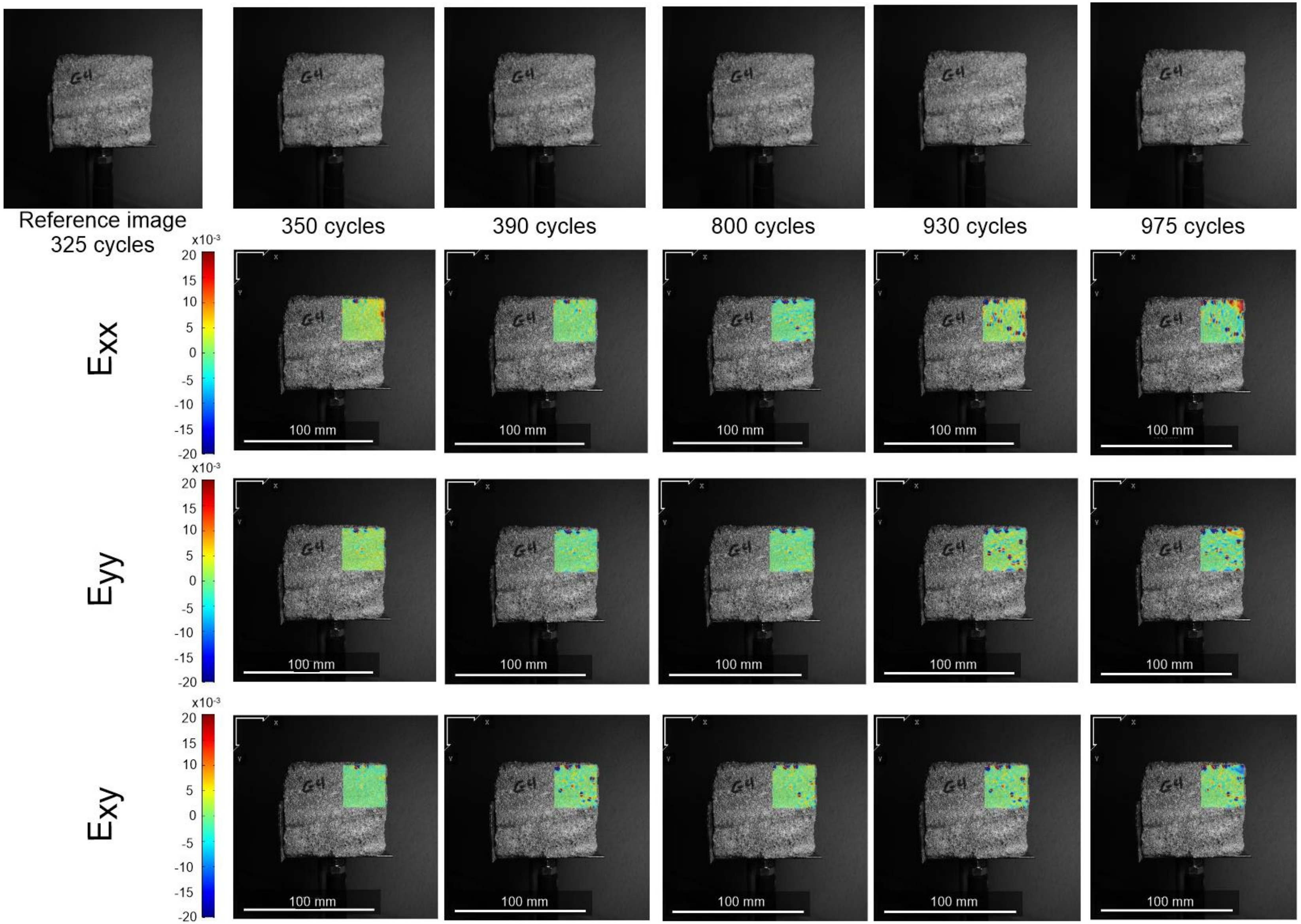

Figure 3-85 DIC analysis for sample C4-face2 from 325 to 975 cycles

## 3.7. Concluding remarks for the experimental program.

An experimental program has been performed to evaluate the possible damage induced by thermal cycles. Samples from La Roque Gageac (LaRG) cliff were submitted to cycles similar to the atmospheric range of temperature, from 10ºC to 50ºC. Their response is evaluated through different laboratory measurements.

The results obtained from this experimental work suggest that atmospheric thermal cycles can induce damage in LaRG limestone, evidenced by strains accumulation, reduction in the elastic wave propagation velocities and strength parameters, and the propagation of fissures.

Some specific observations are summarized below:

- As a consequence of the heterogeneity of the cliff, the composition of the samples is related to the location of extraction. Specimens from blocks felt within the cavern are mainly composed by calcite while samples drilled from the cliff's face by calcite and quartz. Additionally, the average values of porosity are 14% and 21% respectively.
The exposition of the material to the atmospheric conditions can be the reason for the above characteristics, as the calcite can be more easily dissolve by water generating a lower calcite content and higher porosities in the cliffs face.

- Samples obtained from the face of the cliff have an anisotropic thermal expansion. Higher values coincide with the perpendicular direction to the face cliff, which can be related to t the direction where the cliff suffered a decompression during the valley formation geological process

- The thermal expansion remains constant thought the thermal cycles; therefore, the slope and amplitude of the strain-temperature relationship is not affected by the thermal damage (chapter 3.5.1). In the other hand, it is observed that thermal cycles generate small irreversible strains.

- The initial Vp values are also affected by the heterogeneity of the rock. The samples obtained from blocks show higher Vp values than the samples obtained from the face of the cliff. This can be linked to the mineralogical composition and porosity but also to the initial alteration level of the sample due to the exposition of the material to the atmospheric conditions of the cliff. In fact, for samples taken from the same borehole (CH1, CH2 and CH3) the highest Vp value is obtained for the deepest sample (CH3). Moreover, samples CH1 and CH2 shows similar values of Vp, which suggest that the effect of atmospheric conditions affect mostly the first 25 cm of the cliff.

- The evolution of elastic wave propagation velocities through the accumulation of thermal cycles was follow for samples from both locations. All samples present a decrease of this parameter, especially for the P-wave. This response can be explained by the generation and propagation of microcracks (Yavuz, 2011). Samples obtained from blocks that presents higher values of initial Vp, and therefore higher stiffness, shows the lowest decrease of Vp.

- Another evidence that the natural alteration is limited to the first centimeters of the cliff face is that the higher reduction of Vp is found in the deepest sample, indicating that this material was probably more isolated from the atmospheric actions.

- By comparing the Vp values evolution of samples with the same porosity but different mineralogical composition it is found that samples compose by calcite and quartz develop more thermal damage, indicated by a larger Vp decrease.

- One of the main consequences of the thermal damage is the change of the mechanical response of the rock. After 800 cycles, the Uniaxial compressive strength (UCS) and Young`s modulus present a reduction of 10% in comparison with samples with no thermal treatment.

- A potential law can be used to describe the relation between UCS and Vp for samples mainly composed by calcite, indicating a direct relationship between the reduction in Vp (thermal damage) and the weakening of the rock (reduction in UCS).

- The Digital Image Correlation (DIC) technique has shown to be a helpful tool to evaluate the generation and propagation of cracks.

- Thermal cycles at atmospheric range are not able to generate new cracks in LaRG limestone. Results of DIC analysis on prismatic samples without fissures (C1, C2 and C3) do not shows any new crack. In the same way, it is not possible to determine any fissure in the 30 cylindrical samples tested, from visual inspections. Nevertheless, the results obtained in the mechanical response of the rock suggest the generation or propagation of existent micro-fissures.

- DIC analysis on naturally and artificially fissured samples indicate that thermal cycles induce the propagation of existent defects, like cracks, especially when they have no suffer formerly any thermal cycle (artificial crack). Note that the evolution of the artificial crack was observed even from visual inspections, whereas the main natural crack evolves very little. Moreover, from sample C4 it can be observed that thermal cycles induce the detachment of crystals across their boundaries which are weakness zones

- The prismatic sample with a natural crack present the detachment of a small block after 970 cycles, even if any fissure was observed at the beginning of the test program at this level. Based on the results obtained on the other prismatic samples, it can be assumed that when this sample was collected from the site, a local defect existed at this corner and the thermal cycles generated the propagation of it until the detachment of the small block.

# 4. Numerical modeling

## 4.1 Introduction.

The experimental results presented in chapter 3 have evidenced that 'La Roque Gageac' limestone is susceptible to experienced mechanical damage under thermal cycles whose amplitudes are in the range of daily atmospheric variations. This chapter is devoted to the presentation of a numerical model able to reproduce this phenomenon.

From a general point of view, rocks are composed of several minerals with different mechanical and thermal properties. These local heterogeneities result in the development of differential grain expansion during heating, which, in turn, is the source for the build-up of internal stresses. The same effect can develop in single mineral material as a result of heterogeneity in grain or crystal shape and orientation (Le Per and Oter-Duthoit, 1987; Wanne and Young, 2008; Hall and Thorn, 2014).

Internal thermal induced stresses may lead to local material weakening, fissuration or micro-cracking. As a matter of fact, Figure 4-1 presents photomicrographs obtained by Malaga-Starzec et al. (2006) on a sample of marble before and after application of atmospheric temperature cycles. This marble is predominantly composed of calcite (>99%). After 50 thermal cycles, the material experiences an important augmentation of porosity as the result of void development around grains boundary.

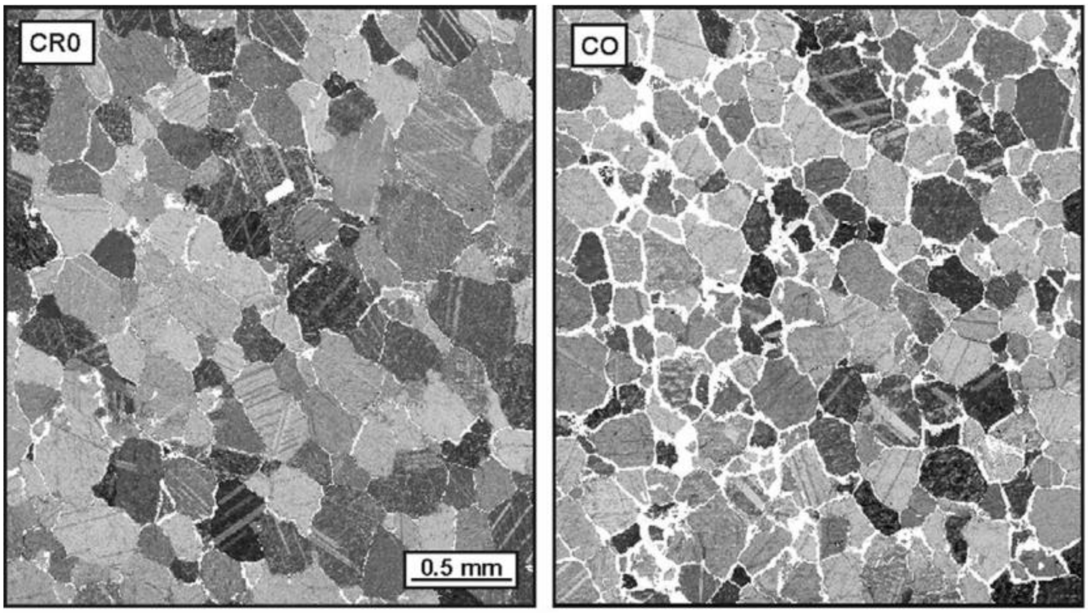

Figure 4-1 Photomicrographs of calcite samples, CR0: Uncycled sample CO: Temperature cycled (Malaga-Starzec et al., 2006)

In the same perspective, Royer-Carfagni (1999) found, from microstructural analyses, that thermally induced stresses are often concentrated at grain interfaces and not inside the grains, leading primarily to grain decohesion rather than grain fracturation. Other authors (Wong, Chau and Wang, 1996; Zimmermann, Carter and Fuller, 2001) have pointed out the grain size distribution of the rock is an important controlling factor in microcracks generation and propagation. On the other hand, several authors (Bodin et al., 2004; Wanne and Young, 2008; Malésys, Vincent and Hild, 2009; Dubois et al., 2012; Lu, Elsworth and Wang, 2013; Walsh and Lomov, 2013) emphasize the time-dependency of fissure propagation.

Rocks microcracking can be represented by a progressive damage of the rock that may affect significantly its macroscopic mechanical properties (Mazars and Pijaudier-Cabot, 1996; Lu, Elsworth and Wang, 2013). As a result, after some time, microcracks may coalesce and eventually culminate in the development of a failure surface across the rock sample, leading to failure (Hall 2004b; Hall 1999; Tiskatine et al. 2016).

The modeling of such process may be indistinctively tackled within the continuum, discrete or hybrid frameworks available in Rock Mechanics. The choice of the method depends mainly on the characteristics of the problem under study (Jing and Hudson, 2002), and, particularly, on the scale focused on the analysis.

As far as concerns thermal damage, two types of approaches are generally considered. The first one focuses on the modeling at the microscale and represents explicitly the grain responses within idealized microstructural patterns (Lu, Elsworth and Wang, 2013). These models are generally developed using the distinct element method and represent the rock as an assembly of particles tight by separable joints. When the model is feed with experimental microscopic data on material heterogeneity and mineralogical arrangement, results have proven to compare well with laboratory observations. They generally show that fissures are develop mostly at grains contacts (Royer-Carfagni, 1999; Zimmermann, Carter and Fuller, 2001; Wanne and Young, 2008; Shushakova, Fuller and Siegesmund, 2013; Walsh and Lomov, 2013; Hoek and Martin, 2014).

On the other hand, the problem can be considered at macroscale by idealizing the rock as a continuum provided with degradation laws for its mechanical properties. These laws aim at representing the macroscopic effect of grain decohesion, fissuration and, more generally, all types of microstructure degradation (Lu, Elsworth and Wang, 2013). This approach has been widely used for the modeling of microcracking phenomena in quasi-brittle materials, like rocks (Mazars and Pijaudier-Cabot, 1996; Shao and Rudnicki, 2000; Lu, Elsworth and Wang, 2013; Chang et al., 2014) or concrete (Mazars and Pijaudier-Cabot, 1989; Jirásek, 1998; Bodin et al., 2004; Dubois et al., 2012; Rojas-Solano, Grégoire and Pijaudier-Cabot, 2013). These materials share common characteristics like heterogeneity due to the presence of different components and reduction in stiffness and strength due to microcracks development. Damage theory is the main tool used for this type of analysis. It consists in considering an irreversible degradation of stiffness parameters according to the evolution of the density of microcracks. The variable controlling damage evolution varies from one formulation to another, and can be driven by the strain rate (Bodin et al., 2004), the strain (Mazars and Pijaudier-Cabot, 1989; Lu, Elsworth and Wang, 2013), the stored energy (Carol, Rizzi and Willam, 2001; Chang et al., 2014) or microcrack propagation characteristic (Shao and Rudnicki, 2000).

Use of discrete and continuum frameworks are not necessarily opposite strategies and they are often and often combined in multiscale modelling. There exist for instance proposals to derive damage model from homogenization techniques applied to Fractures Mechanics operated at the scale of the propagation of one fissure in the material (Pensée, Kondo and Dormieux, 2002; Xie *et al.*, 2012). On the other hand, damage model provided with softening laws will result in the development of shear bands in the material. In computational Mechanics, this bands are considered as “weak discontinuities”, which are strain localization bands delimitated by two surfaces where a jump in deformation occurs. During further loading, the weak discontinuity could end in a “strong discontinuity”, which is a non-volume surface where a jump in displacement exists (Mazars and Pijaudier-Cabot, 1996). Existence of weak and strong discontinuities lead to ill-posed problems from the computational point of view and a large variety of techniques have been proposed to regularize this problem. Between them, the strong discontinuity approach allows to relate the displacement-forces law prevailing inside a fracture to the constitutive law of the bulk material by projecting it in the direction of the fracture. This type of strategy close in some way the loop “Fracture Mechanics- constitutive law-Softening and localization-Strong discontinuity-Fracture Mechanics” and highlight the coupling existing between discontinuous and continuous frameworks.

In this work on thermal damage, it has been chosen to develop a continuum model able to handle numerically boundary values problems in an efficient way. Moreover, the absence of microstructural analysis of damage makes difficult the development any model at lower scale. It is expected that the continuum model developed in this way will further able to model propagation of shear bands and fractures, once implemented in a code provided with regularization techniques to capture localization.

## 4.2 Constitutive model

The constitutive model has been developed with two main objectives:

1) To account in a simple way the phenomenon of bulk rock damage due to the thermal expansion experienced by the minerals that composed the rock. A change in temperature imposes in fact to each mineral grain a change in volume whose value depends on its thermal expansion and orientation. The change in volume will thus vary from grain to grain and internal forces will be generated at grains interfaces to accommodate the local deformations. If high enough, these forces may cause interface decohesion, leading to rock fissuring and damage.
2) To provide a constitutive law able to be used in Finite Element computations of real problems, which generally requires modelling long periods of atmospheric actions, two- or three-dimensional geometrical details and material heterogeneity. In the present state of commonly available computational resources, multiscale modelling is essentially applicable to problems of reduced size, as, for instance, laboratory tests or two-dimensional simple plane strain configurations. Macroscopic constitutive laws are a suitable alternative to limit calculation time in case of larger problems.

Under these constraints, a macroscopic constitutive law based on the behavior of a two-mineral rock skeleton has been developed. This section describes the conceptual bases and the equations of the model.

### 4.2.1 Conceptual bases

Figure 4-2 presents a schema of the Representative Elementary Volume (REV) of the material considered to model the rock. It is a porous composite material whose skeleton is composed by two minerals (components), namely Mineral 1 (provided with the superscript m and Mineral 2 (superscript b). Each mineral k is provided with its own volume ($V_k$), strain ($\varepsilon_{ij}^{k}$) and stress ($\sigma_{ij}^{k}$) components. $V_V$ denotes the volume of pores, $V_s = V_m + V_b$ the volume of the solid phase and $V = V_V + V_s = V_V + V_m + V_b$ the total volume of the composite material. $e = V_V/V_s$ is the void ratio of the material.

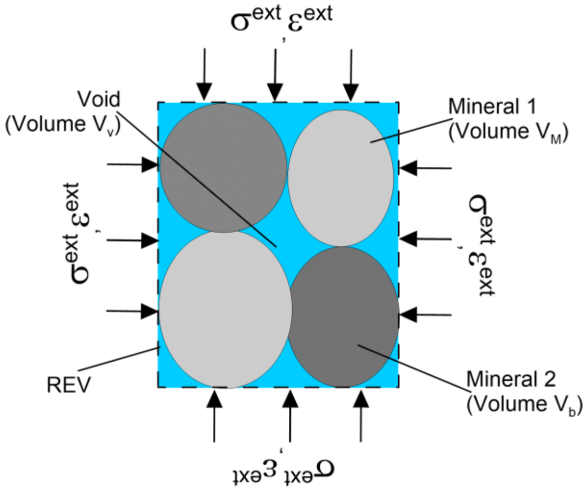

Figure 4-2 Conceptual scheme for the composite material constitutive model

According to these notations, different volumetric strains can be defined. The change in pore volume is given by the so-called internal volumetric strain $d\varepsilon_v^{int}$:

$$\mathrm{d}\varepsilon_v^{int} = -\frac{\mathrm{d}V_V}{V} = -\frac{\mathrm{d}e}{1+e} \qquad \text{Eq. 4-1}$$

The change in volume of mineral 1 is given by the volumetric $d\varepsilon_v^{m}$:

$$\mathrm{d}\varepsilon_v^{m} = -\frac{\mathrm{d}V_m}{V_m} \qquad \text{Eq. 4-2}$$

While the change in volume of mineral 2 is given by the volumetric strain $d\varepsilon_v^{b}$:

$$\mathrm{d}\varepsilon_v^{b} = -\frac{\mathrm{d}V_b}{V_b} \qquad \text{Eq. 4-3}$$

Finally, the change in volume of the REV is given by the volumetric strain of the composite material:

$$\mathrm{d}\varepsilon_v^{ext} = -\frac{\mathrm{d}V}{V} \qquad \text{Eq. 4-4}$$

The volumetric strains defined in this way are related by the restriction prevailing on volumes:

$$\mathrm{d}V = \mathrm{d}V_V + \mathrm{d}V_m + \mathrm{d}V_b \rightarrow \mathrm{d}\varepsilon_v^{ext} = \mathrm{d}\varepsilon_v^{int} + C_m\mathrm{d}\varepsilon_v^{m} + C_b\mathrm{d}\varepsilon_v^{b} \qquad \text{Eq. 4-5}$$

Where $C_m = V_m/V$ and $C_m = V_b/V$ are the respective concentrations of each mineral in the rock. $C_m\mathrm{d}\varepsilon_v^{m}$ and $C_b\mathrm{d}\varepsilon_v^{b}$ are the apparent volumetric strains of each mineral phase (change in volume of the phase divided by the volume of the porous medium). Eq. 4-5 is further extended to all strain components:

$$\mathrm{d}\varepsilon_{ij}^{ext} = \mathrm{d}\varepsilon_v^{int}\delta_{ij} + C_m\mathrm{d}\varepsilon_{ij}^{m} + C_b\mathrm{d}\varepsilon_{ij}^{b} \qquad \text{Eq. 4-6}$$

The main idea of the model is to associate a thermo-mechanical response to each mineral and to further use the restriction provided by Eq. 4-5 to make compatible the external strain with the internal ones. As there are three internal strains, it is necessary to introduce two additional kinematical restrictions between them to close the system. They are be expressed by two functional relationships relating the apparent deformation of each phase to the change in pore volume:

$$X_{ij}^{b} = \frac{c_b\mathrm{d}\varepsilon_{ij}^{b}}{\mathrm{d}\varepsilon_v^{int}} \qquad \text{Eq. 4-7}$$

$$X_{ij}^{m} = \frac{c_m\mathrm{d}\varepsilon_{ij}^{m}}{\mathrm{d}\varepsilon_v^{int}} \qquad \text{Eq. 4-8}$$

$X_{ij}^{b}$ and $X_{ij}^{m}$ are tensor functions describing the internal redistribution of strains within the material and depends therefore on microstructural factors.

According to this scheme, thermal loading will cause a change in volume of the mineral phases, which are not necessarily compatible with the external strain applied to the medium.

Mechanical strains will then develop inside each phase to adapt the change in volume, which will in turn change the stresses in the mineral phases, leading to possible material degradation even in absence of external loads.

As shown in Figure 4-1, most of thermal induced damage often traduces into decohesion of the interface between the two mineral phases and apparition of fissures. Within the two-mineral phase scheme contemplated in this work, interface are not explicitly represented and the degradation mechanism must be assigned to one of the phase. Since both mineral phases play a symmetric role in Eq. 4-5, it can indistinctively allocated to phase 1 or 2. By convention, phase 2 has been chosen to carry the interface response. Henceforward, phases 1 and 2 play an asymmetric role. To distinguish them, mineral phase 1 is denoted “matrix” and mineral phase 2 “bonds”.

Mineralogical composition analysis performed on samples from La Roque Gageac (see section 3.3.1) shows that this limestone is mainly composed by calcite and quartz. For the numerical modeling performed in this work, it is considered that calcite will be represented by the phase 2 (bonds) and quartz by the phase 1 (matrix). In other words, the degradation mechanism related to the mineral boundaries has been chosen to be assigned to the calcite.

Model is finally defined by assigning a stress-strain-temperature constitutive law to each material and setting the equation to compute the external stresses from the stresses in each mineral. These two final steps are described hereinafter.

### 4.2.2 Constitutive law for mineral phase 1 (matrix)

The mineral phase 1 corresponds to the mineral component that does not include the effect of interface degradation. It is thus provided with a non-degrading elastic law. In the work considered in this thesis, a linear cross-anisotropic thermo-elastic law is considered. It is characterized by the Young modulus and the Poisson’s ratio in the isotropic plane, the Young modulus in the orthogonal direction, the cross Poisson’s ratio and shear modulus, and two thermal expansion coefficients (one in the isotropic plane and one in the orthogonal direction). The equation for the elastic law results into:

$$\mathrm{d}\sigma_{\mathrm{ij}}^{\mathrm{m}} = \mathrm{D}_{\mathrm{ijkl}}^{\mathrm{em}}\, \mathrm{d}\varepsilon_{\mathrm{kl}}^{\mathrm{m}} \qquad \text{Eq. 4-9}$$

Where $\sigma_{\mathrm{ij}}^{\mathrm{m}}$ and $\varepsilon_{\mathrm{kl}}^{\mathrm{m}}$ are the stress and strain tensor of the matrix and $\mathrm{D}_{\mathrm{ijkl}}^{\mathrm{em}}$ is the cross-anisotropic elastic tensor.

In order to model the possibility of shear failure for the composite material, a shear failure criterion has been added to this mineral phase. It includes two typical criteria for rock: Mohr-Coulomb and Hoek & Brown with associated or no-associated flow rule and several types of thermo-mechanical hardening/softening laws. In the present work, the Mohr-Coulomb yield criterion (see Eq. 4-10) has been considered.

$$F = \left(\cos\theta^m + \frac{1}{\sqrt{3}}\sin\theta^m \sin\phi'^m\right)J^m - \sin\phi'^m\left(P^m + P_t^m\right) \geq 0 \qquad \text{Eq. 4-10}$$

where:

$P_t^m = c'^m \cot\phi'^m$ is the tensile strength, $c'^m$ the cohesion, $\phi'^m$ friction angle, $P^m$ is the mean stress, $J^m$ the second invariant of deviatoric stress tensor and $\theta^m$ the Lode angle for the matrix.

The numerical simulations of laboratory tests have however shown that the yield criterion has never been reached for the applied thermal load and considered shear resistance parameters. Mineral 1 phase will thus remain in the elastic regime for all the computations.

### 4.2.3 Constitutive law for material 2 (bonds)

Mineral phase 2 (bonds) is the material that carries the effect of the degrading interface between the two phases. As degradation is essentially due to micro-cracks and fissure opening at grain contact, the damage theory provides a suitable macroscopic framework to describe it.

For the sake of the present analysis, the scalar damage proposed by Carol et al. (2001) and enhanced with temperature dependency is considered. This model has been chosen because of its simplicity and conceptual base on thermodynamic principles that prevent any spurious energy dissipation during load cycles.

According to damage theory, bond response is elastic, but the moduli progressively decrease during loading as micro-cracks develop inside the material. This phenomenon is modeled by distinguishing:

a) Strains and stresses acting over the whole bond area labeled $\sigma_{ij}^b$ and $\varepsilon_{ij}^b$. There are apparent quantities acting externally on the bonds.
b) Strains and stresses acting over the unfissured bond area, labeled $\hat{\sigma}_{ij}^b$ and $\hat{\varepsilon}_{ij}^b$. They are effective quantities, acting internally in the bonds.

The relation between these quantities is defined through the parameter D, equal to the ratio of fissured bond area and the whole bond area. Cordebois & Sidoroff (1982) proposed to use a relation based on the equivalence of the energies computed externally $\left(\frac{\sigma_{ij}^b \varepsilon_{ij}^b}{2}\right)$ and internally $\left(\frac{\hat{\sigma}_{ij}^b \hat{\varepsilon}_{ij}^b}{2}\right)$. This condition imposes the following relation between the apparent and effective stress and strain:

$$\hat{\sigma}_{ij}^b = \frac{1}{\sqrt{1-D}}\sigma_{ij}^b \qquad \hat{\varepsilon}_{ij}^b = \sqrt{1-D}\,\varepsilon_{ij}^b \qquad \text{Eq. 4-11}$$

As mention before, the damage theory considers that the response of the material is linear elastic, therefore the intact (unfissured) part of the material follows the law:

$$\hat{\sigma}_{ij}^{b} = D_{ijkl}^{eb0}\,\hat{\varepsilon}_{kl}^{b} \qquad \text{Eq. 4-12}$$

Where $D_{ijkl}^{eb0}$ is the stiffness tensor for the undamaged material, which is considered constant in this formulation. From equations 4-11 and 4-12, it can be obtained the relation between apparent bond stresses and apparent bond strains, defined by the equation 4-13.

$$\hat{\sigma}_{ij}^{b} = D_{ijkl}^{eb}\,\hat{\varepsilon}_{kl}^{b} \qquad \text{Eq. 4-13}$$

Where:

$$D_{ijkl}^{eb} = (1-D)D_{ijkl}^{eb0} \qquad \text{Eq. 4-14}$$

$D_{ijkl}^{eb}$ is the stiffness tensor of damaged material, whose coefficients decrease as micro-fissuration increases.

Carol et al. (2001) proposed to use an alternative damage variable L defined by Eq. 4-15:

$$L = \ln\left(\frac{1}{1-D}\right) \qquad \text{Eq. 4-15}$$

The damage variable L has a null value for the undamaged state and infinitive value when the material is fully damaged. By considering equation 4-15, equations 4-11 and 4-12, can be rewritten as:

$$\hat{\varepsilon}_{ij}^{b} = e^{-L/2}\,\varepsilon_{ij}^{b} \qquad \text{Eq. 4-16}$$

$$\hat{\sigma}_{ij}^{b} = e^{L/2}\,\sigma_{ij}^{b} \qquad \text{Eq. 4-17}$$

$$D_{ijkl}^{eb} = e^{-L}D_{ijkl}^{eb0} \qquad \text{Eq. 4-18}$$

From equation 4-18, L can be simply related to the degradation of bond Young modulus by:

$$L = \ln\left(\frac{E_0}{E}\right) \qquad \text{Eq. 4-19}$$

where $E_0$ and E are the undamaged and damaged bond Young's modulus, respectively.

Additionally, Carol et al. (2001) introduce a loading function (F) to define an elastic domain in the stress space $F(\sigma^{b},\varepsilon^{b})$ in which the stiffness remains undamaged, defined in terms of the elastic (secant) energy. Once the loading surface is reached (F=0), the onset of degradation takes place. In the case of the isotropic damage, the loading function F is defined as:

$$F = u - r(L) = \frac{1}{2}\sigma_{ij}^{b}\varepsilon_{ij}^{b} - r(L) \qquad \text{Eq. 4-20}$$

where u is the bond current (secant) elastic energy and r(L) is the energy damage locus defined as an energy threshold. r evolves generally with the intensity of damage L. Three different laws have been implemented for this evolution:

Linear: $r = r_0 + r_1 L$ Eq. 4-21

Exponential: $r = r_0 e^{r_1 L}$ Eq. 4-22

Logarithmical: $r = r_0 + r_1 \ln(L)$ Eq. 4-23 where, $r_0$ and $r_1$ are model parameters and indicate the initial damage locus and the damage rate, respectively.

A rate dependency is introduced following the theory of Perzyna (1966) proposed for elastoplastic models. In this theory, the plastic multiplier is expressed as a function of the distance between the current stress point and the inviscid plastic locus. This concept can be extended to damage theory by considering that damage multiplier L is a time-dependent function of the distance between the damage locus and the current stress state. The expression for this function is given by:

$$\mathrm{dL} = \frac{\mathrm{dt}}{\eta^{\mathrm{b}}}\langle \mathrm{F} \rangle \qquad \text{Eq. 4-24}$$

where dt is the time increment, $\eta^b$ the bonding viscosity and $\langle\rangle$ are the Macauley brackets.

### 4.2.4 Constitutive law for the composite material

The constitutive law of the composite material is obtained by coupling the ones of the bonds and the matrix. This coupling should insure that the external strain applied on the composite material must be compatible with the strains of the bonds and the matrix, while external stresses must be in equilibrium with the local ones.

#### Strain partition

Compatibility between external and local strains is based on the volume conservation described in section 4.2.1 and summarized by equations 4-5, 4-7 and 4-8 (a similar derivation can be obtained using mass balance equations). It is generally based on the consideration of the tensor functions $\chi_{ij}^{m}$ and $\chi_{ij}^{b}$ related to microstructural features of the material.

As a starting point in the present work, $\chi_{ij}^{m}$ and $\chi_{ij}^{b}$ will be considered as isotropic functions:

$$\chi_{ij}^{b} = X_b \delta_{ij} \qquad \text{Eq. 4-25}$$

$$\chi_{ij}^{m} = X_m \delta_{ij} \qquad \text{Eq. 4-26}$$

Leading to the following expression for the strains inside the matrix and the bonds:

$$c_b d\varepsilon_{ij}^{b} = X_b d\varepsilon_{ij}^{int} \qquad \text{Eq. 4-27}$$

$$c_m d\varepsilon_{ij}^{m} = X_m d\varepsilon_{ij}^{int} \qquad \text{Eq. 4-28}$$

$X_m$ and $X_b$ express the sharing existing between solid component and pore deformations during an incremental straining process. They depend generally on microfabric patterns and relative stiffness between porous medium and its solid components.

These coefficients are considered as descriptors of rock microfabric at a given state of damage. It is moreover expected that part of the load carried by the interface between the two mineral phases (and thus by the bond in the model) is transferred to the matrix when bonds degrade, leading to a decrease in the value of $X_b$. To account for this effect, coefficient $X_b$ is set as a function of damage variable L. The function selected is given by:

$$X_b = X_{b0} e^{-\frac{L}{2}} \qquad \text{Eq. 4-29}$$

Considering $X_m$ and $X_b$ and extending the equation 4-6 to all strain components, it is possible to compute bond and matrix strain increments from the external one:

$$d\varepsilon_{ij}^{ext} = (1 + X_b + X_m) d\varepsilon_{ij}^{int} \rightarrow d\varepsilon_{ij}^{int} = \frac{d\varepsilon_{ij}^{ext}}{1 + X_b + X_m} \qquad \text{Eq. 4-30}$$

$$d\varepsilon_{ij}^{b} = \underbrace{\frac{X_b/c_b}{1 + X_b + X_m}}_{b_\varepsilon} d\varepsilon_{ij}^{ext} = b_\varepsilon d\varepsilon_{ij}^{ext} \qquad \text{Eq. 4-31}$$

$$d\varepsilon_{ij}^{M} = \underbrace{\frac{X_m/c_m}{1 + X_b + X_m}}_{U_\varepsilon} d\varepsilon_{ij}^{ext} = U_\varepsilon d\varepsilon_{ij}^{ext} \qquad \text{Eq. 4-32}$$

## Stress partition

Stress partition are obtained by stating that the work input into the medium under any compatible external strain increment is equal to the sum of the work input into the matrix and the bonds. Labelling ${\sigma_{ij}}^{ext}$, ${\sigma_{ij}}^{m}$ and ${\sigma_{ij}}^{b}$ the stresses acting on the composite medium, matrix and bond, respectively, this condition reads:

$${\sigma_{ij}}^{ext} d\varepsilon_{ij}^{ext*} = c_m {\sigma_{ij}}^{m} d\varepsilon_{ij}^{m*} + c_b {\sigma_{ij}}^{b} d\varepsilon_{ij}^{b*} \qquad \text{Eq. 4-33}$$

where

$$d\varepsilon_{ij}^{ext*} = d\varepsilon_{ij}^{int} + c_m d\varepsilon_{ij}^{m*} + c_b d\varepsilon_{ij}^{b*} \qquad \text{Eq. 4-34}$$

By dividing both sides of equation by $d\varepsilon_{ij}^{ext*}$, the stress partition reads:

$${\sigma_{ij}}^{ext} = \underbrace{\frac{X_m}{1 + X_b + X_m}}_{U_\sigma} {\sigma_{ij}}^{m} + \underbrace{\frac{X_b}{1 + X_b + X_m}}_{b_\sigma} {\sigma_{ij}}^{b} \qquad \text{Eq. 4-35}$$

### Tangent behavior of the composite material

In this framework, matrix strain tensor $\varepsilon_{ij}^{m}$ is associated to matrix stress tensor ${\sigma_{ij}}^{m}$ through the constitutive law of the soil matrix while bond strain tensor $\varepsilon_{ij}^{b}$ is associated to bond stress tensor ${\sigma_{ij}}^{b}$ through the constitutive law for bonds:

$$d{\sigma_{ij}}^{m} = {D_{ijkl}}^{m} d{\varepsilon_{kl}}^{m} \qquad \text{Eq. 4-36}$$

$$d{\sigma_{ij}}^{b} = {D_{ijkl}}^{b} d{\varepsilon_{kl}}^{b} \qquad \text{Eq. 4-37}$$

Finally, from equations 4-31, 4-32, 4—35, 4-36 and 4-37, the constitutive law for the composite material reads:

$$d\sigma^{ext} = U_\sigma d\sigma^{m} + b_\sigma d\sigma^{b} + \sigma^{m} dU_\sigma + \sigma^{b} db_\sigma = U_\sigma D^{m} d\varepsilon^{m} + b_\sigma D^{b} d\varepsilon^{b} + \sigma^{m} dU_\sigma + \sigma^{b} db_\sigma$$

or:

$$d\sigma^{ext} = U_\sigma U_\varepsilon D^m d\varepsilon^{ext} + b_\sigma b_\varepsilon D^b d\varepsilon^{ext} + \sigma^m dU_\sigma + \sigma^b db_\sigma \qquad \text{Eq. 4-38}$$

The change in $U_\sigma$ and $b_\sigma$ are related to the variations in $X_b$ because the change in the damage multiplier. The equations governing this process are:

$$dX_b = -\frac{1}{2}X_{b0}e^{-\frac{L}{2}}dL = -\frac{X_b}{2}dL \qquad \text{Eq. 4-39}$$

$$db_\sigma = d\left(\frac{\chi_b}{1+\chi_b+\chi_m}\right) = -\frac{X_b(1+\chi_m)}{2(1+\chi_b+\chi_m)^2}dL \qquad \text{Eq. 4-40}$$

$$dU_\sigma = d\left(\frac{\chi_m}{1+\chi_b+\chi_m}\right) = \frac{X_b X_m}{2(1+\chi_b+\chi_m)^2}dL \qquad \text{Eq. 4-41}$$

Finally, the tangent matrix of the composite medium is obtained as:

$$D^{ext} = U_\sigma \frac{d\sigma^m}{d\varepsilon^{ext}} + b_\sigma \frac{d\sigma^b}{d\varepsilon^{ext}} + \sigma^M \frac{dU_\sigma}{d\varepsilon^{ext}} + \sigma^b \frac{db_\sigma}{d\varepsilon^{ext}}$$

Or, by reworking the equation:

$$D^{ext} = U_\sigma U_\varepsilon D^m + b_\sigma b_\varepsilon D^b + \left(\sigma^M \frac{dU_\sigma}{dL} + \sigma^b \frac{db_\sigma}{dL}\right)\frac{dL}{d\varepsilon^{ext}}$$

$$D^{ext} = U_\sigma U_\varepsilon D^m + b_\sigma b_\varepsilon \left(D^{eb} - \sigma^b \frac{1}{b_\varepsilon}\frac{dL}{d\varepsilon^{ext}}\right) + \left(\sigma^M \frac{dU_\sigma}{d\chi_b} + \sigma^b \frac{db_\sigma}{d\chi_b}\right)\frac{d\chi_b}{dL}\frac{dL}{d\varepsilon^{ext}}$$

$$D^{ext} = U_\sigma U_\varepsilon D^m + b_\sigma b_\varepsilon \left(D^{eb} - \left[\sigma^b\left(\frac{1}{b_\varepsilon} - \frac{1}{b_\sigma b_\varepsilon}\frac{db_\sigma}{d\chi_b}\frac{d\chi_b}{dL}\right) - \sigma^M \frac{1}{b_\sigma b_\varepsilon}\frac{dU_\sigma}{d\chi_b}\frac{d\chi_b}{dL}\right]\frac{dL}{d\varepsilon^{ext}}\right)$$

$$D^{ext} = U_\sigma \frac{d\sigma^m}{d\varepsilon^{ext}} + b_\sigma \frac{d\sigma^b}{d\varepsilon^{ext}} + \sigma^M \frac{dU_\sigma}{d\varepsilon^{ext}} + \sigma^b \frac{db_\sigma}{d\varepsilon^{ext}}$$

$$D^{ext} = U_\sigma U_\varepsilon D^m + b_\sigma b_\varepsilon D^b - \frac{X_b}{2(1+\chi_b+\chi_m)^2}\left((1+X_m)\sigma^b - X_m\sigma^m\right)dL \qquad \text{Eq. 4-42}$$

In absence of damage (dL = 0), the tangent matrix reduces to:

$$D^{ext} = U_\sigma U_\varepsilon D^m + b_\sigma b_\varepsilon D^b \qquad \text{Eq. 4-43}$$

It is therefore the sum of the tangent matrix of both components, weighted by the product of stress and strain partition coefficients.

A model based a two-phase composite material has already been presented by Vaunat & Gens (2003) (see also Gens et al., 2007) to model the response of structured soils. The similarity is however limited to consideration of the two-phases, since their internal arrangement is fundamentally different. In the bond model presented by Vaunat & Gens (2003), bonds act only as cements between soil particles and can only receive load transferred by the matrix. In the present model, the two minerals phase receive their own part of external load and subscript *m* and *b* can be exchanged without modifying the response of the material. This fundamental aspect of the present model provides it with the capability to model materials made of grains interacting at the same level like rocks.

### 4.2.5 A quote on admissible values for Xm and Xb coefficients.

Central parameters of the model are the coefficients $X_m$ and $X_b$. They provide indeed the relative importance of the matrix and bond models for the composite. These parameters are related to microstructural aspects of the material and can be usually only indirectly derived through back-analysis of the rock stiffness. This process can be complicated in absence of information about values to initiate the back-analysis process. In this section, insights into the possibility to provide restriction for $X_m$ and $X_b$ values on the basis of the method proposed by Hashin & Shtrikman (1963) to obtained the stiffness of a composite material are presented.

The stiffness of the rock (composite material) is usually determined through mechanical tests or calculated from elastic wave propagation velocities (as presented in section 3.4.3). This parameter can also be estimated from the properties of the mineral components of the rock and the pore fluids. Constituent individual stiffness, volume fraction and geometrical arrangement are factors controlling the stiffness of the composite material. The difficulty to assess the effect of grain geometry and arrangement makes however often impossible this derivation.

In this context, an alternative option consist in estimating upper and lower bounds for the moduli of the composite material. Hashin & Shtrikman (1963) proposed a method to obtain these bounds without making any assumption about the geometrical disposition of the phases (spheres embed in a matrix or intercalations of phases bands), and defining them through the strains energy stored in the material when subjected to uniform stress or strains.

According to Hashin & Shtrikman (1963), the upper and lower bounds for bulk modulus of an elastic material made of n components are defined according to equations 4-44 and 4-45 respectively:

$$\mathrm{K}_1^* = \mathrm{K}_1 + \frac{\mathrm{A}_1}{1 + \alpha_1 \mathrm{A}_1} \qquad \text{Eq. 4-44}$$

$$\mathrm{K}_2^* = \mathrm{K}_n + \frac{\mathrm{A}_n}{1 + \alpha_n \mathrm{A}_n} \qquad \text{Eq. 4-45}$$

where:

$$\alpha_1 = -\frac{3}{3\mathrm{K}_1 + 4\mathrm{G}_1}\ , \qquad \alpha_n = -\frac{3}{3\mathrm{K}_n + 4\mathrm{G}_n}$$

$$\mathrm{A}_1 = \sum_{r=2}^{r=n} \frac{\mathrm{C}_r}{\frac{1}{\mathrm{K}_r - \mathrm{K}_1} - \alpha_1}, \quad \mathrm{A}_n = \sum_{r=1}^{r=n-1} \frac{\mathrm{C}_r}{\frac{1}{\mathrm{K}_r - \mathrm{K}_n} - \alpha_n}$$

where, $K_1$ is the highest bulk modulus of the n components and $K_n$ is the lowest value, $G_1$ and $G_n$ are the shear moduli of the corresponding components and $C_r$ the volume fraction of component r, n represents the number of components.

In order to estimate the upper and lower bounds of bulk modulus for the limestone of LaRG three different components are considered (n=3 for Eq. 4-44 and Eq. 4-45): calcite, quartz and air, this last component represents the porosity of the material under dry conditions.

According to Carmichael (1989), the typical values of bulk modulus (K) and shearing (G) modulus for the calcite and quartz, obtained from characteristic values of elastic wave propagation velocities are K= 70 GPa G=30.6 GPa for the calcite and K=35 GPa and G= 44 GPa for the quartz.

Considering these values, and taking into account the two principal minerals observed on the mineralogical composition of samples from the site under study (see section 3.3.1) the upper and lower stiffness bounds for LaRG limestone are estimated according to the method presented by Hashin & Shtrikman (1963).

Following what was observed in the mineralogical analyses; samples obtained from blocks are evaluated with a quartz content of 10%, while samples obtained from the cliff face are considered with a quartz content of 40%. Figure 4-3 and Figure 4-4 present the bounds obtained for the bulk modulus as a function of the porosity, for block and cliff drilled samples respectively. On the same figures, the bounds are compared with the real stiffness values obtained from elastic wave propagation velocities (see section 3.5.2). It can be observed that the experimental values lay between the Hashin & Shtrikman (1963) bounds. Therefore, this method appears to provide appropriated bounds for the bulk modulus that can be used for the rock under study.

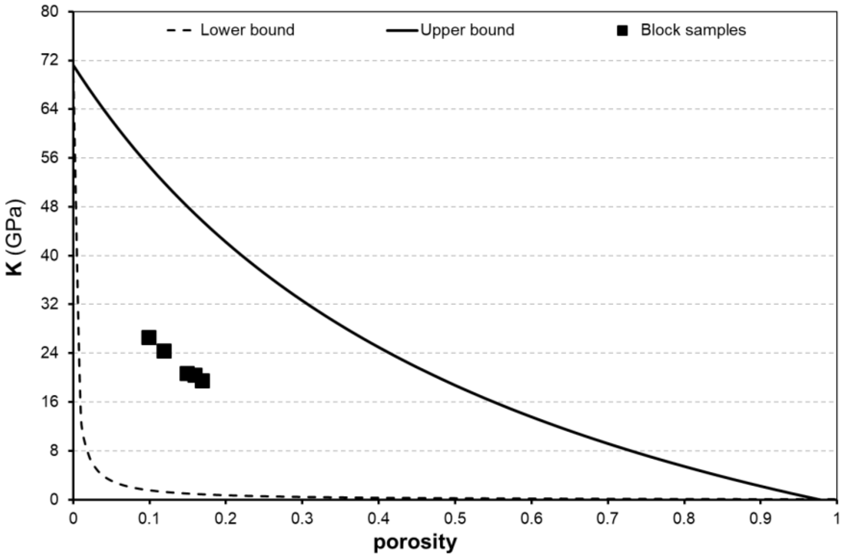

Figure 4-3 Hashin & Shtrikman bulk modulus bounds as a function of porosity for block samples

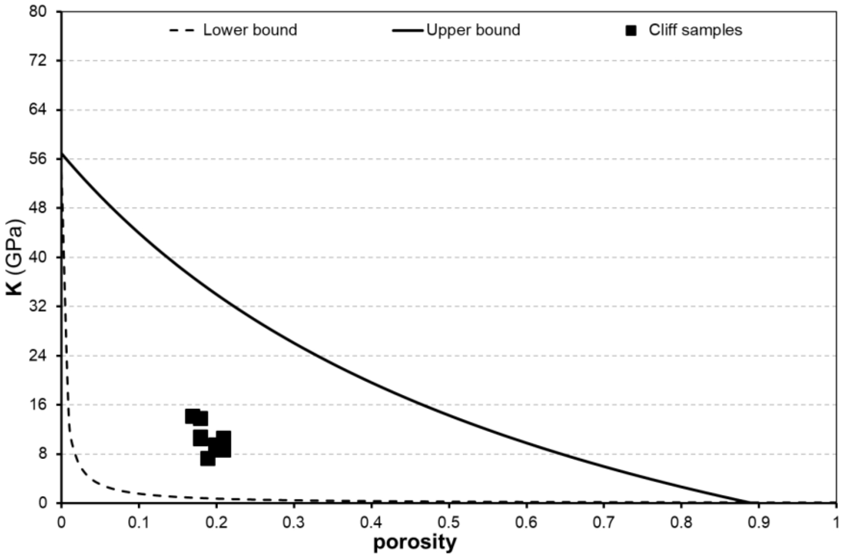

Figure 4-4 Hashin & Shtrikman bulk modulus bounds as a function of porosity for cliff face samples

From equation 4-43 it can be easily proven that the undamaged (that is when dL = 0) bulk modulus of the composite material depends on the bulk modulus and content of matrix and bond materials and on the coefficients $X_m$ and $X_b$, following the equation 4-46. Hence, it can be considered that the coefficients $X_m$ and $X_b$ represents those geometrical characteristics of the arrangement of components, this is to say the microstructural features of the composite material (Mitchell and Soga, 2005).

$$K = \left(\frac{X_m}{1 + X_b + X_m}\right)^2 \frac{1}{C_m} K_m + \left(\frac{X_b}{1 + X_b + X_m}\right)^2 \frac{1}{C_b} K_b \qquad \text{Eq. 4-46}$$

Consequently, if $C_m$, $C_b$, $K_m$, $K_b$, and K are known, it is possible to determine all possible pairs of $X_m$-$X_b$ that guarantee the value of bulk modulus for the composite material (K). Moreover, even if $X_m$ and $X_b$ can reach theoretically any value, the lower and upper bounds of K (calculated according to equations 4-44 and 4-45) restrict these coefficients.

For instance, samples from La Roque Gageac obtained from blocks with a porosity equal to 0.2 should present a bulk modulus that varies between 0.75 GPa to 42.2 GPa, thus the coefficients $X_m$ and $X_b$ must be defined in the range presented in Figure 4-5. It is important to mention that the lower bound is mainly control by the porosity and air parameters. Thus, if the sample was fully saturated instead to unsaturated this boundary will be higher, as the bulk modulus for the water is higher than for the air.

Moreover, the coefficients $X_m$ and $X_b$ also controls the strains (Eq. 4-30) and stress (Eq. 4-35) partitions, thus variations in $X_m$ and $X_b$ may generate higher strains and stresses in the bonding inducing a higher damage in the composite material, even if the initial stiffness is kept constant.

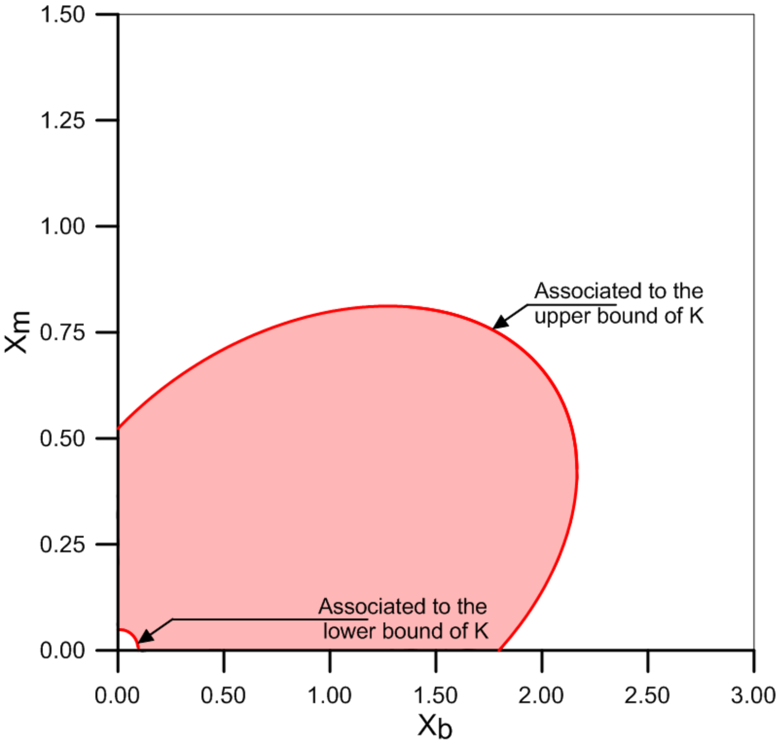

Figure 4-5 Acceptable range of $X_m$-$X_b$ coefficients for block samples with porosity equal to 0.2

## 4.3 Finite element model.

### 4.3.1 Finite Element formulation.

In order to model Boundary Value problems, the constitutive model has been implemented in the Finite Element code CODE_BRIGHT developed at the Universitat Politècnica de Catalunya (Olivella et al. 1996). It deals generally with the solution of thermo-hydro-mechanical coupled problems in geological media. However, since there is no fluid present in the medium under study, only the thermo-mechanical coupling will be considered in the analysis. As discussed by Gens et al. (2007), in case of stiff materials like rocks, the thermo-mechanical coupling acts mainly in one direction (Figure 4-6). Under the presence of energy fluxes and temperature changes, the material experiences a thermal strain, which affects, in turn, the stress state, and eventually, the rock stiffness (bold downward arrow in Figure 4-6). On the other hand, since rock thermal properties depend essentially on mineralogy and porosity, whose changes are low in stiff materials, there will be almost no effects of the mechanical response of the material on the thermal field (thin upward arrow in Figure 4-6).

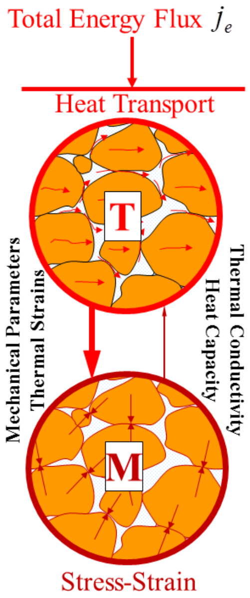

Figure 4-6 Thermo-Mechanical coupling in geological media

The governing equations solved in the Finite Element scheme are the mass balance of the solid phase (Eq. 4-47), the balance of energy (Eq. 4-48) and of momentum (Eq. 4-49) for the medium.

$$\frac{\partial}{\partial t}\big(\rho_s(1-\phi)\big)+\nabla\cdot(j_s)=0 \qquad \text{Eq. 4-47}$$

$$\frac{\partial}{\partial t}\big(E_s\,\rho_s(1-\phi)\big)+\nabla\cdot(i_c)=0 \qquad \text{Eq. 4-48}$$

$$\nabla\cdot\sigma+b=0 \qquad \text{Eq. 4-49}$$

Equation 4-47 allows relating the volumetric deformations in the medium, given by the divergence of solid velocity js, with the porosity changes. Moreover, Eq. 4-48 is a reduced equation of the general equation of the energy balance, where terms of energy fluxes convected by the fluid phases have been removed, since there are no fluids in the medium. As well, because of the assumption of small strain, the energy flux of the solid phase is neglected. As a result, the energy flux is only due to conduction ($i_c$) in the problem considered.

### 4.3.2 Implementation of the constitutive law.

The numerical implementation of the model within the Finite Element framework requires to develop strategies to cope with the discrete equations composing it, that are:

- Damage constitutive model
- Elastoplastic constitutive mode
- Strain partition
- Stress partition
- Evolution equation of $X_b$ coefficient

Moreover, the tangent matrix of the model must be computed to feed the tangent matrix of the global iterative scheme that solves the non-linearities of the Finite Element solution. This calculation is based on the expression given by equation Figure 4-42 that requires the computation of:

- The tangent matrix of the damage model
- The tangent matrix of the elastoplastic model
- dL as a function of the external strain increment

One of the problems found during the integration of the damage model relies on the use of an exponential law for the variation of the stiffness and compliance matrix for the bonds. When linearized, this type of law requires the use of very small time steps to reach acceptable precision. To solve this issue, an alternative non-linear discrete approximation of the exponential has been implemented. It is presented in Appendix C.

### 4.3.3 Model verification.

With the purpose of verify the model implementation, a simple Boundary Value Problem is considered. The geometry of the model considers the cube shown in Figure 4-7. Table 4-1 summarize Modeling parameters considered for this verification. The material is provided with porosity equal to 0.2, matrix and bond contents equal to 0.4 ($C_b$=$C_m$=0.4) and matrix and bond bulk modulus equal to 50 GPa. Under these conditions, the bulk modulus of the composite material is 25 GPa. Thermal expansion of both components is considered equal to $6.\ 10^{-6}$ $^{\text{o}}C^{-1}$ (mean value obtained with thermal expansion tests described in section 3.2.3 and obtained for the rock mass). A thermal ramp, starting from the initial temperature (0 ºC) up to 50 ºC and performed in 1h, is simultaneously applied to all the volume under null stresses. Under these conditions, the strain, stress and thermal fields are constant over the mesh and the response output by the model is a direct reproduction of the thermo-mechanical constitutive law material implemented at Gauss points.

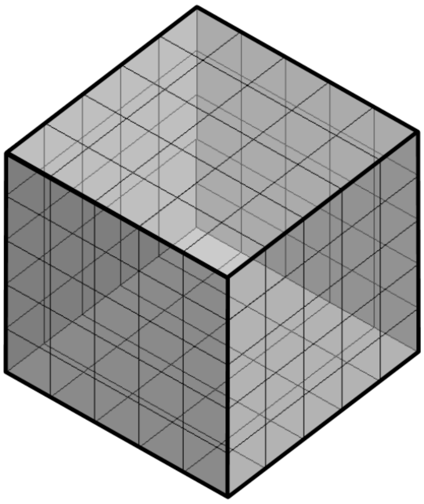

Figure 4-7 CODE_BRIGHT model geometry considered

Table 4-1 Parameters considered for the numerical model analysis

| | | | |
|---|---|---|---|
| Porosity ($\phi$) | 0.2 | Matrix linear thermal expansion - $\alpha_m$ (ºC$^{-1}$) | 6e-6 |
| $C_b$ | 0.4 | Bond linear thermal expansion - $\alpha_b$ (ºC$^{-1}$) | 6e-6 |
| $K_m$ (GPa) | 50 | $r_1$ | 0.01 |
| $K_b$ (GPa) | 50 | $r_0$ (MPa) | 1e-5 |

The solution obtained by the numerical model is compared with an algebraic expression obtained by integrating explicitly the constitutive law along the imposed thermal path under null stress. The integration has been carried out considering temperature increments $\Delta$T equal to 1ºC. To make easier the comparison, no strain rate effect has been considered in the numerical model and algebraic expression.

The algebraic expression is obtained based on the following equations:

1) The strains partition defined by Eq. 4-6:

$$\delta\varepsilon = \delta\varepsilon_{\mathrm{int}} + \mathrm{C_b}\delta\varepsilon_{\mathrm{tot}}^{\mathrm{b}} + \mathrm{C_m}\delta\varepsilon_{\mathrm{tot}}^{\mathrm{m}} \qquad \text{Eq. 4-50}$$

where:

$$\delta\varepsilon_{\mathrm{tot}} = \delta\varepsilon_{\mathrm{mec}} + \delta\varepsilon_{\mathrm{term}} \qquad \text{Eq. 4-51}$$

$\delta\varepsilon_{\mathrm{mec}}$ are the deformations associated to mechanical stresses and $\delta\varepsilon_{\mathrm{term}}$ the strains related to thermal changes:

$$\delta\varepsilon_{\mathrm{term}} = \alpha_{\mathrm{v}}\Delta\mathrm{T} \qquad \text{Eq. 4-52}$$

where $\alpha_{\mathrm{v}}$ is the volumetric thermal expansion of the component and $\Delta\mathrm{T}$ is the temperature variations.

It is important to mention that, because of the strain partition, thermally induced strains and thus stresses will be develop in the two components even if there are not mechanical loads externally applied.

2) The definitions for $X_m$, $X_b$ and $U_e$ (Eq. 4-27, Eq. 4-28 and Eq. 4-32):

$$\delta\varepsilon_{tot}^{m} = \frac{X_m C_b \delta\varepsilon_{tot}^{b}}{X_b C_m} \qquad \text{Eq. 4-53}$$

$$\delta\varepsilon_{tot} = \frac{1}{U_e}\delta\varepsilon_{tot}^{m} \qquad \text{Eq. 4-54}$$

3) The elastic law for both components:

$$\delta P^{b} = K_b\left(\delta\varepsilon_{mec}^{b}\right) = K_b\left(\delta\varepsilon_{tot}^{b} - \delta\varepsilon_{term}^{b}\right) \qquad \text{Eq. 4-55}$$

$$\delta P^{m} = K_m(\delta\varepsilon_{mec}^{m}) = K_m(\delta\varepsilon_{tot}^{m} - \delta\varepsilon_{term}^{m}) \qquad \text{Eq. 4-56}$$

4) The stress partition expression in absence of external loads (Eq. 4-35):

$$\delta p = U_\sigma \delta p^{m} + B_\sigma \delta p^{b} = 0 \qquad \text{Eq. 4-57}$$

5) The bond damage law (Eq. 4-29):

$$K_b = K_{b0} e^{-\lambda^{db}} \qquad \text{Eq. 4-58}$$

$$X_b = X_{b0} e^{-\lambda^{db}/_2} \qquad \text{Eq. 4-59}$$

6) The bond damage loading function:

$$F = u^{b} - r = 0 \qquad \text{Eq. 4-60}$$

where $U^b$ is the energy in the bond defined as:

$$U^{b} = \frac{1}{2} P^{b} \varepsilon_{mec}^{b} \qquad \text{Eq. 4-61}$$

And r is the evolution of damage locus, considered linear:

$$r = r_0 + r_1 \lambda^{db} \qquad \text{Eq. 4-62}$$

$r_0$ is the initial damage locus and $r_1$ is the damage rate.

As the variations in temperature are known, it is possible to obtain the thermal strains for the bonding and matrix, related to thermal expansion coefficients. Considering these values and the expressions Eq. 4-53 and Eq. 4-56 the $\delta\varepsilon_{tot}^{b}$ can be obtained from equation 4-57.

Then, by following the expression Eq. 4-53, $\delta\varepsilon_{tot}^{u}$ can be obtained. It is thus possible to calculate the bond and matrix stresses ($\delta p^m$ and $\delta p^b$), allowing the computation of the new $X_b$ and $K_b$ related to the damage law of the bond.

Figure 4-8 and Figure 4-9 presents the results obtained with the CODE_BRIGHT model and the algebraic expression. It is important to mention that here in after the strains are drawn with rock mechanics convention, in other words, positive values express expansion. Results obtained with both solutions are very similar, however, some small differences are observed at the end of the heating interval, possibly related to the integration scheme of the finite element model.

From Figure 4-9 it is important to point out the strong relationship between the bulk modulus of the composite material and the damage multiplier when no rate dependency is considered.

When the damage multiplier increases a reduction in the bulk modulus is registered. Note that until 0.15 hours, the damage multiplier is constant and equal to zero, therefore K does not present any evolution, remaining equal to its initial value (25 GPa).

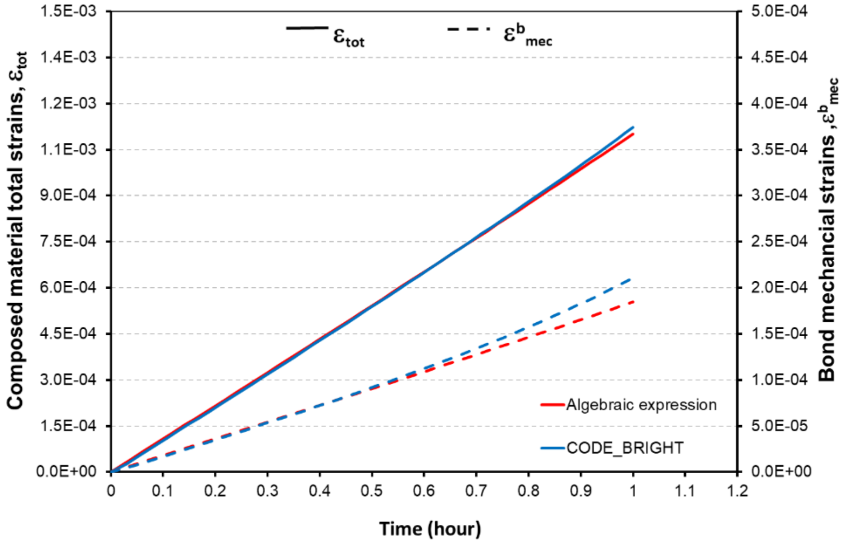

Figure 4-8 Strains evolution comparison between algebraic solution and CODE_BRIGHT model

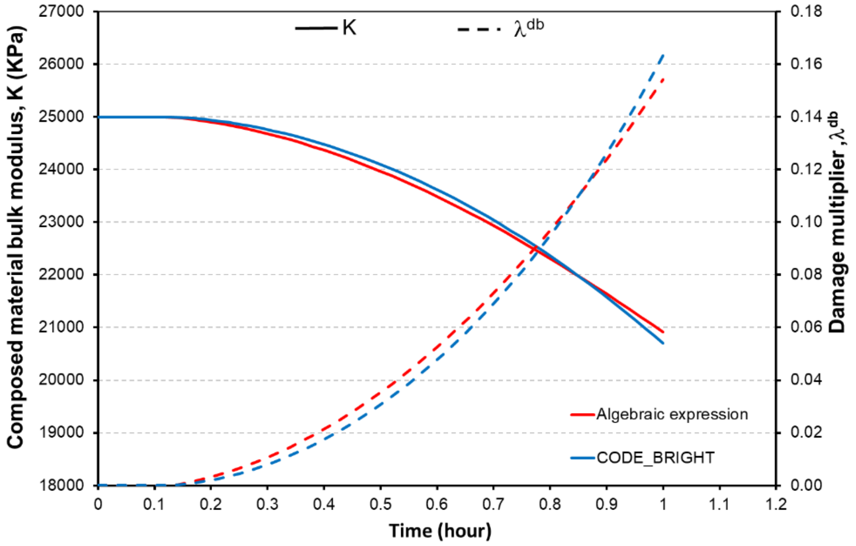

Figure 4-9 Damage multiplier and bulk modulus evolution comparison between algebraic solution and CODE_BRIGHT model

### 4.3.4 Insights into rock damage mechanism.

Insights into the mechanism of rock damage can be looked for by plotting the evolution of the loading function (F) with temperature increment in the bond stress space $p^b$ vs $q^b$.

As mentioned before the loading function (F) defines an elastic domain in the stress space $F(\sigma^b, \varepsilon^b)$ in which the stiffness remains undamaged, in terms of the elastic (secant) energy

This envelope (equation 4-20) can be rewritten in terms of $p^b$, $q^b$ and $\lambda^{db}$, according to Eq. 4-63, by considering a linear damage locus evolution law (Eq 4-21)

$$F = u^b - r^b = \frac{1}{2}\frac{\left(p^b - p_0^b\right)^2}{K_b} + \frac{1}{2}\frac{\left(q^b - q_0^b\right)^2}{G_b} - \left(r_0 + r_1\lambda^{db}\right) = 0 \quad \text{Eq. 4-63}$$

Figure 4-10 presents the damage envelope F = 0 at three principal stages during the first thermal ramp:

1) t = 0 (red curve). The damage locus threshold is given at the initial value of $r_0$ (energy equal to 1. $10^{-5}$ kPa).

2) t = 8 min (green curve), when temperature reaches the value of 10ºC. At that time, the damage locus has already experienced some hardening due to the bond stress increase resulting from the components interaction related to the thermal expansion. From the graph the onset of damage occurs for a temperature close to 5ºC, time at which $p_b$ reaches 1 MPa and the corresponding energy reaches $r_0$.

3) When the temperature reaches 30ºC (blue line), the bond mean stress increases until 5.5 MPa, bringing with it the damage locus.

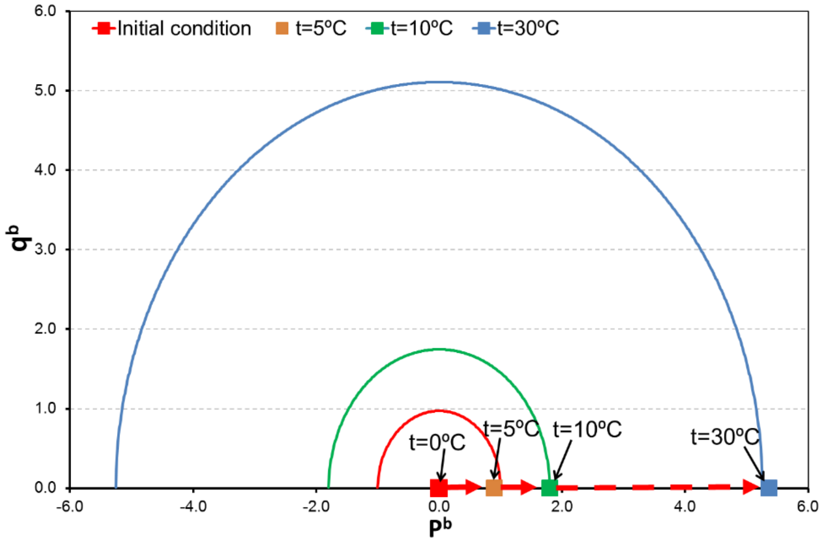

Figure 4-10 Loading function evolution for an increment of temperature between 0ºC to 30ºC

Figure 4-11 presents the evolution of the loading function F during thermal cycles between 10ºC to 50ºC, without considering any rate dependency ($\eta^b$=0). In this case, most of the damage occurs during the first cycle, when the increased bond mean stress reaches 6 Mpa bringing whit it the damage locus. Afterwards, temperature cycles cause changes of mean stress below 6 MPa, that is inside the new elastic zone and no damage occurs.

During the experimental work (see chapter 3), it was observed that maximal damage is not developed in the first thermal cycle; conversely its effects are accumulated during cycles imposition. Moreover, as mentioned before, the thermal damage is mostly related to the propagation of existent microcracks, which is a time-dependent phenomenon.

This indicates that to capture damage accumulation during thermal cycles it is require to include an additional mechanism related to the time dependency of thermal stress inducing micro-cracks propagation.

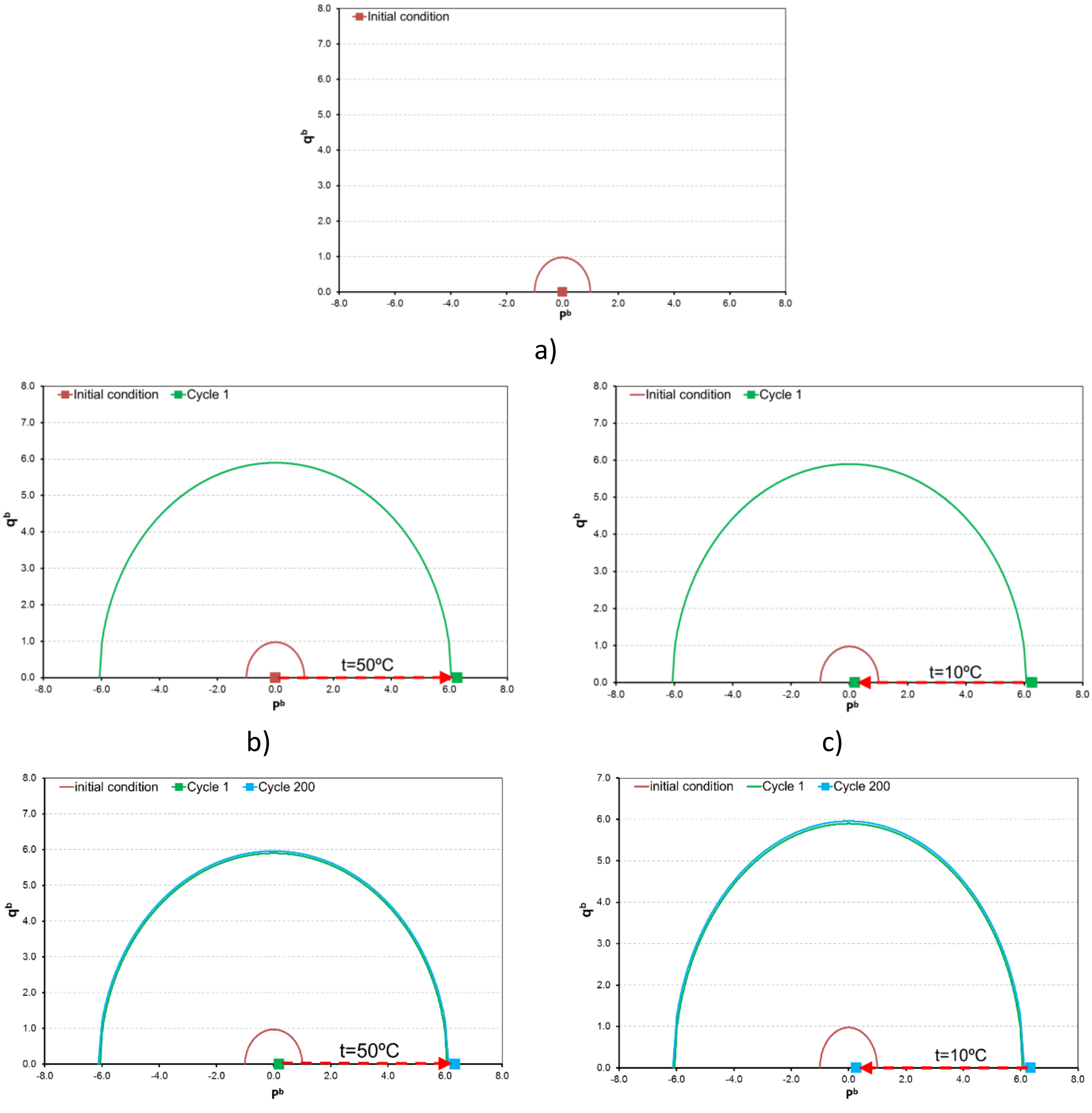

Figure 4-11 Rate-independent loading function evolution for thermal cycling between 0ºC to 50ºC: a) initial condition; b) 1st cycle, end of heating; c) 1st cycle, end of cooling; d) 200th cycle, end of heating; d) 200th cycle, end of cooling

For this reason, a rate dependent damage locus has been introduced in the model. The rate dependency is controlled by the bond viscosity $\eta^b$, taken equal to 100 for this punctual example. Moreover, other test characteristics are kept equal. Figure 4-12 presents the evolution of the loading function F during the thermal loading when the rate dependency is considered.

This rate-dependency allows the bond mean stress to stand outside the loading function for a time that depends on the velocity of hardening of the surface, controlled by the value of $\eta^b$. In this way, a delay is introduced in the development of damage, leading to a more progressive transition between two stages of damage. As well, if temperature cycles are applied at time intervals shorter than the time required to reach the full damage, thus, bond stresses will not be completely developed during a single interval and will proceed for the next one, simulating the rate dependency of micro-cracks development. During cooling, bond mean stress comes back to a lower value inside the elastic zone. The model predicts, therefore, no damage during this stage.

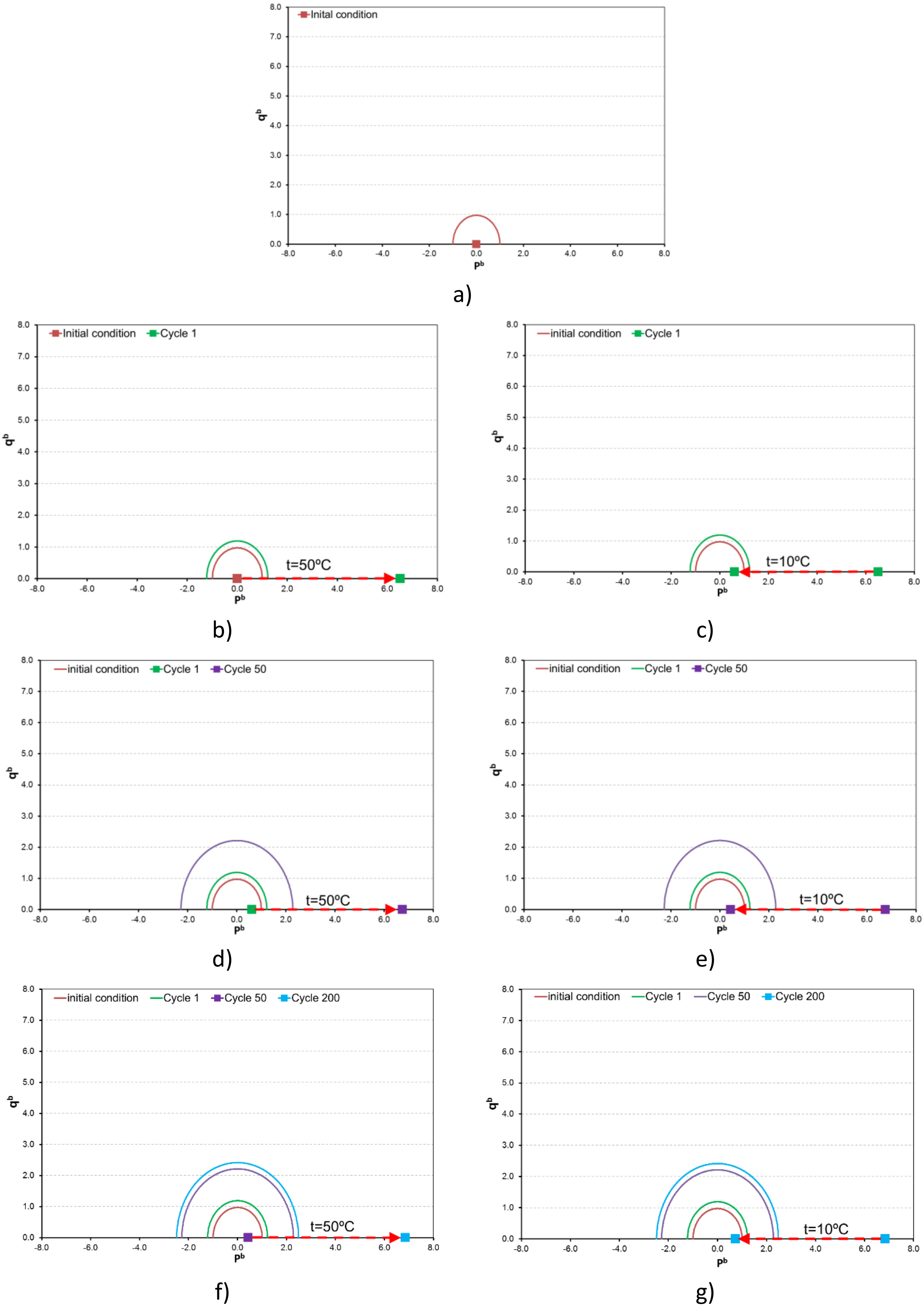

a)

b)

c)

d)

e)

f)

g)

Figure 4-12 Visco-damage loading function evolution for thermal cycling between 0ºC to 50ºC: a) initial condition; b) 1st cycle, end of heating; c) 1st cycle, end of cooling; d) 50th cycle, end of heating; e) 50th cycle, end of cooling; e) 200th cycle, end of heating; f) 200th cycle, end of cooling

## 4.4 Model performance.

The constitutive law presented in section 4.3 considers an important number of parameters: some of them are physical properties, such as rock porosity, volumetric content and stiffness parameters of each component. Others are microstructural characteristics like $X_m$ and $X_b$, or model adjustment parameters as $r_0$ and $r_1$.

In general, from all these parameters, only the porosity and mineralogical content can be easily defined. For this reason, it is interesting to make a sensitivity analysis of the effect of different parameters in the damage evolution of the composite material.

In this perspective, the simplified problem considered in the last section will be analyzed with different sets of parameters. In order to make clearer the effect of each parameter, no time rate is considered.

The sensitivity analysis holds on the ratio between matrix and bond bulk modulus ($K_m/K_b$), thermal expansion (αm/αb ratio) and bond content (Cb). Each analysis will be performed for three different $X_m/X_b$ ratios: 0.5, 1 and 2.

The effect of r1 and r0 are not affected by variations in $X_m$ and $X_b$, in general, a reduction of any of these two parameters will generate higher values of the damage multiplier, therefore a higher reduction in the composite material bulk modulus.

### 4.4.1 Bulk modulus.

Three different scenarios for the bulk modulus are considered Km/Kb = 0.5, 1 and 2. For the sake of comparison, the value considered for the highest component stiffness is 50 GPa. As such, Km/Kb = 0.5 means that Kb= 50 GPa and Km=25 GPa whether Km/Kb = 2 means Km = 50 GPa and Kb = 25 GPa. Volumetric content and thermal expansion are taken equal to 0.4 and 6. 10-6 ºC respectively for both the matrix and the bonds.

Furthermore, it has been verified that coefficients $X_m$ and $X_b$ belong to the admissible zone of bulk modulus. Figure 4-13 shows the Hashin & Shtrikman (1963) bounds envelopes for the considered ratios of Km/Kb. Values considered for Xm/Xb ratio is in all cases located within the admissible zone.

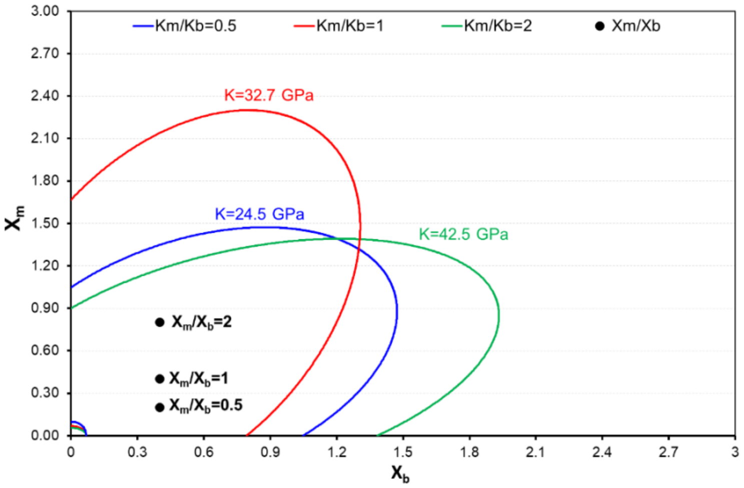

Figure 4-13 Coefficients $X_m$ and $X_b$ considered for the evaluation of different $K_m$ – $K_b$ ratio

### Case $X_m/X_b=0.5$ ($X_m=0.2$ $X_b=0.4$).

The first case considers a material where the bond (damaging component) has a higher effect than the matrix (no-damaging component) on rock response.

Figure 4-14 shows the time evolution of total, bond and matrix strains. When $X_m$ is lower than $X_b$, the total strains registered in the bonds will be higher than those obtained for the matrix, as can be observed in Figure 4-14. Moreover, the highest total strains (whatever is for the composite material, for the matrix or for the bonds) are obtained when the bulk modulus of the matrix is higher than the one of the bonds.

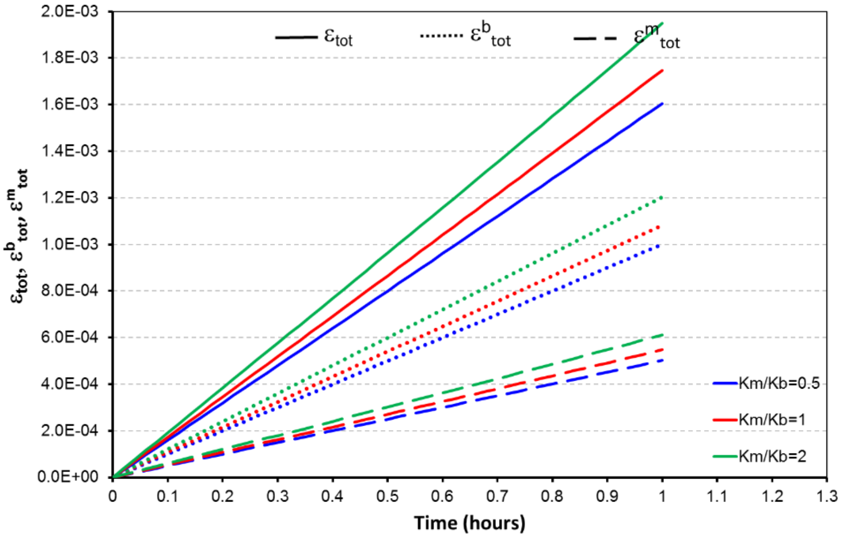

Figure 4-14 Evaluation of bulk moduli with $X_m$/Xb=0.5: total strains evolution

Under null applied external stress, it will be expected that total strains ($\varepsilon_{tot}$) were only controlled by thermal expansion of the materials. Nevertheless, because the microstructural characteristics of the composite material (related to parameters Xm and Xb) the total strains can be higher or lower to thermal strains as a result of restrictions imposed by the presence of two different components.

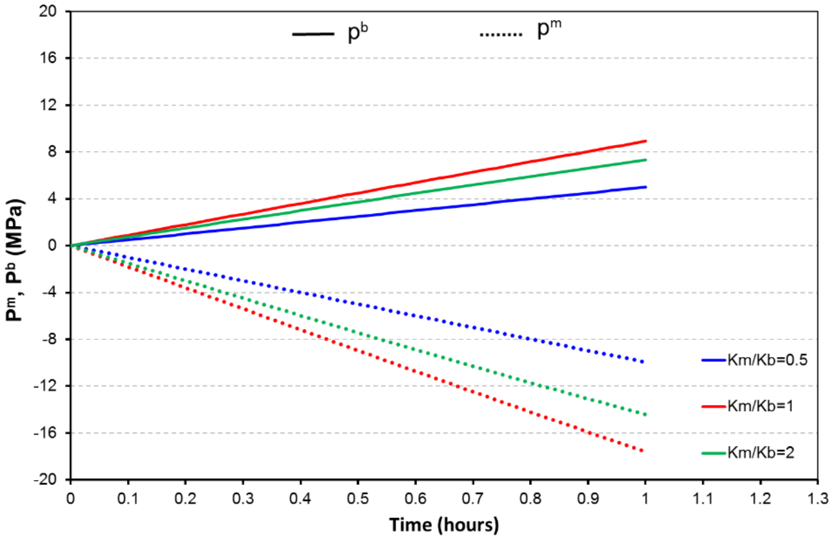

Figure 4-15 Evaluation of bulk moduli for $X_m/X_b=0.5$: internal stresses evolution

The first restriction comes from the stress partition (Eq. 4-35) under null applied external stress. Figure 4-16 shows the evolution of mean bond and matrix stresses resulting from the thermal load. It can be observed that, whatever is the ratio between the bulk moduli of the components, matrix presents compressive stresses, while bonds develop stresses in extension. This is clearly, because, when one component extends, the other must compress to maintain the overall stress equal to zero.

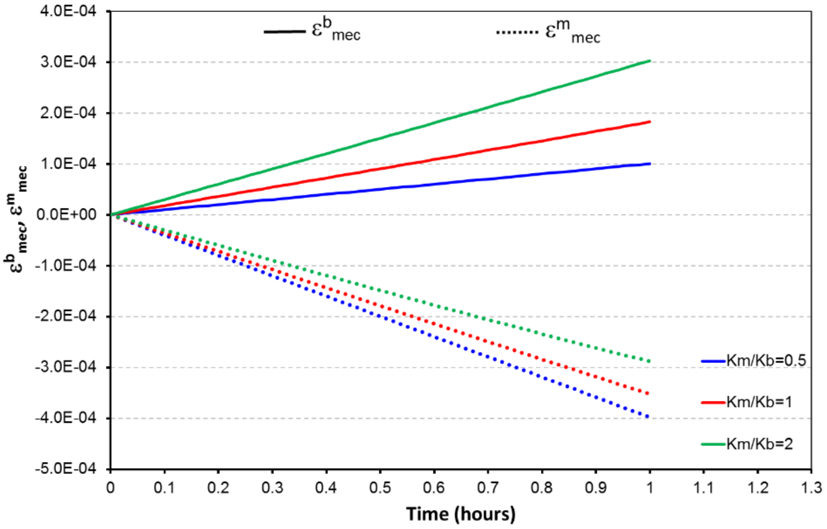

Figure 4-16 Evaluation of bulk moduli for $X_m/X_b$=0.5: matrix and bonding mechanical strains evolution

Additional restrictions are the constitutive laws of the bonds and the matrix that relates internal stresses to internal mechanical strains. Evolution of bond and matrix volumetric strains is shown in Figure 4-16. As the ratio $K_m/K_b$ increases, more mechanical strains are developed in the bonds and less in the matrix. Moreover, for this specific case, bond mechanical strains appear to be higher when the bulk modulus of the matrix is higher than the bulk modulus of the bond. Conversely, matrix mechanical strains are lower than bond mechanical strains when $K_m = 2\ K_b$. This result cannot be directly extrapolated to stresses since they are related to the strains through the stiffness of the component. For example, matrix mechanical strains are higher than bond mechanical strains for $K_m = 0.5\ K_b$ while stresses are lower this is related to the low stiffness of the matrix.

The final restriction is the additivity of mechanical and thermal strains. It imposes that the strain measured externally is not only due to the thermal expansion of the rock but depends also on the values of mechanical strains experienced by rock components. It is why the external strain depends on the ratio between bond and matrix stiffness.

The same explanation holds for the occurrence of rock damage under thermal load. Figure 4-18 shows the evolution of bond damage multiplier ($\lambda^{db}$) together with the degradation of rock bulk modulus *K*. For ratios $K_m/K_b$ equal to 0.5 or 2, bonds are more affected than for ratio $K_m/K_b = 1$ and $\lambda^{db}$ variable increases. Therefore, the bulk modulus of the rock experiences a higher damage. There is no proportional relationship between rock degradation and $K_m/K_b$, but it must be investigated looking at the values of stresses in the damage-prone component of the material.

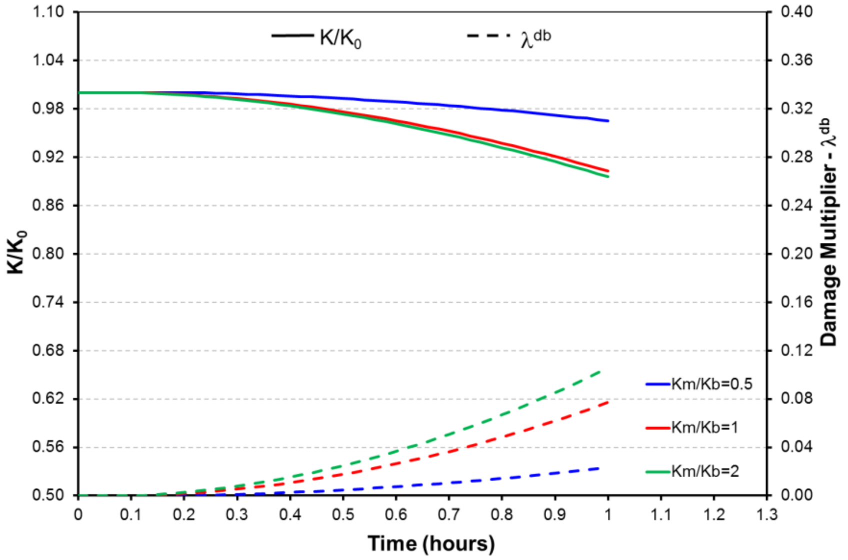

Figure 4-17 Evaluation of bulk moduli for $X_m/X_b=0.5$: bulk modulus and damage multiplier evolution

## *Case Xm/Xb=1 (Xm=0.4 Xb=0.4).*

This case addresses a composite material made of two components having a symmetric effect on the rock behavior. This is obtained by setting equal volumetric content ($c_b = c_m$), equal thermal expansion coefficient and equal values for coefficients $X_m$ and $X_b$. In this case, because the definition of $X_m$ and $X_b$ (equations 4-25 and 4-26), the total strains for the bond and matrix are equal and correspond only to the thermal strains (Figure 4-18). In other words, each component can expand freely under the thermal load without affecting the other component. Therefore, no internal stresses are generated, as can be observed in Figure 4-19.

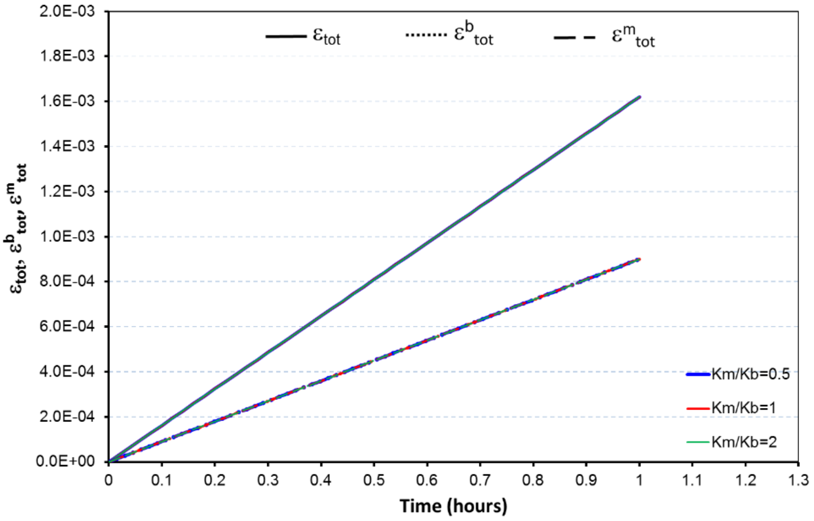

Figure 4-18 Evaluation of bulk moduli for $X_m/X_b=1$: total strains evolution

In other words, because of the specific internal microstructure considered for the composite material, matrix and bond can develop their complete thermal expansion without interacting each other. Consequently, no damage will be registered in the bond (damage multiplier equal to zero) and the composite material bulk modulus will be constant for the complete thermal load (see Figure 4-21). This corroborates the fact that, in the model under consideration, development of thermally induced damage under constant stress is caused by the differential response of its components.

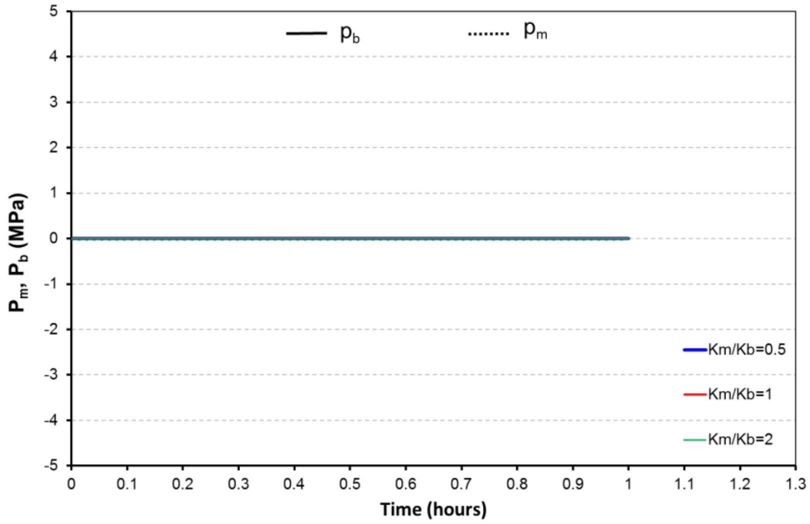

Figure 4-19 Evaluation of bulk moduli for $X_m/X_b$=1: internal stresses evolution

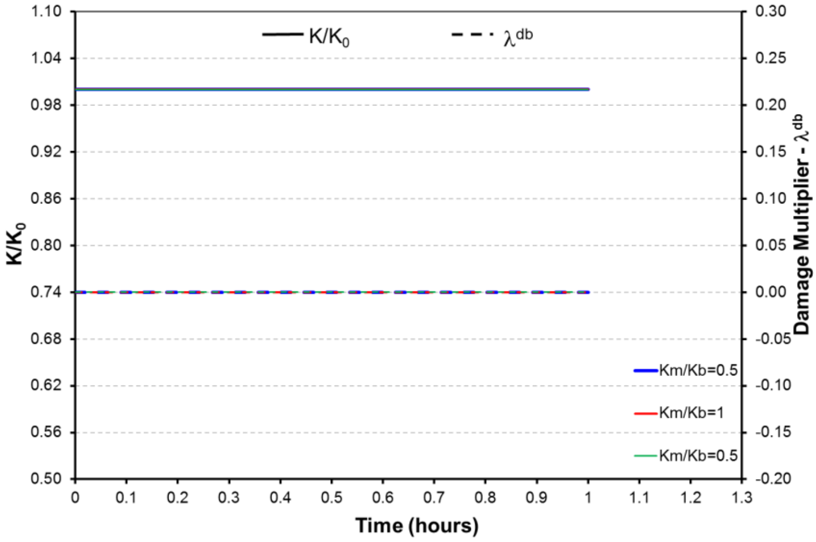

Figure 4-20 Evaluation of bulk moduli for $X_m/X_b$=1: bulk modulus and damage multiplier evolution

### Case Xm/Xb=2 (Xm=0.8 Xb=0.4).

The last case ($X_m$ larger than $X_b$) considers a material where the matrix (not damaging component) has a more pronounced effect than the bonds (damaging component) on rock response.

In this case, the general response obtained will be the opposite of the behavior found for $X_m$ lower than $X_b$. In first place, the total strains are higher for the matrix than for the bond and close to the values of total strains. Additionally, the highest total strains (either in the bond, matrix and composite material) occurred when the bonds are provided with the largest bulk modulus, see Figure 4-21.

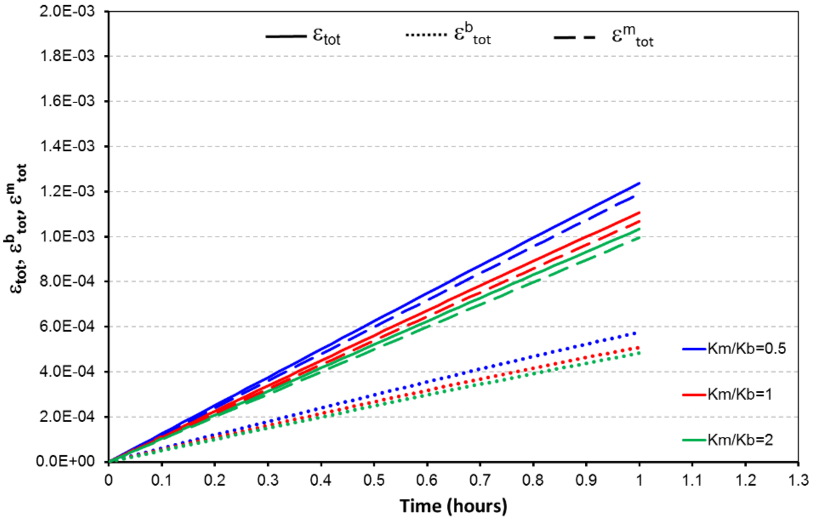

Figure 4-21 Evaluation of bulk moduli for $X_m$/Xb=2: total strains evolution

For this case, total strains in the matrix are higher than thermal strains, therefore, the mechanical strains and internal stresses generated for this component will be positive (extension), as presented in Figure 4-22 and Figure 4-23. Conversely, the bond develops contraction strains and stresses. Nevertheless, just as it was observed for $X_m/X_b$=0.5 the bond strains are greater (in magnitude) when the matrix bulk modulus is higher than the bond bulk modulus.

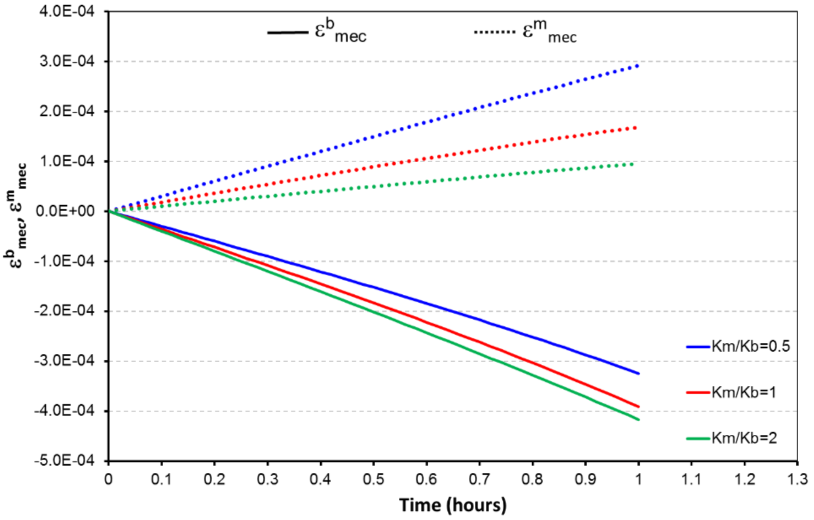

Figure 4-22 Evaluation of bulk moduli for $X_m$/Xb=2: mechanical strains evolution

Because of the different bulk moduli considered, the maximal internal stresses are not directly related to the maximal mechanical strains. In fact, the highest values of internal stresses are developed when $K_m$ is equal to $K_b$, which is not the case where the higher mechanical strains are developed, as can be observed in Figure 4-23 and Figure 4-22. It is interesting to point out that, even if the highest mechanical strains for the bond are developed when $K_m/K_b$=2, the lowest $P^b$ is related to this case. Which can be attributed to the fact that for this specific case the initial $K_b$ is equal to 25 GPa while the other two cases under analysis present a Kb equal to 50 GPa, yet, it is important to remember that $K_b$ is affected by the damage multiplier.

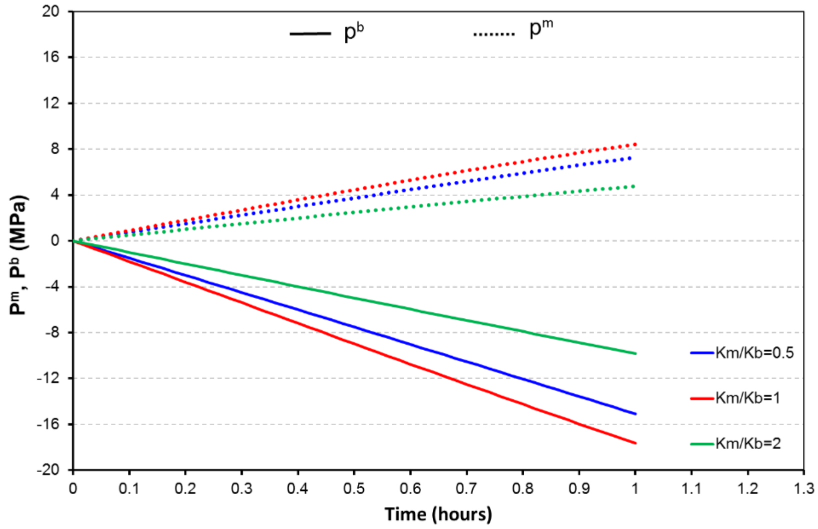

Figure 4-23 Evaluation of bulk moduli with $X_m$/Xb=2 – Internal stress evolution

From Figure 4-24, it can be observed that the damage multiplier increases the most when the two components (matrix and bond) present the same bulk modulus, thus, for this case, the reduction in the bond bulk modulus is higher too.

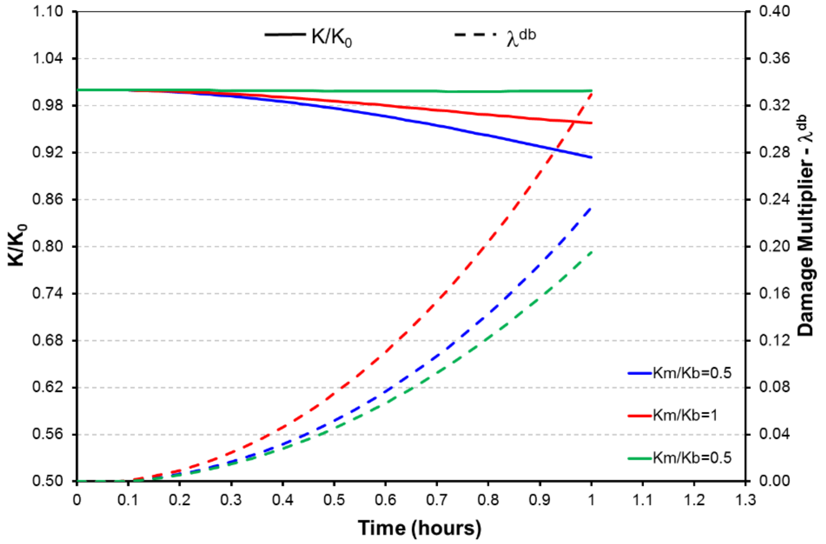

Figure 4-24 Evaluation of bulk moduli for $X_m$/Xb=2: bulk modulus and damage multiplier evolution

Nevertheless, the reduction of bulk modulus for the composite material is higher when the matrix bulk modulus is lower than the bond bulk modulus, this characteristic is related to the values of $X_m$, $X_b$ and the matrix bulk modulus considered. As for the situation under analysis $X_m$ is larger than $X_b$, the stiffness of the composite material is going to be strongly related to the matrix bulk modulus, and remember that for the case $k_m/k_b=1$, $K_m$ is equal to 50 GPa while, for the case $k_m/K_b=0.5$ it is equal to 25 GPa.

Moreover, it is important to remark that the increase in the damage multiplier obtained for $X_m/X_b=2$ is much higher than for the case where $X_m/X_b=0.5$ (Figure 4-17) because the magnitudes of $P^b$ obtained for this last case. Nevertheless, the stiffness of the composite material is going to be strongly related to $K_b$ if $X_m/X_b=0.5$ and to $K_m$ if $X_m/X_b=0.5$. Consequently, the reduction in the composite material bulk modulus is very similar for both cases.

### 4.4.2 Thermal expansion coefficient.

In order to evaluate the effect of the thermal expansion coefficients, three different situations are evaluated: $\alpha_m/\alpha_b$=0.5 ($\alpha_m$ = 3e-6 ºC$^{-1}$ and $\alpha_b$ = 6e-6 ºC$^{-1}$), $\alpha_m/\alpha_b$=1 ($\alpha_m$ = $\alpha_b$ = 6e-6 ºC$^{-1}$) and $\alpha_m/\alpha_b$=2 ($\alpha_m$ = 6e-6 ºC$^{-1}$ and $\alpha_b$ = 3e-6 ºC$^{-1}$). For the sake of simplicity, thermal expansion is considered isotropic. The value of the volumetric thermal expansion coefficient is thus equal to three times the value of the linear one.

The sensitivity analysis on $\alpha_m$ and $\alpha_b$ will be performed for $c_m$ = $c_b$ = 0.4, $K_m$ = $K_b$ and three different relations for $X_m/X_b$ (0.5, 1 and 2).

Similar to the evaluation of the bulk modulus, this analysis is performed by considering three different relations for $X_m/X_b$, in this case, they will be related to the bound defined for $K_m$=$K_b$ (red line in Figure 4-13).

#### *Case $X_m/X_b$=0.5 ($X_m$=0.2 $X_b$=0.4).*

When $X_m$ is lower than $X_b$ the total strains obtained for the bond are higher than those obtained for the matrix, just as was observed before (see section 4.7.1). See Figure 4-25.

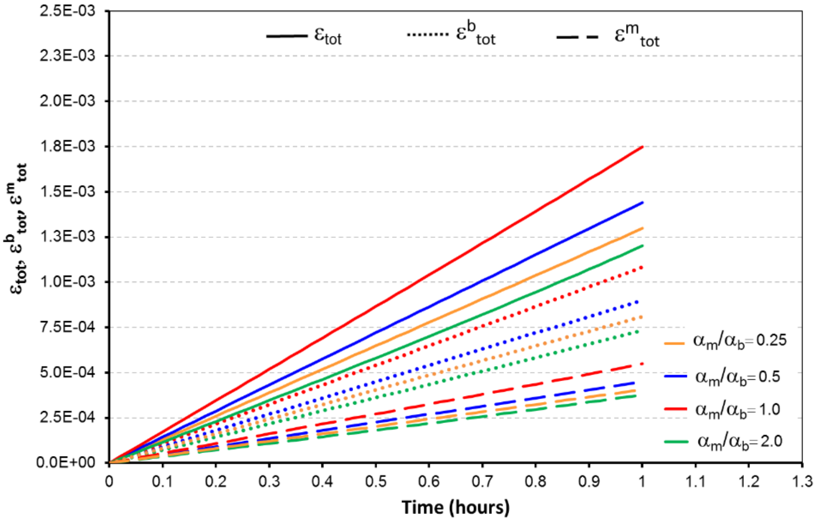

Figure 4-25 Evaluation of thermal expansion coefficient for $X_m$/Xb=0.5: total strains evolution

Furthermore, the highest total strains are related to higher values of $\alpha_m+\alpha_b$, obtained for the case $\alpha_m/\alpha_b$=1. It is interesting to point out that for the cases $\alpha_m/\alpha_b$=0.5 and $\alpha_m/\alpha_b$=2 where the addition of the coefficients is equal ($\alpha_m+\alpha_b$=9e-6 ºC$^{-1}$ in both cases), the highest total strains are obtained when $\alpha_m$ is lower than $\alpha_b$. Moreover, for this case ($\alpha_m/\alpha_b$=0.5) the bond and matrix total strains are equal to the strains due to thermal changes. Thus, no mechanical strains and stresses are obtained, as can be observed in Figure 4-26.

In addition, from Figure 4-26 it can be observed that while the thermal expansion coefficient ratio ($\alpha_m/\alpha_b$) is larger than the ratio $X_m/X_b$, the bond will develop positive stresses (expansion) which mean that the total strains are greater than the strains obtained only by thermal changes. Otherwise, if $\alpha_m/\alpha_b$ is lower than $X_m/X_b$ the total strains obtained in the bond are lower than the strains related to the temperature variations. Thus, the bond present contraction stress (negative values for $P^b$). The opposite response is observed in the matrix.

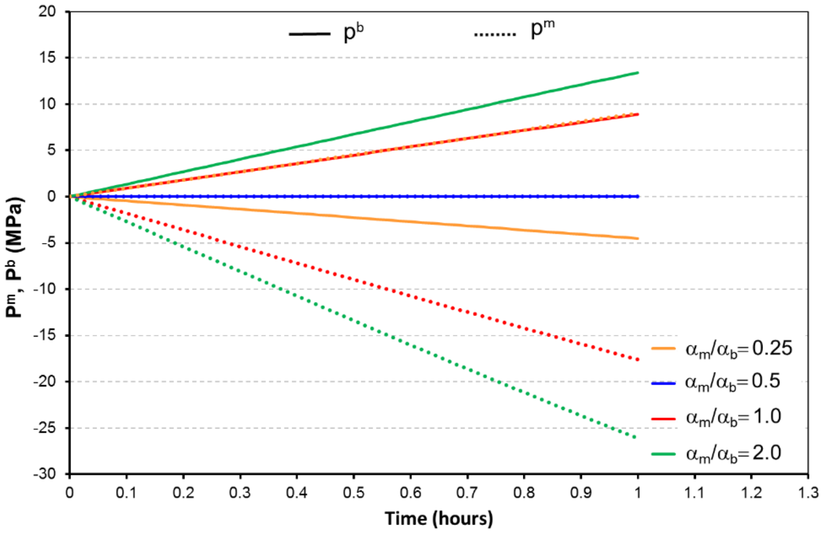

Figure 4-26 Evaluation of thermal expansion coefficient for Xm/Xb=0.5: internal stress evolution

Furthermore, the highest magnitude of $P^b$ is obtained when the thermal expansion coefficient is larger for the matrix than for the bond, as the initial $K_b$ considered for all the cases is the same, this is also related to higher mechanical strains. Hence, the highest increment in damage multiplier is also developed for $\alpha_m/\alpha_b$=2, as presented in Figure 4-27. Consequently, the bond bulk modulus will decrease the most for this case having as consequence the highest decrease in the composite material bulk modulus, because $K_m$ is equal for all the cases under analysis.

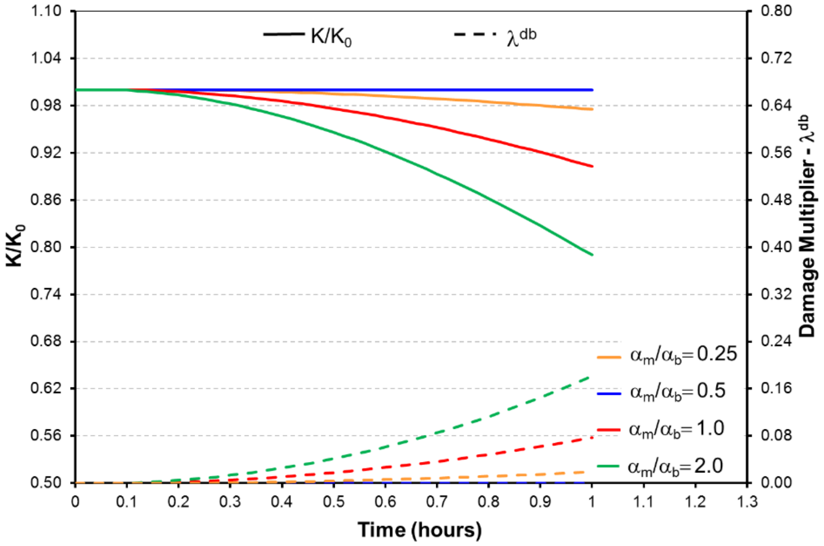

Figure 4-27 Evaluation of thermal expansion coefficient for Xm/Xb=0.5: bulk modulus and damage multiplier evolution

### Case Xm/Xb=1 (Xm=0.4 Xb=0.4).

If $X_m$ is equal to $X_b$, the maximal total strains are going to be related to the case where $\alpha_m+\alpha_b$ is higher ($\alpha_m+\alpha_b$=1). If the addition, the total strains for the bond ($\varepsilon^b_{tot}$) and the matrix ($\varepsilon^m_{tot}$) developed are the same no matters if the thermal expansion of the bond is larger than the thermal expansion for the matrix or vice versa (see $\alpha_m/\alpha_b$=0.5 and $\alpha_m/\alpha_b$=2 in Figure 4-28).

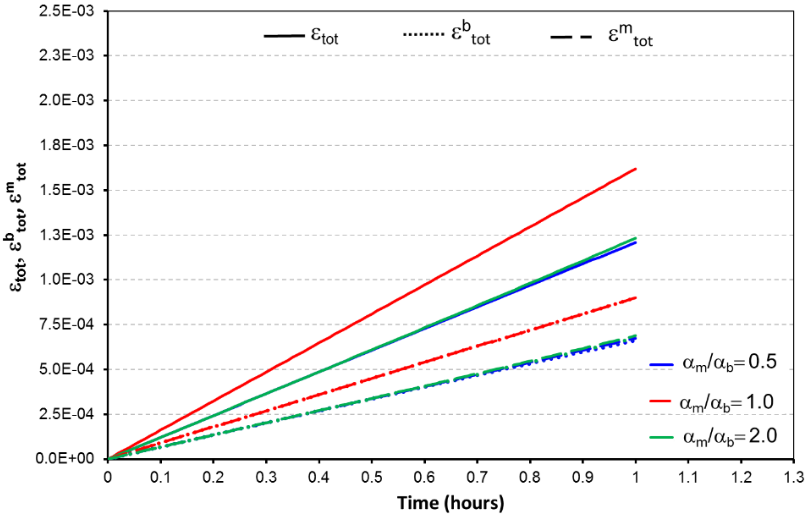

Figure 4-28 Evaluation of thermal expansion coefficient for $X_m$/Xb=1: total strains evolution

Conversely, to what was observed in the analysis of the bulk modulus, if $X_m$ is equal to $X_b$ some mechanical strains and internal stresses are going to be developed in the components, except for the case where $\alpha_m/\alpha_b$ be equal to $X_m/X_b$, as presented in Figure 4-29.

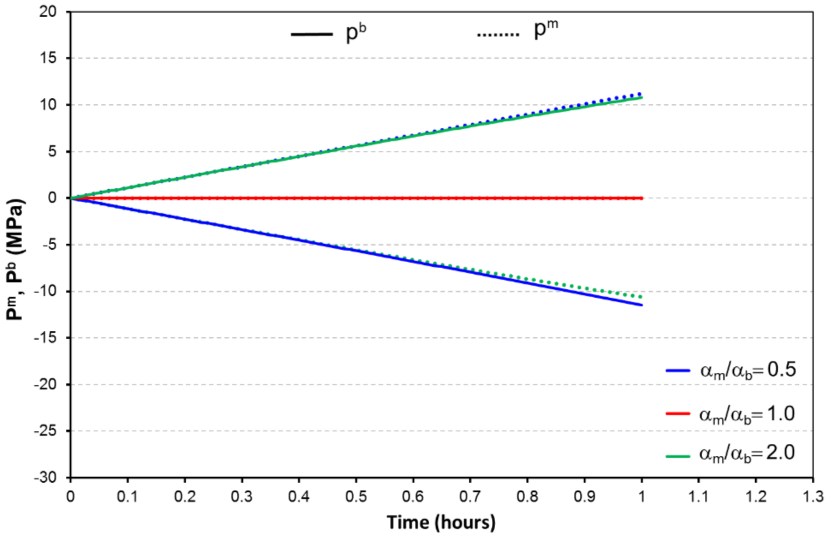

Figure 4-29 Evaluation of thermal expansion coefficient for $X_m$/Xb=1: internal stress evolution

Moreover, if $\alpha_m/\alpha_b$ is higher than $X_m/X_b$ the bond will develop expansion stresses, while the matrix will develop contraction stresses. The opposite response is observed when $\alpha_m/\alpha_b$ is lower than $X_m/X_{b.}$ It is important to realize that because of the values of thermal expansion considered for the cases $\alpha_m/\alpha_b$=0.5 and $\alpha_m/\alpha_b$=2 the magnitude of internal stresses developed in the matrix and in the bond, are similar.

This condition may explain why the evolution of the damage multiplier obtained for these two cases is very similar (Figure 4-30) just like the evolution of the composite material bulk modulus. As any mechanical strains is developed when $\alpha_m$ is equal to $\alpha_b$ no evolution for the damage multiplier or the composite material bulk modulus is observed.

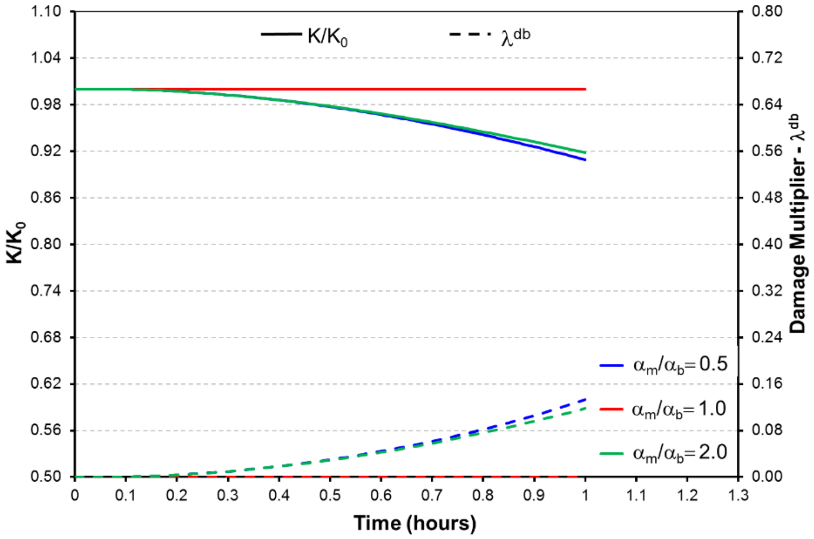

Figure 4-30 Evaluation of thermal expansion coefficient for $X_m$/Xb=1: bulk modulus and damage multiplier evolution

## *Case Xm/Xb=2 (Xm=0.8 Xb=0.4).*

Just as observed in the analysis of bulk modulus, for $X_m$ larger than $X_b$, the response obtained is contrary to what it is obtained when $X_m$ is lower than $X_b$. The total strains are higher for the bond than for the matrix, and the larger total strains are obtained when $\alpha_m/\alpha_b$ is superior to $X_m/X_b$.

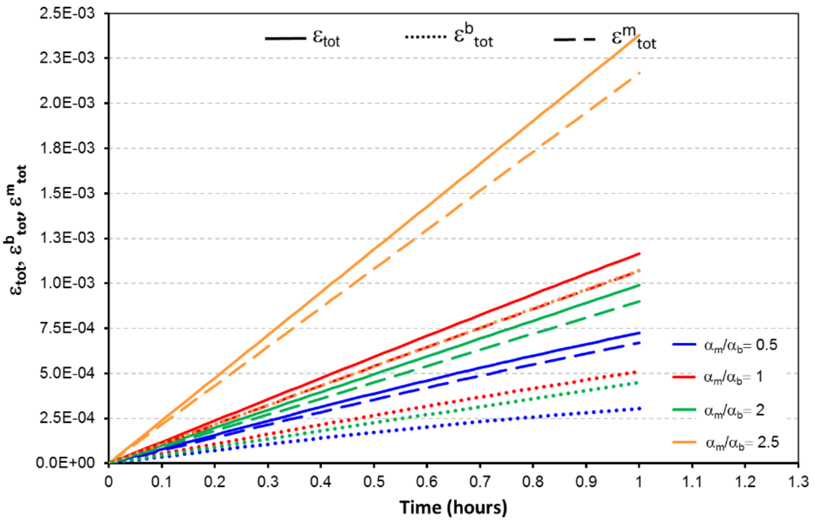

Figure 4-31 Evaluation of thermal expansion coefficient for $X_m$/Xb=2: total strains evolution

Similar to the two scenarios evaluated before, if $\alpha_m/\alpha_b$ is equal to $X_m/X_b$ the total bond and matrix strains will be equal to the deformation related to the thermal variations. Therefore, no mechanical strains and internal stress are developed, as observed in Figure 4-32.

In the other hand, if $\alpha_m/\alpha_b$ is higher than $X_m/X_b$ the bond will develop expansion and the matrix compression stresses, the opposite response is obtained if $\alpha_m/\alpha_b$ is lower than $X_m/X_b$, nevertheless the largest (in magnitude) internal stress are obtained (for the matrix and the bond) for the lowest $\alpha_m/\alpha_b$ ratio.

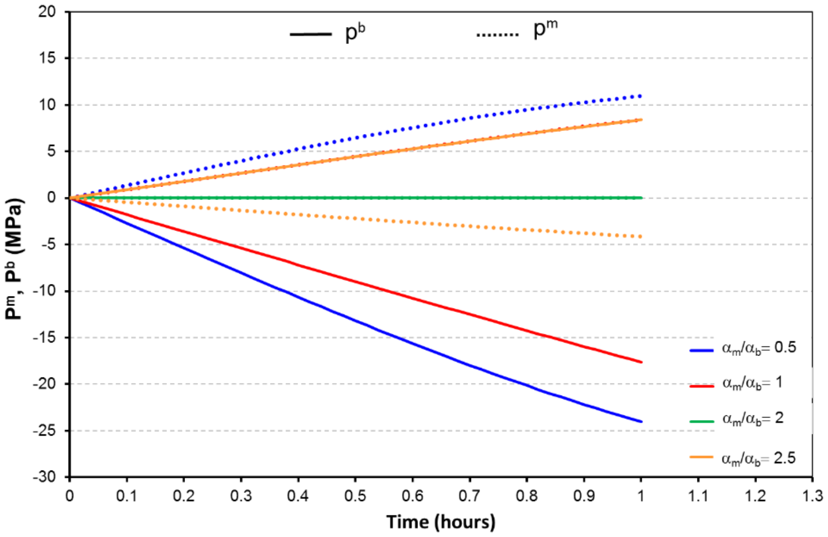

Figure 4-32 Evaluation of thermal expansion coefficient for $X_m$/Xb=2: internal stress evolution

In the same way, the thermal damage multiplier increases the most as the ratio between $\alpha_m$ and $\alpha_b$ is lower (Figure 4-33), hence the composite material bulk modulus reduces the most when $\alpha_m$ is inferior to $\alpha_b$.

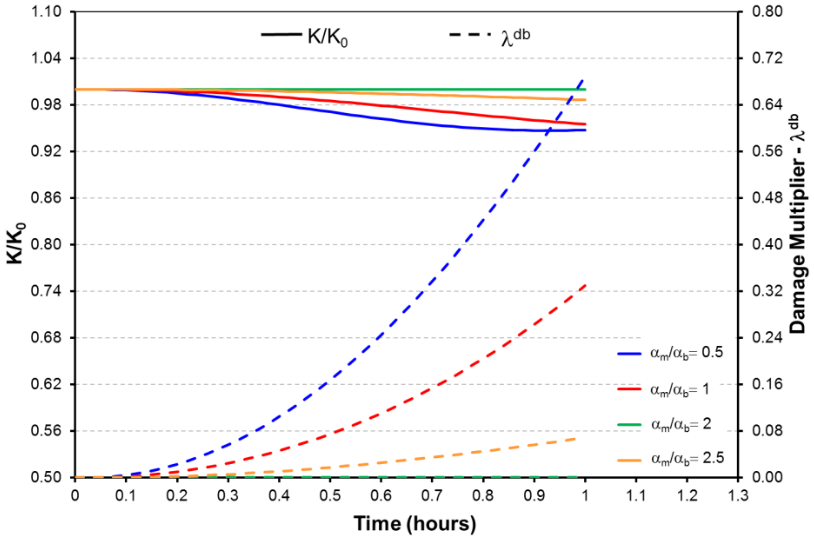

Figure 4-33 Evaluation of thermal expansion coefficient with $X_m$/Xb=2 – bulk modulus and damage multiplier evolution

It is interesting to point out that, for all the cases evaluated the maximal damage multiplier is obtained when $\alpha_b$ is higher than $\alpha_m$ ($\alpha_m/\alpha_b$=0.5) and $X_m$ is higher than $X_b$ ($X_m/X_b$=2). However, for this case the final bulk modulus for the composite material is only 95% of the initial one. Whereas, if $\alpha_b$ is lower than $\alpha_m$ ($\alpha_m/\alpha_b$=2) and $X_m$ is lower than $X_b$ ($X_m/X_b$=0.5), the final bulk modulus is 80% of the initial one. This characteristic is related to the values of $X_m$ and $X_b$ considered. If $X_m$ is higher than $X_b$ the matrix bulk modulus controls in the calculi of the composite material bulk modulus, otherwise, the bond bulk modulus (the one affected by the damage law) will be predominant.

### 4.4.3 Bond content.

In order to evaluate the effect of bonding content ($C_b$) and therefore matrix content ($C_m$) (Eq. 4-20) in the response obtained with the composite material constitutive law, three different scenarios of $C_b$ are considered: $C_b=0.2$ ($C_m=0.6$), $C_b=0.4$ ($C_m=0.4$) and $C_b=0.6$ ($C_m=0.2$).

According to the equation 4-41, the initial bulk modulus of the composite material depends on Cb and Cm, hence, the choice of parameters $X_m$ and $X_b$ must be adjusted to the bounds associated to the Hashin & Shtrikman (1963) bulk modulus bounds. Figure 4-34, presents the ratios considered in the present analysis.

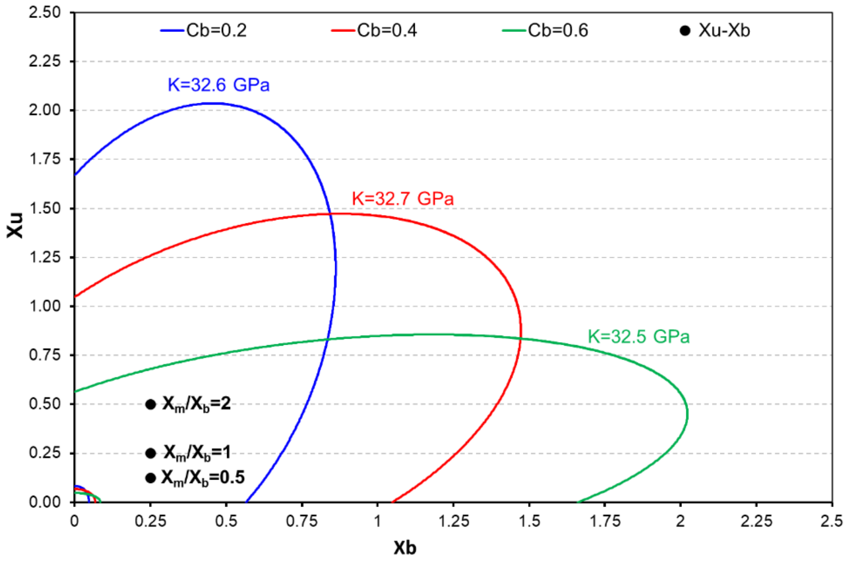

Figure 4-34 Coefficients $X_m$ and $X_b$ considered for the evaluation of different bond content

*Case Xm/Xb=0.5 (Xm=0.125 Xb=0.25).*

As observed in the former analysis, when $X_m$ is lower than $X_b$ the bond develop higher total strains than the matrix, yet, this is observed only if the bond content is lower or equal to the matrix content ($C_b=0.2$ and $C_b=0.4$).

Additionally, the highest values of total strains for the composite material are obtained for $C_b=0.6$, this is also observed for the matrix total strains. Nevertheless, the highest bond total strains are obtained for the lowest bond content, as illustrated in Figure 4-35.

For the case under evaluation ($X_m/X_b=0.5$), the bond develops expansion stresses when its content is lower or equal to the matrix one, whereas, the matrix is submitted to compression stresses, that means that the matrix cannot develop its complete thermal expansion. Otherwise, if the bond content is superior to the matrix, the bond is not able to develop its complete thermal expansion and it is submitted to compression stress, as presented in Figure 4-36.

The highest (in magnitude) internal stress are generated when $C_b$ is equal to 0.2, which is the minimal bond content considered. This may explain why this is the case where the highest damage multiplier is obtained and therefore the highest reduction in the composite material bulk modulus. See Figure 4-37.

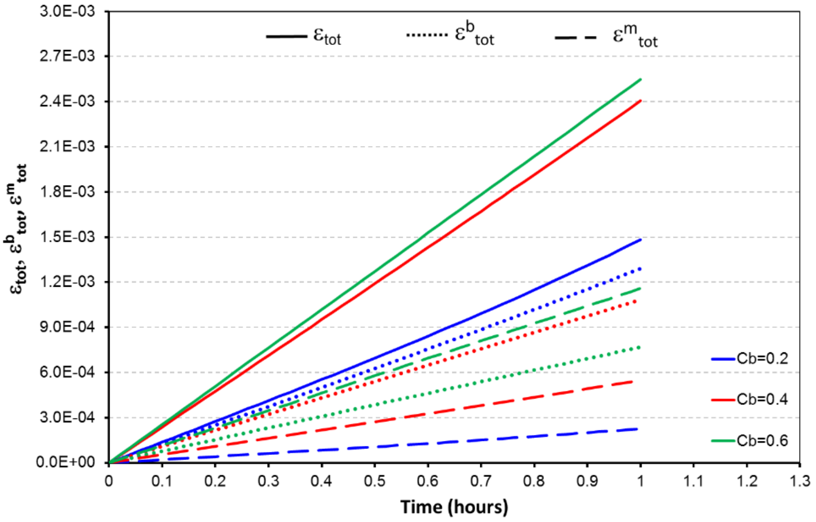

Figure 4-35 Evaluation of bond content for $X_m$/Xb=0.5: total strains evolution

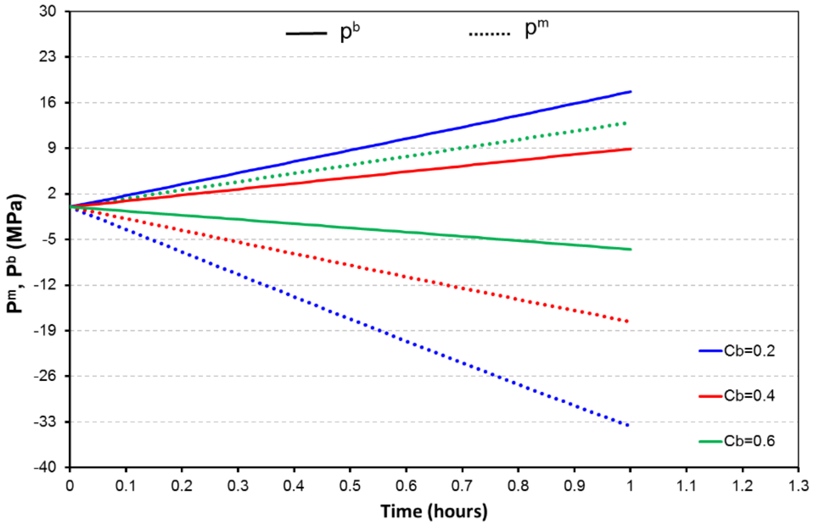

Figure 4-36 Evaluation of bond content for $X_m$/Xb=0.5: internal stress evolution.

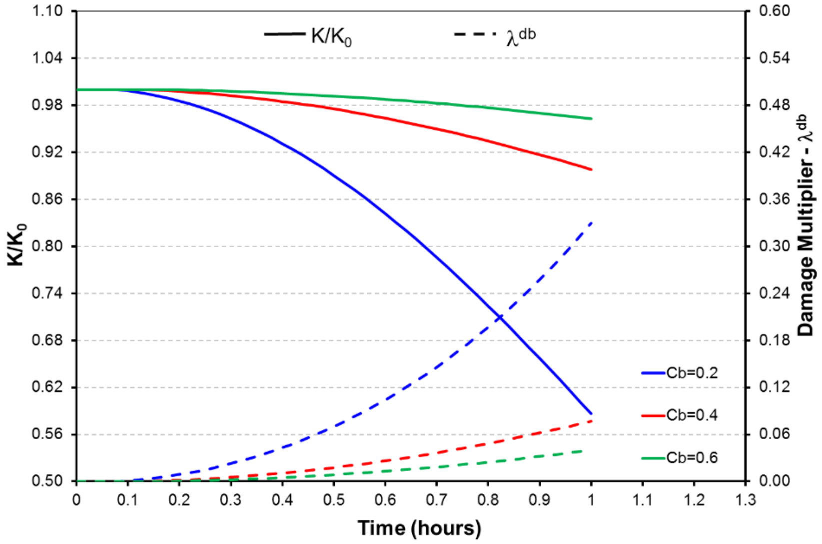

Figure 4-37 Evaluation of bond content for $X_m$/Xb=0.5: bulk modulus and damage multiplier evolution

### Case Xm/Xb=1 (Xm=0.25 Xb=0.25).

When equal values of $X_m$ and $X_b$ are considered, the highest total strains for the composite material are obtained when the material is composed by the same content of bond and matrix (Cb=0.4 in Figure 4-38). Moreover, for this case, the bond and matrix total strains are equal to the thermal strains; therefore, no internal stresses are developed, as presented in Figure 4-39.

For a bond content of 0.2 and 0.6 the total strains for the composite material are very similar, it is important to remember that for these two cases the content of bond and matrix are alike too, for $C_b$=0.2, $C_m$=0.6 and for $C_b$=0.6, $C_m$=0.2.

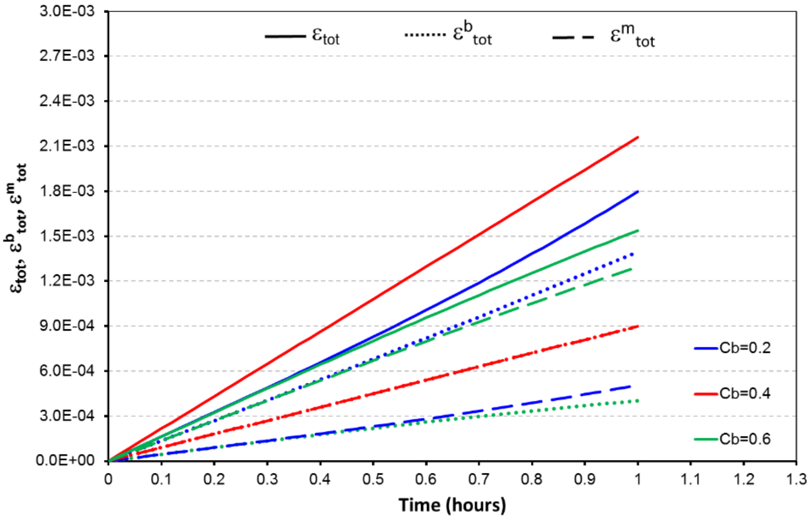

Figure 4-38 Evaluation of bond content for $X_m$/Xb=1: total strains evolution

This characteristic generates that the bond stress for $C_b$=0.2 are equal to the matrix stress when $C_b$=0.6, as the thermal expansion coefficients considered are also equal for both components. Moreover, if the bonding content is equal to 0.6 the matrix is submitted to expansion stress while the bond is submitted to compression, and the completely opposite response is observed when the bond content is equal to 0.2, see Figure 4-39.

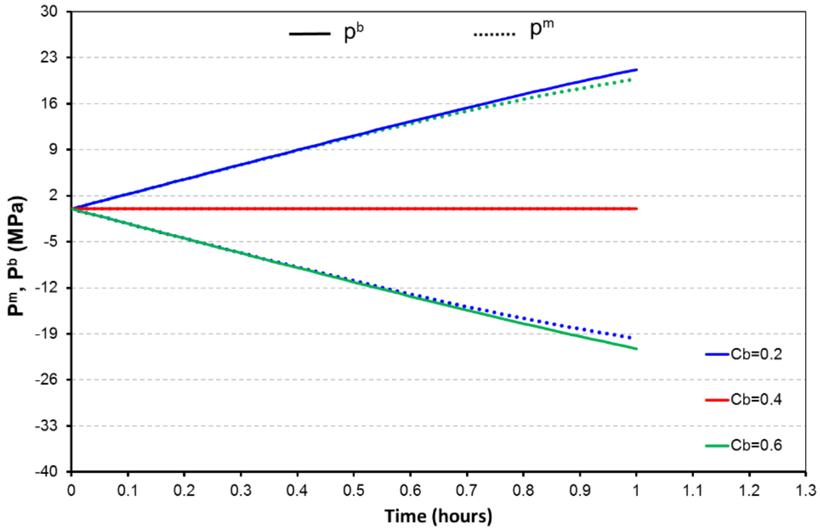

Figure 4-39 Evaluation of bond content for $X_m$/Xb=1: internal stress evolution

Because the magnitude of bond stress and strains are equal when the bond content is 0.2 and 0.6, the damage multiplier coefficient evolves very similarly for these two cases, as illustrated in Figure 4-40. Therefore, the bond bulk modulus reduces the same too. Nevertheless, if the bonding content is lower than the matrix content (Cb=0.2) a higher reduction of the composite material bulk modulus is observed. This condition is related to the fact that the composite material bulk modulus is directly proportional to the coefficient $U_\varepsilon$, that is itself inversely proportional to $C_b$.

In other words, if the bond content is lower than the matrix content the bulk modulus of the composite material will be strongly related to the bond bulk modulus, (affected by the damage law)

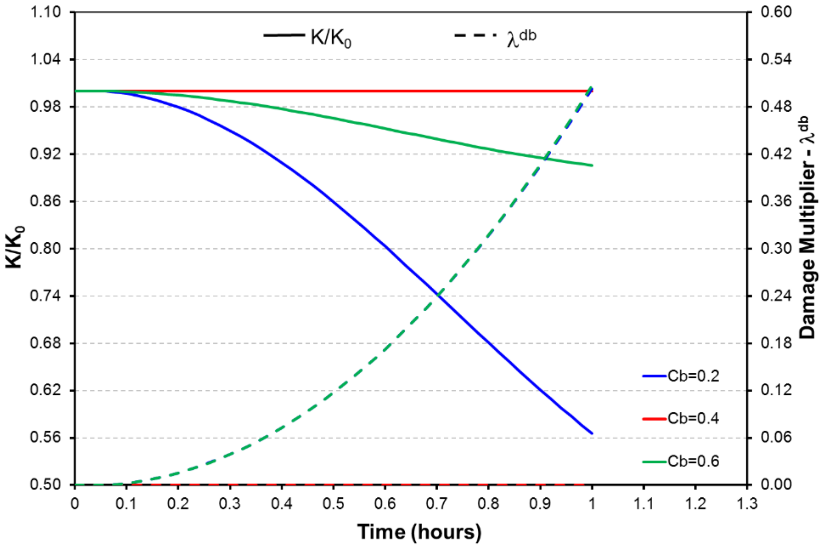

Figure 4-40 Evaluation of bond content for $X_m$/Xb=1: bulk modulus and damage multiplier evolution

## *Case Xm/Xb=2 (Xm=0. 5 Xb=0.25).*

As observed in the previous analysis, the response obtained when $X_m$ is larger than $X_b$ is the opposite to what is obtained for $X_m$ lower than $X_b$ ($X_m/X_b$=0.5) In first place, the total strains for the composite material are higher for the lowest bond content, while for the case $X_m/X_b$=0.5 this is obtained for $C_b$=0.6. Moreover, the matrix total strains are higher than the bond total strains if the bond content is equal or higher to the matrix content, as shown in Figure 4-41.

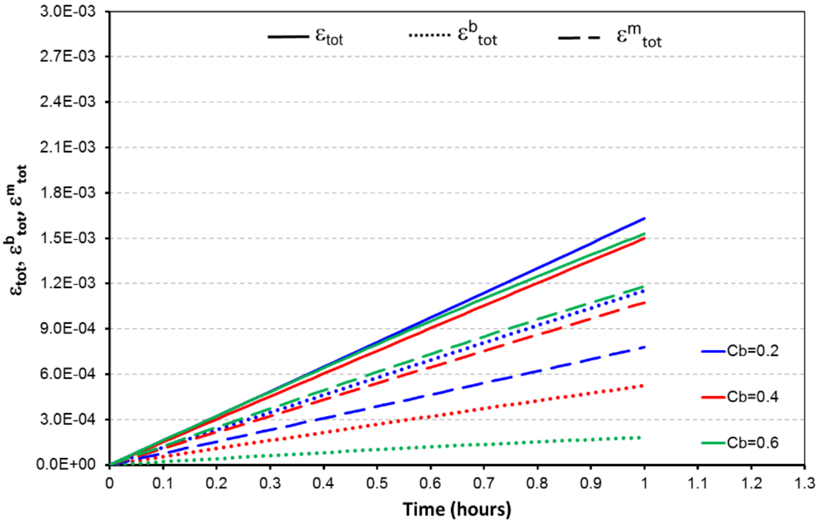

Figure 4-41 Evaluation of bond content with $X_m$/Xb=2 – Total strains evolution

Because of the total strains developed in the components, some mechanical strains are generated and therefore internal stresses appear too. When $C_b$=0.4 and 0.6 the matrix develops expansion stresses, and if $C_b$ is equal to 0.2, the matrix will be submitted to compression stress (see Figure 4-42).

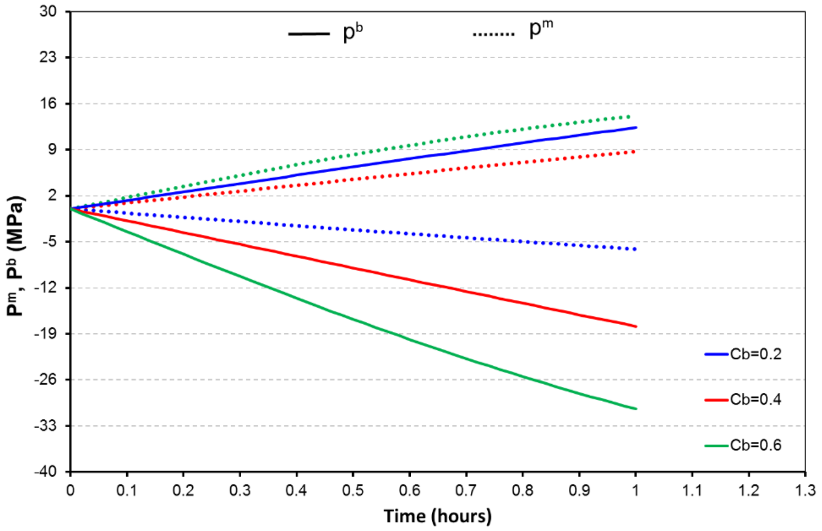

Figure 4-42 Evaluation of bond content for $X_m$/Xb=2: internal stress evolution

By comparing Figure 4-42 and Figure 4-43 it can be observed that the maximal bond stress is obtained when the bond content is 0.6, as usual, this is related to a higher increase of damage multiplier, therefore to a higher reduction of the bond bulk modulus. Nonetheless, the composite material bulk modulus is not much affected by this reduction. This can be associated to two different phenomena: first, the value of $X_m$ considered is larger than $X_b$, which generates that K is principally controlled by $K_m$. In the other hand, K is less affected by $K_b$ as higher is $C_b$. This last condition explains why even if the damage multiplier for $C_b$=0.2 increases the less; the reduction of the bulk modulus of the composite is the highest.

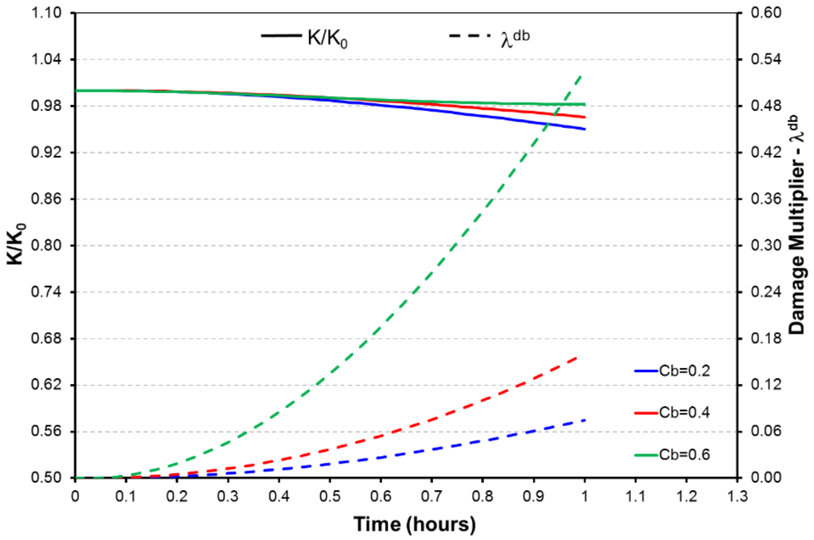

Figure 4-43 Evaluation of bond content for $X_m$/Xb=2: bulk modulus and damage multiplier evolution

### 4.4.4 Final remarks on model performance.

- If the coefficients related to the material microstructure, $X_m$ and $X_b$, are equal, and the composite material is form by two materials with similar properties, each component will be able to expand or contract without generating any internal stresses, therefore no damage is observed.
- The response obtained when $X_m$ is higher than $X_b$ is the opposite of the one observed when $X_m$ is lower than $X_b$
- According to the stiffness of the composite material—K expression, this parameter is directly proportional to the matrix and bond stiffness and inversely proportional to the matrix and bond content. K will be strongly related to the matrix stiffness if $X_m$ is higher than $X_b$ and to the bond stiffness if $X_b$ is higher than $X_m$.
- In general, the evolution of damage multiplier is directly proportional to the stresses developed in the bonding.
- The degradation of the bond stiffness is directly related to the damage multiplier increasing.

## 4.5 Modelling of experimental results.

The model is now used to reproduce the response of cyclic thermal tests performed in the laboratory and presented in section 3. Six tests have been modelled: two of them were performed on samples extracted from fall blocks (B3 and B7) and four on samples obtained from boreholes drilled from the cliff face (CV4, CV5, CH2 and CH3). CV4 and CV5 cored in the vertical direction, CH2 and CH3 in the horizontal one.

Table 4-2 Parameters used for the numerical modeling of samples

| | | Sample B3 | Sample B7 | Sample CV4 | Sample CV5 | Sample CH2 | Sample CH3 |
|---|---|---|---|---|---|---|---|
| Bond | $K_{b0}$ (MPa) | 75000 | 75000 | 75000 | 75000 | 75000 | 75000 |
| | $r_1$ | 0.002 | 0.002 | 0.001 | 0.001 | 0.001 | 0.001 |
| | $r_0$ | 1e-5 | 1e-5 | 1e-5 | 1e-5 | 1e-5 | 1e-5 |
| | Axial $\alpha_b$ (ºC$^{-1}$) | 2.5e-6 | 2.0e-6 | 6.0e-6 | 6.5e-6 | 4.2 e-6 | 6.0e-6 |
| | Radial $\alpha_b$ (ºC$^{-1}$) | 3.0e-6 | 3.0e-6 | 2.2 e6 | 3.0 e6 | 2.0 e-6 | 3.0 e6 |
| | $\eta^b$ | 1000 | 1000 | 1000 | 1000 | 1000 | 1000 |
| Matrix | $K_m$ (MPa) | 35000 | 35000 | 35000 | 35000 | 35000 | 35000 |
| | Axial $\alpha_m$ (ºC$^{-1}$) | 2.5e-6 | 2.0e-6 | 6.0e-6 | 6.5e-6 | 4.2 e-6 | 6.0e-6 |
| | Radial $\alpha_m$ (ºC$^{-1}$) | 3.0e-6 | 3.0e-6 | 2.2 e6 | 3.0 e6 | 2.0 e-6 | 3.0 e6 |
| | $\phi'_m$ | 30 | 30 | 30 | 30 | 30 | 30 |
| | $C`^m$ (MPa) | 46 | 46 | 46 | 46 | 46 | 46 |
| Composite material | Density $\gamma$ (kg/m3) | 2340 | 2340 | 2340 | 2340 | 2340 | 2340 |
| | Porosity | 0.12 | 0.18 | 0.2 | 0.2 | 0.18 | 0.17 |
| | $C_b$ | 0.78 | 0.72 | 0.4 | 0.5 | 0.41 | 0.415 |
| | $C_m$ | 0.1 | 0.1 | 0.4 | 0.3 | 0.41 | 0.415 |
| | $X_b$ | 1.1 | 0.67 | 0.23 | 0.23 | 0.24 | 0.35 |
| | $X_m$ | 0.28 | 0.3 | 0.52 | 0.32 | 0.49 | 0.61 |
| Thermal properties | Specific heat $C_s$ (J Kg$^{-1}$ K$^{-1}$) | 800 | 800 | 800 | 800 | 800 | 800 |
| | Thermal conductivity $\lambda_{dry}$ (W.m.K$^{-1}$) | 1 | 1 | 1 | 1 | 1 | 1 |

According to the framework developed, the limestone rock is considered as composed by two mineral phases. Mineral phase 1 corresponds to the matrix and is endowed with a linear cross-anisotropic thermo-elastic law and Mohr-Coulomb shear failure criterion. Mineral phase 2 corresponds to the called bonds and is modelled using a damage cross-anisotropic thermos-elastic law. As the limestone is essentially composed by quartz and calcite, the elastoplastic (matrix) and damage (bonds) materials are respectively associated to the more brittle (quartz) and the degrading phases (calcite) phases. For both materials, isotropic mechanical elastic parameters and cross-anisotropic thermal expansion coefficients have been considered.

The parameters considered for material are listed on Table 4-2.

They include physical properties: volumetric fraction of voids (porosity), matrix ($c_m$) and bonds ($c_b$), whose measured values vary from sample to sample. Matrix is associated to the hardest mineral phase (quartz) while bonds are associated to the calcite phase, more susceptible to experience degradation. In block samples, quartz volumetric fraction has been found close to 10%. Conversely, in cored samples, quartz and calcite appeared to have a similar volumetric fraction. One exception corresponds to sample CV5, whose proportion is around 40%/60%. Porosity has been obtained from laboratory density tests (see section 3.2).

Rock thermal properties have been taken from the measurements performed on sample B4 and presented in section 3.4.1.

In order to reduce the number of parameters to estimate, it has been considered that matrix and bonds are provided with the same thermal expansion coefficient. Under this assumption, the thermal coefficient was obtained for each sample from the external strains measurements presented in section 3.5.1. It is important to point out that, according to test results, thermal expansion coefficient has been considered anisotropic and two different values have been defined for the axial and radial directions.

Bulk modulus of quartz and calcite phases are taken from the typical values presented by Carmichael, 1989. Once fixed $K_m$, $K_b$, $c_m$ and $c_b$ for each sample, it is possible to back-analyzed $X_m$ and $X_b$ from the measurements of rock bulk modulus presented in section 3.5.2 and under the restrictions provided by Hashin & Shtrikman bounds. Table 4-3 presents the comparison between experimental values of rock modulus and the values obtained by the model after back-analyzing $X_m$ and $X_b$. Figure 4-45 presents an example of the verification carried out on sample CH3, which indicate that the values selected for $X_b$ and $X_m$ obey with the Hashin-Shtrikman lower and upper bounds. For block samples, $X_b$ parameter appears to be higher than $X_m$ while the opposite holds for the cliff samples.

Table 4-3 Initial bulk modulus values (MPa)

| | Experimental results | Numerical modeling |
|---|---|---|
| B3 | 24300 | 24020 |
| B7 | 19330 | 19360 |
| CV4 | 10470 | 10750 |
| CV5 | 8590 | 8300 |
| CH2 | 10360 | 10200 |
| CH3 | 14030 | 13550 |

Damage properties have been back-analyzed from the experimental results, looking for a unique value of damage locus and damage rate for samples belonging to each type of material. For the first type (material of fallen blocks), the damage rate appears to be twice higher that for the second type (material of cores).

As far as concerns to the rate dependency of the damage locus, a unique value (1000 $s^{-1}$) has been set for all the samples.

Finally, typical values have been chosen for the cohesion and the friction angle of matrix. These parameters will in fact not be activated in the computations because shear failure criterion has never been reached.

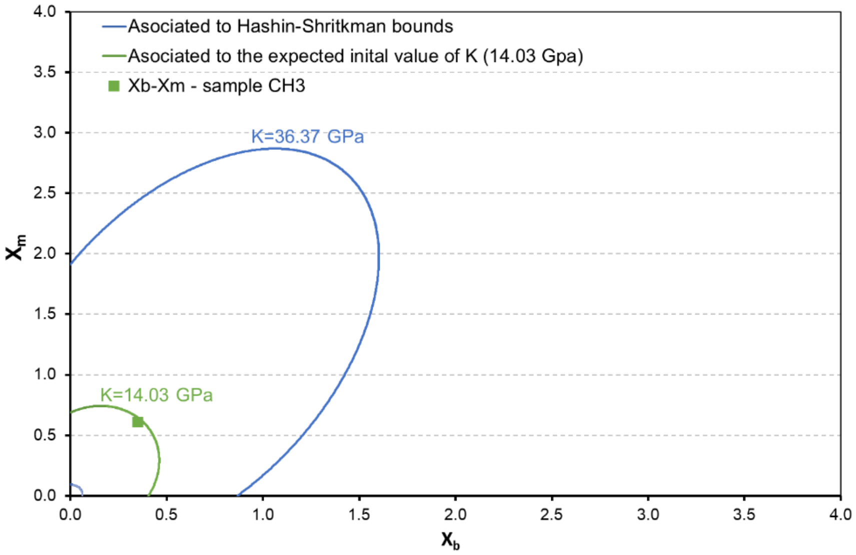

Figure 4-44 Coefficients $X_b$ and $X_m$ considered for the numerical modeling of sample CH3

### 4.5.1 Performed analyses

In a first step, in order to investigate the capability of the constitutive law to model the degradation of elastic moduli under thermal cycles, laboratory tests will be simulate as a material point. To do it, the cubic geometry presented in Figure 4-7 is used and temperature variations are applied simultaneously at all the nodes of the problem. In this type of modelling, thermal gradients are null and there is no heat front propagation inside the samples, which corresponds to the case of a quasi-steady state heating process. The response computed at all Gauss points of the model is then the same and draw the stress-strain-temperature relationship of the material governed by constitutive law.

Figure 4-45 and Figure 4-46 present the evolution of the rock bulk modulus computed respectively for the block and core samples. They compared favorably with the evolution obtained from test results for all the samples. It must be empathized that $X_b$ and $X_m$ are the only parameters with no direct relationship with material physical properties that have been changed from sample to sample.

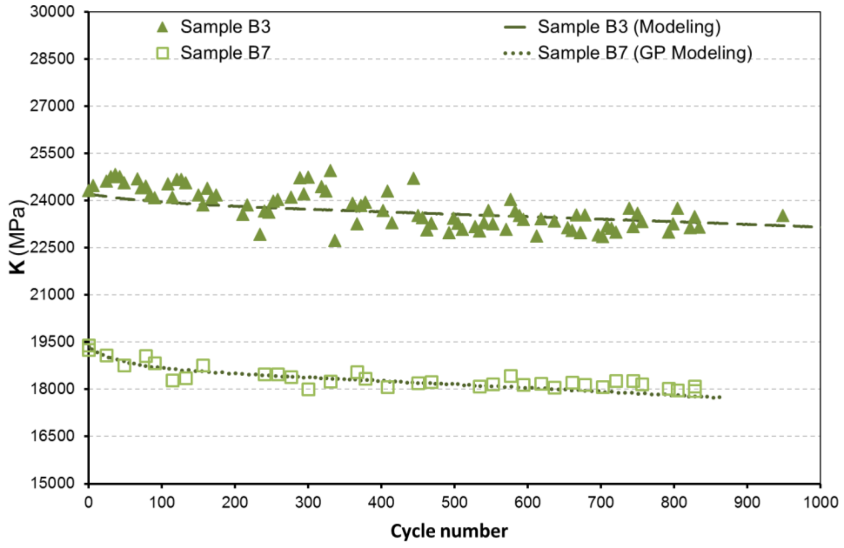

Figure 4-45 Gauss point modeling for block samples

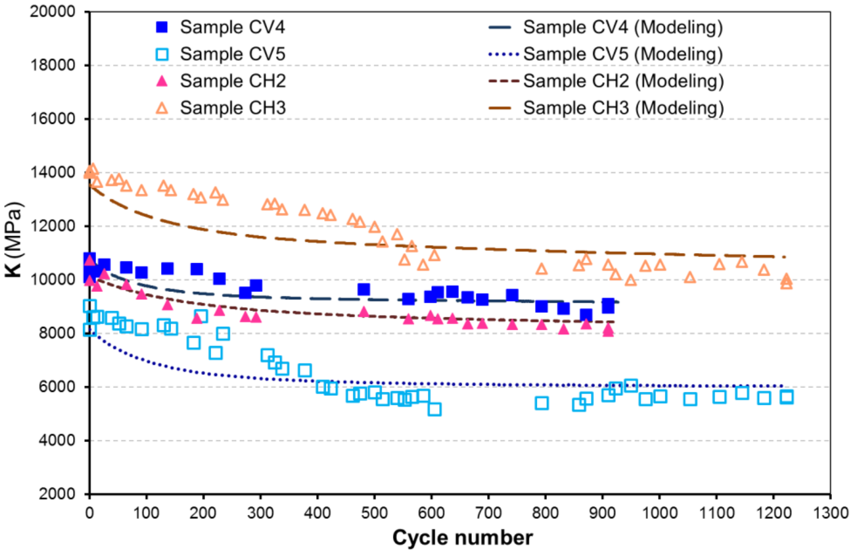

Figure 4-46 Gauss point modeling for cliff samples

In a second step, each test has been modelled as a boundary value problem. The objective of these simulations is to better represent the test conditions and particularly the additional effect of the spatial variation of thermal expansion due to heat front propagation and regression on the damage of the rock.

The sample geometry considered for the analysis is shown in Figure 4-47. It consists of an axisymmetric geometry with diameter equal to 5 cm and height to 10 cm. Temperature variations are prescribed at all the outer boundary. Results will be presented in the next sections for all the samples and at points labelled A and B in the figure.

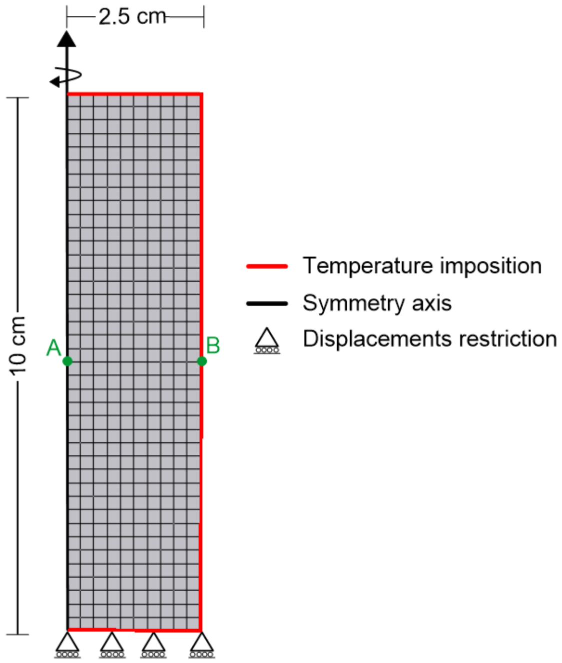

Figure 4-47 Geometry and mesh for the axisymmetric model

### 4.5.2 Sample B3.

The evolution of the bulk modulus computed by the Finite Element model at point A and B is shown in Figure 4-48 and compared with the measurements. The time evolution of K obtained by the constitutive law is also shown in the figure.

It can be observed that the evolution computed by the model is within the range of measured data and follows the general trend of elastic degradation evidenced by the test. However, model is not able to reproduce the K-variations measured at lower numbers of cycles. Data scattering makes nevertheless difficult to conclude about the origin of these discrepancies.

Aditionally, the Finite Element model predicts a reduction of bulk modulus at the sample axis (point A) lower than at samples surface (point B). This effect can be attributed to two main effects. In first place, the amplitude of temperature cycles is less at the axis than at the boundary as the result of the heat diffusion process inside the sample. And in the other hand the axisymmetric condition reduces the radial and circumferential strain at point A and all the damage is mostly related to the development of axial strain.

Moreover, the highest bulk modulus reduction is observed in the elements where the boundary conditions are imposed, as can be observed in Figure 4-49, where the distribution of bulk modulus inside the sample is presented for different cycles. Note that the bulk modulus is lower in elements where the temperature variations are imposed at two boundaries (the external corners).

Similar results are obtained in the evolution of damage multiplier thought the imposition of thermal cycles, presented in Figure 4-50. It can be observed that damage multiplier increases the most on the boundary of the sample (point B) than at the axis (point A), which can be linked to lower bulk modulus values at point B than at point A.

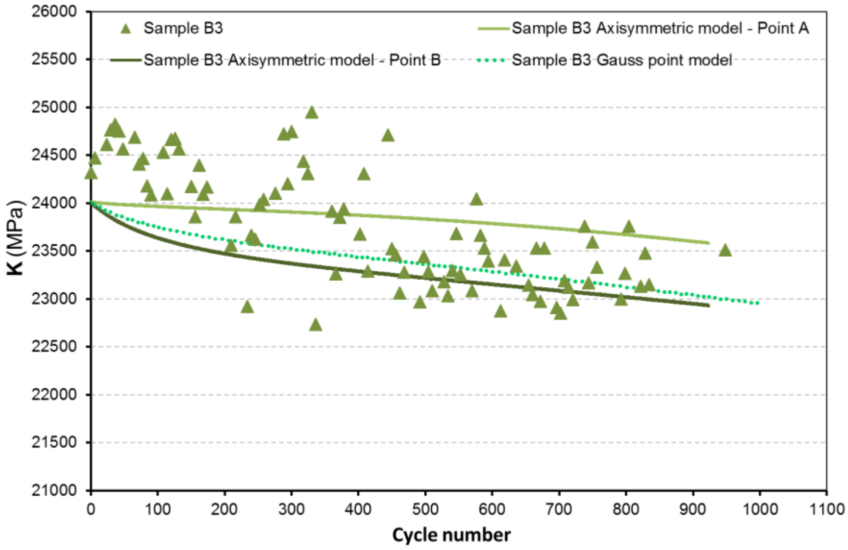

Figure 4-48 Sample B3: Bulk modulus evolution

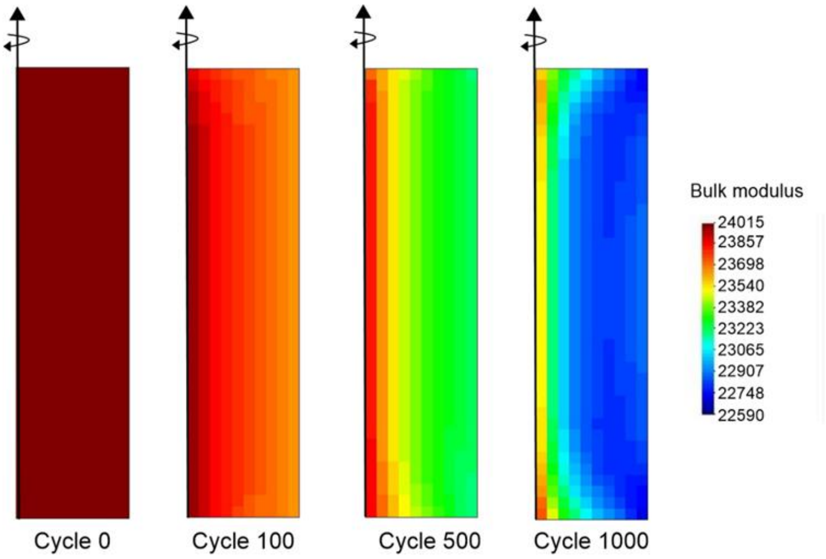

Figure 4-49 Sample B3: Bulk modulus evolution in the sample

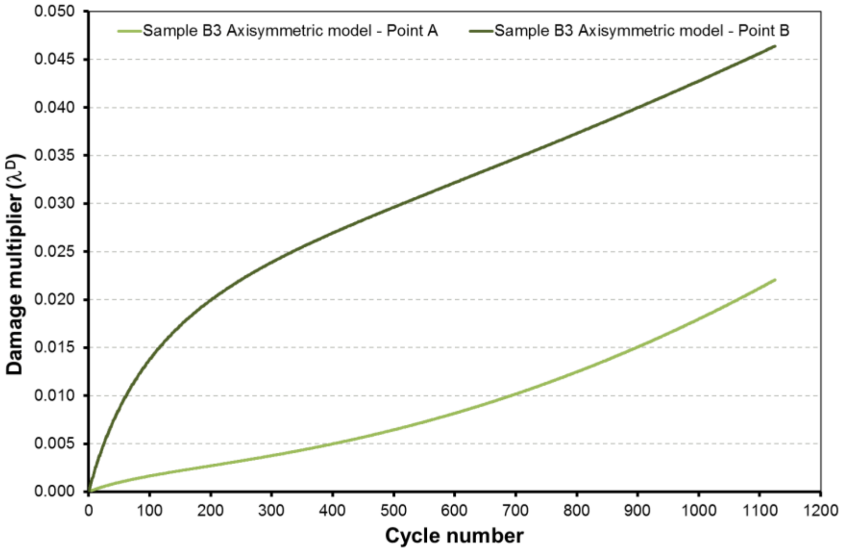

Figure 4-50 Sample B3: Damage multiplier evolution

As mention on section 4.4, the evolution of the composite material bulk modulus when $X_b$ is higher than $X_m$ is directly related to the evolution of the damage multiplier. This may explained why, the bulk modulus distribution inside the sample is very similar to the evolution of damage multiplier, as can be observed by comparing Figure 4-49 and Figure 4-51. Remember that thermal cycles generate an augmentation in the damage multiplier (higher values in red) related to a reduction in the bulk modulus (lower values in blue).

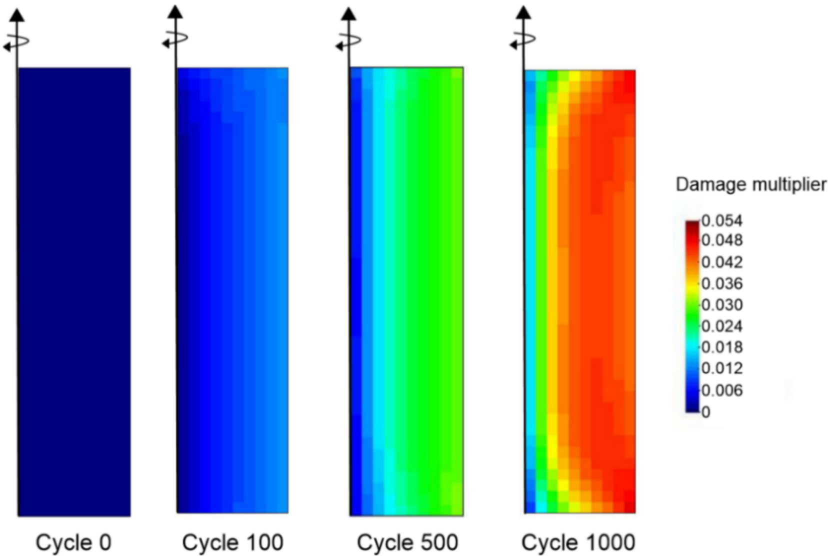

Figure 4-51 Sample B3: Damage multiplier evolution in the sample

The finite element model generates a small strains accumulation, contrary to what was observed in the experimental program (see section 3.5.1). After 1000 thermal cycles the model predicts an axial strains accumulation of 8.22e-6 m/m and an accumulation equal to 1.26e-5 m/m in radial direction both in negative direction (compression). Figure 4-52 and Figure 4-53 presents the comparison between measurements and results obtained with the asymmetrical model for axial and radial strains respectively. The model results considered are obtained at point B, as the strain measurements were performed at the boundary of the sample.

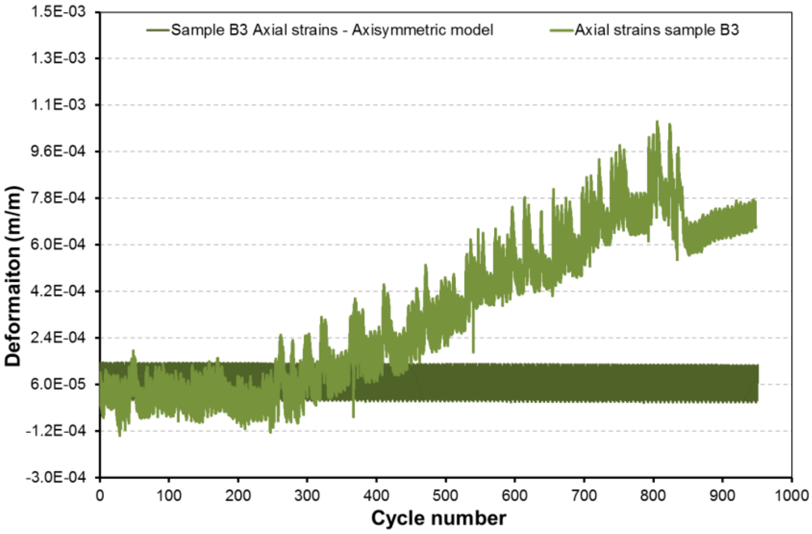

Figure 4-52 Sample B3: Axial strains

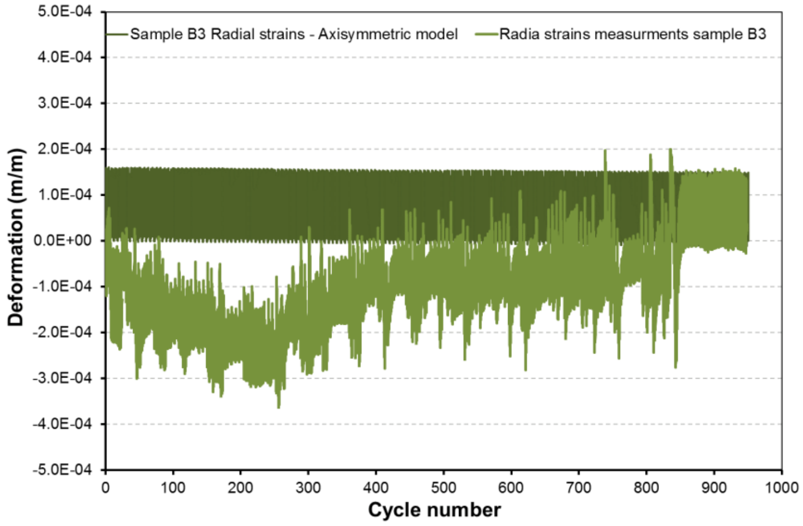

Figure 4-53 Sample B3: Radial strains

These small variations in strains indicate that the reduction in bulk modulus is mostly related to a stress accumulation. This phenomenon can be related to the conditions of the problem under evaluation, as the only external load imposed is the thermal variations, the strains associated will be related to the thermal expansion coefficient of the material, which is invariable. Moreover, the damage generates a stress transfer between the components, because the bond stiffness reduction.

Figure 4-54 presents the evolution of the mean stress with the imposition of thermal cycles at the two points of analysis at the axis (Point A) and at the boundary (Point B). Higher stresses are developed in the sample axis than at the boundary. Moreover, the stresses at the boundary developed an important increment through the imposition of thermal cycles, associated to the stiffness reduction obtained at this point. While, the stress at point A remains more or less constant for the whole analysis time.

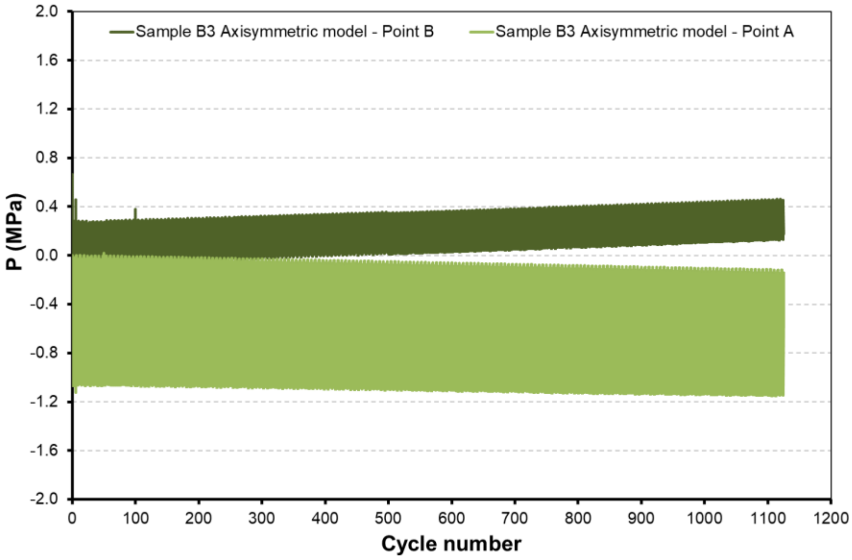

Figure 4-54 Sample B3: Mean stress evolution

Nevertheless, from Figure 4-55 it can be observed that strains response obtained for a 24 hours period is very similar to the measurements, validating the thermal expansion coefficients considered.

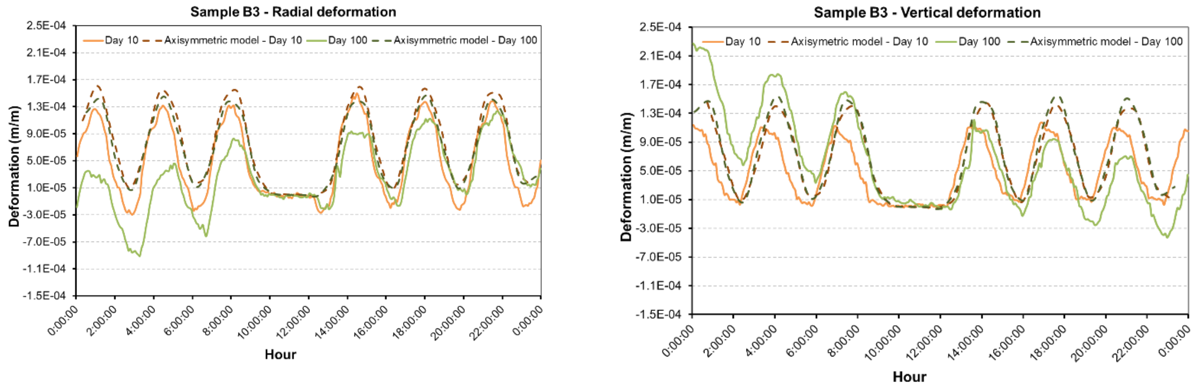

a) b)

Figure 4-55 Sample B3: Strains amplitude a) radial strains b) axial strains

### 4.5.3 Sample B7.

The evaluation of thermal damage on sample B7 was follow only by measurements of elastic wave propagation, thus the evaluation of the finite element model is only related to stiffness evolution

Figure 4-56 presents the bulk modulus evolution predicted with the numerical models and measured data. Similar to sample B3 case, the bulk modulus reduces less at the axis sample (point A) than at its face (point B). Results obtained with the Gauss Point model are closer to the results obtained at point B, because the temperature evolution imposed for the gauss point model is the one registered at the boundary of the sample. Good agreement is obtained with the finite element model and measurements.

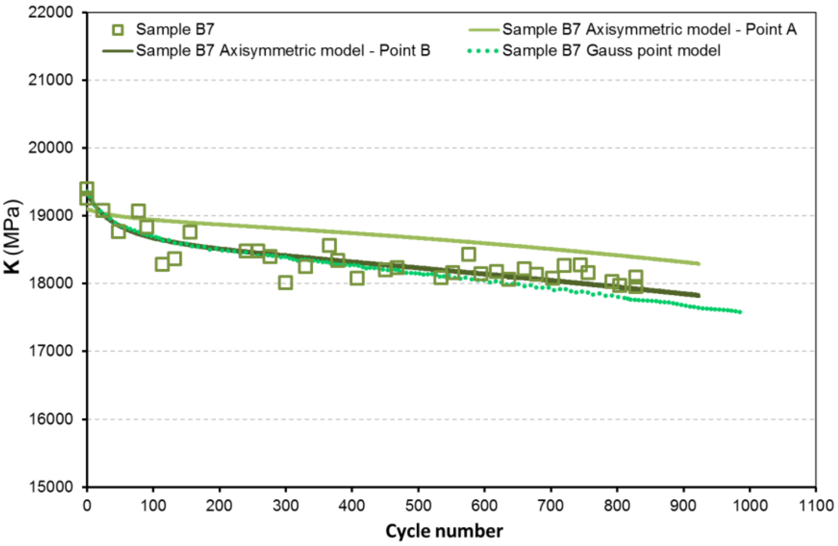

Figure 4-56 Sample B7: Bulk modulus evolution

Figure 4-57 presents the evolution of the damage multiplier obtained at points A and B, for the modeling time the damage multiplier at point B (sample surface) is much higher than at point A (sample axis). Moreover, from Figure 4-58 it can be observed that the evolution of damage multiplier through the thermal cycles for sample B7 is similar to the one obtained for sample B3 (Figure 4-51).

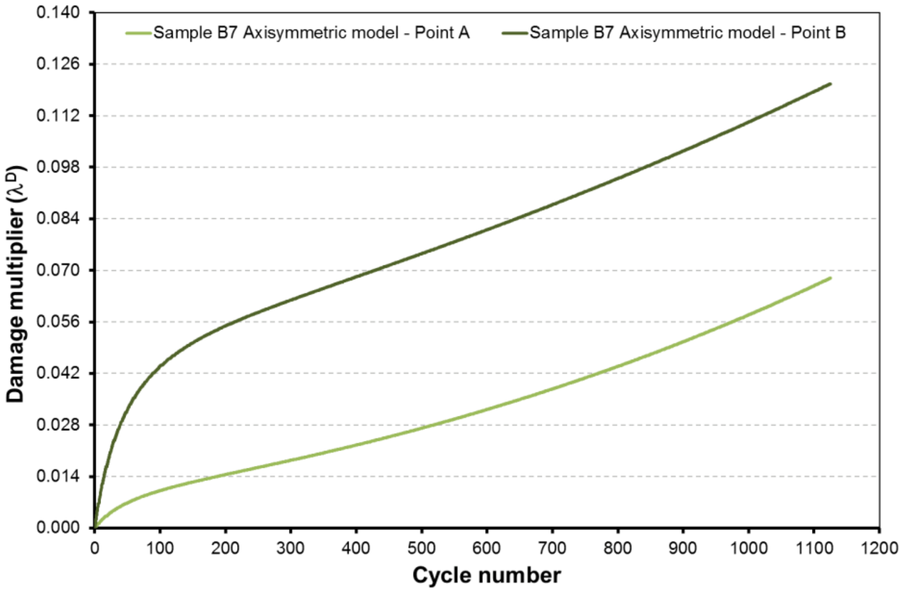

Figure 4-57 Sample B7: Damage multiplier evolution

By comparing the results obtained on samples B3 and B7 that constitute samples obtained from blocks, and therefore similar mineralogical composition, it is observed that the maximal damage multiplier after 1000 thermal cycles is higher in sample B7 (0.12) than in sample B3 (0.05), which is related to the differential stiffness reduction observed in both samples.

The axial and radial thermal expansion coefficients selected for the numerical modeling of sample B7 were obtained from the deformation measurements obtained in other block samples (sample B1, B2 and B3). The radial and axial strains obtained are presented in Figure 4-59. In this case a small strains accumulation is obtained (-3.19e-5 m/m in axial direction and -4.15e-5 m/m in radial direction), nonetheless, the reduction in bulk modulus is mostly related to stress increasing.

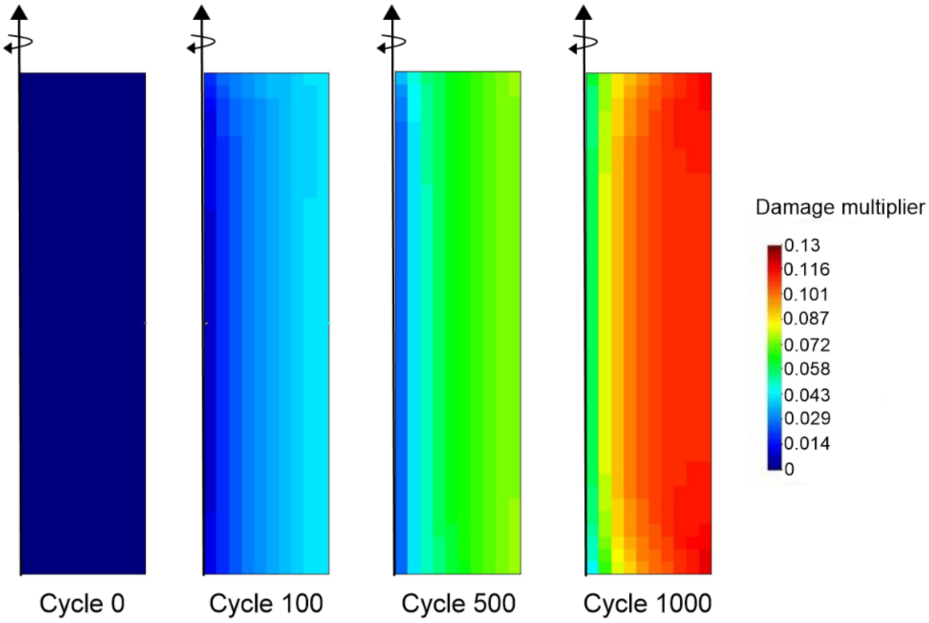

Figure 4-58 Sample B7: Damage multiplier evolution in the sample

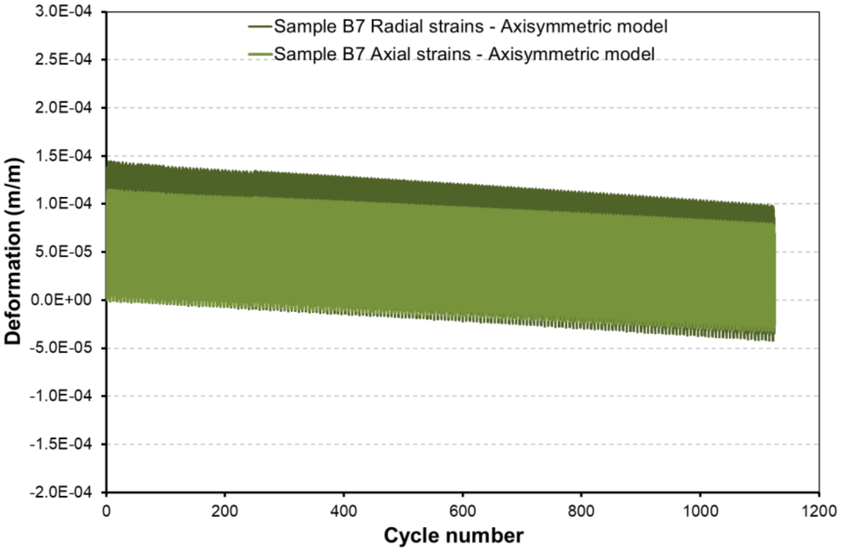

Figure 4-59 Sample B7: Axial and radial strains evolution

### 4.5.4 Sample CV4.

Results obtained for the bulk modulus evolution on sample CV4 is presented in Figure 4-60. It reduces more in the axis of the sample (point A) than at the boundary (point B) with the imposition of thermal cycles. Some discrepancies between the element finite model prediction and measurements are observed especially for the first 500 cycles, nevertheless, after this moment modeling results obtained are closer to the laboratory data.

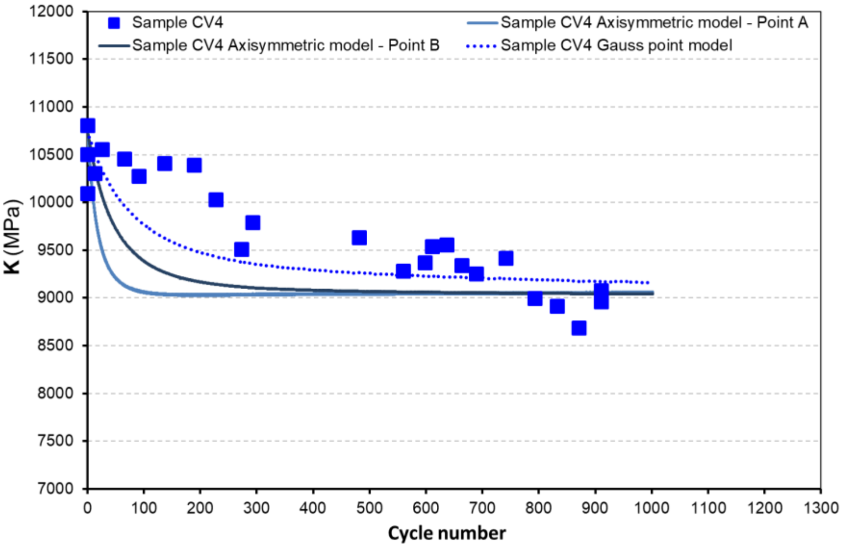

Figure 4-60 Sample CV4: Bulk modulus evolution

Figure 4-61 shows the stiffness evolution in the sample for punctual thermal cycles, showing that the stiffness obtained with the finite element model at cycle 500 and cycle 1000 are very similar and almost constant for the whole sample, while for cycle 100 it is lower closer to the symmetry axis.

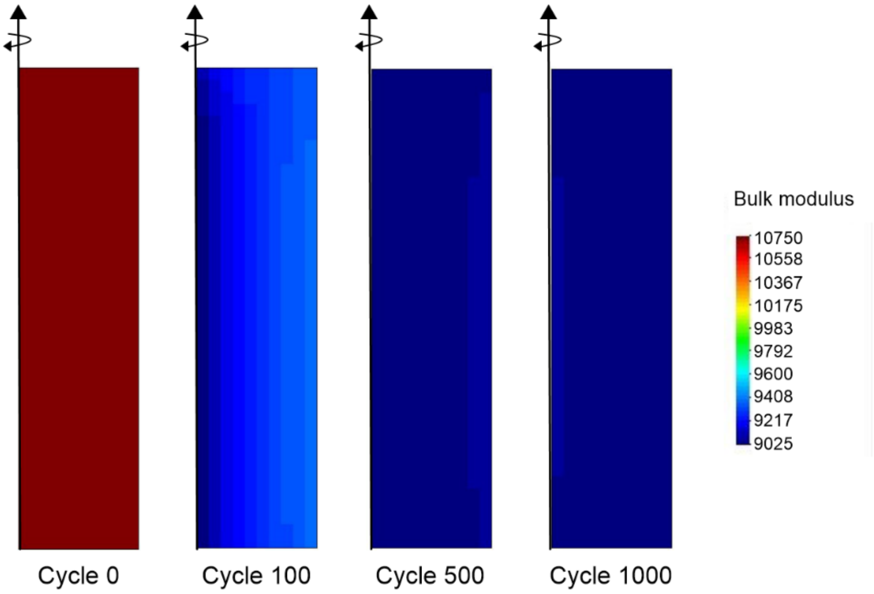

Figure 4-61 Sample CV4: Bulk modulus evolution in the sample

It is important to remark that the response obtained with sample CV4 is the opposite of the calculated on samples B3 and B7. This is higher bulk modulus at the axis (point A) than at the surface (Point B). This can be related to the thermal expansion coefficients considered in the modeling of sample CV4, thermal expansion coefficient in axial direction is 3 times the one considered in radial direction (see Table 4-2). This may generate that internal stresses are higher at the axis of the sample, inducing more damage as can be observed on Figure 4-62 (higher damage multiplier at point A than B), and as result, higher reduction in the bulk modulus for point A than point B.

Moreover, the bulk modulus obtained for the Gauss Point model (Figure 4-60) is higher than the values obtained with the axisymmetric model, since for the GP model an isotropic the thermal expansion coefficient and equal to one third of the volumetric value was considered, thus no additional stresses that may affect the bulk modulus evolution were generated.

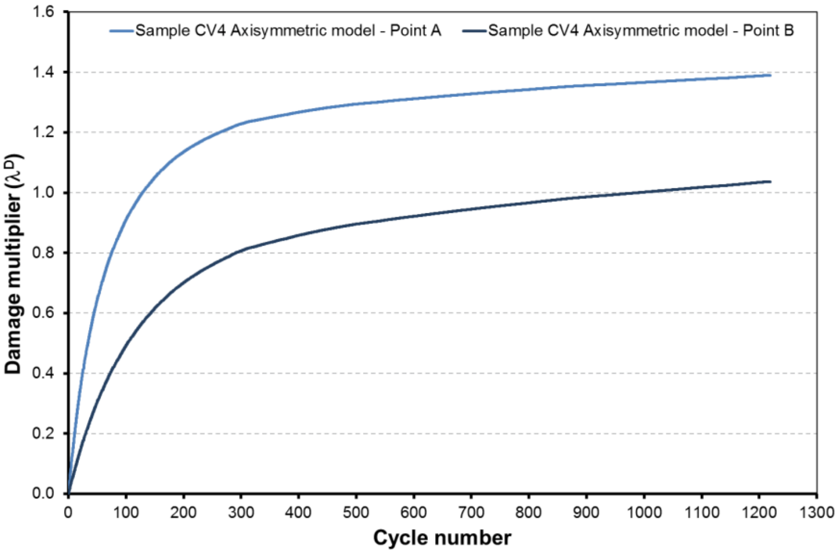

Figure 4-62 Sample CV4: Damage multiplier evolution

As mentioned before, for the numerical modeling of samples drilled from the face of the cliff the parameter of $X_m$ is higher than $X_b$, which makes that the evolution of bulk modulus is not strictly related to the evolution of damage multiplier (see section 4.7).

In fact, damage multiplier for points A and B (Figure 4-62) increases for the whole modeling time (1200 cycles) while the bulk modulus (Figure 4-60) remains constant after cycle 500. Nevertheless, it is important to point out that the damage multiplier presents a very steep tendency for the first 400 cycles, which can be related to a higher stiffness reduction.

By comparing Figure 4-61 and Figure 4-63, it can be remarked that the distribution of stiffness in the sample CV4 is different to the damage multiplier distribution (the opposite to what was observed in the block samples), nevertheless, the elements with lower bulk modulus coincides with higher damage multiplier values.

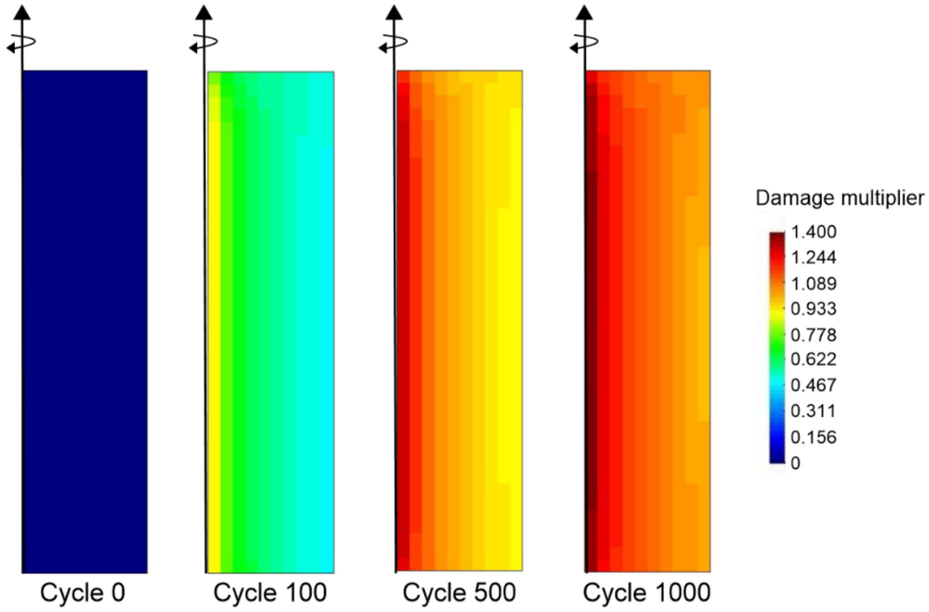

Figure 4-63 Sample CV4: Damage multiplier evolution in the sample

The maximal values of damage multiplier are much higher (10 times higher) than those observed with the modeling of block samples. Values of damage multiplier obtained (higher than 1) are related to the effect of the rate dependency considered for the reproduction of samples.

Additionally, strains measurements in sample CV4 were follow during the thermal cycling imposition, Figure 4-64 and Figure 4-65 presents the axial and radial strains predicted with the finite element model and measurements. For this case a slight strains accumulation is obtained with the axisymmetric model, -1.10e-4 m/m in axial and -7.25e-5 m/m in radial direction after 1000 thermal cycles, lower accumulated values, not to mention opposite direction to what it is observed with the experimental measurements. Moreover, the strains amplitudes (Figure 4-66) are adequately reproduce by the model.

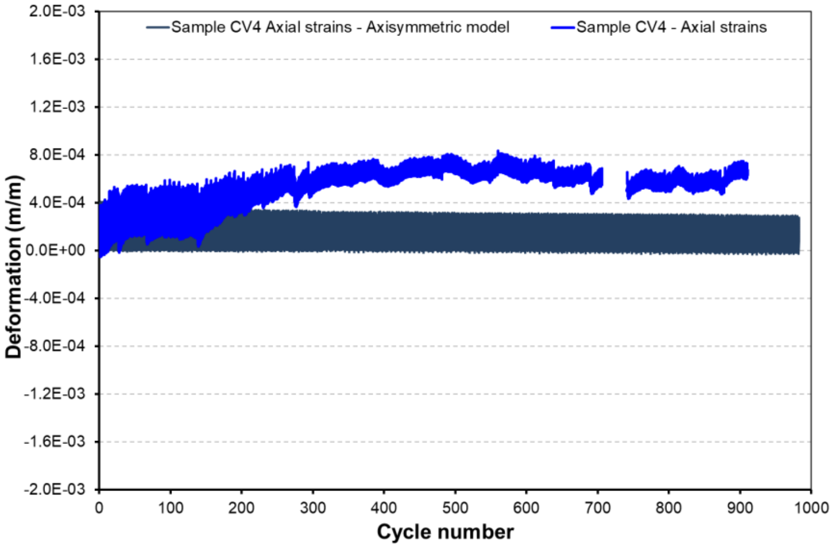

Figure 4-64 Sample CV4: Axial strains evolution

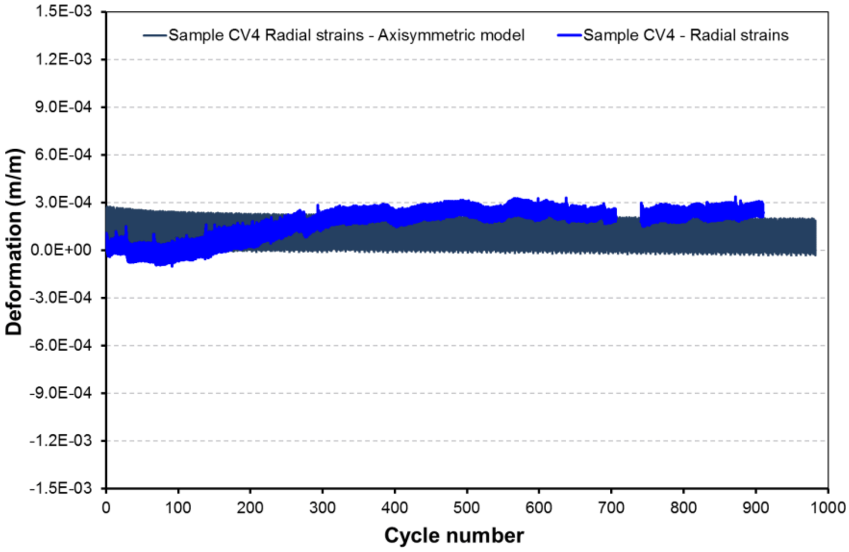

Figure 4-65 Sample Cv4: Radial strains evolution

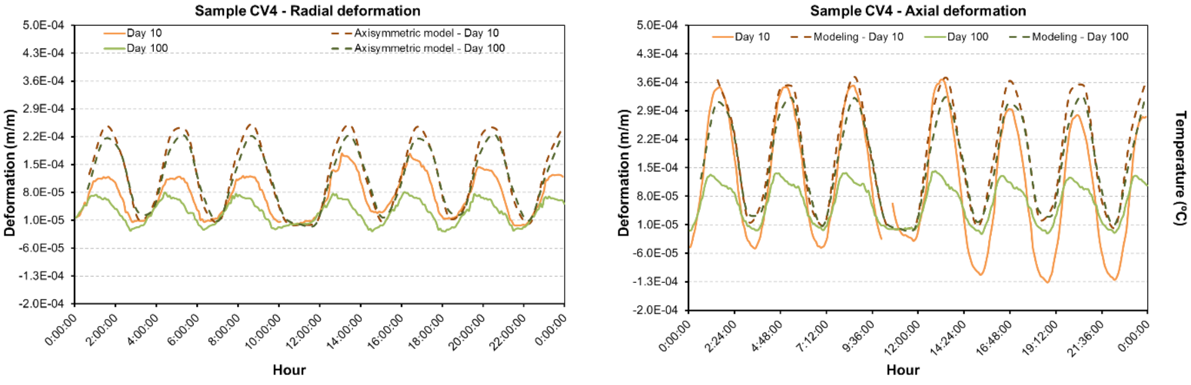

a) b)

Figure 4-66 Sample CV4: Strains amplitude a) radial strains b) axial strains

Therefore, the stiffness reduction observed is mainly related to an increment in the internal stresses. Figure 4-67 presents the evolution of mean stress at point A and B, stresses developed at the axis are higher than at the boundary, similar to what is observed on block samples (see

Figure 4-54). Stresses at point A presents shows an important reduction while the stresses at point B shows a slight increment.

Moreover, it can be observed that the mean stress reduction in point A is higher for the first 300 cycles, this can be related to the damage multiplier evolution (Figure 4-62) that shows an important increment for this period.

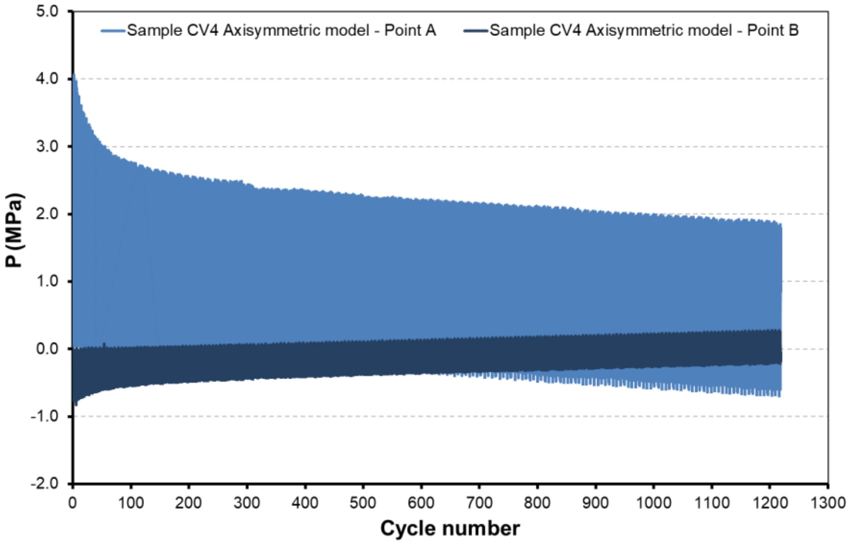

Figure 4-67 Sample CV4: Mean stress evolution

### 4.5.5 Sample CV5.

Sample CV5 presents the highest decrease (34%) in bulk modulus for all the samples evaluated in the experimental program (section 3), additionally, the initial bulk modulus for this sample is very low. From the mineralogical composition of samples (section 3.3.1) it was observed that samples obtained from the cliff presented a quartz content may reaches the 50%. This is why, the bonding and matrix content are considered equal for the numerical modeling of these. However, with this condition it is not possible to obtain the initial bulk modulus value and the evolution observed for sample CV5. Consequently, the matrix content (quartz) was reduced.

Despite this correction in the bond and matrix content, the bulk modulus obtained with the numerical modeling after 1200 thermal cycles is slightly higher than the value registered in the experimental study (500 MPa higher), see Figure 4-68. Nevertheless, it can be considered that the results obtained with the numerical model is a good approximation for the response of this sample, after 1200 thermal cycles a reduction of 27% in the bulk modulus is obtained.

From Figure 4-68, it can be remarked that similar to sample CV4, the bulk modulus reduces faster at the axis (point A) than at the boundary of the sample (point B). Furthermore, the bulk modulus evolution obtained with the Gauss Point model is placed above the evolution obtained with the axisymmetric model at point A and B. It is also important to point out that similar to what it is observed with the measurements, the bulk modulus show almost any evolution after 500 cycles.

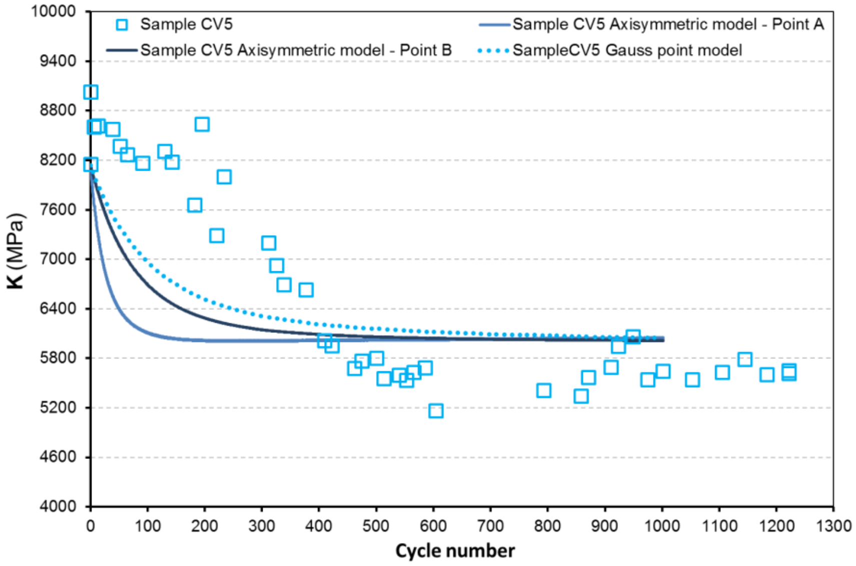

Figure 4-68 Sample CV5: Bulk modulus evolution

An interesting relation between the bulk modulus (Figure 4-68) and damage multiplier (Figure 4-69) evolution is observed. The response of the first 500 cycles shows an important reduction of bulk modulus associated to a damage multiplier increment, after this point the bulk modulus tends to a stable value and the damage multiplier continue to increase but with a less steeper response.

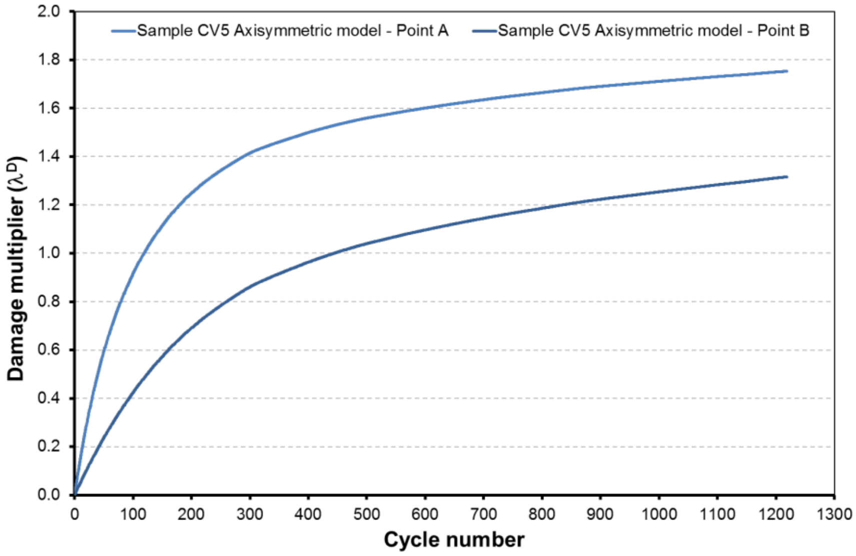

Figure 4-69 Sample CV5: Damage multiplier evolution

Analogous to sample CV4 and as can be assumed from the bulk modulus evolution, the damage multiplier is higher at point A than at point B. Moreover, the value obtained after 1200 cycles is higher than the one registered for sample CV4 but with similar magnitude order.

During the experimental program, the deformation was not measured in sample CV5, thus the thermal expansion coefficient consider for this sample was adjusted form the strains measurements performed in other vertically drilled samples (CV1 and CV4). Figure 4-70 shows the strains response obtained with the axisymmetric model of sample CV5 in axial and radial direction. It can be observed that this sample shows a strains reduction with thermal cycles imposition, especially for the first 400 cycles, the same period that presents higher damage multiplier increasing. Again, the stiffness reduction is mostly related to the accumulation of stresses.

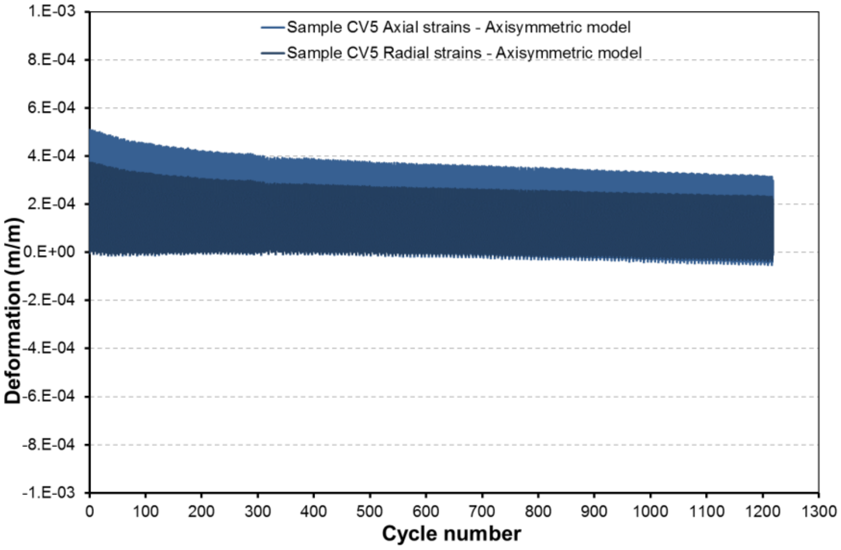

Figure 4-70 Sample CV5: Axial and radial strains evolution

### 4.5.6 Sample CH2.

The response of bulk modulus obtained for sample CH2 is presented in Figure 4-71, it can be observed that the finite element model reproduces adequately the data measured during the experimental program. In the same way to what was observed in the other cliff samples, the bulk modulus reduces the most in the axis than the sample boundary, and the results obtained with the GP model shows a lower stiffness reduction. From Figure 4-72 it can be observed that the bulk modulus is smaller as closer is the element to the symmetry axis, as is expected from the bulk modulus evolution at points A and B.

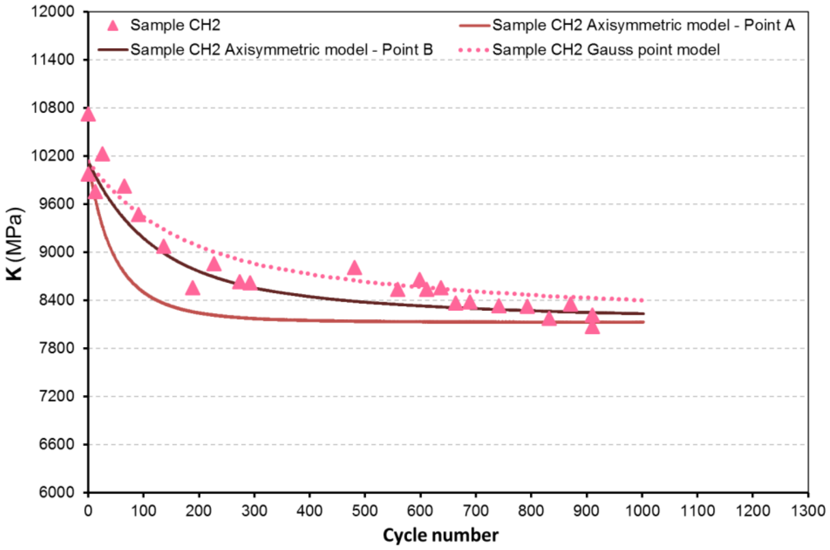

Figure 4-71 Sample CH2: Bulk modulus evolution

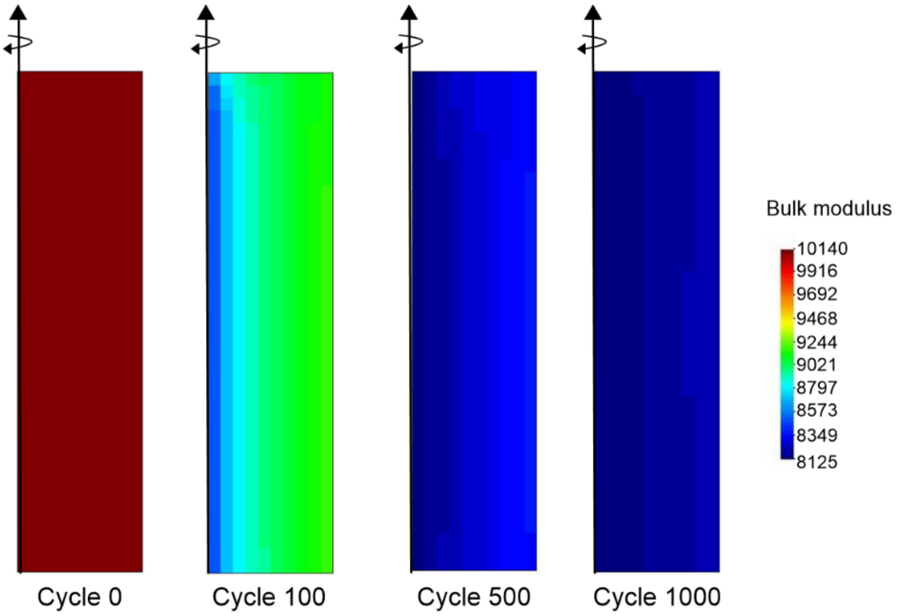

Figure 4-72 Sample CH2: Bulk modulus evolution in the sample

The stiffness evolution observed for sample CH2 at the boundary and within the sample (Figure 4-71) are directly related to the damage multiplier evolution (Figure 4-73). Damage multiplier at point A (axis of the sample) is higher than the one obtained at point B (sample boundary). In fact, from Figure 4-74 and Figure 4-72 it can be remarked that the damage multiplier decrease from the center to the boundary of the sample and higher values of damage multiplier are related to lower bulk modulus values.

Moreover, as observed in the modeling of samples CV4 and CV5, the higher increments of damage multiplier observed for the first cycles (until cycle 300) is related to a higher reduction in the stiffness for this period.

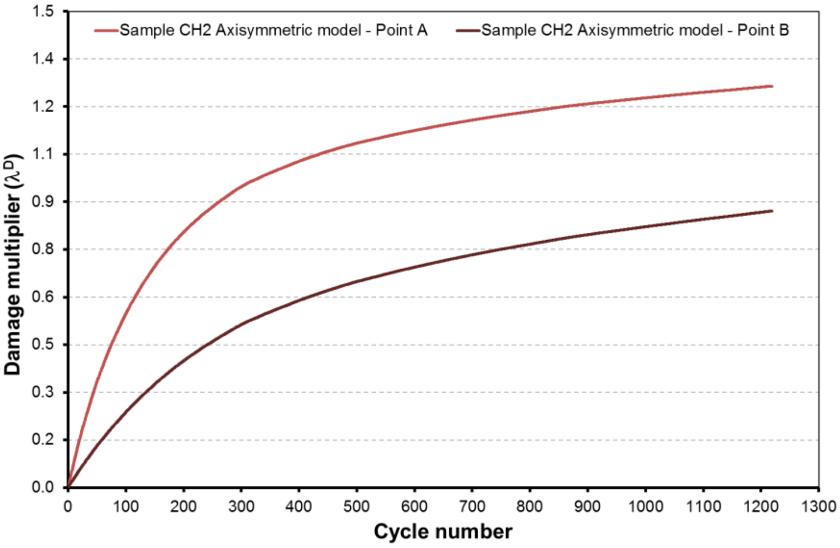

Figure 4-73 Sample CH2: Damage multiplier evolution

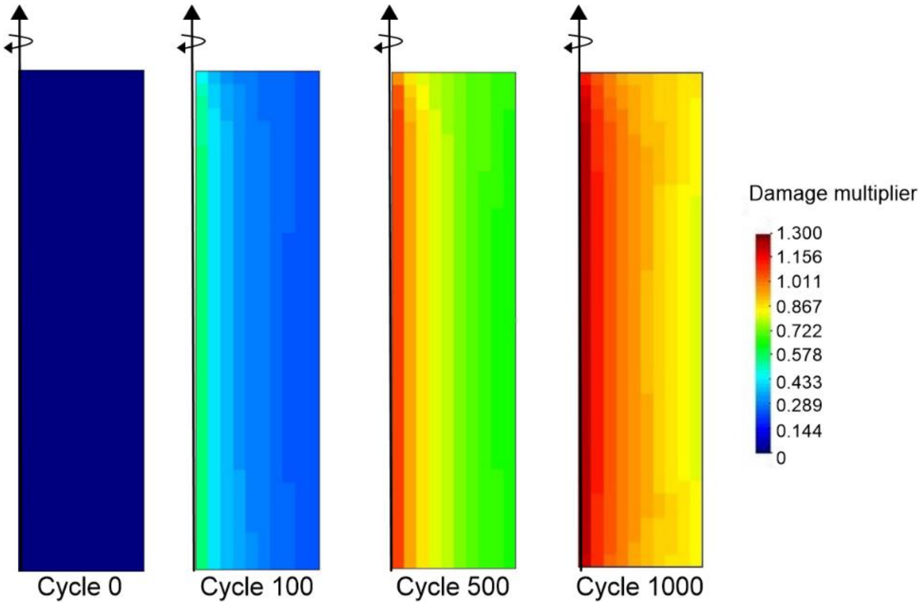

Figure 4-74 Sample CH2: Damage multiplier evolution in the sample

Strains measurements were performed on sample CH2 during the experimental program. Figure 4-75 and Figure 4-76 presents the results obtained from the numerical modeling for radial and axial strains respectively, at the boundary of the sample, compared with the measurements results.

Similarly, to what was observed with the former numerical model results, while the measured data presents an important strains accumulation, the finite element model predictions shows a slightly strain accumulation, -7.44e-5 m/m in axial and -5.36e-5 m/m in radial direction.

Therefore, the variation in bulk modulus due to thermal cycles is mostly related to internal stress accumulation in the composite material, as presented in Figure 4-77, where it can be observed that the mean stress at point A (sample axis) shows an important reduction, especially for the first 300 cycles.

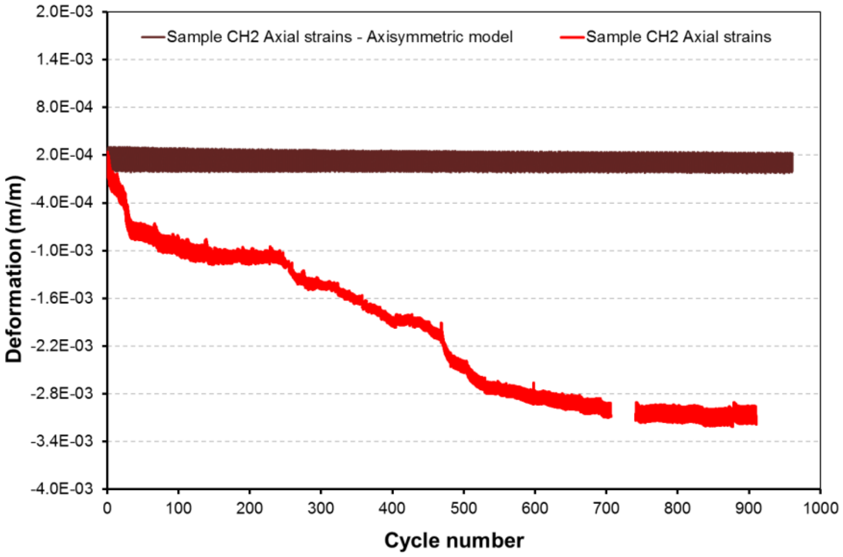

Figure 4-75 Sample CH2: Radial strains evolution

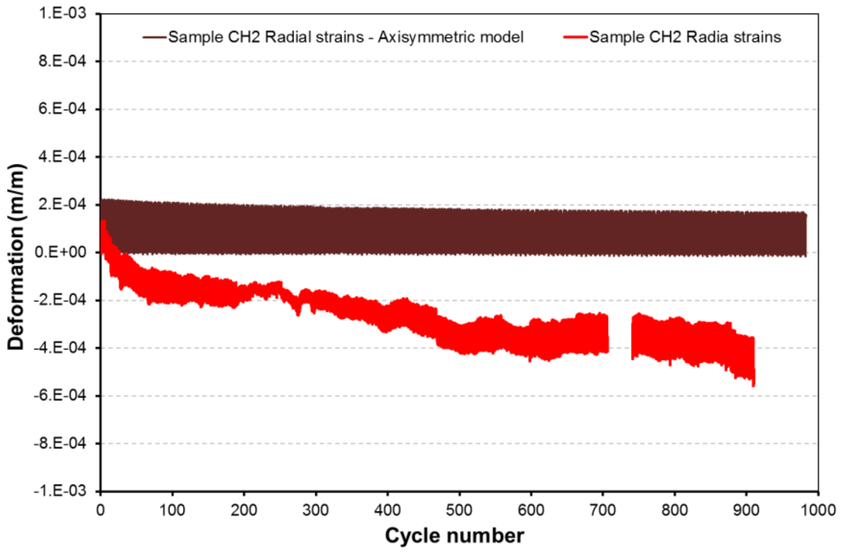

Figure 4-76 Sample CH2: Axial strains evolution

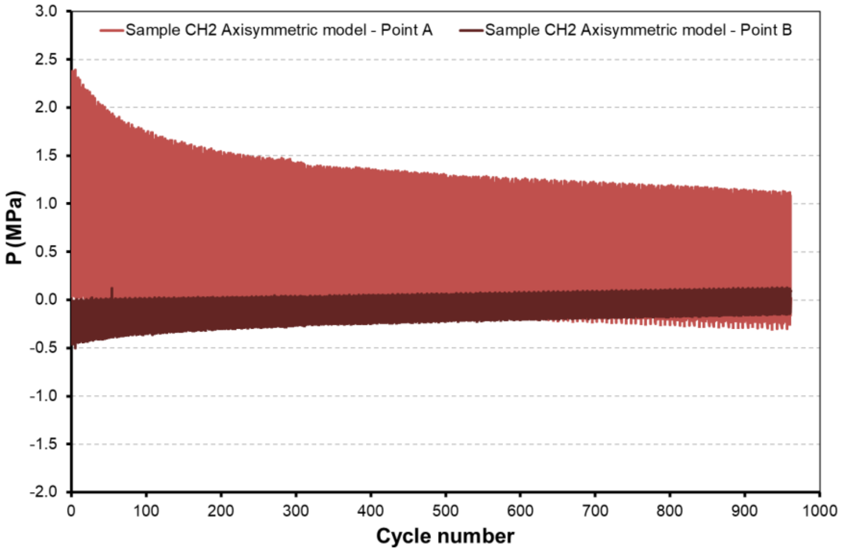

Figure 4-77 Sample CH2: Mean stress evolution

Nevertheless, the model is capable to reproduce the strains variations measured for 24 hours of thermal cycling (6.5 cycles between 10ºC to 50ºC) as illustrated on Figure 4-78, validating the values of thermal expansion considered, (much higher in axial than in radial direction)

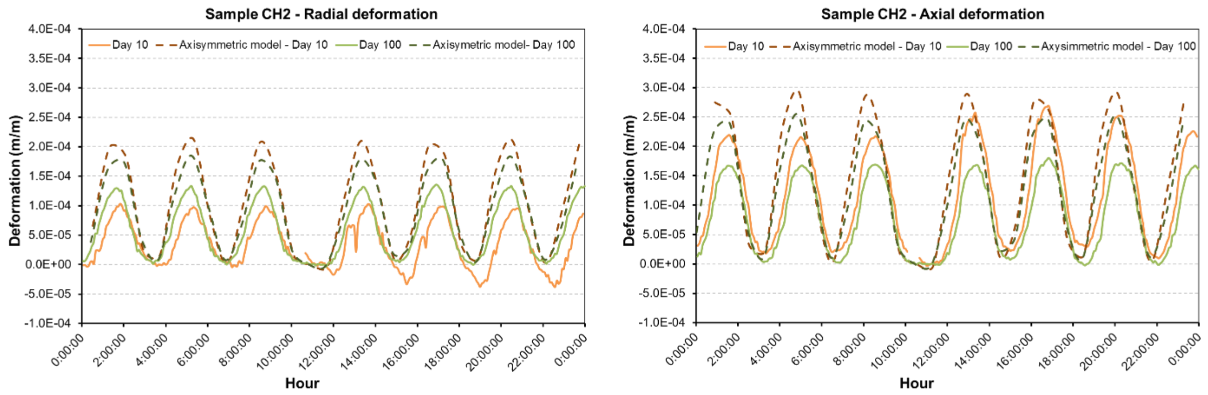

a) b)

Figure 4-78 Sample CH2: Strains amplitude a) radial strains b) axial strains

### 4.5.7 Sample CH3.

Sample CH3 presents the highest bulk modulus reduction observed for the 5 horizontally drilled samples evaluated during the experimental program, a reduction of 29% from the initial value is obtained after more than 1000 cycles of temperature. Additionally, this sample presented the highest initial bulk modulus value for all the samples drilled from the cliff, see section 3.5.2.

Figure 4-79 shows the evolution of the bulk modulus obtained with the finite element models in comparison with the experimental data measured. It can be remarked that for the first cycles, the numerical model results present some differences with the measurements. Nevertheless, the total variation in stiffness is adequately reproduced by the numerical models, note that after cycle 600 the data are follows closely by the modeling results.

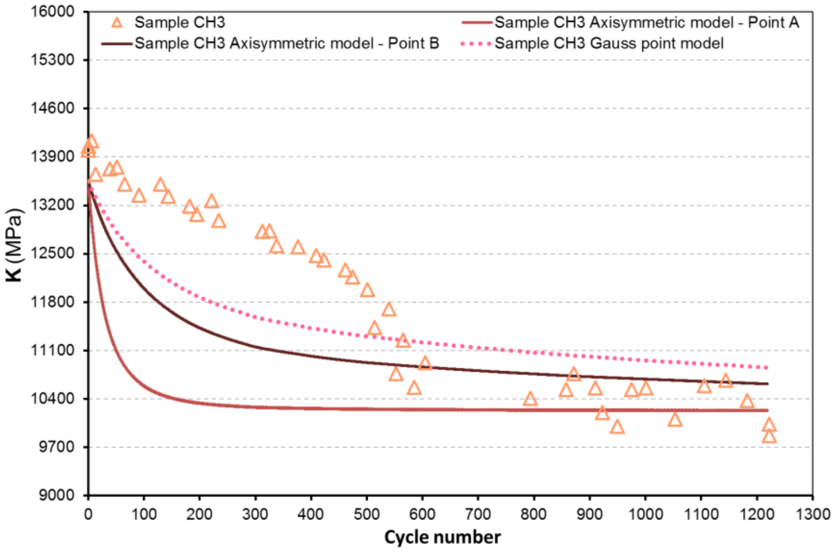

Figure 4-79 Sample CH3: Bulk modulus evolution

In absence of strains measurements, the thermal expansion coefficients considered for this sample are defined according to the deformation obtained for other horizontally drilled samples (CH2 and CH4). The thermal expansion considered in axial direction is higher (3 times) than the radial one.

This anisotropy generates that the bulk modulus reduces the most in the axis of the sample (point A) than on the boundary (Point B), see Figure 4-79. Moreover, as for the GP model the thermal expansion coefficient considered is equal to a third part of the volumetric thermal expansion, less internal stresses are generated, which leads that stiffness is less affected by the thermal cycles.

Moreover, the stiffness of the material presents an important reduction for the first 200 cycles at point A, while the evolution of this parameter at point B is softer (Figure 4-79). This characteristic is linked to the evolution of the damage multiplier at these two points, see Figure 4-80. Damage multiplier evolution at point A presents a more steeper response than the one observed at point B.

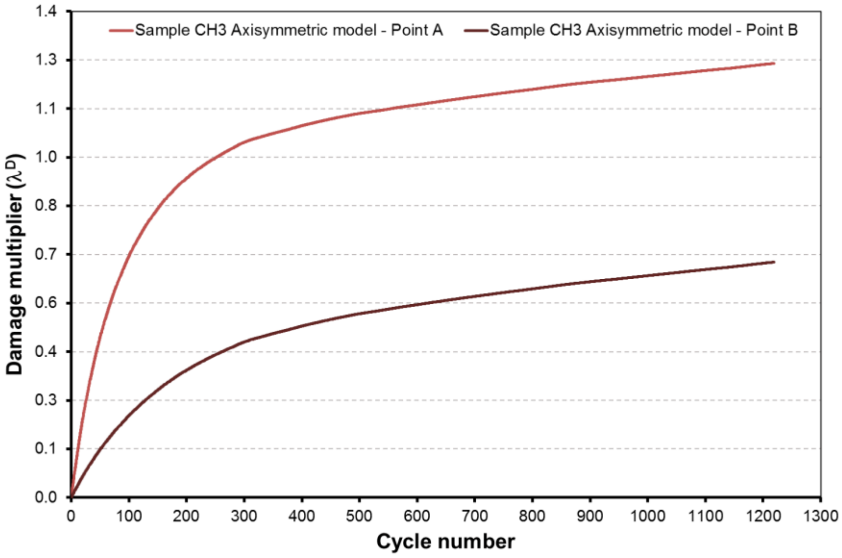

Figure 4-80 Sample CH3: Damage multiplier evolution

As mentioned before, during the experimental program no strain gauges were installed on sample CH3, thus there are no strains measurements on this sample. Nonetheless, the axial and radial strains obtained with the axisymmetric model are presented in Figure 4-81. It can be noted that a slightly strains accumulation is obtained with the imposition of thermal cycles, an accumulation of -6.57 e-5 m/m and -4.85 e-5 m/m is obtained respectively, in radial and axial direction after 1000 thermal cycles. Moreover, the axial strains are higher than the radial ones, due to the thermal expansion coefficient values considered for this sample.

It is important to point out that all samples considering for the numerical modeling indicate that strains accumulation is developed in a negative sense (compression). Moreover, the strains accumulation obtained from the numerical model of samples obtained from the cliff is almost 10 times higher than the strains accumulation found on samples obtained from blocks, this feature can be related to higher damage observed on cliff samples.

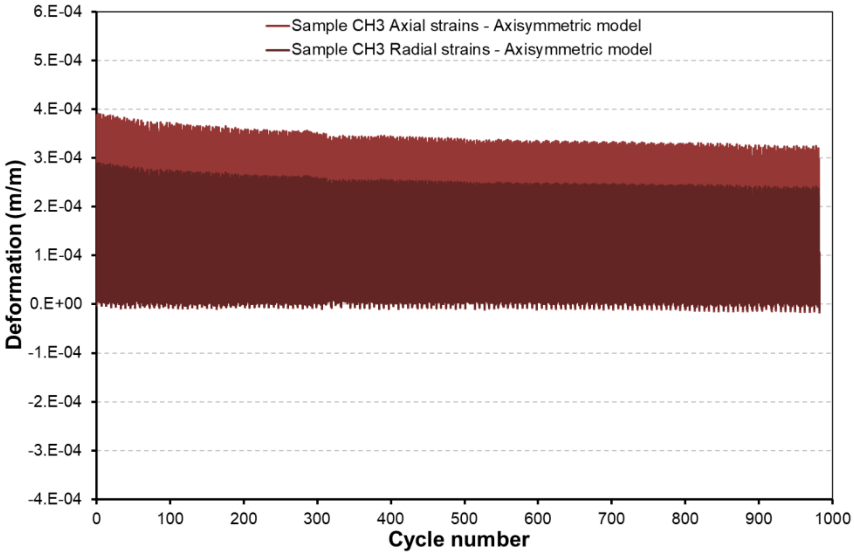

Figure 4-81 Sample CH3: Strains evolution

## 4.6 Conclusions for the numerical modeling

A composite material constitutive law has been proposed with the aim of reproducing thermal damage from a macroscopical point of view. The principal objective is to be able to reproduce the effect of thermal cycles on the mechanical response of the material. The numerical model presented accomplishes this objective.

Some specific observations are presented below:

- Thermal damage is interpreted as due to interactions between the thermal expansion of the different minerals that compose the rocks. This effect can be adequately reproduced by the composite constitutive law as this model is based on the modeling interactions between two different components provided with their own stresses, strains and constitutive laws.

- The theoretical results presented by Hashin & Shtrikman (1963) to define the bounds for the bulk modulus of composite materials has shown to be provide an adequate range to the measurements of La Roque Gageac limestone. The stiffness values measured in the samples belong to the range defined with this method, considering typical stiffness values for calcite and quartz (two main components of this rock) and samples mineralogical composition.

- The coefficients $X_m$ and $X_b$ are indicators of the microstructural arrangement of the rock, including mineral content and stiffness and grain arrangement, which controls *in fine* the stiffness of the composite material.

- The undamaged stiffness obtained experimentally on LaRG limestone samples presents a wide range of variations, between 7000 MPa and 26000 MPa. Taken into account that these samples are mainly composed by calcite and quartz, the constitutive model is able to reproduce this wide range of stiffness values, considering fixed values of the mineral stiffness ($K_m$ and $K_b$) and different microstructural features, mineralogical content and geometrical arrangement.

- The coefficients $X_m$ and $X_b$ have an important effect on the stiffness of the composite material, its initial value and evolution. If $X_b$ is higher than $X_m$ then the response of the composite material is mainly controlled by the bond response, otherwise the stiffness of the composite material is governed by the matrix response.

- The bulk modulus bounds defined by Hashin & Shtrikman (1963) are used to restrict the microstructural coefficients $X_m$ and $X_b$.

- The composite constitutive law has been implemented in finite element method code (CODE_BRIGHT). It has also been explicitly integrated within an algebraic expression with the aim to provide an verification for model implementation in the code. Results have shown a good agreement, validating the model implementation.

- Variations in temperature generate internal stresses (matrix and bond stress). When bonding stresses exceed the elastic limit defined by the bond loading function, the bond suffers damage and the loading function increases homothetically.

- If no bond rate dependency is considered and thermal cycles are imposed, almost all the damage will be developed for the first cycle of temperature. However, this characteristic does not correspond to what is observed in the experimental program, moreover, the thermal damage is a fracture propagation phenomenon. Thus, the response is time dependent. In order to reproduce this phenomenon, rate dependency has been introduced in the bond damage model.

- The numerical model is used to reproduce the response observed during the experimental program on 6 different samples: 2 obtained from blocks, 2 vertically drilled and 2 horizontally drilled from the face of the cliff. This modeling task is developed with two different approaches. In first place, each sample is modelled as a Gauss Point. Afterwards sample have been simulated as a boundary problem with an axisymmetric geometry. Both approaches give a good approximation of the response observed in the samples.

- For the numerical modeling of block samples, coefficient $X_b$ and bond fraction has been taken higher than coefficient $X_m$ and matrix fraction. Therefore, the evolution of the composite material bulk modulus is manly controlled by the bond bulk modulus. On the other hand, for the samples cored from the face of the cliff, values of $X_m$ is taken higher than $X_b$, and matrix and bond fractions are the same. In that case, the composite material bulk modulus is governed by the matrix stiffness.

- Samples obtained from blocks present more damage at the boundary of the sample (higher damage multiplier and lower bulk modulus) while samples obtained from the cliff developed more damage at the axis of the sample. This can be related to the thermal expansion coefficient considered. Block samples have similar thermal expansions in axial and radial direction, while for the cliff samples the thermal expansion coefficient obtained in axial direction is almost 3 times the one considered in radial direction. This generates higher internal stresses in the center of the cliff samples and finally a higher damage multiplier.

- The damage multiplier obtained after more than 1000 thermal cycles is much higher for samples obtained from the cliff face (1.5) than for the block samples (0.13). This characteristic is related to the initial bulk modulus measured in the samples. It is higher in the block samples and experiences a lower reduction than in the cliff samples. In fact, higher values of final damage multiplier are linked to higher reductions in the bulk modulus.

- For all the tested samples, it has been observed a link between the evolution of damage multiplier and the bulk modulus.

- The results obtained with the numerical modeling of samples show a slight strains accumulation, contrary to what is observed in the experimental program results, where high values of strains accumulation are developed. Nevertheless, it is important to mention that with the numerical modeling the strains accumulate in negative direction (compression). While measurements on samples accumulate in equally in positive or negative direction, however it is important to take into account that measured strains do not show any identifiable response.

- The numerical model is able to reproduce the strains amplitude registered during a 24 hours interval (6 cycles for block samples and 6.5 for cliff samples). The stiffness variations computed by the numerical model are mainly related to stress accumulation.

- The composite material constitutive law proposed has generally a good capability to reproduce the behavior of LaRG samples experimentally observed. It is an important tool to understand and explain the different experimental patterns observed in the samples.

# 5. Conclusions

## 5.1. Concluding remarks.

The phenomenon of thermal damage is evaluated from the case of La Roque Gageac cliff, a site that has suffered several rockfalls. The last event occurred in 2010, leads to the installation of an instrumentation system that follows displacements and temperature at the cliff, during more than 6 years. From these measurements, it is observed that there is a strong relationship between the deformations in the cliff and the temperature.

The deformations registered with the extensometers in the site are not reversible, in other words, there is an accumulation of deformations through the time (thermal cycles). In the same way, the jointmeters also show irreversible opening of the cracks with the thermal cycles. It is important to mention that according to the jointmeters measurements, the opening of the fissures is related to cold periods, explaining why most of the rockfalls observed on the site are registered during the winter.

The instrumentation observations show that temperature is a controlling factor on the deformation of the cliff. Based on this, an experimental program is developed on limestone samples from La Roque Gageac, showing that the temperature rates registered in the site are able to induce damage in this limestone and to generate the propagation of existent fissures.

Because of the heterogeneity of the limestone of the cliff, samples were extracted from different locations (within the cavern and at the cliff face). It should be remarked that differences on the mineralogical composition are observed regarding the original location of the samples, furthermore, this heterogeneity also generates differences in the response to the thermal cycles observed.

The behavior of the samples through thermal cycles is evaluated with the evolution of three principal measurements: deformations, elastic wave propagation velocity and uniaxial compressive strength. All these parameters show an evolution with the applications of thermal cycles.

In general, the samples present some strains accumulation. However, the behavior observed do not give any response that can be linked to point of extraction of the samples and/or the mineralogical composition or the sample direction regarding the cliff face. Except by the fact that samples obtained from the cliff face show highest thermal expansion in the perpendicular direction of the cliff face, which is the direction where the cliff suffered major decompression during the valley formation.

Furthermore, the elastic wave propagation velocity has shown to be a good parameter to evaluate the damage in rocks, because of its sensitiveness to the presence of internal micro-fissures, moreover, as it is a nondestructive measurement, its evolution can be followed for the whole experimental program. It is observed that thermal cycles generate a reduction in the elastic wave propagation velocities, especially evident in P waves (VP), that might be related to the presence of internal micro-fissures because any visible crack was observed in the face of the samples.

From the elastic wave propagation velocities, the dynamic strength parameters of the rock can be estimated. Samples from La Roque gageac shows a reduction in the dynamic bulk modulus through the imposition of thermal cycles. Moreover, from VP values the uniaxial compression strength (UCS) can be estimated for samples obtained from inside the troglodyte cavern. The UCS also presents a reduction with the imposition of thermal cycles.

It was observed that atmospheric thermal cycles are not capable to generate any new macro-fissure in the limestone from La Roque Gageac, at least at photo scale. Nevertheless, the propagation of existent fissures is well identified.

The thermal damage on rocks is a topic of interest for several authors, in fact, many experimental programs have been focused on the effect of thermal damage in rocks from different lithologies. However, these studies are generally focused on high temperatures, such as those observed during fires or in underground waste disposal. The experimental program presented in this work shows that atmospheric thermal rates can also generate damage in the rock matrix.

From the results obtained in the experimental program, the phenomenological characteristics of the thermal damage in rocks are defined. They are used to establish the bases considered to proposed a constitutive law capable to reproduce the effect of thermal cycles on the mechanical response of the limestones from La Roque Gageac. With this purpose, a composite material constitutive law is prosed.

From a phenomenological point of view the thermal damage is related to the interaction between the thermal response of the minerals that composed the rock. This characteristic is taken into account by the numerical model as it considers that the material (rock) is composed of two materials and the interaction between them define the response of the composite material.

The constitutive model proposed considers parameters that characterized the microstructural arrangement as one of the principal characteristics that defined the response of the composite material. In fact, by considering typical strength values for quartz and calcite (the main minerals conforming La Roque gageac limestone) it is possible to reproduce all the varieties of responses observed in the experimental program, only by changing these microstructural parameters.

The composite material constitutive law has the ability to reproduce the behavior of the samples from LaRG evaluated in the experimental program. It is an important tool to understand and explain the different experimental patterns observed in the samples.

The experimental study and numerical model presented in this work shows that atmospheric thermal cycles appreciated in the region of La Rock Gageac may induce a damage in the rock matrix reducing its strength and helping to the propagation of the existent fissures, which confirm the idea that thermal cycles may be the triggering factor for the instabilities registered on the site.

## 5.2. Future development.

Based on the experimental results obtained during this thesis and the numerical model proposed some lines of future work are open, some of them are proposed bellow:

- From insitu observations it is observed that the water does not have a controlling role in the instabilities registered in the cliff of La Roque Gageac, in the same way, the experimental program showed that by isolating the thermal effect a considerable damage can be observed in the material. Nevertheless, it must be remembered that this cliff is subjected to the actions of the whole climatological conditions, for this reason it can be interesting to evaluate if the relative humidity plays a role in the thermal damage of this limestone.

- During the experimental program, it was observed that any new fracture was generated because of the thermal cycling, nevertheless, if there is a pre-existent crack these thermal cycles induce its propagation, that can be related to the reduction in strength of the rock mass. In order to have a quantitative evaluation of how thermal damage affect the propagation of fissures, it will be necessary to performed toughness tests on samples that were subjected to thermal cycles.

- The evaluation of thermal damage performed in this thesis is focused on the limestone from La Roque Gageac, it could be interesting to evaluate if thermal cycles produce the same effect with similar phenomenology in other types of lithologies, moreover, if the numerical model proposed in this work is also able to reproduce the response observed in those other lithologies.

- The numerical model proposed is capable to reproduce the effect of strength and stiffness reduction in the rock due to the thermal cycles, nevertheless the phenomena of propagation of fractures is not directly considered. This phenomenon could be included in the numerical modeling. In the finite elements scheme, this can be performed by two strategies. One option is to represent the existent crack as a weak zone and its propagation as the localization of damage through a non-local formulation (Pijaudier & Bazant 1987; Mazars & Pijaudier-Cabot 1996; Jirásek 1998). Another options is to define the extent crack as a joint element and discretize the continuum medium with zero-thickness elements (Carol & Prat 1997; Segura & Carol 2004) thus the propagation of this fissure will be achieved by the opening and relative displacement of those elements.

- Finally, it is important to be able to model the real case of the cliff of La Roque Gageac. This should be performed focusing in the joints response, as it is where the instrumentation system is installed, for this it will be necessary to have the crack propagation and response included in the model. Whit the numerical model of the case it is expected to estimate the real risk level.

# References

AFNOR (2002) ‘Détermination de la vitesse de propagation des ondes ultrasonores en laboratoire’, AFNOR, (NF P 94-411), pp. 1–7.

AFNOR (2005) ‘Détermination du coeffcient linéare de dilatation Thermique’, AFNOR, (NF EN 14581), pp. 1–11.

Al-Shayea, N. A. (2004) ‘Effects of testing methods and conditions on the elastic properties of limestone rock’, Engineering Geology, 74(1–2), pp. 139–156.

ASTM (2010) ‘Standard test method for compressive strength and elastic moduli of intact rock core specimens under varying states of stress and temperatures’, D7012-10, (C), pp. 1–8.

Astruc, G. (1988) *Le paléokarst quecynois au paléogéne altérations et sédimentations associées - Documents du BRGM N$^{o}$133*.

Blaber, J., Adair, B. and Antoniou, A. (2015) ‘Ncorr : Open-Source 2D Digital Image Correlation Matlab Software Ncorr : Open-Source 2D Digital Image Correlation Matlab Software’, Experimental mechanics, 55(6), pp. 1105–1122.

Bodin, D., Pijaudier-Cabot, G., de La Roche, C., Piau, J.-M. and Chabot, A. (2004) ‘Continuum damage approach to asphalt concrete fatigue modeling’, *Journal of Engineering Mechanics*, 130(6), pp. 700–708.

Bornert, M., Brémand, F., Doumalin, P., Dupré, J. C., Fazzini, M., Grédiac, M., Hild, F., Mistou, S., Molimard, J., Orteu, J. J., Robert, L., Surrel, Y., Vacher, P. and Wattrisse, B. (2009) ‘Assessment of digital image correlation measurement errors: Methodology and results’, Experimental Mechanics, 49(3), pp. 353–370.

Brotóns, V., Tomás, R., Ivorra, S. and Alarcón, J. C. (2013) ‘Temperature influence on the physical and mechanical properties of a porous rock: San Julian’s calcarenite’, Engineering Geology. Elsevier B.V., 167, pp. 117–127.

Bureau de recherches géologiques et minières (BRGM) (1987) *Carte gèologique de la France à 1/50 000 Feuille Sarlat - La Caneda*.

Carmichael, R. S. (1989) *CRS practical handbook of physical properties of rocks and minerals*. Edited by CRS Press. Boca Raton.

Carol, I. and Prat, P. (1997) ‘Normal/Shear cracking model: Application to discrete crack analysis’, *Journal of Engineering Mechanics*, 123(August), pp. 765–773.

Carol, I., Rizzi, E. and Willam, K. (2001) ‘On the formulation of anisotropic elastic degradation. I. Theory based on a pseudo-logarithmic damage tensor rate’, *International Journal of Solids and Structures*, 38, pp. 491–518.

Casperson, M. C., Carroll, J. D., Lambros, J., Sehitoglu, H. and Dodds, R. H. (2014) ‘Investigation of thermal effects on fatigue crack closure using multiscale digital image correlation experiments’, International Journal of Fatigue. Elsevier Ltd, 61, pp. 10–20.

Chang, X., Hu, C., Zhou, W., Ma, G. and Zhang, C. (2014) ‘A combined continuous-discontinuous approach for failure process of quasi-brittle materials’, *Science China Technological Sciences*, 57(3), pp. 550–559.

Chen, Y. L., Ni, J., Jiang, L. H., Liu, M. L., Wang, P. and Azzam, R. (2014) ‘Experimental study on mechanical properties of granite after freeze-thaw cycling’, Environmental Earth Sciences, 71(8), pp. 3349–3354.

Ciccotti, M. and Mulargia, F. (2004) ‘Differences between static and dynamic elastic moduli of a typical seismogenic rock’, Geophysical Journal International, 157(1), pp. 474–477.

Cordebois, J. P. and Sidoroff, F. (1982) ‘Endommagement anisotrope en élasticité et plasticité’, *Journal de Mécanique Théorique et Apliquée*, Numéro Spé, pp. 45–60.

Dautriat, J., Bornert, M., Gland, N., Dimanov, A. and Raphanel, J. (2011) ‘Localized deformation induced by heterogeneities in porous carbonate analysed by multi-scale digital image correlation’, Tectonophysics. Elsevier B.V., 503(1–2), pp. 100–116.

Dubois, F., Moutou-Pitti, R., Picoux, B. and Petit, C. (2012) ‘Finite element model for crack growth process in concrete bituminous’, *Advances in Engineering Software*. Elsevier Ltd, 44(1), pp. 35–43. doi: 10.1016/j.advengsoft.2011.05.039.

Franzoni, E., Sassoni, E., Scherer, G. W. and Naidu, S. (2013) ‘Artificial weathering of stone by heating’, Journal of Cultural Heritage. Elsevier Masson SAS, 14(3 SUPPL), pp. e85–e93.

Gasc-Babier, M., Girmaand, G. and Gendre, V. (2014) ‘Laboratory analysis of thermal fatigue in limestone’, in Rock Engineering and Rock Mechanics: Structures in and on Rock Masses - Proceedings of EUROCK 2014, ISRM European Regional Symposium, pp. 285–290.

Gasc-Babier, M., Virely, D. and Guittard, J. (2015) ‘Termal fatigue in rocks- La Roque-Gageac’s case study’, *ISRM Congress 2015 Proceedings - Int. Symposium on Rock Mechanics*.

Gens, A., Vaunat, J., Garitte, B. and Wileveau, Y. (2007) ‘In situ behaviour of a stiff layered clay subject to thermal loading: observations and interpretation’, *Géotechnique*, 57(2), pp. 207–228.

Gómez-Heras, M., Smith, B. J. and Fort, R. (2006) ‘Surface temperature differences between minerals in crystalline rocks: Implications for granular disaggregation of granites through thermal fatigue’, Geomorphology, 78(3–4), pp. 236–249.

Goudie, A. S. and Viles, H. A. (2000) ‘The thermal degradation of marble’, Acta universitais carolinae, 35(SUPP), pp. 7–16.

Gunasekaran, S., Anbalagan, G. and Pandi, S. (2006) ‘Raman and infrared spectra of carbonates of calcite structure’, Journal of Raman Spectroscopy, 37(9), pp. 892–899.

Hall, K. (1999) ‘The role of thermal stress fatigue in the breakdown of rock in cold regions’, *Geomorphology*, 31, pp. 47–63.

Hall, K. (2004) ‘Evidence for freeze–thaw events and their implications for rock weathering in northern Canada’, *Earth Surface Processes and Landforms*, 29(1), pp. 43–57.

Hall, K. and Thorn, C. E. (2014) ‘Thermal fatigue and thermal shock in bedrock: An attempt to unravel the geomorphic processes and products’, *Geomorphology*. Elsevier B.V., 206, pp. 1-13.

Hartlieb, P., Toifl, M., Kuchar, F., Meisels, R. and Antretter, T. (2016) ‘Thermo-physical properties of selected hard rocks and their relation to microwave-assisted comminution’, Minerals engineering. Elsevier Ltd, 91, pp. 34–41.

Hashin, Z. and Shtrikman, S. (1963) ‘A variational approach to the theory of the elastic behaviour of multiphase materials’, *Journal of the Mechanics and Physics of Solids*, 11(2), pp. 127–140.

Hayatdavoudi, A., Chitila, D. and Boukadi, F. (2015) ‘Effect of cyclic temperature, water vapor and exposure time on micro fracture propagation in shale’, in International symposium on Rock Mechanics, pp. 1–12.

Hild, F. and Roux, S. (2006) ‘Digital image correlation: from displacement measurement to identification of elastic properties–a review’, Strain, 42, pp. 69–80.

Hoek, E. and Brown, E. (1997) ‘Practical estimates of rock mass strength’, International Journal of Rock Mechanics and Mining Sciences, 34(8), pp. 1165–1186.

Hoek, E. and Brown, E. T. (1980) ‘Empirical Strength Criterion for Rock Masses’, Journal of the Geotechnical Engineering Division, pp. 1013–1035.

Hoek, E. and Martin, C. D. (2014) ‘Fracture initiation and propagation in intact rock – A review’, *Journal of Rock Mechanics and Geotechnical Engineering*. Elsevier Ltd, 6(4), pp. 287–300.

Huang, C. K. and Kerr, P. F. (1960) ‘The Infrared Study of the Carbonate Minerals’, The American Mineralogist, 45, pp. 311–324.

Hudson, J. A. and Harrison, J. P. (1997) ‘Intact rock’, in Engineering rock mechanics An introduction to principles. Oxford: Elsevier Science Ltd., pp. 85–112.

Hudson, J. and Harrison, J. (1997) Engineering Rock Mechanics: An Introduction to the Principles.

Inserra, C., Biwa, S. and Chen, Y. (2013) ‘Influence of thermal damage on linear and nonlinear acoustic properties of granite’, International Journal of Rock Mechanics and Mining Sciences. Elsevier, 62, pp. 96–104.

Jing, L. and Hudson, J. A. (2002) ‘Numerical methods in rock mechanics’, *International Journal of Rock Mechanics & Mining Sciences*, 39(4), pp. 409–427.

Jirásek, M. (1998) 'Nonlocal models for damage and fracture: Comparison of approaches', *International Journal of Solids and Structures*, 35(31–32), pp. 4133–4145.

Kendrick, J. E., Smith, R., Sammonds, P., Meredith, P. G., Dainty, M. and Pallister, J. S. (2013) 'The influence of thermal and cyclic stressing on the strength of rocks from Mount St. Helens, Washington', Bulletin of Volcanology, 75(7), pp. 1–12.

Koch, A. and Siegesmund, S. (2004) 'The combined effect of moisture and temperature on the anomalous expansion behaviour of marble', Environmental Geology, 46(3–4), pp. 350–363.

Lagneau, M. V. (2014) Crack propagation in reservoir rocks in the CO 2 storage context. Université Paris-Est.

Launeau, P., Bouchez, J. L. and Benn, K. (1990) 'Shape preferred orientation of object populations: automatic analysis of digitized images', Tectonophysics, 180(2–4), pp. 201–211.

Launeau, P. and Cruden, A. R. (1998) 'Magmatic fabric acquisition mechanisms in a syenite: Results of a combined anisotropy of magnetic susceptibility and image analysis study', Journal of Geophysical Research, 103(B3), pp. 5067–5089.

Launeau, P. and Robin, P.-Y. F. (1996) 'Fabric analysis using the intercept method', Tectonophysics, 267(1–4), pp. 91–119.

Le Per, M. and Oter-Duthoit, L. (1987) 'Désagrégation des parios rocheuses et climat: approche thermique et thermodynamique', *BUlletin de l'association française pour l'etude du quaternaire*, 3, pp. 147–159.

Leiss, B. and Weiss, T. (2000) 'Fabric anisotropy and its influence on physical weathering of different types of Carrara marbles', Journal of Structural Geology, 22(11–12), pp. 1737–1745.

Lu, Y. L., Elsworth, D. and Wang, L. G. (2013) 'Microcrack-based coupled damage and flow modeling of fracturing evolution in permeable brittle rocks', *Computers and Geotechnics*, 49, pp. 226–244.

Luque, a., Ruiz-Agudo, E., Cultrone, G., Sebastián, E., Siegesmund, S., Sebasti??n, E. and Siegesmund, S. (2011) 'Direct observation of microcrack development in marble caused by thermal weathering', Environmental Earth Sciences, 62(7), pp. 1375–1386.

Mahmutoglu, Y. (1998) 'Mechanical Behaviour of Cyclically Heated Fine Grained Rock', Rock Mechanics and Rock Engineering, 31(3), pp. 169–179.

Malaga-Starzec, K., Åkesson, U., Lindqvist, J. E. and Schouenborg, B. (2006) 'Microscopic and macroscopic characterization of the porosity of marble as a function of temperature and impregnation', Construction and Building Materials, 20(10), pp. 939–947.

Malésys, N., Vincent, L. and Hild, F. (2009) 'A probabilistic model to predict the formation and propagation of crack networks in thermal fatigue', *International Journal of Fatigue*, 31(3), pp. 565–574.

Martínez-martínez, J., Benavente, D. and García-del-cura, M. A. (2011) 'Spatial attenuation : The most sensitive ultrasonic parameter for detecting petrographic features and decay processes in carbonate rocks', Engineering Geology. Elsevier B.V., 119(3–4), pp. 84–95.

Martínez-Martínez, J., Benavente, D. and García-del-Cura, M. A. (2012) 'Comparison of the static and dynamic elastic modulus in carbonate rocks', Bulletin of Engineering Geology and the Environment, 71(2), pp. 263–268.

Martínez, J. (2008) Influencia De La Alteración Sobre Las Propiedades Mecánicas De Calizas, Dolomías Y Mármoles. Evaluación Mediante Estimadores No Destructivos (Ultrasonidos). Universidad de Alicante.

Mazars, J. and Pijaudier-Cabot, G. (1996) 'From damage to fracture mechanics and conversely: A combined approach', *International Journal of Solids and Structures*, 33(20–22), pp. 3327–3342.

Mazars, J. and Pijaudier-Cabot, G. (1989) 'Continuum Damage Theory—Application to Concrete', *Journal of Engineering Mechanics*, 115(2), pp. 345–365.

Mitchell, J. K. and Soga, K. (2005) 'Soil deposits - Their formation, structure, geotechnical properties, and stability', in *Fundamentals of soil behavior*. John Wiley. New Jersey, pp. 195–250.

Morgan, S. P. (2015) An Experimental and Numerical Study on the Fracturing Processes in Opalinus Shale, Massachusetts institute of technology. Massachusetts Institute of Technology.

Najibi, A. R., Ghafoori, M., Lashkaripour, G. R. and Asef, M. R. (2015) 'Empirical relations between strength and static and dynamic elastic properties of Asmari and Sarvak limestones, two main oil reservoirs in Iran', Journal of Petroleum Science and Engineering. Elsevier, 126, pp. 78–82.

Nguyen, T. L., Hall, S. a., Vacher, P. and Viggiani, G. (2011) 'Fracture mechanisms in soft rock: Identification and quantification of evolving displacement discontinuities by extended digital image correlation', Tectonophysics. Elsevier B.V., 503(1–2), pp. 117–128.

Olivella, S., Gens, A., Carrera, J. and Alonso, E. E. (1996) 'Numerical formulation for a simulator (CODE_BRIGHT) for the coupled analysis of saline media', Engineering Computations. MCB UP Ltd, 13(7), pp. 87–112.

Pensée, V., Kondo, D. and Dormieux, L. (2002) 'Micromechanical analysis of anisotropic damage in brittle materials', *ASCE J. Engng Mech.*, 128(August), pp. 889–897.

Perzyna, J. K. (1966) 'Fundamental problems in viscoplasticity', *Advances in applied mechanics*, 6, pp. 243–377.

Pijaudier, C. G. and Bazant, Z. P. (1987) 'Non local Damage Theory', *Journal of engineering mechanics*, 113(10), pp. 1512–1533.

PLatel, J. P. (1987) *Le crétacé supérieur de la plate-forme septentrionale du basin d'Aquitaine Stratigraphie et évolution géodynamique*. University de Bordeaux III.

PLatel, J. P. (1996) 'Stratigraphie, sédimentologiie et evolution géodynamique de la plate-forme carbonatée di Crétacé supérieur du nord du bassin d'Aquitaine', *Géologie de la France*, 4, pp. 33–58.

PLatel, J. P. (1999) *Carte géologique de la France à 1/50 000, feuille Terrasson (784), terrains crétacés. Orléans : BRGM ; notice explicative de la partie crétacée par Platel J.P.*

Rojas-Solano, L. B., Grégoire, D. and Pijaudier-Cabot, G. (2013) 'Interaction-based non-local damage model for failure in quasi-brittle materials', *Mechanics Research Communications*. Elsevier Ltd., 54, pp. 56–62..

Royer-Carfagni, G. . (1999) 'On the thermal degradation of marble', *International journal of rock mechanics and mining sciences*, 36, pp. 119–126.

Ruiz, D. (2013) Thermo-mechanical analysis of the stability of a rock-cliff under climatic actions, upcommons.upc.edu. Universidad Politécnica de Cataluña.

Segura, J. M. and Carol, I. (2004) 'On zero-thickness interface elements for diffusion problems', *International Journal for Numerical and Analytical Methods in Geomechanics*, 28(9), pp. 947–962.

Shao, J. F. and Rudnicki, J. W. (2000) 'Microcrack-based continuous damage model for brittle geomaterials', *Mechanics of Materials*, 32(10), pp. 607–619.

Shushakova, V., Fuller, E. R. and Siegesmund, S. (2013) 'Microcracking in calcite and dolomite marble: Microstructural influences and effects on properties', *Environmental Earth Sciences*, 69(4), pp. 1263–1279.

Siegesmund, S., Ullemeyer, K., Weiss, T. and Tschegg, E. K. (2000) 'Physical weathering of marbles caused by anisotropic thermal expansion', International Journal of Earth Sciences, 89(1), pp. 170–182.

Sousa, L. M. O., Suárez del Río, L. M., Calleja, L., Ruiz de Argandoña, V. G. and Rodríguez Rey, A. (2005) 'Influence of microfractures and porosity on the physico-mechanical properties and weathering of ornamental granites', Engineering Geology, 77(1–2), pp. 153–168.

Tiskatine, R., Eddemani, A., Gourdo, L., Abnay, B., Ihlal, A., Aharoune, A. and Bouirden, L. (2016) 'Experimental evaluation of thermo-mechanical performances of candidate rocks for use in high temperature thermal storage', Applied Energy. Elsevier Ltd, 171, pp. 243–255.

Trauth, N., Astruc, G., Archanjo, J., Dubreuilh, J., Martin, P., Cauliez, N. and Fayconnier, D. (1985) 'Géodynamique des altérations ferralitiques sur roches sédimentaires, en bordure sud-ouest crétacée du Massif Central: paysages sidérolitiques en Quercy Blanc, Haut-Agenais, Bouriane et Périgord Noir', *Géologie de la France*, 2, pp. 151–160.

Tung, S. H. and Sui, C. H. (2010) 'Application of digital-image-correlation techniques in analysing cracked cylindrical pipes', Sadhana - Academy Proceedings in Engineering Sciences, 35(5), pp. 557–567.

Vazquez-Moreno, T. and BLanco-Varela, M. T. (1981) 'Tabla de frecuencias y relacionados con la química del cemento', Materiales de construccion, 31(182), pp. 31–48.

Vaunat, J. and Gens, A. (2003) 'Bond degradation and irreversible strains in soft argillaceous rock', in *Panamerican conference on soil mechanics and geotechnical engineering*, pp. 479–484.

Virely, D., Ansaldi, B. and Baro, P. (2010) *Project DOSM Falaises de La Roque Gageac Évaluation de l ' aléa chutes de masses rocheuses, mouvement dénsemble - Fascicule 3*.

Virely, D. and Guittard, J. (2010a) *Project DOSMS: La Roque Gageac Contexte géographique, géologique et géomécanique Fascicule 1*.

Virely, D. and Guittard, J. (2010b) *Project DOSMS: La Roque Gageac Contexte géographique, géologique et géomécanique Fascicule 2*.

Walsh, S. D. C. and Lomov, I. N. (2013) 'Micromechanical modeling of thermal spallation in granitic rock', International Journal of Heat and Mass Transfer. Elsevier Ltd, 65, pp. 366–373.

Walsh, S. D. C. and Lomov, I. N. (2013) 'Micromechanical modeling of thermal spallation in granitic rock', *International Journal of Heat and Mass Transfer*. Elsevier Ltd, 65, pp. 366–373.

Wanne, T. S. and Young, R. P. (2008) 'Bonded-particle modeling of thermally fractured granite', International Journal of Rock Mechanics and Mining Sciences, 45(5), pp. 789–799.

Wong, R. H. C., Chau, K. T. and Wang, P. (1996) 'Microcracking and grain size effect in Yuen Long marbles', *International Journal of Rock Mechanics and Mining Sciences & Geomechanics* Abstracts, 33(5), pp. 479–485.

Xie, N., Zhu, Q. Z., Xu, L. H., Shao, J. F. and Xie, N. (2012) 'A micromechanics-based elastoplastic damage model for quasi-brittle rocks', *Computers and Geotechnics*, 38(8), pp. 970–977.

Yang, D., Bornert, M., Chanchole, S., Wang, L., Valli, P. and Gatmiri, B. (2011) 'Experimental investigation of the delayed behavior of unsaturated argillaceous rocks by means of Digital Image Correlation techniques', Applied Clay Science. Elsevier B.V., 54(1), pp. 53–62.

Yavuz, H. (2011) 'Effect of freeze-thaw and thermal shock weathering on the physical and mechanical properties of an andesite stone', Bulletin of Engineering Geology and the Environment, 70(2), pp. 187–192.

Yavuz, H., Altindag, R., Sarac, S., Ugur, I. and Sengun, N. (2006) 'Estimating the index properties of deteriorated carbonate rocks due to freeze-thaw and thermal shock weathering', International Journal of Rock Mechanics and Mining Sciences, 43(5), pp. 767–775.

Yavuz, H., Demirdag, S. and Caran, S. (2010) 'Thermal effect on the physical properties of carbonate rocks', International Journal of Rock Mechanics and Mining Sciences. Elsevier, 47(1), pp. 94–103.

Zimmermann, a., Carter, W. C. and Fuller, E. R. (2001) 'Damage evolution during microcracking of brittle solids', *Acta Materialia*, 49(1), pp. 127–137.

# Appendices

## *Appendix A. Mercury intrusion porosimetry.*

In order to evaluate if atmospheric thermal cycles may have any identifiable effect on the porosimetry of La Roque Gageac limestone, the porosity of four small samples submitted to 0, 276, 420 and 630 cycles between 10ºC to 50ºC were analyzed with the mercury intrusion porosimetry technique.

Figure A-1 presents the pore size distribution obtained for the 4 samples, it can be observed that all samples present similar response, therefore there is any remarkable response on the porosity when samples are subjected to thermal cycles. For these samples, a predominant pore size of 1.56 μm is observed.

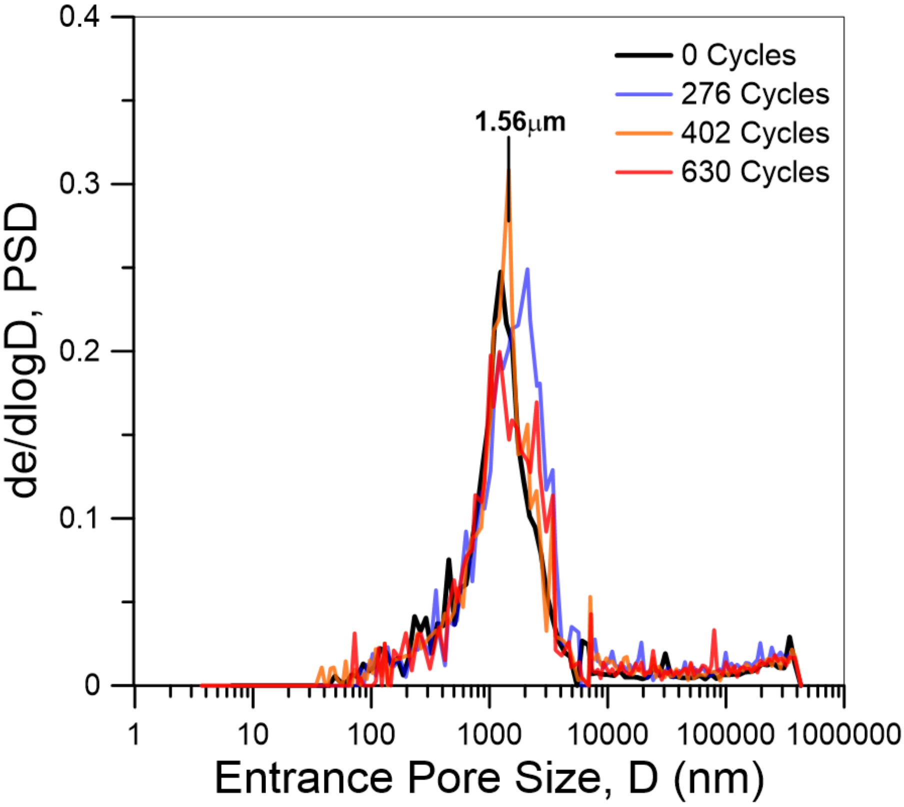

Figure A-1. Pore size distribution for samples submitted to thermal cycles

## *Appendix B. Digital image correlation analysis on samples C1 and C3.*

Figure A-2 and Figure A-3 presents the results obtained with the digital image correlation analysis performed on sample C1 with and without the speckle pattern applied to the face under analysis. In the same way Figure A-4 and Figure A-5 give the results obtained for sample C3.

It can be observed that any new fissure is observed at least at photo scale, similar to what was observed on sample C2 and presented in section 3.6.2. It is important to point out that the results obtained with the three samples are comparable, in terms of strains magnitude and distribution, which corroborates that the small strains observed can be attributed to variations on the illumination pattern. Moreover, with the three samples evaluated it is observed that for this strain magnitude the face with the speckle pattern presents less noise.

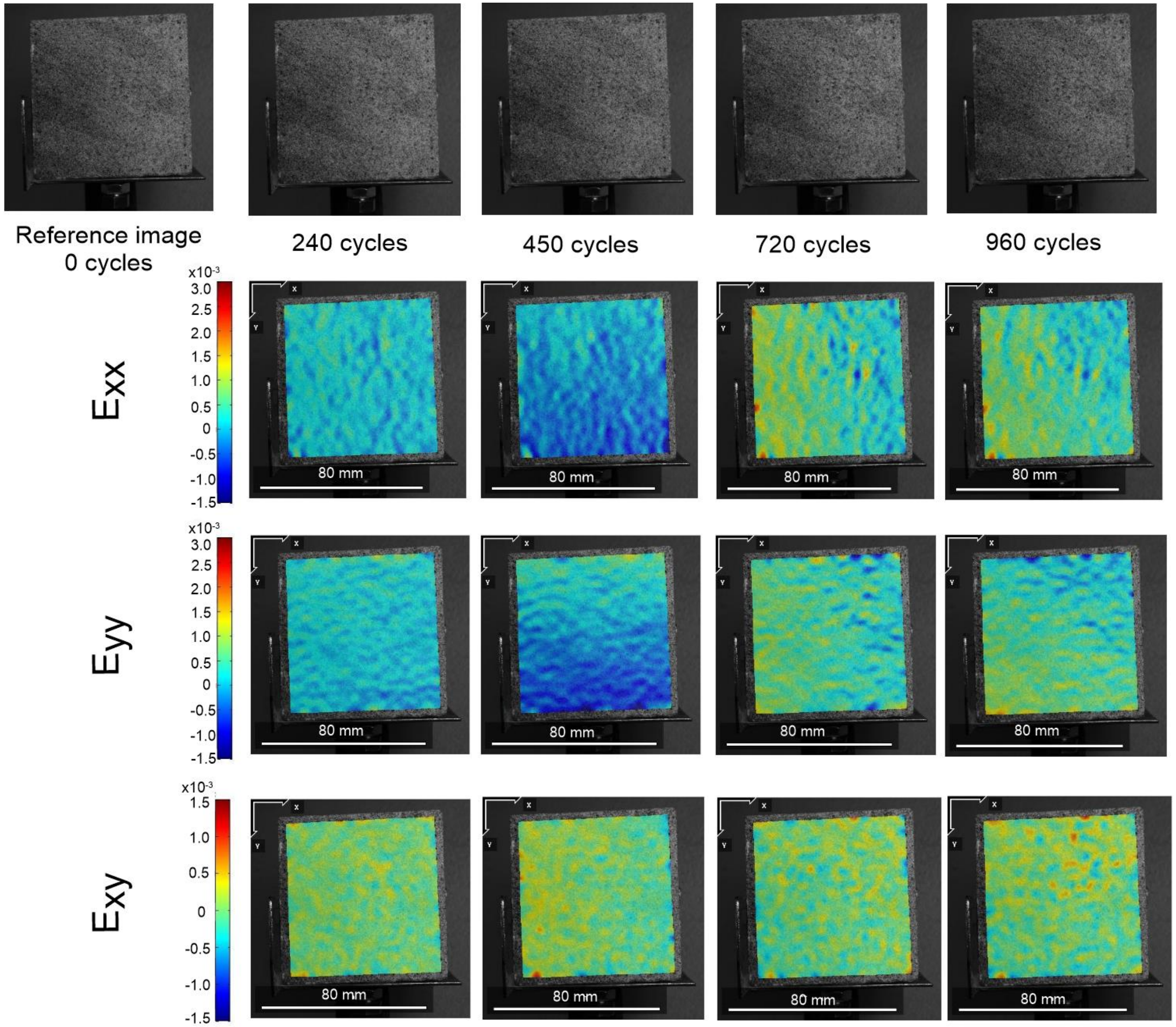

Figure A-2 DIC analysis for sample C1 – face with speckle pattern

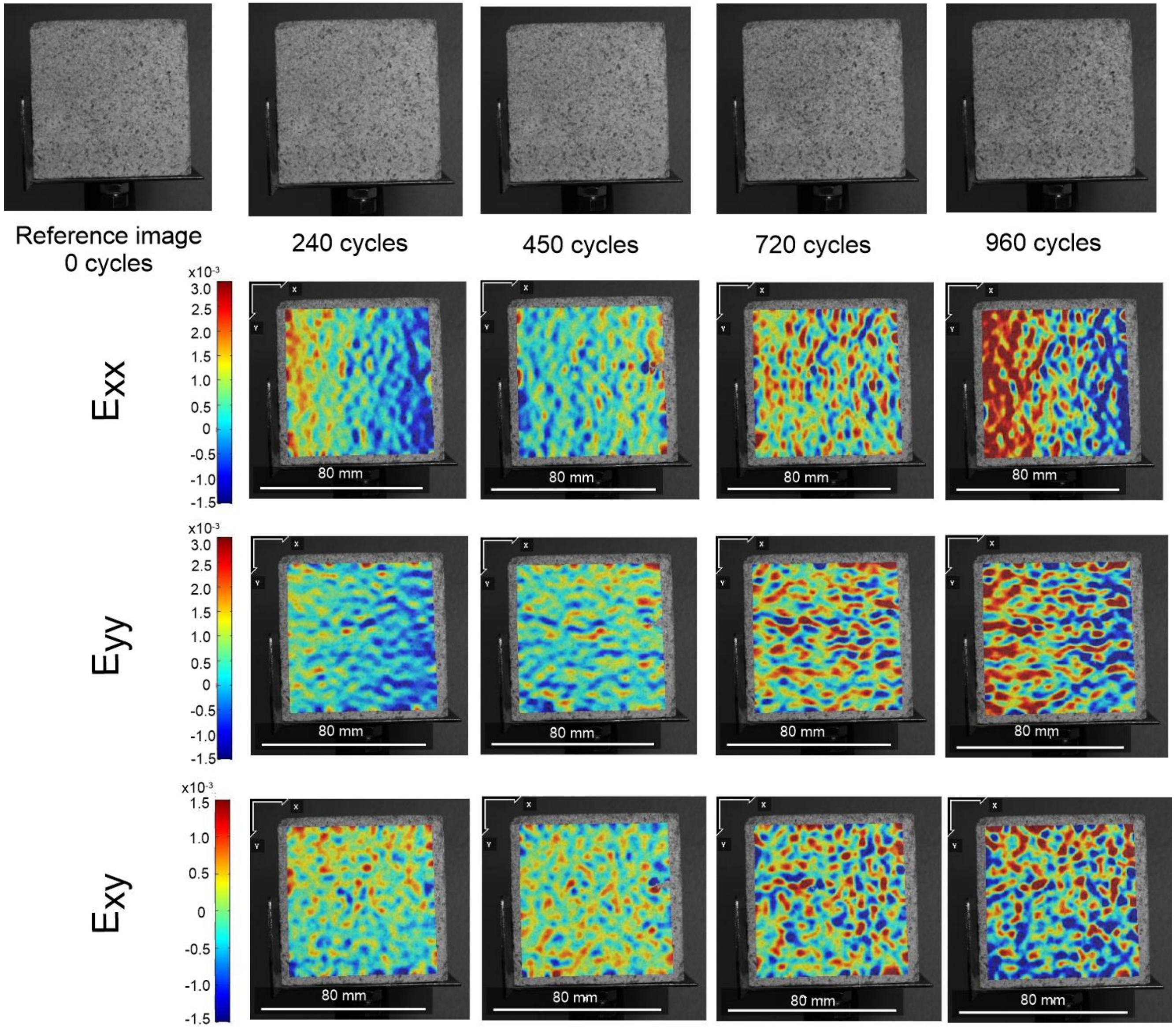

Figure A-3 DIC analysis for sample C1 – face without speckle pattern

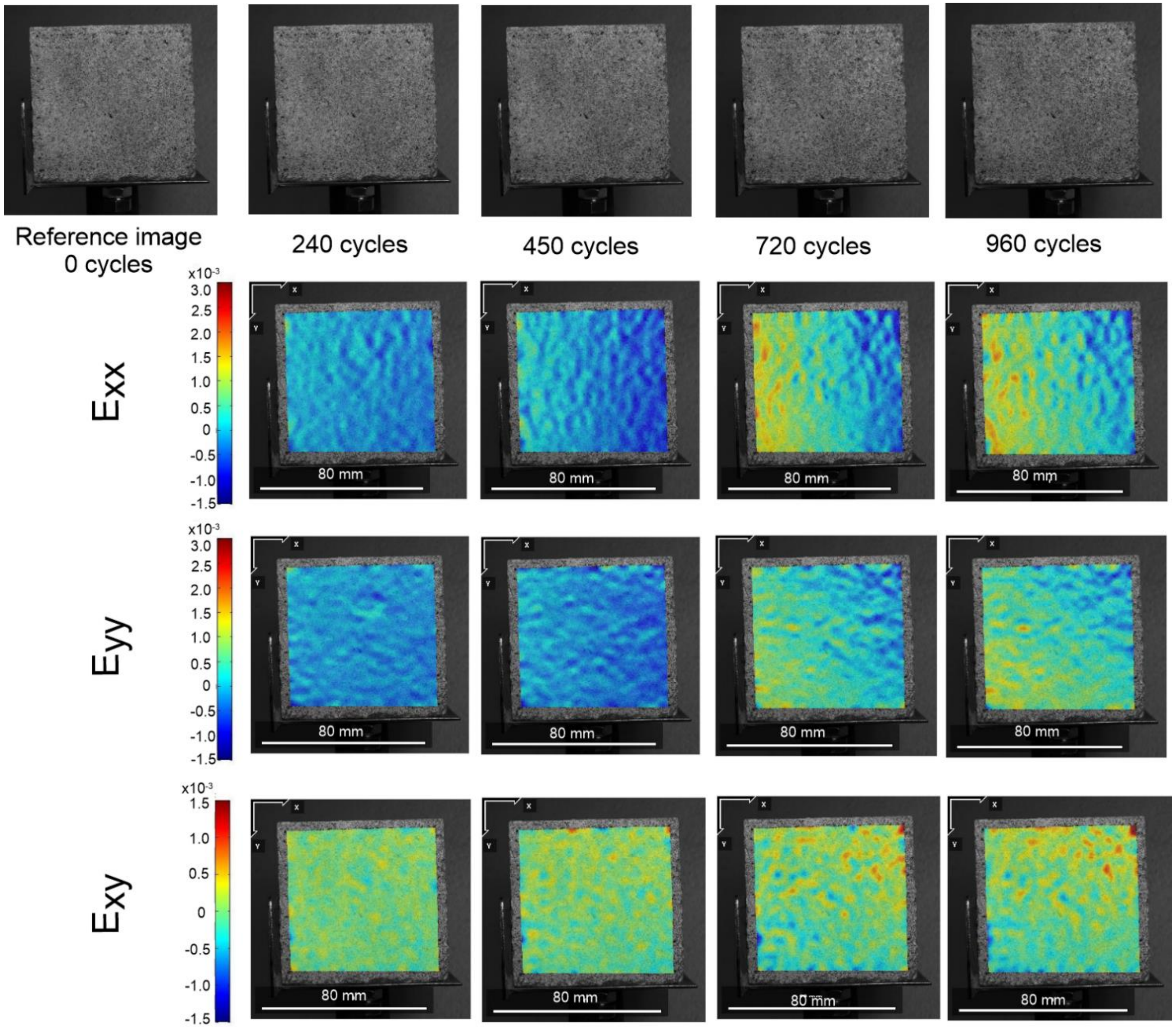

Figure A-4 DIC analysis for sample C3 – face with speckle pattern

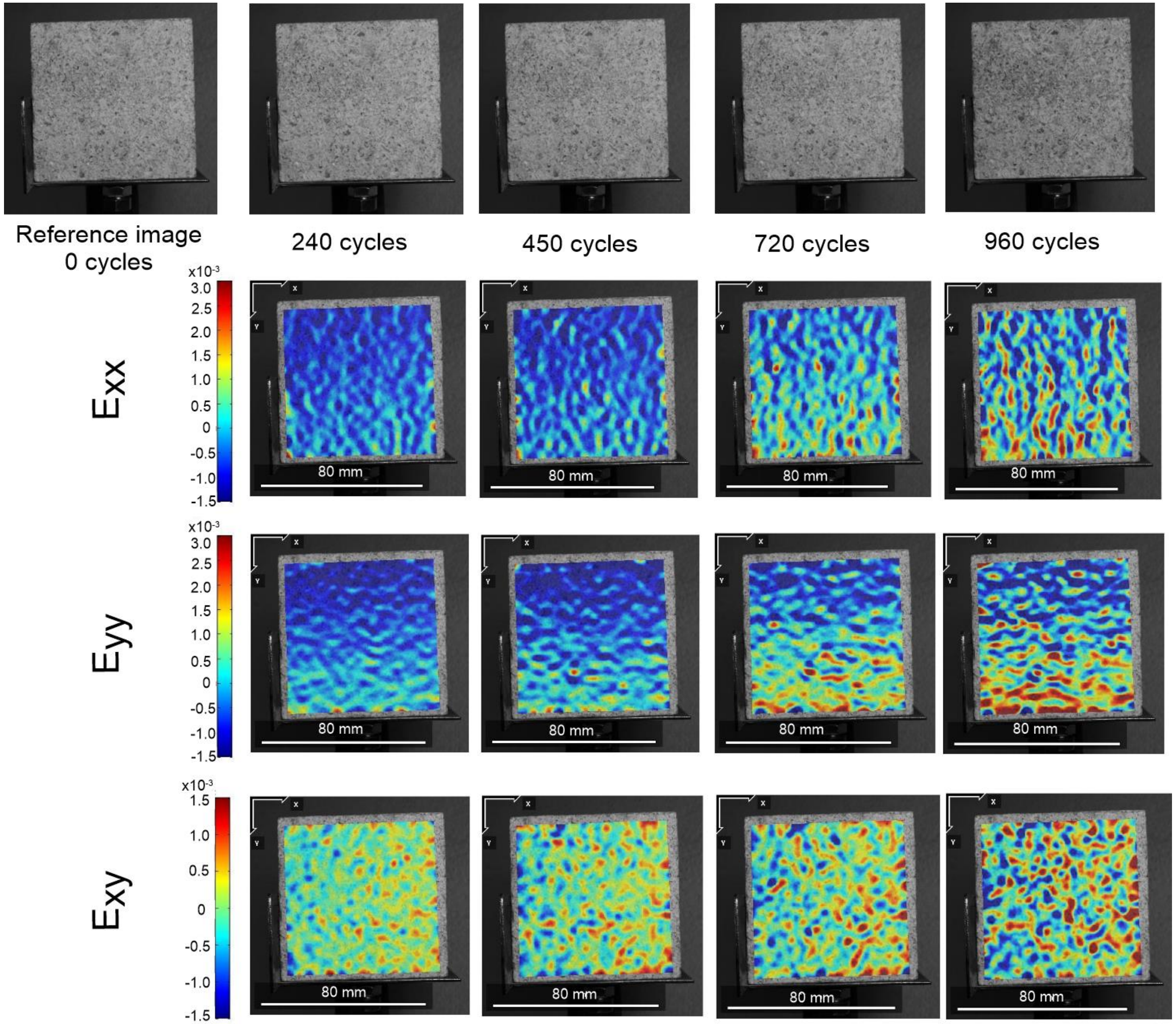

Figure A-5 DIC analysis for sample C3 – face without speckle pattern

# Appendix C. Implementation of bond model (damage law).

## C.1 Rate equations for general bond damage model.

Implementation is based on the implicit integration scheme proposed by Simo and Hughes, (1998) for elastoplastic models. The scheme is generally used to integrate all model equations: damage rate equations (bond model), elastoplastic rate equations (matrix model) and bond-matrix coupling equations (stress and strain partition and $X_m$ and $X_b$ dependency). In order to use this scheme, damage model is described by the general rate equations proposed by Carol et al. (2001) who showed that they are similar to those of elastoplasticity. They include the elastic law, the flow rule, the hardening law and the Kuhn-Tucker condition.

$d\sigma_{ij}^{b} = D_{ijkl}^{eb}(d\varepsilon_{kl}^{b} - d\varepsilon_{kl}^{db})$ with $D_{ijkl}^{eb}$ bond secant (damaged) elastic stiffness matrix

$d\varepsilon_{ij}^{db} = r_{ij}^{db} d\lambda^{db}$ with $r_{ij}^{db}$ bond damage rule

$dr_{k}^{db} = h_{k}^{db} d\lambda^{db}$ with $h_{k}^{db}$ bond damage evolution law
and $r_{k}^{db}$ bond damage evolution parameters

$F^{db} d\lambda^{db} = 0$ with $F^{db} \leq 0$ bond damage loading function
and $d\lambda^{db} \geq 0$ bond damage multiplier

where $d\lambda^{db}$ is equal to the parameter *dL* defined by Carol et al. (2001).

The strain entering in the mechanical model is defined as the difference between the total ($\varepsilon_{ij}^{totb}$) and the thermal strains ($\varepsilon_{ij}^{tempb}$).

$$\varepsilon_{ij}^{b} = \varepsilon_{ij}^{totb} - \varepsilon_{ij}^{tempb}$$

Bond strain $\varepsilon_{ij}^{b}$ and bond stress $\sigma_{ij}^{b}$ are related by the secant stiffness and compliance matrix:

$$\sigma_{ij}^{b} = D_{ijkl}^{eb} \varepsilon_{kl}^{b}$$

$$\varepsilon_{ij}^{b} = C_{ijkl}^{eb} \sigma_{kl}^{b}$$

The secant matrix $D_{ijkl}^{eb}$ is related to the initial (undamaged) secant matrix $D_{ijkl}^{eb0}$ by the damage law:

$$D_{ijkl}^{eb} = e^{-L} D_{ijkl}^{eb0}$$
$$C_{ijkl}^{eb} = e^{L} C_{ijkl}^{eb0}$$

Finally, the damage loading function is defined in terms of energy:

$F^{db} = u^{b} - r(\lambda^{db})$ with $u^{b} = \frac{1}{2}\sigma_{ij}^{b}\varepsilon_{ij}^{b}$ bond current (secant) elastic energy
and $r(\lambda^{db})$ is the bond damage locus

Within this formalism, the flow rule is directly the strain tensor:

$$r_{ij}^{db} = \frac{\partial F^{db}}{\partial \sigma_{ij}^{b}} = \frac{\partial u^{b}}{\partial \sigma_{ij}^{b}} = \frac{1}{2}\left(\varepsilon_{ij}^{b} + \sigma_{kl}^{b}\frac{\partial \varepsilon_{ij}^{b}}{\partial \sigma_{kl}^{b}}\right) = \frac{1}{2}\left(\varepsilon_{ij}^{b} + \underbrace{\sigma_{kl}^{b} C_{ijkl}^{eb}}_{\varepsilon_{ij}^{b}}\right) = \varepsilon_{ij}^{b}$$

The hardening

$$h^{db} = -\frac{\partial F^{db}}{\partial \lambda^{db}} = \frac{\partial r}{\partial \lambda^{db}}$$

The evolution of the damage locus can be defined by three different expressions:

Linear: $r = r_0 + r_1\lambda^{db}$ in which case, $h^{db} = r_1$

Exponential: $r = r_0 e^{r_1\lambda^{db}}$ in which case, $h^{db} = r_1 r$

Logarithmical $r = r_0 + r_1 \ln\left(\frac{1+\lambda^{db}}{1+\lambda_0^{db}}\right)$ in which case, $h^{db} = \frac{r_1}{1+\lambda^{db}}$

## *C.2 Discrete equations for the damage model.*

### *Elastic law.*

The scheme used to solve the discrete equation is not directly based on the linearization of the rate equations. The presence of an exponential in the damage law makes indeed inaccurate its approximation by a linear function, leading to small steps and a high number of sub-increments in the integration procedure. Alternatively, the discrete stress increment has been directly expressed as the difference between its value at the beginning and the end of the step:

$$\Delta\sigma_{ij}^{b}\Big|^{n+1} = D_{ijkl}^{eb}\Big|^{n+1}\varepsilon_{kl}^{b}\Big|^{n+1} - D_{ijkl}^{eb}\Big|^{n}\varepsilon_{kl}^{b}\Big|^{n} = D_{ijkl}^{eb}\Big|^{n}\left(e^{-\Delta\lambda^{bd}\big|^{n+1}}\varepsilon_{kl}^{b}\Big|^{n+1} - \varepsilon_{kl}^{b}\Big|^{n}\right)$$

$$\Delta\sigma_{ij}^{b}\Big|^{n+1} = D_{ijkl}^{eb}\Big|^{n}\left(e^{-\Delta\lambda^{bd}\big|^{n+1}}\varepsilon_{kl}^{b}\Big|^{n+1} - \left(\varepsilon_{kl}^{b}\Big|^{n+1} - \Delta\varepsilon_{kl}^{b}\right)\right)$$

$$\Delta\sigma_{ij}^{b}\Big|^{n+1} = D_{ijkl}^{eb}\Big|^{n}\left(\Delta\varepsilon_{kl}^{b} - \varepsilon_{kl}^{b}\Big|^{n+1}\left(1 - e^{-\Delta\lambda^{bd}\big|^{n+1}}\right)\right)$$

$$\Delta\sigma_{ij}^{b}\Big|^{n+1} = D_{ijkl}^{eb}\Big|^{n}\left(b_{\varepsilon}\big|^{n+1}\Delta\varepsilon_{kl}^{ext} - \varepsilon_{kl}^{b}\Big|^{n+1}\left(1 - e^{-\Delta\lambda^{bd}\big|^{n+1}}\right)\right)$$

The previous equations implicitly state the following discrete flow rule

$$\Delta\varepsilon_{ij}^{d}\Big|^{n+1} = \varepsilon_{ij}^{b}\Big|^{n+1}\left(1 - e^{-\Delta\lambda^{bd}\big|^{n+1}}\right)$$

It can be noted that the classical discrete linearization of the damage law is recovered by developing in series the term within parenthesis up to order 1. However, as previously indicated, this linearization has not been considered for accuracy issues.

$$\Delta\varepsilon_{ij}^{d}\Big|^{n+1} = \varepsilon_{ij}^{b}\Big|^{n+1}\Delta\lambda^{bd}\Big|^{n+1}$$

Noting:

$$\Delta\sigma_{ij}^{bT}\Big|^{n+1} = D_{ijkl}^{eb}\Big|^{n} b_{\varepsilon}\big|^{n}\Delta\varepsilon_{ij}^{ext}\Big|^{n+1}$$

$$\sigma_{ij}^{bT}\Big|^{n+1} = D_{ijkl}^{eb}\Big|^{n}\left(b_{\varepsilon}|^{n}\Delta\varepsilon_{ij}^{ext}\Big|^{n+1} + \varepsilon_{ij}^{b}\Big|^{n}\right)$$

the bond trial stress increment and the stress increment tensor, the system of discrete equations becomes:

$$\Delta\sigma_{ij}^{b}\Big|^{n+1} = e^{-\Delta\lambda^{bd}|^{n+1}} D_{ijkl}^{eb}\Big|^{n}\Delta\varepsilon_{ij}^{b}\Big|^{n+1} + \left(1 - e^{-\Delta\lambda^{bd}|^{n+1}}\right) D_{ijkl}^{eb}\Big|^{n}\Delta\varepsilon_{ij}^{b}\Big|^{n+1} - \left(1 - e^{-\Delta\lambda^{bd}|^{n+1}}\right) D_{ijkl}^{eb}\Big|^{n}\varepsilon_{kl}^{b}\Big|^{n+1}$$

$$\Delta\sigma_{ij}^{b}\Big|^{n+1} = e^{-\Delta\lambda^{bd}|^{n+1}} D_{ijkl}^{eb}\Big|^{n}\Delta\varepsilon_{ij}^{b}\Big|^{n+1} - \left(1 - e^{-\Delta\lambda^{bd}|^{n+1}}\right) D_{ijkl}^{eb}\Big|^{n}\left(\underbrace{\varepsilon_{kl}^{b}\Big|^{n+1} - \Delta\varepsilon_{ij}^{b}\Big|^{n+1}}_{\varepsilon_{kl}^{b}|^{n}}\right)$$

$$\Delta\sigma_{ij}^{b}\Big|^{n+1} = e^{-\Delta\lambda^{bd}|^{n+1}} \underbrace{D_{ijkl}^{eb}\Big|^{n} b_{\varepsilon}|^{n+1}\Delta\varepsilon_{ij}^{ext}\Big|^{n+1}}_{\frac{b_{\varepsilon}|^{n+1}}{b_{\varepsilon}|^{n}}\Delta\sigma_{ij}^{bT}|^{n+1}} - \left(1 - e^{-\Delta\lambda^{bd}|^{n+1}}\right)\underbrace{D_{ijkl}^{eb}\Big|^{n}\varepsilon_{kl}^{b}\Big|^{n}}_{\sigma_{ij}^{b}|^{n}}$$

### *Damage evolution law.*

The discrete expression of the hardening law simply reads:

$$\Delta r^{db}\Big|^{n+1} = \frac{\partial r^{db}}{\partial\lambda^{db}}\bigg|^{n+1} \Delta\lambda^{db}\Big|^{n+1}$$

### *Kuhn-Tucker condition.*

The Kuhn-Tucker condition is given by

$$F^{db}\Big|^{n+1} = 0 \text{ if } \Delta\lambda^{db}\Big|^{n+1} > 0$$

and

$$\Delta\lambda^{db}\Big|^{n+1} = 0 \text{ if } F|^{n+1} = 0$$

### *Stress point algorithm for damage model.*

The stress point algorithm is based on an implicit scheme. The Newton-Raphson procedure is used to solve the non-linearity of the system.

#### *Newton-Raphson procedure*

The NR procedure aims at cancelling the residues of the elastic law ($res_{ij}^{\sigma^{b}}$), hardening rule ($res^{r^{db}}$) and Kuhn-Tucker condition ($res^{F^{db}}$). There residues read:

$$res_{ij}^{\sigma^{b}}\Big|^{n+1} = \Delta\sigma_{ij}^{b}\Big|^{n+1} - e^{-\Delta\lambda^{bd}|^{n+1}} \frac{b_{\varepsilon}|^{n+1}}{b_{\varepsilon}|^{n}}\Delta\sigma_{ij}^{bT}\Big|^{n+1} + \left(1 - e^{-\Delta\lambda^{bd}|^{n+1}}\right)\sigma_{ij}^{b}\Big|^{n}$$

$$res^{r^{db}}\Big|^{n+1} = \Delta r^{db}\Big|^{n+1} - \frac{\partial r^{db}}{\partial\lambda^{db}}\bigg|^{n+1} \Delta\lambda^{db}\Big|^{n+1}$$

$$res^{F^{db}}\Big|^{n+1} = F^{db}\Big|^{n+1}$$

The cancellation is performed by developing each residue at 1st order:

$$res_{ij}^{\sigma^{b}}\Big|_{it+1}^{n+1} = res_{ij}^{\sigma^{b}}\Big|_{it}^{n+1} + \frac{\partial res_{ij}^{\sigma^{b}}}{\partial\sigma_{kl}^{b}}\bigg|_{it}^{n+1} \delta\sigma_{kl}^{b}\Big|_{it+1}^{n+1} + \frac{\partial res_{ij}^{\sigma^{b}}}{\partial r^{db}}\bigg|_{it}^{n+1} \delta r^{db}\Big|_{it+1}^{n+1} + \frac{\partial res_{ij}^{\sigma^{b}}}{\partial\lambda^{db}}\bigg|_{it}^{n+1} \delta\lambda^{db}\Big|_{it+1}^{n+1}$$

$$\left.\mathrm{res}^{r^{db}}\right|_{it+1}^{n+1} = \left.\mathrm{res}^{r^{db}}\right|_{it}^{n+1} + \left.\frac{\partial \mathrm{res}^{r^{db}}}{\partial \boldsymbol{\sigma}_{\mathbf{ij}}^{\mathbf{b}}}\right|_{it}^{n+1} \left.\delta\sigma_{ij}^{b}\right|_{it+1}^{n+1} + \left.\frac{\partial \mathrm{res}^{r^{db}}}{\partial r^{db}}\right|_{it}^{n+1} \left.\delta r^{db}\right|_{it+1}^{n+1} + \left.\frac{\partial \mathrm{res}^{r^{db}}}{\partial \lambda^{db}}\right|_{it}^{n+1} \left.\delta\lambda^{db}\right|_{it+1}^{n+1}$$

$$\left.\mathrm{res}^{F^{db}}\right|_{it+1}^{n+1} = \left.\mathrm{res}^{F^{db}}\right|_{it}^{n+1} + \left.\frac{\partial \mathrm{res}^{F^{db}}}{\partial \sigma_{ij}^{b}}\right|_{it}^{n+1} \left.\delta\sigma_{ij}^{b}\right|_{it+1}^{n+1} + \left.\frac{\partial \mathrm{res}^{F^{db}}}{\partial r^{db}}\right|_{it}^{n+1} \left.\delta r^{db}\right|_{it+1}^{n+1} + \left.\frac{\partial \mathrm{res}^{F^{db}}}{\partial \lambda^{db}}\right|_{it}^{n+1} \left.\delta\lambda^{db}\right|_{it+1}^{n+1}$$

Jacobian values take the following expression for the model under consideration:

$$\left.\frac{\partial \mathrm{res}_{ij}^{\sigma^{b}}}{\partial \sigma_{kl}^{b}}\right|_{it}^{n+1} = \delta_{ik}\delta_{jl}$$

$$\left.\frac{\partial \mathrm{res}_{ij}^{\sigma^{b}}}{\partial r^{db}}\right|_{it}^{n+1} = 0$$

$$\left.\frac{\partial \mathrm{res}_{ij}^{\sigma^{b}}}{\partial \lambda^{db}}\right|_{it}^{n+1} = -\left(-b_{\varepsilon}\big|_{it}^{n+1} e^{-\Delta\lambda^{bd}\big|_{it}^{n+1}} + \left.\frac{\partial b_{\varepsilon}}{\partial \lambda^{db}}\right|_{it}^{n+1} e^{-\Delta\lambda^{bd}\big|_{it}^{n+1}}\right) \frac{\Delta\sigma_{ij}^{bT}\Big|^{n+1}}{b_{\varepsilon}|^{n}} + e^{-\Delta\lambda^{bd}\big|_{it}^{n+1}} \sigma_{ij}^{b}\Big|^{n}$$

$$\left.\frac{\partial \mathrm{res}_{ij}^{\sigma^{b}}}{\partial \lambda^{db}}\right|_{it}^{n+1} = e^{-\Delta\lambda^{bd}\big|_{it}^{n+1}} \left[\left(b_{\varepsilon}\big|_{it}^{n+1} - \left.\frac{\partial b_{\varepsilon}}{\partial \lambda^{db}}\right|_{it}^{n+1}\right) \frac{\Delta\sigma_{ij}^{bT}\Big|^{n+1}}{b_{\varepsilon}|^{n}} + \sigma_{ij}^{b}\Big|^{n}\right]$$

Because:

$$\frac{\partial b_{\varepsilon}}{\partial \lambda^{db}} = \frac{1}{c_b} \frac{\partial \frac{\chi_b}{1+\chi_b}}{\partial \chi_b} \frac{\partial \chi_b}{\partial \lambda^{db}} = \frac{1}{c_b}\left(\frac{(1+\chi_b+\chi_m)-\chi_b}{(1+\chi_b+\chi_m)^2}\right)\left(-\frac{\chi_0}{2} e^{-\frac{\lambda^{bd}}{2}}\right) = -\frac{1}{2c_b}\frac{\chi_b(1+\chi_m)}{(1+\chi_b+\chi_m)^2}$$

$$\frac{\partial b_{\varepsilon}}{\partial \lambda^{db}} = -\frac{b_{\varepsilon}\,(1+\chi_m)}{2(1+\chi_b+\chi_m)}$$

$$b_{\varepsilon} - \frac{\partial b_{\varepsilon}}{\partial \lambda^{db}} = b_{\varepsilon}\left(1 + \frac{1+\chi_m}{2(1+\chi_b+\chi_m)}\right) = b_{\varepsilon}\frac{3+2\chi_b+3\chi_m}{2+2\chi_b+2\chi_m}$$

$$\left.\frac{\partial \mathrm{res}^{r^{db}}}{\partial \sigma_{ij}^{b}}\right|_{it}^{n+1} = 0$$

$$\left.\frac{\partial \mathrm{res}^{r^{db}}}{\partial r^{db}}\right|_{it}^{n+1} = 1 - \Delta\lambda^{bd}\big|_{it}^{n+1} \left.\frac{\partial^2 r^{db}}{\partial \lambda^{d}\,\partial r^{db}}\right|_{it}^{n+1}$$

$$\left.\frac{\partial \mathrm{res}^{r^{db}}}{\partial \lambda^{db}}\right|_{it}^{n+1} = \left.\frac{\partial r^{db}}{\partial \lambda^{db}}\right|_{it}^{n+1} - \Delta\lambda^{bd}\big|_{it}^{n+1} \left.\frac{\partial^2 r^{db}}{\partial {\lambda^{db}}^2}\right|_{it}^{n+1}$$

$$\left.\frac{\partial \mathrm{res}^{F^{db}}}{\partial \sigma_{ij}^{b}}\right|_{it}^{n+1} = \left.\frac{\partial F^{db}}{\partial \sigma_{ij}^{b}}\right|_{it}^{n+1} = \varepsilon_{ij}^{b}\big|_{it}^{n+1}$$

$$\left.\frac{\partial \mathrm{res}^{F^{db}}}{\partial r^{db}}\right|_{it}^{n+1} = \left.\frac{\partial F^{db}}{\partial r}\right|_{it}^{n+1} = -1$$

$$\left.\frac{\partial \mathrm{res}^{F^{db}}}{\partial \lambda^{db}}\right|_{it}^{n+1} = \left.\frac{\partial F^{db}}{\partial \lambda^{db}}\right|_{it}^{n+1} = u^{b}\big|_{it}^{n+1} - \frac{\eta^{b}}{dt}$$

$\eta^b$ is a parameter of viscosity. Note that the dependency of $F^{db}$ on $\lambda^{db}$ through *r* is already considered in $\frac{\partial \mathrm{res}^{F^{db}}}{\partial r^{db}}$ (r and $\lambda^{db}$ are considered independent variables in the derivation).

$$\frac{\partial u^b}{\partial \lambda^{db}} = \frac{1}{2}\sigma_{ij}^b \frac{\partial \varepsilon_{ij}^b}{\partial \lambda^{db}} = \frac{1}{2}\sigma_{ij}^b \frac{\partial\left(C_{ijkl}^{eb}\sigma_{kl}^b\right)}{\partial \lambda^{db}} = \frac{1}{2}\sigma_{ij}^b \frac{\partial\left(e^{\lambda^{db}} C_{ijkl}^{eb0}\right)\sigma_{kl}^b}{\partial \lambda^{db}} = \frac{1}{2}\sigma_{ij}^b C_{ijkl}^{eb}\sigma_{kl}^b = \frac{1}{2}\sigma_{ij}^b\varepsilon_{ij}^b = u^b$$

### *Tangent Matrix.*

Finally, the tangent matrix of the damage model must be provided to construct the tangent matrix of the composite model that will enter in the global tangent stiffness matrix of the Finite Element scheme. It is obtained by stating the consistency condition on the damage loading function.

$$dF^{db} = \frac{\partial F^{db}}{\partial \sigma_{ij}^b} d\sigma_{ij}^b + \frac{\partial F^{db}}{\partial r^{db}} dr^{db} + \frac{\partial F^{db}}{\partial \lambda^{db}} d\lambda^{db}$$

$$dF^{db} = \frac{\partial F^{db}}{\partial \sigma_{ij}^b} D_{ijkl}^{eb}\left(d\varepsilon_{kl}^b - r_{kl}^{db} d\lambda^{db}\right) + \frac{\partial F^{db}}{\partial r^{db}} h^{db} d\lambda^{db} + \frac{\partial F^{db}}{\partial \lambda^{db}} d\lambda^{db} = 0$$

$$dF^{db} = \frac{\partial F^{db}}{\partial \sigma_{ij}^b} D_{ijkl}^{eb}\left(b_\varepsilon d\varepsilon_{kl}^{ext} - \varepsilon_{kl}^b d\lambda^{db}\right) + \left(\frac{\partial F^{db}}{\partial r^{db}} h^{db} + \frac{\partial F^{db}}{\partial \lambda^{db}}\right) d\lambda^{db} = 0$$

The increment of damage multiplier can then be obtained as:

$$d\lambda^{db} = \frac{\dfrac{\partial F^{db}}{\partial \sigma_{ij}^b} D_{ijkl}^{eb} b_\varepsilon}{\underbrace{\dfrac{\partial F^{db}}{\partial \sigma_{ij}^b} D_{ijkl}^{eb}\varepsilon_{kl}^b}_{-H_{cr}^{db}} \underbrace{- \dfrac{\partial F^{db}}{\partial r^{db}} h^{db} - \dfrac{\partial F^{db}}{\partial \lambda^{db}}}_{H^{db}}} d\varepsilon_{kl}^{ext} = b_\varepsilon \frac{\varepsilon_{ij}^b D_{ijkl}^{eb}}{\underbrace{\varepsilon_{ij}^b\sigma_{ij}^b}_{2u^b} - \dfrac{\partial F^{db}}{\partial r^{db}} h^{db} - \dfrac{\partial F^{db}}{\partial \lambda^{db}}} d\varepsilon_{kl}^{ext}$$

$$d\lambda^{db} = b_\varepsilon \frac{\sigma_{kl}^b}{u^b + h^{db} + \dfrac{\eta^b}{dt}} d\varepsilon_{kl}^{ext}$$

which leads to the following tangent matrix.

$$d\sigma_{ij}^b = D_{ijkl}^{eb}\left(b_\varepsilon d\varepsilon_{kl}^{ext} - r_{kl}^{db} d\lambda^{db}\right) = D_{ijkl}^{eb}\left(b_\varepsilon d\varepsilon_{kl}^{ext} - \varepsilon_{kl}^b d\lambda^{db}\right) = b_\varepsilon D_{ijkl}^{eb} d\varepsilon_{kl}^{ext} - \sigma_{ij}^b d\lambda^{db}$$

$$d\sigma_{ij}^b = \left( b_\varepsilon D_{ijkl}^{eb} - \underbrace{\frac{b_\varepsilon \sigma_{ij}^b \sigma_{kl}^b}{2u^b - \dfrac{\partial F^{db}}{\partial r^{db}} h^{db} - \dfrac{\partial F^{db}}{\partial \lambda^{db}}}}_{\sigma_{ij}^b \frac{\partial \lambda^{db}}{\partial \varepsilon_{kl}^{ext}}} \right) d\varepsilon_{kl}^{ext} = b_\varepsilon \underbrace{\left( D_{ijkl}^{eb} - \frac{\sigma_{ij}^b \sigma_{kl}^b}{u^b + h^{db} + \dfrac{\eta^b}{dt}} \right)}_{D_{ijkl}^b} d\varepsilon_{kl}^{ext}$$

# Effect of thermal cycles on rock massif stability.

This Ph.D. thesis deals with the effect of atmospheric thermal cycles in rocks. Focused on the real case of La Roque Gageac, a small town located in France, which experiences rock fall risks related to the atmospheric thermal variations.

An experimental study is performed, in order to isolate the effect of atmospheric thermal cycles in the La Roque Gageac limestone. Rock samples were submitted to thermal cycles. The damage induced in the samples is evaluated through different measurements.

In order to reproduce the macroscopic mechanical response of the rock under the applied thermal cycles, a constitutive model based on the concept of composite material defined by Vaunat & Gens (2003) is developed. This constitutive model has been implemented in the finite elements code CODE_BRIGHT and validated with the experimental results.